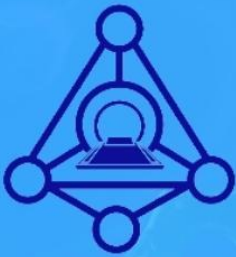


AiJR

AIJR Abstracts



LASICOM



Abstracts of

1st International Conference on Computational & Applied Physics

ICCAPH'2021

Editor: **BOUAMRA Faiza**

Organized by:

**Surfaces, Interfaces and Thin Films Laboratory (LASICOM),
Department of Physics, Faculty of Science,
University Saad Dahleb Bida 1, Algeria**

26–28 September 2021



2022

ICCAP'2021

BOUAMRA Faiza
(Editor)

Abstracts of
1st International Conference on
Computational & Applied Physics

ICCAP'2021 (26th –28th September 2021)

Organized by

Surfaces, Interfaces and Thin Films Laboratory (LASICOM),
Department of Physics,
Faculty of Science,
University Saad Dahleb Blida 1,
Algeria

Published by

AIJR Publisher, Dhaurahra, Balrampur, India 271604



Abstracts of 1st International Conference on Computational & Applied Physics (ICCAP'2021)
26th –28th September 2021

Editor

Dr. Faiza Bouamra

Head of Surfaces, Interfaces and Thin Films Laboratory- LASICOM
University of Blida1- Faculty of Sciences - Physics Department
BP270 Route de Soumaa - Blida

Conference Organizers

Surfaces, Interfaces and Thin Films Laboratory (LASICOM), Department of Physics, Faculty of Science, University Saad Dahleb Blida 1, Algeria

Conference Venue

Online (Virtual)

ISBN: 978-81-954993-3-5

DOI: <https://doi.org/10.21467/abstracts.122>

Type

Abstract Book

Series

AIJR Abstracts

Published

08 March 2022

Number of Pages

206

Copyeditors

- Ritika Dubey
- Praneeta

Imprint

AIJR Books

© 2022 [Copyright](#) held by the author(s) of the individual abstract. Abstracts are not considered as pre-publication and hence author(s) are free for subsequent publications. Abstracting is permitted with credit to the source.

This is an open access book under Creative Commons Attribution-NonCommercial 4.0 International (CC BY-NC 4.0) license, which permits any non-commercial use, distribution, adaptation, and reproduction in any medium, as long as the original work is properly cited.

Published by



AIJR Publisher, Dhaurahra, Balrampur, India 271604

Disclaimer

This abstract book has been produced using author-supplied copy via conference organizer. Editing has been restricted to some formatting and style where appropriate. No responsibility is assumed by the publisher or conference organizer for any claims, instructions, methods, diagnosis, treatment, or policy contained in the abstracts: it is recommended that these shall be verified independently. Further, the conference organizer & AIJR publisher both remain neutral with regard to jurisdictional claims in published maps and institutional affiliations.

ICCAP'2021

Table of Contents

Disclaimer.....	i
About the Conference.....	ix
Scientific Committee.....	xi
Acknowledgement.....	xii
The Superexchange Mechanism in Crystalline Compounds: The Case of KMF_3 (M=Mn, Fe, Co, Ni) Perovskites	1
Novel Visualization of Crystal Structure and Energetics.....	2
Ab Initio Calculation of Chirality in Crystals.....	3
Continuum Solvation for Finite and Infinite Periodic Systems in Crystal	4
Lattice Dynamics and Thermal Properties of Materials.....	5
Crystal17: A Modern Tool for Ab Initio Solid State Chemistry & Physics	6
Looking at Benchmarks for Density Functional Calculations	7
Understanding Structure and Properties of $MgCl_2$ Supported Ziegler-Natta Nanoclusters by DFT, Spectroscopy and Machine Learning: How Modelling Uncovers the Origin of Industrial Catalysis.....	8
Magnetism and Half-Metallicity of Solids from the Spin Polarization of P Orbitals.....	10
Enhanced Figure of Merit in Molecular Junctions	11
Intensity-based Wide-field Magneto-optical Microscopy	12
Boosting the Performance of Magnetic Nanoparticles: Magnetic Field-assisted Assembly and Magnetic Functionalization	13
Heterostructures Based on Functionalized Graphene and Free-standing Graphene Membranes.....	14
Effect of the Substrate on the Structural Properties of Cu_2ZnSnS_4 Thin Films Synthesized by Electrodeposition	15
Monte Carlo Method Study of Thin Films of The Spin-1 Ashkin Teller Model in the Presence of the Crystal Field	17
Dielectric Characterization by Impedance Meter of Thin Films $Bi_2S_{3(0.6)}ZnS_{(0.4)}$ Composites.....	18

Green Synthesis and Characterization of Silver Nanoparticles	23
FEM Simulation and Performance Evaluation of MEMS Pressure Sensor Based on Capacitive Effect Using Molybdenum and Tungsten	25
Effect of Extended Gettering during the Emitter Formation on the Electrical Performance of Multicrystalline Silicon Based Solar Cells	27
Efficient Synthesis and Characterization of Highly Pure Nanosilica from Sand.....	29
Positron Annihilation Lifetime Spectroscopy in Neutrons Irradiated CR39 Polymer	31
Synthesis and Characterization of FeCo Nanoparticles by Hydrothermal Method.....	33
Microstructural Investigation of ZnO Nanowires for Therapeutic Applications	35
Real Time Ultrasoft Longitudinal Photons Self Energy at Next to-leading Order in Hot Scalar QED	36
Sensing Properties and Sensitivity Improvement of an Asymmetric Waveguide with Dispersive Left-handed Material.....	40
Towards the Optimization of the Performance of N-I-P Microcrystalline Silicon nc-Si:H Flexible Solar Cells .	42
(2+1) D Massless Dirac Equation in Anti de-Sitter Space	44
Spin-polarized DFT Calculation of the Magneto-electronic Properties Under Pressure of the YCrSb Half-heusler Alloy	51
Mechanical Characteristics of Polyester Filled with Palm Fibers and Ash Particles.....	53
Superstatistical Properties of Ionization Rates of Li^+	54
Raman and IR Spectroscopy of SnO_2 Nanostructures with Oxygen Vacancies: An Ab-Initio Calculations	57
Numerical Simulation of the Influence of an Sb layer on a Cu (In,Ga)Se₂ Solar Cells Performance	60
Mechanical and Anisotropy Properties of SrCdPt Compound under Pressure	61
Effect of Annealing Time on Electrodeposited ZnS Thin Films	63
Effect of Electric and Magnetic Field on the Transport Coefficients of a Non-Equilibrium Gas by the Monte Carlo Method.....	65
Comparative Simulation of the Perovskite Solar Cell	68
Buckling Analysis of Carbon Nanotube-Reinforced Composite Plates Resting on Elastic Foundation.....	70
Study of n/p solar cell based on ITO/Si Heterojunction	71
Synthesis and Characterization of Layered Double Hydroxide Based on Zn and Cr Used for Anion Exchange .	73

Theoretical Study of the Structural Electronic Properties of half-Heusler RbInSn Alloy	74
Study of Microstructural and Electrical Properties of the (P)A-Si : H/(N)C-Si Heterojunction:Uncooled MicrobolometerApplication	75
DCF Method for Dispersion Compensation in Optical Fiber Link for LongHaul Communication.....	77
First-Principles Predictions of the Electronic, Optical and Thermoelectric Properties of the New Zintl-Phase Sr_2CdAs_2	78
Solvent Effect on Hyper-Rayleigh Scattering (HRS) First Hyperpolarizability of Substituted Polyene: Ab Initio Study	81
Ab-initio Investigation of Structural, Electronic and Topological Properties of Half- Heusler Compounds: TiRh_z ($Z=\text{Sb,Bi}$).	83
Thermal And Dynamic Study of Confluent Round Jet of Different Diameters	86
First Principles Investigation of Structural and Electronic Properties of AlN/GaN Superlattices Growth Along Various Crystallographic Axes	88
Dangling Bonds Parameters Effect on Dark and Illuminated Conductivity in a-Si:H Absorber Layer for Solar Cells Applications.....	90
The Window Layer Doping Effect on the Performance of a $\text{SiO}_x\text{:H}$ Based Solar Cells	92
Study of Ultra-Fast Phenomena Generated in Femtosecond Laser-material Interactions.....	95
Special Finite Element Modeling for Predicting the Mechanical Properties of CarbonNanotubes at the Atomic Scale	97
Improvement of Positron Annihilation Lifetime Spectrometer Resolution: AComparative Study.....	98
Thermal Properties of the Klein-Gordon Oscillator in Deformed Space.....	100
Role of Hydroxyl Group in CO Adsorption on SnO_2 (110) Surface Investigated by a First-principle Study	102
The Effect of Aluminum Sources On $(\text{Gd}_{0.7}\text{Lu}_{0.3})_3\text{Al}_5\text{O}_{12}$ Cubic Garnet Structure Synthesized by Co Precipitation Method	104
Structure Properties of $\text{LiAl}(\text{WO}_4)_2$ Solid Solution	106
The Influence of Preparation Parameters on Structural and Optical Properties of n-Type Porous Silicon.....	108
Study the Structural Properties of $\text{WO}_3\text{:Fe}$ Thin FilmsElaborated by Spray Pyrolysis Technique at 450 °C.....	110
Calculation of the Structural Properties of GdBO_3 by the Theoretical Method ab-initio	111
Computational Determination of theMagneto-electronic Properties of $\text{Ce}_{1-x}\text{Cu}_x\text{O}_2$ ($x=12.5\%$): Emerging Materials for Spintronic Devices.....	113

First-Principles Calculations of Structural, Elastic, and Electronic Properties of Antiperovskites Ca_3SiO and Ca_3GeO	115
Hyperfine Structures ab-initio Calculations of the $2p^4(^3P)3d^{25+1}L_J$ States in the Fluorine Atom	117
Synthesis of Zeolites from Pure and Natural Products, Modification and Application in Wastewater Treatment	119
Characterization (FT-Raman, FT-IR Spectra) of 3,5-Dimethoxybenzaldehyde $\text{C}_9\text{H}_{10}\text{O}_3$ and Compared with Density Functional Theory (DFT)	121
Cathodoluminescence Calculation of AlGaN/GaN Quantum-Wells by Monte Carlo Model: Effect of Compositional and Temperature	123
Bloch Surface Waves Based Biosensor Using a Ternary Photonic Crystal	126
Hyperfine Structure of the $3p^4s^4p$ State of the Chlorine Atom	128
First-principles Calculations of the Physical Properties and Stability of ScN	130
Surface Metal Effect on I(V) Characteristics Ti/6H-SiC Schottky Diode at Room Temperature	133
Adsorption of Anticancer Drug Molecule on Single Wall Carbon Nanotube: An ab-initio Study	135
First Principal Study of Physical Properties of Rare Earth Based Heusler Compounds X_2RuPb (X= Sc, Y and La)	137
Elaboration and Characterization of Black Silicon for Photovoltaic Solar Cells	139
Structural Investigations Studies of Antimony-Tungsten and Sodium Metaphosphate Glass Systems with NaPO_3 as Additive	141
In-depth Analyses of P-type Silicon Solar Cells by Laser-Induced Breakdown Spectroscopy (LIBS)	144
Diagnosis of an Unknown Solar Cell by Electrical Characterization	146
Affecting Parameters on Polymers Surface Treatment by Atmospheric Pressure Plasma Jets	148
Crystal Structure and Comparative Study via Hirshfeld Surface Analyses of Charge Transfer Compounds Based on Anthranilic Acid	150
Effect of Various Auxiliary Acceptors on the Optical and Photovoltaic Properties of a D-A'- π -A Sensitizing Dye. DFT and TD-DFT Study	152
Preparation and Characterizations of MgFe_2O_4 Spinel Semiconductor	153
Numerical Thickness Optimization Study of CIGS Based Solar Cells with SCAPS-1D	155
Influence of Porosity on the Structural and Electronic Properties of Porous Silicon	157

Label-free Biosensor Based on Photonic Crystal Microcavity for Malaria Detection with High Sensitivity	159
Ab-Initio Study of the Ferromagnetic Half-Metallic Perovskite KMgO_3	161
Ab Initio Calculations of the Structural and Electronics Properties of Double Tungstates $\text{NaY}(\text{WO}_4)_2$	164
First-principles Study of Structural, Electronic, Elastic and Thermal Properties of XPd_3 ($X = \text{Ca}, \text{Mg}$)	166
Synthesis and Characterization of Polystyrene (PS)/Copper Oxide CuO Nanocomposites	167
Theoretical Study of Structural and Electronics Properties of Lithium Niobate LiNbO_3	169
Effect of Doping with Niobium on the Properties of Titanium Dioxide Thin Films Prepared by Sol Gel (Spin-coating) Process	171
Structural, Electronic, Elastic and Thermodynamic Properties of ReAuSn	174
Investigation of Deposition Temperature and Time Effect on the Quality of FSF in n-PERT Solar Cells Using Phosphorus Doped Paper Sheets	177
Ab-initio Study of the Optoelectronic Properties of CsXCl_3 Perovskites ($X = \text{Pb}, \text{Sn}$ or Ge)	179
High Spin Polarization and Mechanic Stability of Half-Heusler Compounds: CrFeSn and CrFeGe as a Candidate in the Spin-FETs for Spintronic Applications	180
Investigation of an Additional Oxidation in-situ Step During Boron Diffusion Processes on P^+ Emitter Properties	182
Effect of Heat Treatment on Structural and FTIR and Lowercase	183
Characterization of Interfacial and Mechanical Properties Between Fiber and Polymer Matrix in Composite Materials	186

ICCAP'2021

About the Conference

The 1st International Conference on Computational & Applied Physics, ICCAP'2021, was organized on 26th to 28th September 2021. The Conference has been organized by Surfaces, Interfaces and Thin Films Laboratory (LASICOM), of Physics Department, Sciences Faculty of Borda University of Algeria. The Conference have variety of Plenary Lectures, Oral Session and E-Poster Presentations.

The conference has several goals at the same time such as:

- provides opportunities for the delegates to exchange new ideas and application experiences to establish relations and collaboration with world-Renowned speakers.
- The conference provides also a platform to discuss and an open meeting with world-Renowned speakers in all areas of Physics and their Applications
- Gathering Algerian and foreign scientists and researchers and offer them the opportunity to exchange information, update knowledge in different areas of research and discuss the orientations of scientific research from the international community
- Involve doctorates & students of master and present them the interest of the fields of materials physics and its applications
- Present the main novelties in the field of computational and applied physics.
- Establish collaborations with foreign specialist laboratories in the field of computational and applied physics.

For this, four topics of different domain of physics are presented:

Topic 01: Quantum Simulation of Physical Properties of low dimension and Periodic Systems.

Topic 02: First-Principals Modeling of Excited-State and response Phenomena in Materials.

Topic 03: Exotic Phenomena in Magnetism and Electronic Transport.

Topic 04: Synthesis and Characterization of Materials.

ICCAP'2021

Scientific Committee

Conference Chair

Dr. Faiza BOUAMRA

LASICOM Laboratory, Faculty of Science, University of Saad Dahleb Blida 1, Algeria

Vice Conference Chair

Dr. Abderrahim Guittoum

Nuclear Research Center of Algiers, Algeria

Scientific Committee

PROF. RUDOLF SCHAEFER, GERMANY

PROF. ANDREA EHRMANN, GERMANY

PROF. ROBERTO DOVESI, ITALY

PROF. MICHEL RÉRAT, FRANCE

PROF. LOUNIS SAMIR, GERMANY

PROF. HANSON ROBERT, US

PROF. JEAN-MARC GRENECHE, FRANCE

PROF. MARTIN KALBAC, CZECH REPUBLIC

PROF. ANNA MARIA FERRARI, ITALY

PROF. DERBAL MOURAD, ALGERIA

PROF. BARTOLOMEO CIVALLERI, ITALY

PROF. KLAUS DOLL, ITALY

PROF. JEAN-PIERRE FLAMENT, FRANCE

PROF. MARIE-LIESSE DOUBLET, FRANCE

PROF. DOROTHÉE BERTHOMIEU, FRANCE

PROF. NADJIB BAADJI, ALGERIA

PROF. BELKHIR HAFID, ALGERIA

PROF. BELLAL RACHID, ALGERIA

PROF. NASSIMA BENBRAHIM, ALGERIA

PROF. LAYACHI LOUAIL, ALGERIA

Acknowledgement

First,

The organizers would like to thank all participants to the ICCAP'2021 and invited speakers for agreeing to take part in this conference;

- 1- Prof. Roberto Dovesi, Theoretical Chemistry Group, Chemistry Department, University of Turin, Italy
- 2- Prof. Michel Rérat, E2S UPPA, CNRS, IPREM Université de Pau et des Pays de l'Adour, France.
- 3- Prof. Robert Honsan, St. Olaf College, Northfield, USA
- 4- Prof. Silvia Maria Casassa, Theoretical Chemistry Group, Chemistry Department, University of Turin, Italy
- 5- Prof. Anna Maria Ferrari, Torino, Italy
- 6- Prof. Nadjib Baadji, University of M'sila, Algeria.
- 7- Prof. Andrea Savin, Sorbonne, France
- 8- Prof. Frederic Labat, ENS-Paris
- 9- Dr. Maddalina D'Amore, Theoretical Chemistry Group, Chemistry Department, University of Turin, Italy
- 10- Prof. Bennacer Badis, University of Guelma, Algeria
- 11- Prof. Jana Kalbáčová Vejpravová, Heyrovský Institute of Physical Chemistry, Czech Republic
- 12- Prof. Rudolf Schaefer, Institute of Solid State and Materials research, Dresden, Germany
- 13- Prof. Martin Kalbáč, Heyrovský Institute of Physical Chemistry, Czech Republic,
- 14- Prof. Bachir Bouhafis, University of Sidi Bel Abbes, Algeria

Secondly,

We would like to thank sponsors:

As Diamond sponsors we have:

- "Directorate General for Scientific Research and Technological Development, **DGRSDT**"
- **EURL Adichim** for his precious financial assistance.

As platinum sponsors:

- 'Thematic Science and Technology research Agency, **ATRST**'
- **Sonelgaz** group.

As gold sponsors:

- SARL Biosphere
- SARL Sinal
- Sidal Group.

Sponsors



ICCAP'2021

P01

The Superexchange Mechanism in Crystalline Compounds: The Case of KMF_3 (M=Mn, Fe, Co, Ni) Perovskites

Roberto Dovesi¹, Fabien Pascale², Philippe D'Arco³, Francesco Gentile⁴, and Valentina Lacivita⁵

¹Dipartimento di Chimica, Università di Torino, Via P. Giuria 5, 10125 Torino, Italy

²Université de Lorraine - Nancy, CNRS, Laboratoire de Physique et Chimie Théoriques, UMR 7019, Vandoeuvre-les-Nancy, France

³Sorbonne Université, CNRS-INSU, Institut des Sciences de la Terre, ITeP UMR 7193, F-75005 Paris, France

⁴Dipartimento di Ingegneria Chimica, dei Materiali e delle Produzioni Industriali DICMAPI, Università degli Studi di Napoli Federico II, Piazzale Vincenzo Tecchio 80, 80125, Napoli, Italy

⁵Samsung Semiconductors Inc., Advanced Materials Lab, 10 Wilson Rd., Cambridge, MA 02138, USA

*Corresponding author

ABSTRACT

The ferromagnetic and antiferromagnetic wavefunctions of four KMF_3 (M= Mn, Fe, Co and Ni) perovskites have been obtained quantum-mechanically with the CRYSTAL code, by using the Hartree-Fock (HF) Hamiltonian and three flavours of DFT (PBE, B3LYP and PBE0) and an *all-electron* Gaussian type basis set. In the Fe and Co cases, with d^6 and d^7 occupation, the JahnTeller distortion of the cubic cell is as large as 0.12 \AA . Various features of the superexchange interaction energies (SIE), namely additivity, dependence on the M-M distance, on the \widehat{MFM} angle, and on the adopted functional, are explored. The effect of SIE on the equilibrium geometry and volume of the unit cell is discussed, and it is shown that the key quantity is the spin polarization of the (closed shell) F ions along the M-F-M path. The effect of this *magnetic pressure* is evaluated quantitatively for the first time.

The superexchange coupling constant J , evaluated at the HF level and through the Ising model, underestimates the experimental values by about 60-70%. The more sophisticated Yamaguchi model (that takes into account the contamination of the FM and AFM spin states) does not reduce the discrepancy. These latter are bracketed by HF and PBE0. For PBE, the overestimation is huge.

Finally, Mulliken population data, charge and spin density maps and density of states are used to illustrate the electronic structure.



P02

Novel Visualization of Crystal Structure and Energetics

Robert M. Hanson

Professor of Chemistry, St. Olaf College Northfield, MN

*Corresponding author

ABSTRACT

I am a firm believer in the idea that you have to have the right tool for the right job. And that good tools are inherently community resources. It has been my delight to be a toolmaker and designer in the area of molecular visualization for the past 15 years. In this presentation I will discuss some of my favorite visualizations developed for Jmol over that time, with a focus on the area of solid-state physics and crystal structure. We will take a look at visualization of structure, energy, and symmetry. We will see how a simple accidental switch from a minus to a plus sign completely changes the perspective on close contacts, how solid-state phase transitions can be visualized as subtle changes in symmetric normal modes, and how the elegant use of "[3 + n]D" symmetry allows the description and visualization of incommensurately modulated structures in a variety of colorful and dynamic ways. We'll see how reciprocal lattices and Brillouin zones can be interactively constructed and explored by students and professionals alike.



P03

Ab Initio Calculation of Chirality in Crystals

Michel Rérat

E2S UPPA, CNRS, IPREM Université de Pau et des Pays de l'Adour, France

*Corresponding author

ABSTRACT

The chirality of a free molecule in solution is relatively easy to determine by measuring its optical activity or rotatory power, but this is not the case in the solid state. Indeed, the absolute structure of tartaric acid, for example, as obtained from the magnitude and sign of the chirality, χ , did not become available until 150 years after the discovery of Pasteur. This is due to the fact that, in solids, χ is a small quantity that contributes weakly to the refractive index n of crystal, and its circular birefringence, according to the expression: $n \sim \varepsilon^{1/2} \pm \varepsilon \omega \chi$ (for a non-magnetic material), where ε is the relative dielectric matrix and ω is the light frequency.

On the other hand, the quantum mechanical calculation of optical rotatory power as other magnetic response properties has its own issues due in particular to the choice of the gauge origin, R , in the angular momentum expression: $L = (r - R) \times \nabla_r / i$. If the gauge invariance is well solved for the magnetic properties of molecules, the appropriate form of the angular momentum operator is not a straightforward matter for periodic systems (see Ref.: Rérat and Kirtman, JCTC 17, 4063, 2021, <https://doi.org/10.1021/acs.jctc.1c00243>).

This theoretical work will be detailed in my presentation, with applications on minerals and molecular crystals.



P04

Continuum Solvation for Finite and Infinite Periodic Systems in Crystal

Frédéric Labat

Chimie ParisTech, PSL University, Institute of Chemistry for Life and Health Sciences – UMR 8060, Chemical Theory and Modelling Group, F-75005 Paris, France

*Corresponding author

ABSTRACT

In this contribution, we present recent progress made in the generalized finite-difference continuum solvation model recently implemented in the CRYSTAL code [1,2], with applications both to finite molecular systems and infinite periodic ones such as polymers, nanotubes, helices, and surfaces.

In particular, the self-consistent reaction-field procedure used to compute the electrostatic contribution to the solvation energy has recently been extended to consider a variety of atomic charges models belonging to the Class II and Class IV families [3,4].

In addition, the Cavitation, Dispersion and Structural effects model [5] for non-electrostatic contributions to the solvation energy and related nuclear gradients has also been implemented [6] and reparametrized [7], together with a fully analytical procedure for the calculation of the solvent-accessible surface area and its nuclear gradients [8] which has been generalized to periodic systems [9].

We discuss application of the proposed continuum solvation model to selected finite and infinite periodic systems, compare its performances to reference continuum solvation models and present the main current areas of development and application currently considered.

References

- [1] R. Dovesi, A. Erba, R. Orlando, C. M. Zicovich-Wilson, B. Civalleri, L. Maschio, M. Rérat, S. Casassa, J. Baima, S. Salustro and B. Kirtman *WIREs Comput Mol Sci.* 8, e1360 (2018).
- [2] F. Labat, B. Civalleri and R. Dovesi *J. Chem. Theory Comput.* 14, 5969-5983 (2018).
- [3] A. V. Marenich, S. V. Jerome, C. J. Cramer and D. G. Truhlar *J. Chem. Theory Comput.* 8, 527-541 (2012)
- [4] D. Vasseti and F. Labat *Int. J. Quantum Chem.* 121, e26560 (2020)
- [5] A. V. Marenich, C. J. Cramer and D. G. Truhlar *J. Phys. Chem. B* 113, 6378–6396 (2009)
- [6] I. Can Oğuz, D. Vasseti and F. Labat *Theor. Chem. Acc.* 140, 99 (2021)
- [7] D. Vasseti, I. Can Oğuz and F. Labat *J. Chem. Theory Comput.*, submitted
- [8] S. Hayryan, C. K. Hu, J. Skřivánek, E. Hayryane, I. Pokorný *J. Comput. Chem.* 26, 334 (2005)
- [9] D. Vasseti, B. Civalleri and F. Labat *J. Comput. Chem.* 41, 1464-1479 (2020).



P05

Lattice Dynamics and Thermal Properties of Materials

Bennacer Badis

Physics Laboratory at Guelma, University of Guelma P.O Box 401 Guelma 24000, Algeria

*Corresponding author

ABSTRACT

In this talk, we present studies on some binaries (SrX ($X=\text{S, Se, Te}$) and ternaries ($\text{LiB}^{\text{II}}\text{C}^{\text{V}}$) compounds by using first principles methods. The dynamical and vibrational properties are investigated by the density functional perturbation theory (DFPT). The phonon dispersion curves and their density of states will be presented. Instability and phase transition will be discussed in terms of mode softening. The calculated bond force constants for the ternaries give an indication on the nature of the bonds. The calculated phonon dispersions in conjunction with the quasi-harmonic approximation are used to predict the temperature and pressure dependence of various quantities such as the thermal expansion coefficient, the bulk modulus and the heat capacity.

At the end of this talk the phase transitions and lattice dynamics in perovskite-type hydride $\text{Li}_x\text{Na}_{1-x}\text{MgH}_3$ alloy will be presented.

Keywords: Ab initio methods, VCA, lattice dynamics, thermal expansion.



P06

Crystal17: A Modern Tool for Ab Initio Solid State Chemistry & Physics

S. Casassa

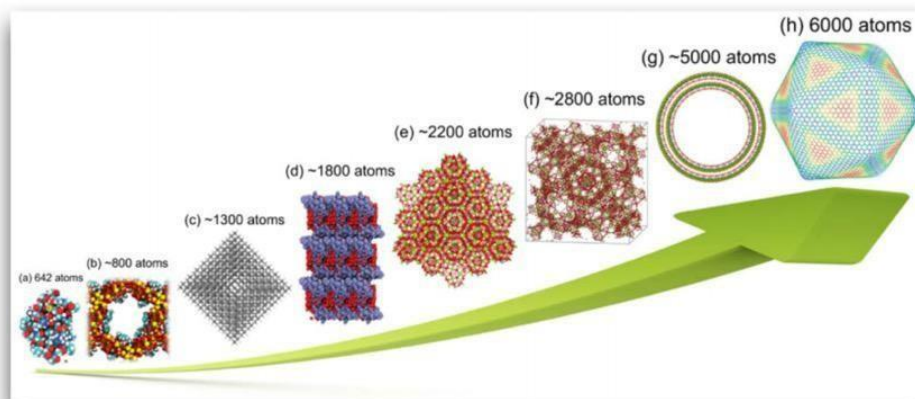
Theoretical Chemistry Group, Chemistry Department, University of Turin, Italy

*Corresponding author

ABSTRACT

The CRYSTAL *ab initio* package for solid state chemistry and physics is presented. First, the theoretical background is shortly recovered to allow for a better understanding of the limitations and peculiarity of the code. Then, some features are discussed with reference to some applications of both fundamental and technological interest. In particular:

- the massive parallel implementation of the code that allows for the modeling of realistic systems;
- the frequencies calculation complemented by the IR and Raman spectra reconstruction;
- the recent transport properties algorithm as applied to derive the thermoelectric performance of several materials (InGaN and Half-Heusler alloys, nanotubes, etc.)
- the new extension of the topological analysis of the charge density to f - and g - type basis functions which opens the way to the study of lanthanide and actinide compounds.



References

1. R. Dovesi et al., WIREs Comput. Mol. Sci. 8, e1360 (2018).
2. S. Casassa, A. Erba, J. Baima, R. Orlando, J. Comp. Chem. 36, 1940 (2015).
3. R. Orlando, M. Delle Piane, I. J. Bush, P. Ugliengo, M. Ferrabone, R. Dovesi, J. Comput.Chem. 33, 2276 (2012).
4. L. Maschio, B. Kirtman, S. Salustro, C. Zicovich-Wilson, R. Orlando, and R. Dovesi J. Phys.Chem. A 117, 11464 (2013)
5. A. Cossard, J.K. Desmarais, S. Casassa, C. Gatti and A. Erba, J. Phys. Chem. Lett. 12, 1862(2021).
6. H. C. Aroussi, N. L. Marana, F. Hamdache, R. Houaria, S. Bahlouli and S. Casassa, J. Phys.



P07

Looking at Benchmarks for Density Functional Calculations

Pascal Pernot¹, Andreas Savin²¹Institut de Chimie Physique, UMR8000 CNRS, Université Paris-Saclay, F-91405, Orsay, France²Laboratoire de Chimie Théorique, CNRS and UPMC Université Paris 06, Sorbonne University, F-75252 Paris, France

*Corresponding author

ABSTRACT

Benchmarks presenting the accuracy of computational methods tend to replace personal experience and study in their choice. This has the advantage of being adapted to the huge amount of computational material produced through easily available programs, but hide a series of pitfalls. In particular, a more careful look at the benchmark is needed than just looking at summarizing numbers like the mean absolute error.



P08

Understanding Structure and Properties of MgCl₂ Supported Ziegler-Natta Nanoclusters by DFT, Spectroscopy and Machine Learning: How Modelling Uncovers the Origin of Industrial Catalysis

Maddalena D'Amore^{1*}, Gentoku Takasao², Hiroki Chikuma², Toru Wada², Toshiaki Taniike^{2*}, Fabien Pascale³, and Anna Maria Ferrari¹

¹Dipartimento di Chimica, Università di Torino, Italy

²Graduate School of Advanced Science and Technology, Japan Advanced Institute of Science and Technology, 1-1 Asahidai, Nomi, Ishikawa, 923-1292, Japan

³Université de Lorraine - Nancy, CNRS, Laboratoire de Physique et Chimie Théoriques, Vandoeuvre-les Nancy

*Corresponding author

ABSTRACT

MgCl₂-supported Ziegler-Natta (ZN) catalysts for olefin polymerization are intrinsically complex multi-component systems, whose composition is the result of a long optimization process, mostly achieved in an empirical manner, either through a trial and error approach or through the more modern high-throughput screening of all the possible parameters. As it happens in many catalysts, nano-size and disorder are key features of ZN catalysts.ⁱ The structural and surface properties of MgCl₂ strongly depend on its activation that allows moving from the two crystalline polymorphs of MgCl₂ (α and β phases) to a high-surface-area material actually suitable for catalytic applications (δ -MgCl₂). MgCl₂ as a support material offers unique advantages in terms of abundance and distribution of stereo-specific highly active sitesⁱⁱ, together with the regulation of the morphology of the produced polymer. The presence of multiple components interacting with each other and their sensitivity to moisture are the main difficulties encountered in the attempt to investigate these systems from an experimental point of view, which opened routes to quantum mechanics to provide insights into those complex systems.

The seminal MgCl₂ models as obtained from molecular mechanics in the 1980s presented the (110) and (104) lateral surfaces as the putative surfaces for the adsorption of monomeric TiCl₄ and dimeric species, respectively giving rise the first to a nonstereospecific site, whereas Ti₂Cl₈ dimers would form on the (104) surface adducts with stereospecific properties. However, recent DFT studies have claimed the crisis of those models,^{iii,iv} warning about the critical thermodynamic stability of Ti_xCl_{4x} species on flat and regular MgCl₂ surfaces and moving towards a much more complex morphology of the δ -MgCl₂ particles, where defective sites (such as steps, corners, and interfaces between two different surfaces) play a major role.

We recently investigated the effect of nanosize and structural disorder on the MgCl₂ support of Ziegler-Natta catalysts in terms of induced changes to its vibrational spectroscopic fingerprint by resorting to both periodic and cluster models. In particular, we adopted the inelastic neutron scattering (INS)^v technique as a method for the characterization of materials with a certain degree



of defectivity and our investigation shows the central role of quantum mechanical simulations for a correct interpretation and valorization of the experimental INS spectra. Due to the nanosized nature of investigated catalysts, understanding the structure and properties of $\text{MgCl}_2/\text{TiCl}_4$ clusters is a key to uncover the origin of Ziegler-Natta catalysis. In particular, vibrational spectroscopy can sensitively probe the morphology and active species of $\text{MgCl}_2/\text{TiCl}_4$. We determined vibrational spectroscopic fingerprints of 50MgCl_2 and $50\text{MgCl}_2/3\text{TiCl}_4$ which were obtained by non-empirical structure determination based on an evolutionary algorithm and DFT.^{vi} The adsorption of CO, TiCl_4 and Ti_2Cl_8 dimers was also modelled on each of coordinatively unsaturated Mg^{2+} sites available for binding including so-called defect sites, which are likely present at the surface of activated MgCl_2 nano-crystals and plausible sites for strong TiCl_4 species adsorption. Vibrational analysis (IR and Raman) on plausible models of $\text{TiCl}_4/\text{MgCl}_2$ clusters revealed that IR response is useful to distinguish between the different ways of binding of TiCl_4 on different sites of adsorption, whereas Raman response provides a clear fingerprint of supported TiCl_4 species.

References

1. Zannetti, R.; Marega, C.; Marigo, A.; Martorana, A. J. *Polym. Sci. Part B Polym. Phys.* 1988, 26 (12), 2399–2412.
2. Correa, A.; Piemontesi, F.; Morini, G. and Cavallo, L. *Macromol.* 2007, 40, 9181-9189.
3. (a) Seth, M.; Margl, P.M.; Ziegler, T. *Macromolecules* 2002, 35, 7815. (b) D'Amore, M.; Credendino, R.; Budzelaar, P. H. M.; Causá, M.; Busico, V. J. *Catal.* 2012, 286, 103–110.
4. (a) Boero, M.; Parrinello, M.; Terakura, K. *J. Am. Chem. Soc.* 1998, 120, 2746; (b) Boero, M.; Parrinello, M.; Huffer, S.; Weiss, H. *J. Am. Chem. Soc.* 2000, 122, 501; (c) Boero, M.; Parrinello, M.; Weiss, H.; Huffer, S.; *J. Phys. Chem. A* 2001, 105, 5096.
5. D'Amore, M.; Piovano, A.; Vottero, E.; Rudic, S.; Groppo, E.; Bordiga, S.; Civalieri, B. *ACS Appl. Nano Mater.* 2020, 3, 11118-11128.
6. D'Amore, M.*; Takasao, G.; Chikuma, H.; Wada, T.; Taniike*, T.; Pascale, F. and Ferrari, A.M.: *J. Phys. Chem. C* 2021, <https://doi.org/10.1021/acs.jpcc.1c05712>.

P09

Magnetism and Half-Metallicity of Solids from the Spin Polarization of P Orbitals

Bouhafs Bachir

Laboratoire de Modélisation et Simulation en Sciences des Matériaux, Université Djillali Liabès de Sidi Bel-Abbès, Sidi Bel-Abbès, 22000, Algeria

ABSTRACT

Heusler alloys are of great scientific and technological interest. In addition, devices based on Heusler alloys exhibit a development of new structures with ferromagnetic behavior using transition metals or elements that are inherently non-magnetic. Half-Heusler type XYZ and full-Heusler type X_2YZ alloys without transition metals, mainly called d^0 ferromagnetic half-metals (FHM) is a recent research field. The particular interest of their ferromagnetic character as well as of the half-metallic (HM) nature with possible applications in spintronic systems does not come from magnetic elements. This series of strongly ferromagnetic materials mentioned above is composed of non-magnetic elements compared to those predicted by Groot *et al.* in 1983. Recently, some studies have also demonstrated the presence of half-metallicity in compounds without partially filled d atomic orbitals such as alkaline earth carbides and nitrides.

The first-principles electronic structure calculations were applied to predict the ferromagnetism HM in the alkali metals and alkaline earth metals based full Heusler, quaternary Heusler and half Heusler ternary alloys. However, to our best knowledge, there are no experimental or theoretical studies on the various phases of half-Heusler alloys, as well as their phonon dynamics and thermodynamic properties.

In the present work, a comprehensive study was conducted for the α , β and γ phases of the half-Heusler alloys using first principles calculations based on the density functional theory (DFT) with and without spin polarization to explore their structural, elastic, dynamic phonon, thermodynamic, electronic and magnetic properties. The alloys studied have been shown to be energetically, elastically and dynamically stable. This implies that the experimental synthesis of these alloys under standard conditions is possible. In addition, the considered half-Heusler alloys are half metals with potential applications in spintronic devices.



Enhanced Figure of Merit in Molecular Junctions

BAADJI Nadjib

LPMA, Physics department university of Mohamed Boudiaf- M'Sila, M'sila, Algeria

ABSTRACT

In order to convert the wasted heat into useful energy, thermoelectric devices are designed to maximize the figure of merit ZT defined as the ratio of the electric and thermal conductivity times the Seebeck coefficient. However, most of devices suffer from the small value of ZT ($ZT < 1$) and use mostly doped semiconductors. Here, we show that molecular junctions can have a higher value of ZT , paving the way for efficient thermoelectric devices. Using the density functional theory combined with non-equilibrium Green's function, we calculate, in linear response regime and Landauer-Buttiker approach, the figure of merit for different types of junctions. The molecular junctions have values of $ZT > 3$ and can be increased by an order of magnitude by different physical and chemical means.

References

- [1] P. Gehring *et al.* "Complete mapping of the thermoelectric properties of a single molecule" *Nature Nanotechnology*, **16**, 426 (2021).
- [2] P. Gehring, J. M. Thijssen, & H. S. van der Zant, "Single-molecule quantum-transport phenomena in break junctions". *Nat. Rev. Phys.* **1**, 381–396 (2019).
- [3] B. K. Agarwalla, J.-H. Jiang & D. Segal, "Thermoelectricity in molecular junctions with harmonic and anharmonic modes". *Beilstein J. Nanotechnol.* **6**, 2129 (2015).
- [4] M. Di Ventra, "Electrical Transport in Nanoscale Systems", Cambridge University Press: New York, NY, USA, (2008).
- [5] R. Berman "Thermal Conduction in Solids", Clarendon Press, Oxford, UK, 1976
- [6] G. Cuniberti, G. Fagas, K. Richter, K. (Eds.) "Introducing Molecular Electronics", Springer: New York, NY, USA, (2005).



P11

Intensity-based Wide-field Magneto-optical Microscopy

Schäfer Rudolf

Leibniz Institute for Solid State and Materials Research (IFW) Dresden, Helmholtzstrasse 20, D-01069 Dresden, Germany and Institute for Materials Science, Technische Universität Dresden, D-01062 Dresden

ABSTRACT

In conventional Kerr- and Faraday microscopy the sample is illuminated with plane-polarized light and a magnetic domain contrast is generated by an analyzer making use of the Kerr- or Faraday rotation. In this presentation we review possibilities of analyzer-free magneto-optical microscopy based on magnetization-dependent intensity modulations of the light: (i) The transverse Kerr effect can be applied for in-plane magnetized material, demonstrated for an FeSi sheet. (ii) Illuminating the same sample with circularly polarized light leads to a domain contrast with a different symmetry as the conventional Kerr contrast. (iii) Circular polarization can also be used for perpendicularly magnetized material, demonstrated for a garnet film and an ultrathin CoFeB film. (iv) Plane-polarized light at a specific angle can be employed for both, in-plane and perpendicular media. (v) Perpendicular light incidence leads to a domain contrast on in-plane materials that is quadratic in the magnetization and to a domain boundary contrast. (vi) Domain contrast can even be obtained without polarizer. In cases (ii) and (iii), the contrast is generated by MCD (Magnetic Circular Dichroism, i.e. by the differential absorption of left and right circularly polarized light, induced by magnetization components along the direction of light propagation) while MLD (Magnetic Linear Dichroism, i.e. by the differential absorption of linearly polarized light, induced by magnetization components transverse to the propagation direction) is responsible for the contrast in case (v). The domain boundary contrast is due to the magneto-optical gradient effect in metallic samples. A domain boundary contrast can also arise due to interference of phase-shifted magneto-optical amplitudes. All reported contrasts can be applied directly for domain imaging. In any case they need to be considered also in conventional magneto-optical Kerr microscopy and MOKE magnetometry as they can be superimposed on any regular Kerr signal.

References

R. Schäfer, P.M. Oppeneer, A. Ognev, A. Samardak, and I.V. Soldatov: Analyser-free, intensity-based wide-field magneto-optical microscopy. Accepted for Appl. Phys. Rev. (2021)



P12

Boosting the Performance of Magnetic Nanoparticles: Magnetic Field-assisted Assembly and Magnetic Functionalization

Jana K. Vejpravova

Charles University, Faculty of Mathematics and Physics, Ke Karlovu 5, 121 16 – Prague 2, Czechia

ABSTRACT

Magnetic properties of single-domain nanoparticles are defined by the phase composition, particle size, and lattice/spin disorder. Beyond a single-particle level, the so-called collective effects, such as dipolar interactions, reform the magnetic properties. Recently, the organization of nanoparticles into anisotropic structures represents a smart, bottom-up approach for creating highly anisotropic magnets with mesoscopic control over magnetic anisotropy. Such architectures are of interest for many applications, like drug delivery, bioanalysis, data and energy storage, sensors, and catalysis. Recently, the magnetic field (MF)-assisted self-assembly of magnetic colloids into organized nanostructures like fibers, chains, tubes, and circles has attracted enormous attention. In this talk, the most promising strategies of MF-assisted organization of magnetic nanoparticles will be presented. Moreover, a new approach – the so-called MF-assisted click chemistry, based on the thermo reversible Diels–Alder reaction in the presence of an external MF will be introduced. This concept enables the preparation of highly anisotropic assemblies of nanosized magnets that can be reversibly decomposed by thermal treatment. Finally, a concept of hybrid nanoparticles functionalized with magnetic molecules will be introduced.



P13

Heterostructures Based on Functionalized Graphene and Free-standing Graphene Membranes

Martin Kalbac

J. Heyrovsky Institute of Physical Chemistry of the Czech Academy of Sciences, Dolejškova 2155/3, 182 23 Prague,
Czech Republic

ABSTRACT

Functionalization of 2D materials enhances potential for application of these materials. Here, we propose a strategy for resist free lithographical approach for localized functionalization of graphene using photochemically modulated reaction. It will be shown how controlled functionalization can be applied to optimize function of supercapacitor in graphene/PANI composite. Furthermore, I will discuss preparation of active graphene membrane by deposition of cerium oxide nanoparticles using pulsed laser deposition in ultra-high vacuum conditions and a systematic study of the influence of preparation conditions on ceria nanoparticles and their interaction with CVD graphene. Finally, the influence of graphene membrane on cerium oxide catalytic properties towards methanol will be discussed.



001

Effect of the Substrate on the Structural Properties of $\text{Cu}_2\text{ZnSnS}_4$ Thin Films Synthesized by Electrodeposition

Loumafak Hafaifa¹, Fatiha Daoudi², Radia Boudaira³, Omar Meglali^{2,4,*} and Assia Bouraiou²

¹Department of Physics, Ziane Achour University, Algeria.

²Materials Science and Informatics Laboratory, Ziane Achour University, Algeria.

³Department of Physics / Mentouri University, Algeria.

⁴Faculty of Sciences / Mohamed Boudiaf University, Algeria.

*Corresponding author

Introduction

The quaternary compound $\text{Cu}_2\text{ZnSnS}_4$ semiconductor have gained much attention in recent years due to its promising optical properties¹. Moreover, low cost, cheap, earth-abundant as well as non-toxicity of its elements^{1,2}. In addition, this semiconductor is considered as one of the potential absorber materials for the next-generation solar cells³.

The aim of the present work is to deposit the CZTS thin films on the ITO and the FTO substrates by the one-step electrodeposition method followed by the sulphurization. The influence of the ITO and FTO on structural properties of the elaborated CZTS film was then investigated.

Experimental

Two samples named CZTS_{ITO} and CZTS_{FTO} were grown respectively on ITO/glass and FTO/glass substrates by electrodeposition process. Copper chloride, zinc sulfate heptahydrate, tin chloride dehydrate and sodium thiosulphate pentahydrate were used respectively as Cu, Zn, Sn and S ions sources. In order to obtain a pH of nearly 4.2 for all the electrolyte bath tartaric acid solution is added to the used complexing agent trisodium citrate. The deposition was carried out at room temperature for 40 min with an applied potential of -7.2 V. After deposition, the samples were rinsed by deionized water and dried under the air.

The CZTS_{ITO} and CZTS_{FTO} elaborated films were locked up with 30 mg of sulphur powder into a glass capsule, filled with argon-neon gas mixture at a fixed pressure of 10 mbar, then the glass capsules were annealed in the furnace at 550°C during 60 min and under a fixed heating rate of 20°C min⁻¹. Finally, the capsules were cooled down naturally to room temperature in the furnace. The structural properties were investigated by X-ray diffraction (XRD).

Results and Discussion

The results of X-ray diffraction analyses indicated that the two elaborated films have kesterite tetragonal crystal structure. From the XRD patterns of CZTS_{ITO} and CZTS_{FTO} films (**Fig. 1 (a) and (b)**), we observed the peaks located at $2\theta \approx 28.43, 32.83, 47.31, 56.07^\circ$. These peaks are assigned to (112), (004)/(020), (220)/(024) and (132)/(116) planes, which are characteristic of CZTS phase under its kesterite structure (JCPDS 98-017-1983). The crystalline parameters *a* and *c* are 5.460 Å and 10.969 Å for CZTS_{ITO} and 5.442 Å and 10.915 for CZTS_{FTO} . The crystallite size *C*_s, lattice strain *ε* and dislocation density *δ* are calculated. The crystallite size of CZTS_{ITO} and CZTS_{FTO} is 113.6 and 347 nm.



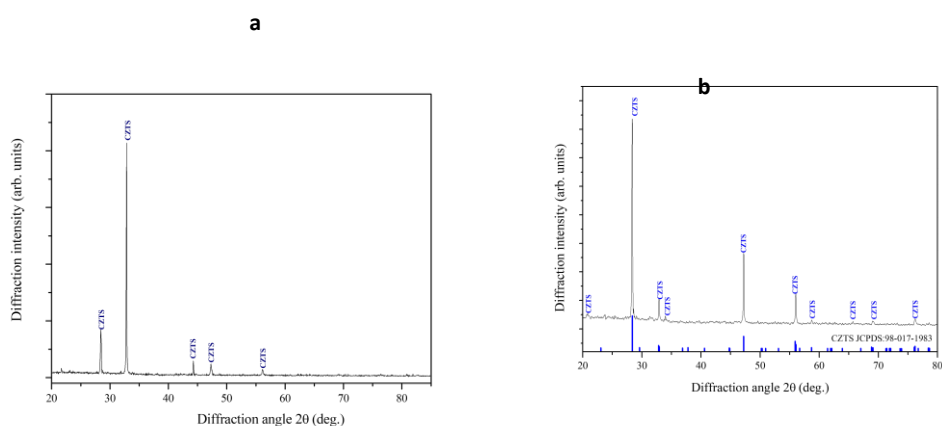


Fig.1: XRD patterns of sulfurized CZTS thin Films at 550°C deposited on: (a) ITO/glass substrate, (b) FTO/glass substrate.

Conclusion

In summary, copper zinc tin sulfide CZTS thin films were successfully synthesized on the ITO/glass and FTO/glass substrates by one-step electrodeposition process followed by sulphurization at 550°C for 60 min. For both substrates (ITO and FTO), XRD characterization confirms the formation of CZTS phase under its kesterite structure. We have also found that the CZTS_{FTO} film exhibits better crystal quality and high purity.

References

1. Song X, Ji X, Li M, Lin W, Luo X, Zhang H. «A review on development prospect of CZTS based thin film solar cells» *International Journal of Photoenergy*. 2014; 2014: 1-11.
2. Kong L, Deng J X. «First-Principles Study on Electronic and Optical Properties of Kesterite and Stannite Cu₂ZnSnS₄ Photovoltaic Absorbers» *Materials Science Forum, Trans Tech Publ*. 2015; 815:80-88.
3. Boudaira R, Meglali O, Bouraiou A, Attaf N, Sedrati C, Aida M S. «Optimization of sulphurization temperature for the production of single-phase CZTS kesterite layers synthesized by electrodeposition» *Surface Engineering*. 2020; 36: 1000-1011.

O02

Monte Carlo Method Study of Thin Films of The Spin-1 Ashkin Teller Model in the Presence of the Crystal Field

Amel Benmansour^{1*}, Smaine Bekhechi² and Badr-Eddine Nabil Brahmi²

¹Department of physics/ Laboratory of Automatics, Faculty of Sciences, University of Tlemcen, BP119, Algeria

²Department of physics /Research Laboratory of Theoretical Physics, Faculty of Sciences,
University of Tlemcen, BP119, Algeria

*Corresponding author

ABSTRACT

Using Monte Carlo simulations based on the Metropolis algorithm, we have investigated magnetic properties and phase diagrams of the spin-1 Ashkin Teller model magnetic thin films. The effects of the crystal field D/J_{2b} and four-spins coupling ($J_{4s}/J_{2b}, J_{4b}/J_{2b}$), has been studied in detail. Therefore, the phase diagrams in the $(k_B T_c/J_{2b}, J_{2s}/J_{2b})$ plane, exhibits the special point $(R_s = J_{2s}/J_{2b})_{sp}$, for different values of D/J_{2b} , wherein all film thicknesses having the same critical temperature. In addition, the magnetization profiles present a first order phase transition behavior. Then, we found rich phase diagrams with first- and second-order phase transitions that meet at tricritical points, that are dependent on the film thickness N .

Keywords: Thin Films, Ashkin Teller model, Phase diagrams, Crystal field, Special point.



003

Dielectric Characterization by Impedance Meter of Thin Films $\text{Bi}_2\text{S}_3(0.6)\text{ZnS}(0.4)$ Composites

Benattou Halima

Laboratory of elaboration and characterizations of the materials, Electronics Department, Djillali Liabes
University of Sidi Bel Abbes, Algeria

ABSTRACT

An impedance in module and phase form of thin films $\text{Bi}_2\text{S}_3(0.6)\text{ZnS}(0.4)$ composites was measured in terms of frequency and temperature using *HP4192* impedance meter. Semicircular arcs were obtained. These arcs were theoretically simulated to get the equivalent circuit parameters and to model the different processes taking place in the solid thin films. AC conductivity study expresses the behavior of disordered materials where transport occurs by hopping assisted by phonon between localized states near the Fermi level. The complex permittivity obtained from electrical measurements reflects losses and dissipation of energy in thin films, and it is attributed to the interfacial and dipolar polarization.

Table 1: The estimated relaxation time values; resistance "R" and capacity "C" obtained by the adjustment of the curves

	$\tau=1/2\pi f$ (n.sec)	Rg [Ω]	Cg [Farad]
T =20°C	212,314	2245421.08259	$1,0951.10^{-13}$
T =40°C	231,68	1372065.77403	$2,1253.10^{-13}$
T =60°C	397,39	838439,57249	$4,5417.10^{-12}$

Table 2: conductivity ' σ_{AC} ' values taken at low frequencies, the exponent 'S' and the density of states at the Fermi level calculated for $\text{Bi}_2\text{S}_3(0.6)\text{ZnS}(0.4)$ thin film

T [°C]	σ_{AC} [$\Omega.\text{cm}$] ⁻¹	S	$N(E_F) \times 10^{20}$ [$\text{eV}^{-1}.\text{cm}^{-3}$]
20	0,02530	0,2033	0,4347
40	0,0358	0,11866	0,58412
60	0,05435	0,11665	1,3035



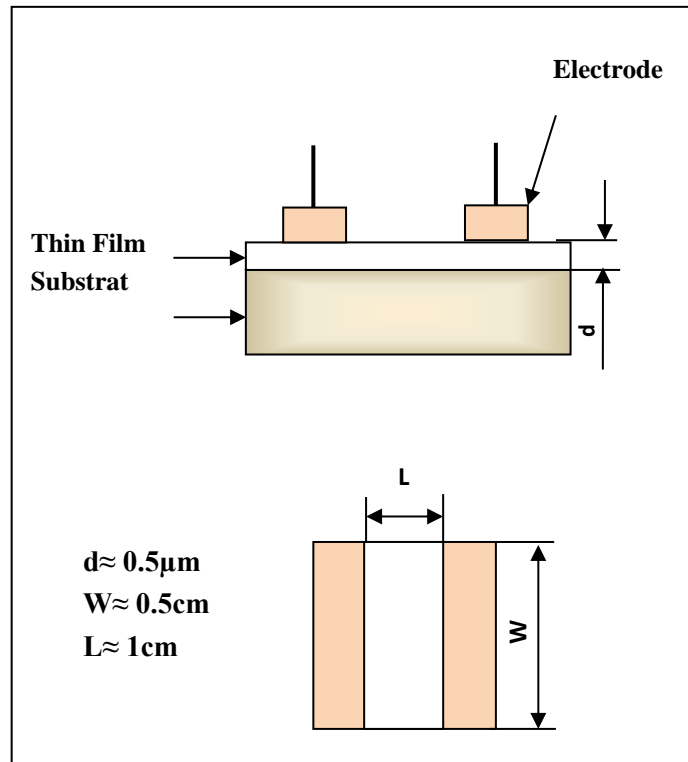


Fig 1: coplanar configuration of the sample

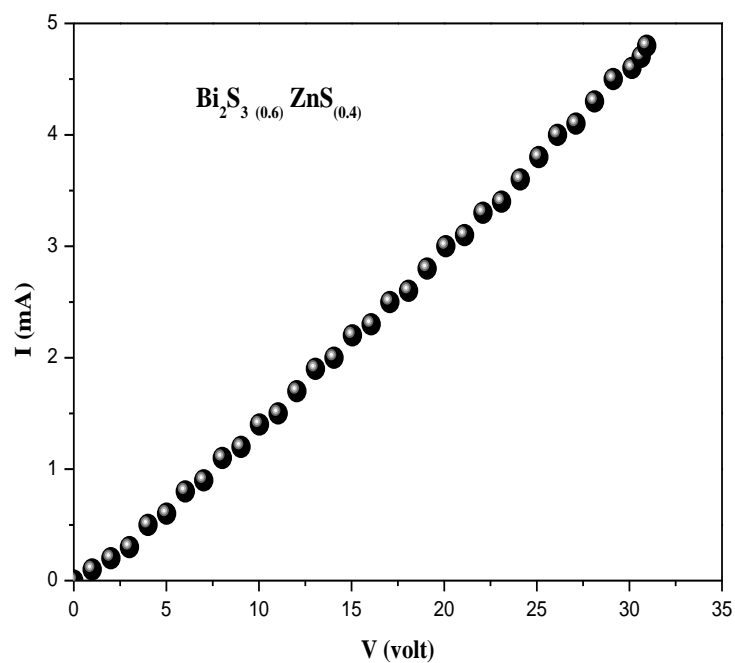


Fig 2: Characteristic I(V) of the sample

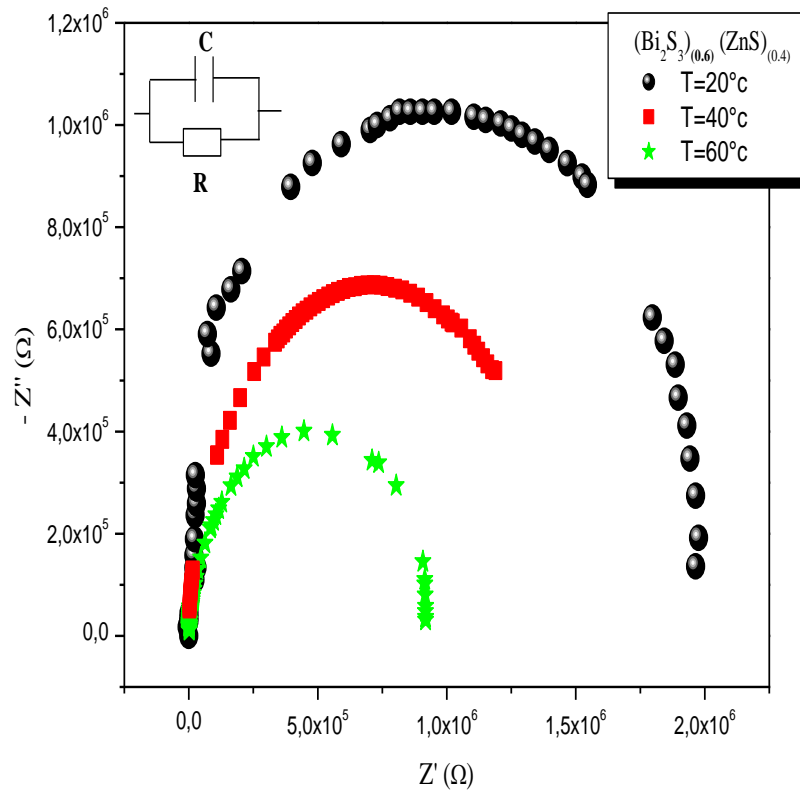


Fig.3: Impedance imaginary part. vs real part and equivalent electrical circuit top left.

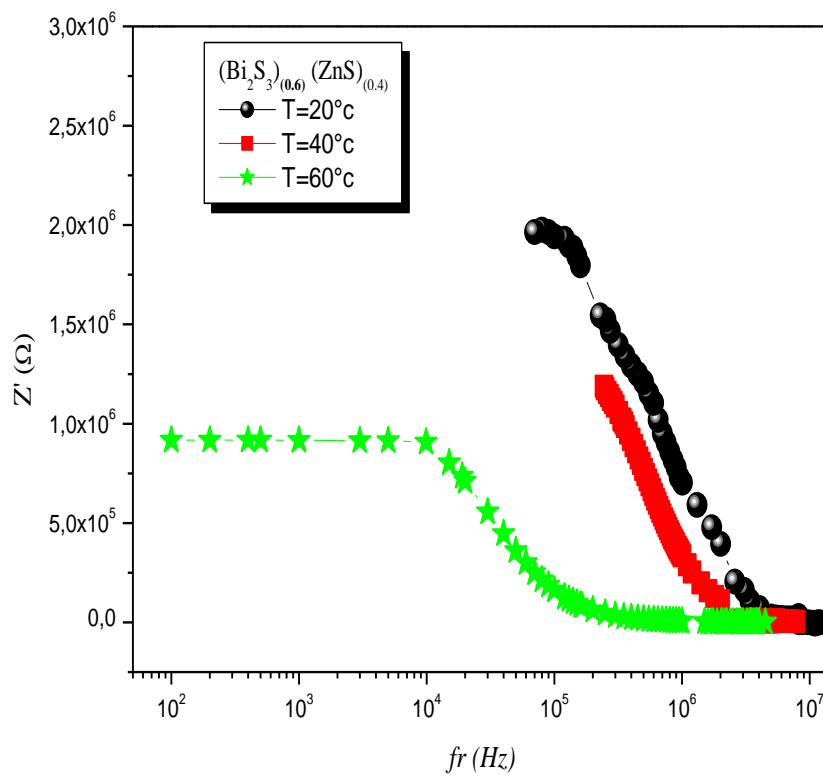


Fig 4: impedance real part Z' vs. frequency and temperature

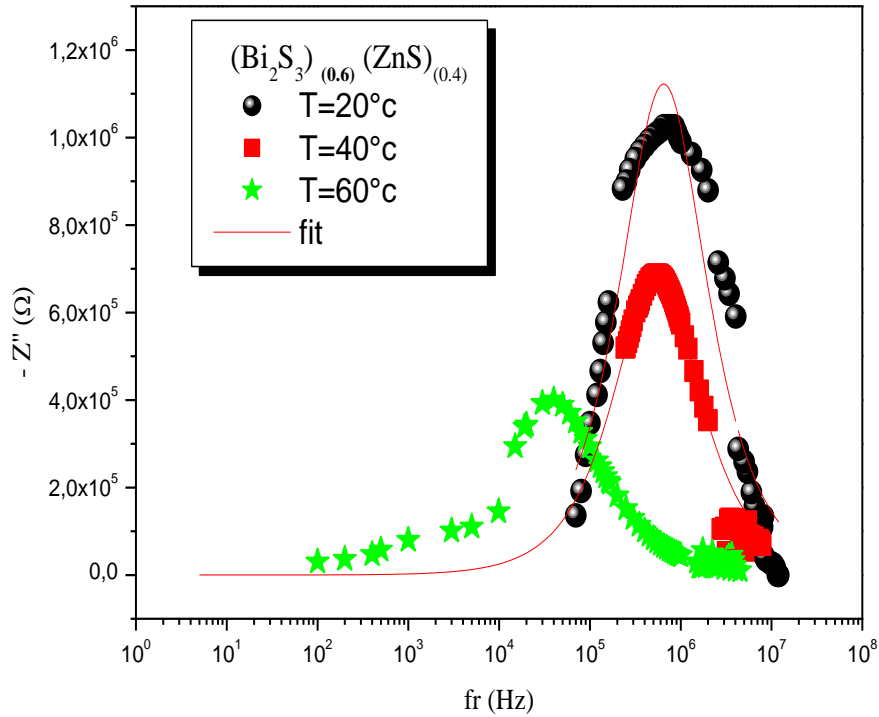


Fig 5: impedance imaginary part Z'' vs. frequency and temperature

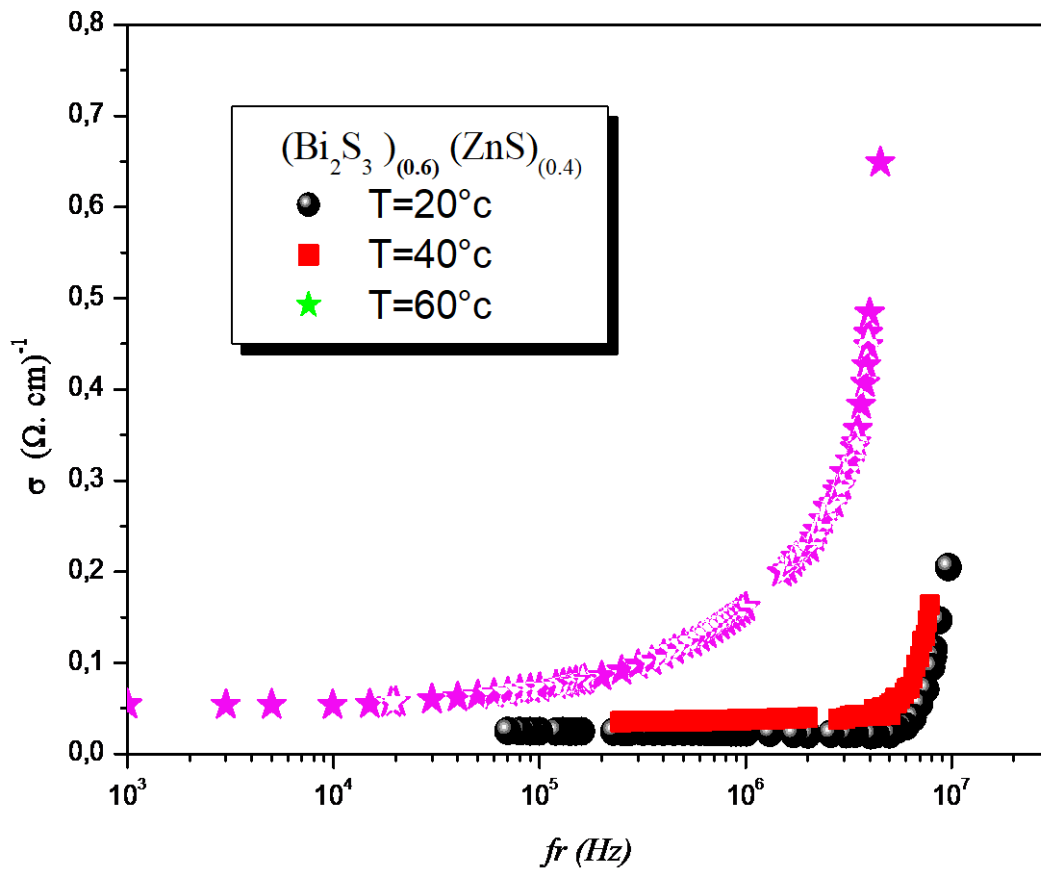


Fig.6: Electrical conductivity .vs frequency and temperature.

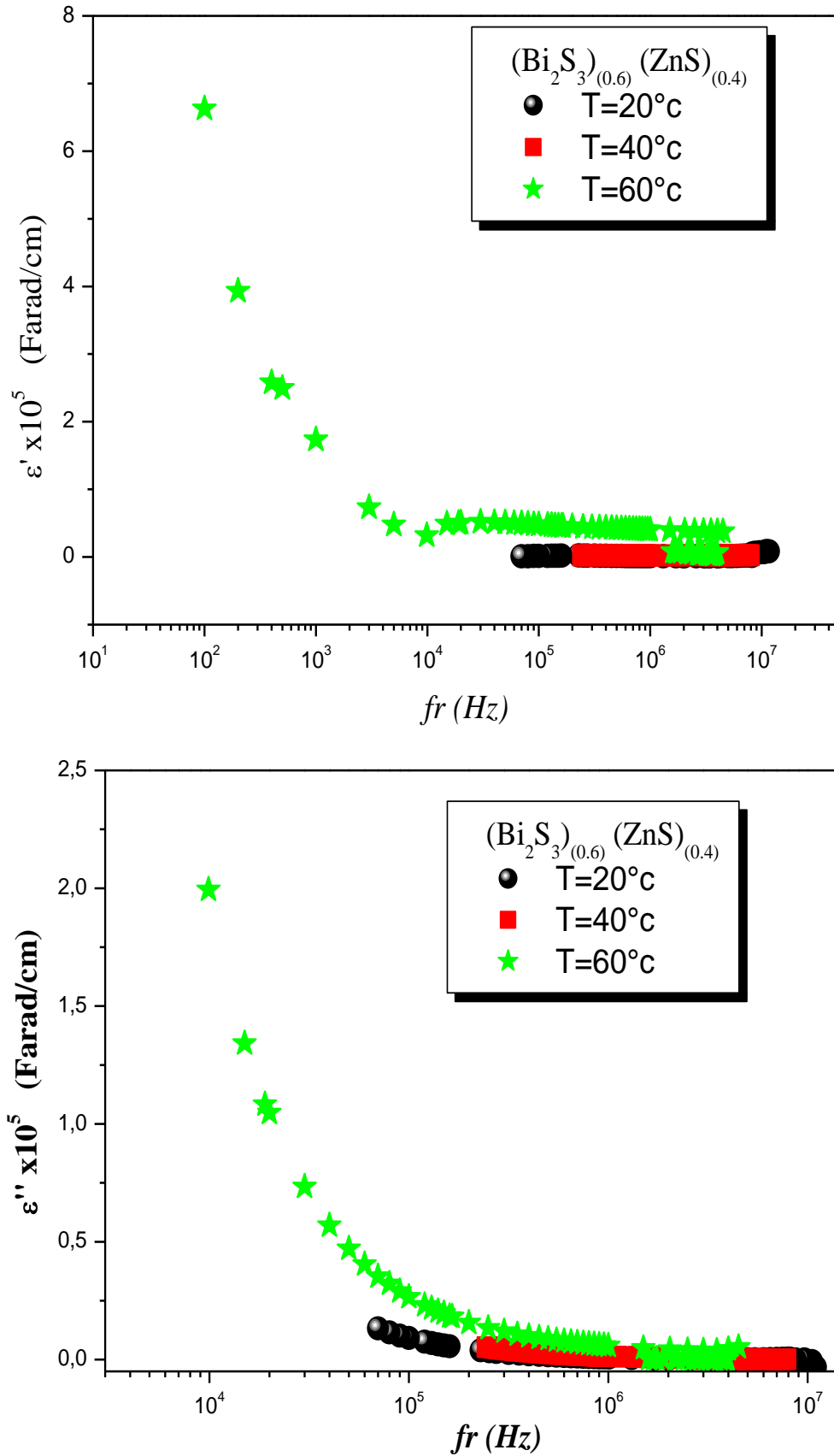


Fig 7: (ϵ') and (ϵ'') variations vs. Frequency and temperature

Keywords: *Bi₂S₃, ZnS, thin-film composites, impedance meter, electric and dielectric properties.*

O04

Green Synthesis and Characterization of Silver Nanoparticles

Bessi Assia^{1*}, B.Laidi Baya², Lakhal Noussaiba²

¹Laboratoire de chimie physique moléculaire et macromoléculaire « LCPMM », Saad Dahleb University, Route Soumâa BP 270, Blida09000, Algeria

²Departement of chemistry, Saad Dahleb University, Route Soumâa BP 270, Blida 09000, Algeria

*Corresponding author

ABSTRACT

In this study, we have successfully green synthesized the silver nanoparticles (Ag NPs) using Lotus Corniculatus aqueous extract as the natural reducing and stabilizing agent, and aqueous AgNO₃ solution as a precursor using a new approach which attracts the interest of researchers worldwide. The as-prepared was characterized by Ultraviolet–Visible (UV–Vis) spectrophotometry, X-ray diffractometry (XRD), Fourier transform infrared (FT-IR) spectroscopy and scanning electron microscopy with energy dispersive X-ray (SEM with EDX).

Introduction

Because of their size-dependent physical and chemical properties, nanoparticles are gaining attention [1]. Metallic silver nanoparticles (AgNPs) have received considerable attention for their potential application as a biocide in products ranging from facade paints to textiles, which is reflected in recent product inventories [2].

Experimental

A volume of the extract (96 ml) is placed in a beaker, with stirring a solution of silver nitrate (1 mM) was added drop by drop, the obtained mixture has an orange-yellow color. The mixture was stirred overnight and its color becomes brown. After that, a precipitate appeared. After precipitation of the solid phase, the latter is dried in an oven at a temperature of 80 °C, in order to obtain a powder. This powder is calcined for 3 hours at a temperature of 400 °C with a rise of 2 °C /min.

Results and Discussion

In order to confirm the composition and crystallinity of the obtained nanopowder, XRD was used for further detection and analysis. As shown in figure-1, The synthesized Ag NPs were identified by XRD analysis as a cubic face-centered crystal system [3] and the average crystallite size is 11 nm. The aqueous suspension of Ag NPs shows a UV–Vis absorption maxima of 390 nm demonstrating NPs formation. FT-IR analysis identified the presence of functional groups in the aqueous extract responsible for the production of stable AgNPs. As shown in figure-1 SEM showed that the nanoparticles were spherical in shape with nanometric size.



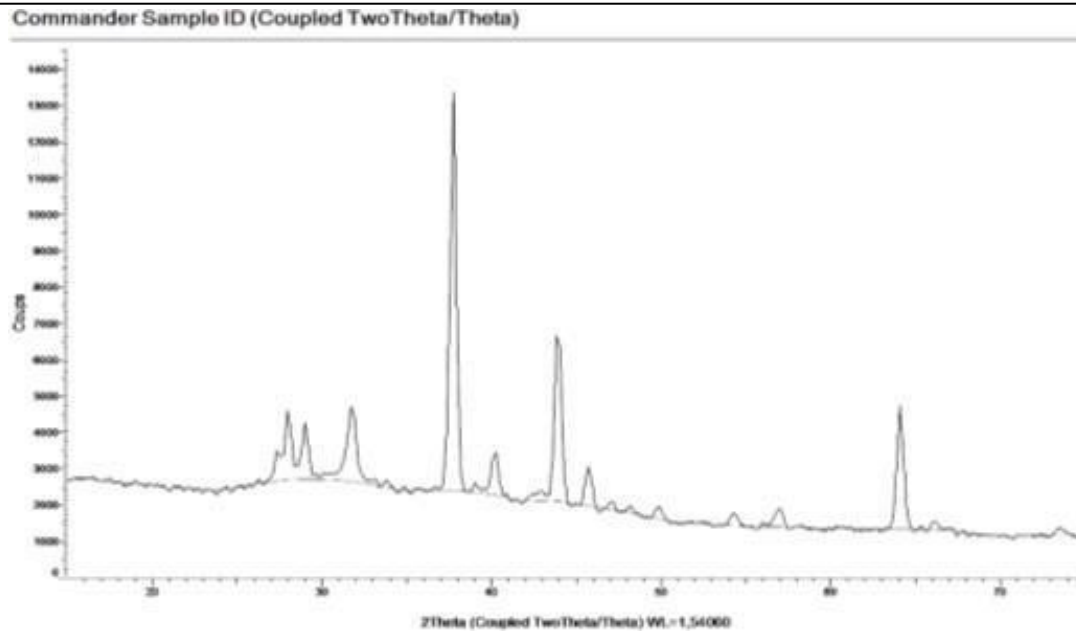


Figure-1: XRD pattern of Ag NPs.

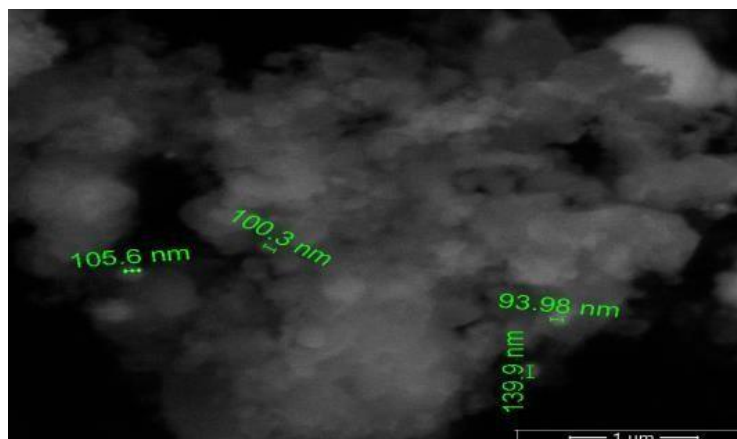


Figure-2: Scanning Electron Micrograph of biosynthesized silver NPs

Conclusion

These biosynthesized nanoparticles can be used multifield purpose medical applications.

References

- [1]. Gade, A., et al., *Biofabrication of silver nanoparticles by Opuntia ficus-indica: in vitro antibacterial activity and study of the mechanism involved in the synthesis*. Current Nanoscience, 2010. **6**(4): p. 370-375.
- [2]. Kaegi, R., et al., *Behavior of metallic silver nanoparticles in a pilot wastewater treatment plant*. Environmental science & technology, 2011. **45**(9): p.3902-3908.
- [3]. Fidel Martinez-Gutierrez, Peggy L Olive, Adriana Banuelos, Erasmo Orrantia, Nereyda Nino, Elpidio Morales Sanchez, Facundo Ruiz, Horacio Bach, and Yossef Av-Gay, "Synthesis, characterization, and evaluation of antimicrobial and cytotoxic effect of silver and titanium nanoparticles," *Nanomedicine: Nanotechnology, Biology and Medicine* **6** (5), 681-688

005

FEM Simulation and Performance Evaluation of MEMS Pressure Sensor Based on Capacitive Effect Using Molybdenum and Tungsten

Nadir BELGROUNE^{1*} and MZ AHMED³

^{1*}Micro & Nano Physics Group, Physics Department, Faculty of Sciences, University Saad Dahlab Blida 1 (USDB1), P.O.Box 270, 09000 Blida, Algeria

²Electrical Engineering Department, Al-Hussein Bin Talal University, P.O. Box 20, 71111Ma'an, Jordan

*Corresponding author

ABSTRACT

Microsystems have experienced a great deal of development during the last years leading to more complex systems for sensing, analyzing, and actuating. It combines and integrates miniaturized sensors, actuators and electronics in a single device for various applications in different fields [1-2]. One of the major applications of these devices is the Micro Electromechanical System (MEMS) pressure sensors for tire pressure measurements [3-4]. In addition, these integrated devices have been used in airbag deployment in automobiles since the nineties of the last century [3]. There are several types of pressure sensors, the most common MEMS pressure sensors categorizes are the piezoresistive and capacitive effect one. Recently, (MEMS) capacitive pressure sensor gains more advantage over micromachined piezoresistive pressure sensor due to its high sensitivity, low power consumption, IC compatibility, better thermal stress etc. [5]. The working principle of capacitive effect MEMS sensor is based on two parallel plates acting as electrodes of capacitors and separated by air gap, thus forming a square diaphragm. When the pressure over the sealed cavity changes, the pressure difference causes the membrane to deflect. The study of plate mechanical deflection in these devices calls on various notions of solid mechanics and electrical potential grouped together under the name of electro-mechanics in connection with the applied pressure. An electro-mechanical response of a capacitive pressure sensor would open a wide horizon of uses and should intensify the integration of MEMS devices. In general, the MEMS pressure sensor based on capacitive effect has many sorts of detecting and measurement problems related to external variables such as ambient or working temperature [4], therefore, different materials such as silicon, graphene, titanium, tungsten, molybdenum were investigated to obtain the material which has improved resistivity against temperature variation. In this paper, an analysis, FEM simulation of electrical and mechanical effects of MEMS based capacitive pressure sensor with high pressure sensitivity and small size, using the electro-mechanics interface by COMSOL Multiphysics software are described. This includes diaphragm deflection, sensitivity, capacitance vs. pressure analysis and thermal considerations. Subsequently, the detailed description of the model concept, its operating principle, the geometric parameters and the pressure and thermal effects simulation are presented. Therefore, a discussion of the simulation results with a focus on the sensitivity of the sensor and its performance against temperature are compared to other work [5-6]. In addition, the packaging stress effect on diaphragm deflection, sensitivity and capacitance vs. pressure analysis and thermal studies under the working



range of 290 to 300 K° are investigated. The pressure and temperature variation affect the magnitude of the diaphragm deflection and consequently on the capacitance and sensitivity (the gradient of the curve Capacitance Vs Pressure) of the MEMS sensor. The simulation results showed that the molybdenum capacitive MEMS pressure sensor has high resistivity against temperature variation with a change in capacitance of 0.01% in the prementioned operating temperature range, while other materials depicted in other works showed a variation of 5.535% and 1.564% for silicon and graphene at the same operating temperature range [5,6].

Keywords: MEMS Sensors, Capacitive Pressure Sensors, COMSOL MULTIPHYSICS, FEM simulation.

References

1. D. K. Miu, Y. C. Tai: Silicon micro-machined scaled technology, IEEE Trans. Industr. Electron. 42 (1995) 234–239.
2. T. R. Hsu: MEMS and Microsystems (McGraw-Hill, Boston 2002)
3. H. Kapels, R. Aigner, C. Kolle: Monolithic surface micro-machined sensor system for high pressure applications, Technical Digest, Int. Conf. Solid-State Sens. Actuators, Munich 2001 (Transducers Conference, Chicago 2001) 56–59.
4. W. H. Ko, Q. Wang: Touch mode capacitive pressure sensors, Sens. Actuators 75 (1999) 242–251.
5. N. Anadkat, M J S Rangachar, Simulation based Analysis of Capacitive Pressure Sensor with COMSOL Multiphysics, International Journal of Engineering Research & Technology (IJERT). Vol. 4 Issue 04, April-2015.
6. Rashed Al Amin and al., Simulation Analysis of Capacitive Pressure Sensor for MEMS Using Graphene, International Conference on Materials, Electronics & Information Engineering, ICMEIE-2015.

006

Effect of Extended Gettering during the Emitter Formation on the Electrical Performance of Multicrystalline Silicon Based Solar Cells

Nabil Khelifati ^{1*}, Baya Palahouane ¹, Brahim Mahmoudi ¹, Hakim Amrouche ¹, Djoudi Bouhafs ¹,
Seddik-El-Hak Abaisia ²

¹Division DDCS, Centre de Recherche en Technologie des Semi-conducteurs pour l'Energétique (CRTSE), Algiers,
Algeria

²Departement de Physique, Faculté des Sciences, Université M'hamed Bougara de Boumerdes (UMBB),
Boumerdes, Algeria

*Corresponding author

ABSTRACT

Crystalline silicon (c-Si) wafers are widely used as precursor elements in solar cells manufacturing, and constitute more than 95% of the overall industrial market¹. The contamination of c-Si wafers, especially the multicrystalline one (mc-Si), by metallic impurities (Fe, Cr, Ni, etc.) is considered as a serious disadvantage. The presence of such impurities can drastically limit the efficiency potential of the solar cells. Nevertheless, most metallic impurities can be partially removed from the whole bulk of the Si wafer, using gettering process. It refers to a thermal treatment step that activates the diffusion of interstitial impurities from the bulk of the wafer to less important superficial regions². In this present work we studied the impact of extended gettering on the electrical performance of Al-BSF solar cells fabricated in our center CRTSE by using mc-Si wafers of different initial qualities.

The wafers used were p-type mc-Si, 1.5 Ω .cm and 300 μ m. Three sets of sister wafers were taken from top, middle and bottom of the ingot. These wafers were used to fabricate three sets of solar cells; the "set A" is prepared only through n⁺ emitter formation at 875°C/20 min, and for "set B" the emitter process was followed by an annealing during 120 min at 850°C, whereas in "set C" a second annealing was added at 670°C for 120 min. After this step, the solar cells of the three sets were fabricated by the same process sequences and in the same conditions. The characterization techniques used were mainly quasi-steady-state photoconductance (QSSPC), Sun-Voc and solar simulator.

The initial effective minority carrier lifetime measured by QSSPC; 9.6 μ s (bottom), 3.2 μ s (middle) and 2.5 μ s (top) are, respectively, associated to the following efficiencies measured by solar simulator: 14%, 13.8% and 12.2%. It is clear that the increment of lifetime provokes the improvement of solar cells performance. The effect of the bulk lifetime (τ_b), affected by the gettering, on the maximum power density ($J_{sc} \times V_{oc}$) supplied by each solar cell is illustrated in Fig. 1. The findings showed a significant increase of 6 mW/cm² when τ_b varies from 5 μ s to 50 μ s. This result was separately confirmed by PC1D simulation. Using a method based on the modeling of the impurity-limited lifetime (τ_{imp}), we demonstrated that the decrease in the density of Cr, Ni or Zn in the material bulk is the possible cause of the improvement of the solar cells efficiency, and this is through the improvement of τ_b .



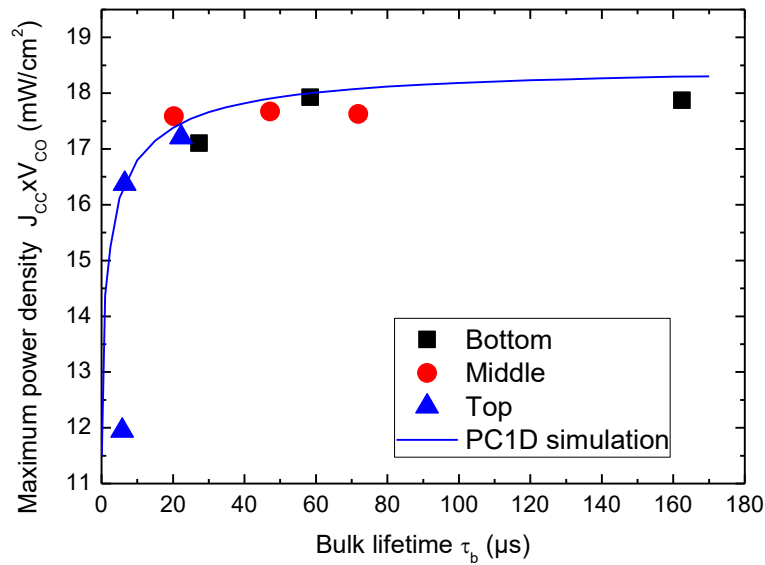


Fig.1: Effect of the bulk lifetime (τ_b) on the maximum power density ($J_{sc} \times V_{oc}$) produced by the solar cells.

References

1. Benda V, «Photovoltaics, Including New Technologies (Thin Film) and a Discussion on Module Efficiency», Editor(s): Trevor M. Letcher, Future Energy (Third Edition), Elsevier, 2020, 375-412.
2. Khelifati N, «Effet du gettering étendu sur les métaux de transition 3d dans le silicium multicristallin destiné aux cellules photovoltaïques», Thèse Doctorat. 2019, Université de Boumerdes.

O07

Efficient Synthesis and Characterization of Highly Pure Nanosilica from Sand

Nassima Meftah^{1,2*} and Amina Hani^{1,2}

^{1*}Department of physics, Faculty of Exact Sciences, University El-Oued, 39000 El-Oued, Algeria

²VTRS Laboratory, University of El-Oued, P. Box 789, 39000, El Oued, Algeria

*Corresponding author

ABSTRACT

This study aims to extract pure silica nanoparticles from sand dunes by using an economical and simple extraction method. The chemical analyses by XRF and FTIR of the synthesized silica confirm the high purity of the silica (~98% SiO₂), while the XRD pattern shows an amorphous structure of the synthesized silica. However, the microstructural analysis displays that the extracted silica particles size is in the range of nanometers. These results confirm the formation of silica nanoparticles and support the use of the new product for advanced material applications.

Introduction

In recent years, due to their excellent physical properties, silica nanoparticles have attracted great interest in several applications such as separation, catalysis, optics, and biomedicine¹⁻⁴. Basically, sodium silicate and tetraethyl orthosilicate (TEOS) are the main precursors for the silica production. However, the high price of these precursors stimulated the researchers to find substitute natural and low-cost resources for Nanosilica and also its extraction process⁵. Silica sand is one of the alternative sources that are very abundant in Sahara and very rich in SiO₂. This work aims to extract and characterize highly pure nano-silica through a facile chemical method from Algeria sand as a low-cost silica source.

Experimental Study

The sand sample was collected from the North-East of Algerian Sahara, which contained 75wt% of quartz (Fig.1-a). The synthesis of silica nanoparticles was carried out by three stages. First, the sand sample was stirred in HCl at room temperature and was washed with distilled water to remove the impurities. In order to obtain the sodium silicates, a mixture of sodium hydroxide and silica sand was mixed and was heated at 300 °C. The obtained product was diluted with distilled water and stirred with a hot plate stirrer, and then followed by titration of the solution with HCl to form a clean white gel. The final silica gel was washed, dried at 100°C, and then ground. The produced silica was characterized using several techniques as X-Ray Fluorescence (XRF), Fourier transform infrared (FTIR), X-ray diffraction (XRD), and scanning electron microscopy (SEM).

Results and Discussion

The chemical analysis by X-ray fluorescence spectroscopy (XRF) and Fourier transform infrared (FTIR) indicate that the new obtained product consisted of highly pure silica particles (~98% SiO₂). The XRD pattern confirms the amorphous structure of the synthesized silica (Fig1-b). Moreover, the scanning



electron microscopy (SEM) analysis reveals that the extracted silica particles' size is in the range of the nanometers. These results corroborate that high purity silica nanoparticles were successfully prepared from sand dunes by using a cost-effective method. Hence, the extracted nanoparticles of silica might be used for nanotechnology applications.

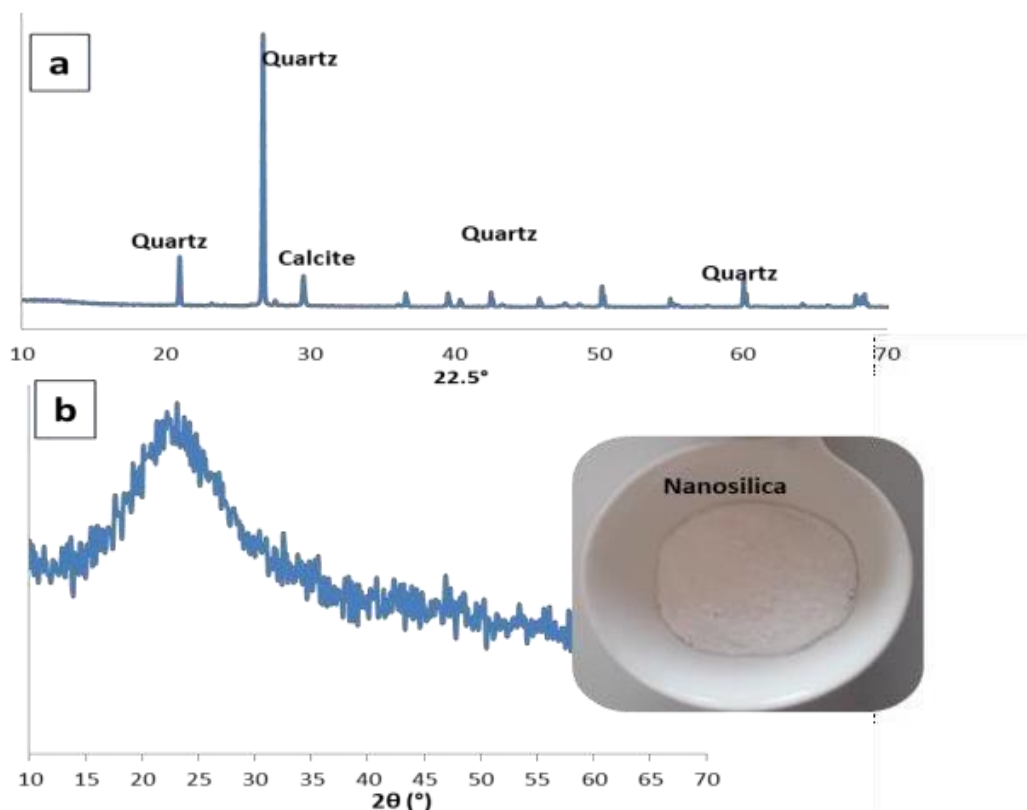


Fig.1: XRD spectra of (a) the silica sand and (b) of the prepared nano-silica.

Conclusion

Silica nanoparticles were extracted from Sand dunes using a simple and low-cost method. The results show that the extracted silica particles from sand have high purity. XRD analysis confirms the amorphous nature of the prepared silica. However, the SEM micrograph confirms the nanometers size of the prepared silica particles.

References

1. Barhoum A, Rahier H, Benelmekki M, Assche G Van. « Recent Trends in Nanostructured Particles: Synthesis, Functionalization, and Applications» *Fundamentals of Nanoparticles*. Elsevier, 2018. 605- 639.
2. Jeelani PG, Mulay P, Venkat R, Ramalingam C. «Multifaceted Application of Silica Nanoparticles» *A Review. Silicon*. 2020;12(6)
3. Velmurugan P, Shim J, Lee KJ, et al. « Extraction, characterization, and catalytic potential of amorphous silica from corn cobs by sol-gel method» *J Ind Eng Chem*. 2015;29:298-303.
4. Sun B, Zhou G, Zhang H. «Synthesis, functionalization, and applications of morphology-controllable silica-based nanostructures: A review» *Prog Solid State Chem*. 2016;44(1):1-19.
5. Owoeye SS, Jegede FI, Borisade SG. «Preparation and characterization of nano-sized silica xerogel particles using sodium silicate solution extracted from waste container glasses» *Mater Chem Phys*. 2020;248(February):122915

008

Positron Annihilation Lifetime Spectroscopy in Neutrons Irradiated CR39 Polymer

S. Limam^{1*}, A. Guittoum², R. Krause-Rehberg³, Z. Mokrani², M. Izerrouken⁴, U. Yashi⁵

¹UR-MPE, M'hamed Bougarra University, Boumerdes, 35000, Algeria

²Nuclear Research Centre of Algiers, 02 Bd Frantz Fanon, BP 399, Alger-Gare, Algiers, Algeria

³Department of Physics, Martin Luther University Halle, 06099 Halle, Germany

⁴Nuclear Research Centre of Draria, BP 43. Sebala. Draria, Algiers, Algeria

⁵Physics Department, Faculty of Arts and Sciences, Marmara University, Goztepe Campus, 34722 Kadikoy, Istanbul, Turkey

*Corresponding author

Introduction

Positron Annihilation Spectroscopy (PAS) is considered as one of the powerful nuclear probe techniques where the angstrom size could be tracked¹. The availability of PAS proved in the characterization of metals², semiconductors and polymers³. It is well demonstrated the success of using PAS to determine the free volumes (0.1-1 nm), voids(>1nm) and layer properties in polymeric system. Positron Annihilation Lifetime Spectroscopy (PALS) based on the measure of positron life time spanned inside matter. CR39 is an amorphous polymer, sensitive to charged particles, gamma rays and neutrons. One of the known uses, is being as solid state nuclear track detector (SSNTD)⁴. Actually, we can characterize the CR39 as an amorphous polymer using the free volume key (kind of defects existed in polymers) which has an important correlation with the macroscopic properties.

Experimental Study

CR39 samples have been irradiated with fast neutron at fluencies of 2.1×10^9 , 4.1×10^9 and 15×10^9 n/cm². Then, The PALS measurements were carried out with a digital positron annihilation lifetime spectrometer. For each irradiated sample, an in-situ annealing treatment has been carried out during the PALS measurement taking the following values; 303, 323, 343, 363K.

Results and Discussion

The analyses of positron lifetime spectra shown increase of the ortho-Positronium component τ_3 with increasing annealing temperature, T. Such an increase of τ_3 has been related to a change in the size of latent tracks created via the backscattered atoms, especially the protons. A linear behavior of τ_3 has been found as it is clear in Fig A.

Conclusion

The effect of annealing temperature on the evolution of the ortho-Positronium lifetime, τ_3 , has been studied using positron annihilation lifetime spectroscopy. From the analysis of positron lifetime spectra, we observed an increase of τ_3 with increasing annealing temperature. We think that this result can be used to predict the neutron fluencies in the case of CR39 irradiated with a fast neutron



field.

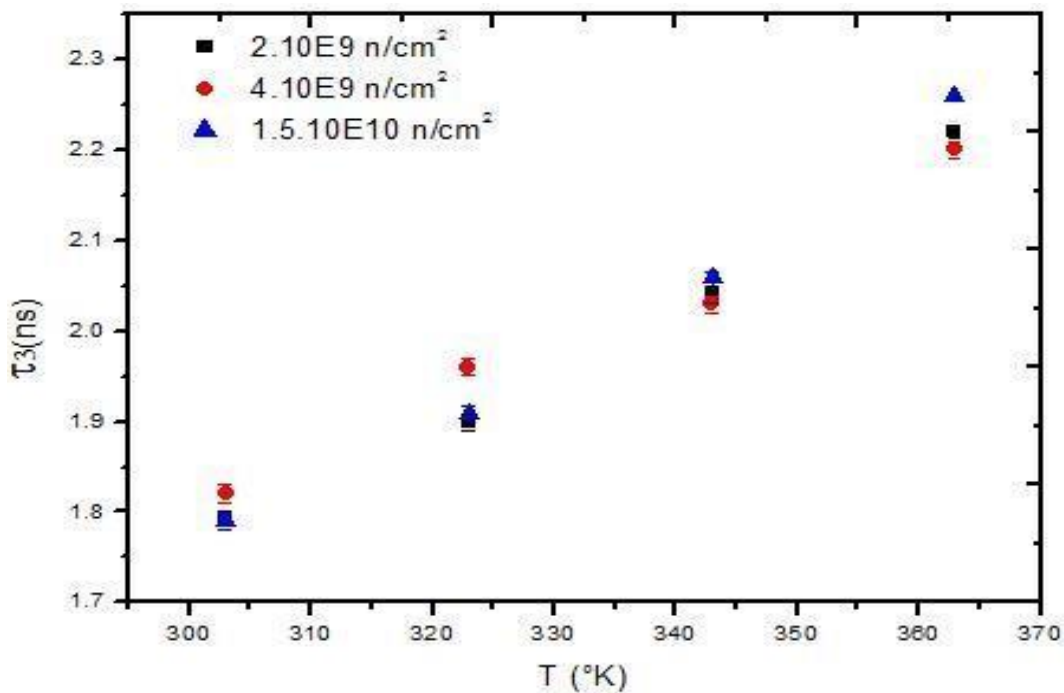


Fig. A Evolution of τ_3 (ns) versus in-situ annealing temperature T(°K) for the irradiated samples.

Acknowledgments

I would thank Dear teacher, my honored Supervisor Dr. *GUITTOUM ABDERRAHIM* for the excellent formation that had ever got before and I would also thank the Boumerdes University for giving the chance to do a PhD study.

References

- [1] Y.C. Jean, P.E. Mallon, D.M. Schrader, "Principles and Application of Positron and Positronium Chemistry". World Scientific, Singapore, 2003
- [2] T.McMullen, R.J. Douglas, N.Etherington, B.T.A.McKee, A.T.Stewart, E.Zaremba, "Positron annihilation at divacancies in metals", Metal Phys, Vol. 11, pp. 1435-1444, 1981.
- [3] F. Faupel, J. Kanzow, K. Günther-Schade, C. Nagel, P.Sperr, G. Köge, 'Positron Annihilation Spectroscopy In Polymers', Materials Science Forum, Vol. 445, pp. 219-223, 2004.
- [4] B.G. Cartwright, E.K. Shirk, P.B. Price, "A nuclear-track recording polymer of unique sensitivity and resolution". Nucl. Instrum. Methods Vol.153, pp.457-460, 1978

009

Synthesis and Characterization of FeCo Nanoparticles by Hydrothermal Method

Imane Bouelkreb^{1*}, Abderrahim Guittoum², Messaoud Hemmous² and Nadia Boukherroub¹

¹Department of physics, Faculty of sciences, University of Boumerdes

²Nuclear Research Centre of Algiers, 02 Bd Frantz Fanon, BP 399, Alger-Gare, Algiers, Algeria

*Corresponding author

Introduction

Magnetic nanomaterials are of major interest due to the wide range of potential technological applications in which these materials can be used¹, such as high-density data storage, catalysis and medical diagnosis^{2,3}. Transition metallic materials, especially Co, Fe and Ni, and their alloys, exhibit particular properties that are rather different from those of their corresponding bulk counterparts^{4,5}. FeCo is considered as a very attractive system due to its magnetic, catalytic, and mechanical properties compared to the elemental Fe and Co metals⁶. Previously, many methods have been used to elaborate FeCo NPs, such as mechanical alloying, electrodeposition and thermal decomposition. More recently, chemical routes, hydrothermal method notably, became a common way for the synthesis of bimetallic alloys, because they offer the ability for a controllable composition and morphology during the synthesis process. Furthermore, the hydrothermal route, i.e., the co-reduction of metal salts by an appropriate reducing agent, is distinguished by its simplicity, low cost, and also flexibility in the choice of synthesis parameters⁷. However, due to the highly broad difference in the reduction potentials of metals, the synthesis of binary alloys by co-reduction of metal salts faces major difficulties. Thus, the convenient choice of synthesis parameters⁸ is still a challenging purpose and requires further research.

Experimental Study

1.1 Synthesis of FeCo NPs

In a typical synthesis process of FeCo NPs, a solution is first prepared by dissolving predetermined quantities of precursors: (FeSO₄.7H₂O and chloride CoCl₂.6H₂O) in ethanol/water mixing solution. Then, sodium hydroxide is added drop wise to the metal salts solution under vigorous stirring. Afterwards, N₂H₄.H₂O (hydrate hydrazine 85%) is added to the above solution. The mixed solution was heated at 100 °C for 30 min and then cooled down to room temperature. The black fluffy product at bottom of the solution was collected using a magnetic bar, and cleaned with deionized water and absolute ethanol. The process was repeated several times. The final product was dried in air at 50 °C for 4 h. A series of five powder samples was prepared with different predetermined masses of precursors, and will be named as S-1, S-2, S-3, S-4 and S-5, respectively.

1.2 Sample Characterization

The room temperature x-ray diffraction (XRD) patterns of the FeCo NPs powders were recorded in a Philips X-PertPro diffractometer equipped with a Cu K α radiation ($\lambda=1.54060$ Å). The scanning range was from 30 to 100° with a step of 0.02° in 2 θ . The morphology of the FeCo powders was studied through several images obtained with a PHILIPS ESEM XL 30 FEG scanning electron microscope (SEM)



equipped with Energy Dispersive X-ray analyser (EDX).

Results and Discussion

The alloys with the compositions Fe₁₀Co₉₀, Fe₁₅Co₈₅, Fe Co , Fe Co and Fe Co were synthesized via hydrothermal route. The XRD patterns of the binary alloys show the presence of many peaks that can be indexed as the Bragg reflections belonging to two different phases: body faced cubic (BCC) and face-centered cubic (FCC) crystal structures. It can be observed that additional impurity phases such as iron oxide and cobalt oxide are not present, indicating the purity of the synthesized powders. The phase composition, lattice parameter, a(nm), and the mean crystallite size, <D(nm)>, were obtained using the Scherrer method by the X'Pert HighScore software. The SEM micrographs of the five FeCo NPs samples evidenced that the morphology of the synthesized FeCo nanostructures changes with the change of the Fe/Co content.

Conclusion

We have successfully synthesized pure FeCo NPs by means of a low cost and surfactant-free hydrothermal method at low temperatures (105 °C) and short annealing periods (30 min) using sodium hydroxide (NaOH). The concentration of NaOH had a significant role on the co-reduction of metal salts and favors the formation of alloy phase and its morphology. Moreover, the line-broadening analysis of the XRD patterns tells us that the average values of NP size for all samples were found to be below 30 nm, which indicates the nanometric state of elaborated powders.

References

- [1] M. Faraji, Y. Yamini, M. Rezaee, J. Iran. Chem. Soc. 7 (2010).
- [2] S. Mørup, M. Hansen, C. Frandsen, Magnetic Nanoparticles, (2018).
- [3] K. Çetin, F. Denizli, H. Yavuz, T. Qureshi, D. Türkmen, A. Denizli, Hacet. J. Biol. Chem. 47 , 143–152 (2019).
- [4] A. Cid, J. Simal-Gandara, J. Inorg. Organomet. Polym. Mater. (2019).
- [5] Bouremana, A. Guittoum, M. Hemmous, B. Rahal, J. Suñol, D. Martínez-Blanco, J. Blanco, P. Gorria, N. Benrekaa, J. Magn. Magn. Mater. s 358–359, 11–15 (2014).
- [6] M. Rafique, L. Pan, M. Farid, J. Alloys Compd. 656, 443–451 (2016)
- [7] M.Y. Rafique, L. Pan, M.Z. Iqbal, D. Javed .Qurat ul ain, H. Qiu, R. Din, M.H. Farooq, Z. Guo, J. Alloys Compd. 550, 423–430 (2012).
- [8] A. Bensouilah, A. Guittoum, M. Hemmous, D. Martínez-Blanco, P. Gorria, J. Blanco, J. Supercond. Nov. Magn. ,1–7 (2019).

O10

Microstructural Investigation of ZnO Nanowires for Therapeutic Applications

Chahra YOUNSI^{1*}, Manel BOULOUDENINE², Rafik CHEMAM³

¹Badji Mokhtar Annaba University, LERE Laboratory, Physics Department, PO Box 12 (23000) Annaba ALGERIA

²Mohamed Cherif Messâadia University, Science of Materials Department, 41000 Souk.Ahras ALGERIA.

³Badji Mokhtar Annaba University, LPR Laboratory, Physics Department, PO Box 12 (23000) Annaba-ALGERIA

*Corresponding author

ABSTRACT

Zinc oxide (ZnO) is known as an important semiconductor, which has been studied extensively in the past few years due to its fundamental and technological importance [1]. Many attractive properties of ZnO, such as wide bandgap (3.37 eV), large exciton binding energy and excellent chemical stability, [2] suggest a great many possible practical applications such as in gas sensors, ceramics, field-emission devices and luminescent materials [3] and therapeutic. Size and crystalline morphologies play important roles in these applications, which have driven researchers to focus on the synthesis of nanocrystalline ZnO [4].

This work aims to the synthesis and characterization of zinc oxide nanowires for therapeutic applications. ZnO nanowires are synthesized by hydrothermal method using a novel synthesized protocol. The elaboration hydrothermal conditions are optimized in order to have the longest nanowires with the lowest diameter.

The structural properties, morphological and elementary analysis of the growth NWs, are carried out respectively by X-ray Diffraction (DRX), Scanning Electron Microscopy (SEM) and Energy Dispersive spectroscopy (EDS). XRD results reveals a very good crystallinity of ZnO-Nws in a hexagonal würtzite phase. Scanning Electron Microscopy (SEM) shows single-crystals of ZnONPs with nearly wires shapes. The crystalline refinement in the ZnO-Nws are investigated by X-ray peak broadening. Williamson Hall (W_H) analysis and size strain plot method are used to study the individual contributions of crystallite sizes and lattice strain on the peak broadening of the ZnO-Nws.

Acknowledgments

Zinc Oxide nanowires, hydrothermal method, XRD, SEM, Williamson–Hall analysis

References

1. S. Hingorani, V. Pillai, P. Kumar, M.S. Muntai, D.O.Shah, Mater. Res. Bull. 28(1993) 1303
2. X. Zhao, S.C. Zhang, C. Li, B. Zheng, H. Gu, J. Mater.Synth. Process. 5 (1997) 227.
3. A. Khorsand Zak , W.H. Abd. Majid a, M.E. Abrishami b, Ramin Yousefi. 13 (2011) 251e256



O11

Real Time Ultrasoft Longitudinal Photons Self Energy at Next to-leading Order in Hot Scalar QED

Amel Youcefi¹, Karima Bouakaz^{1*}, Abdessamad Abada²

¹Department of Physics, Laboratoire de Physique des Particules et de Physique Statistique, Ecole Normale Supérieure, BP 92 Vieux-Kouba, Algiers

²Department of Physics, United Arab Emirates University, P. O. B. 17551, Al Ain, United Arab Emirates

*Corresponding Author

ABSTRACT

We determine a compact analytic expression for the complete next-to-leading contribution to the retarded Longitudinal Photons self-energy with ultrasoft momentum in the framework of hard-thermal-loop (HTL) -summed perturbation of massless Scalar QED at high temperature. The calculation is done using real-time formalism. The real part and the opposite of the imaginary part of the retarded Longitudinal Photons self-energy are related to the next-to-leading order contributions of energy and damping rate respectively.

Keywords: Soft Photons Energy and Damping Rate; Resummation; Hard Thermal Loop

Introduction

In recent years, there has been steadily increasing activity aimed at analyzing the phase structure of Quantum Chromodynamics (QCD), the quantum field theory of strong interactions. A detailed understanding of the properties of the deconfined phase of QCD, the so-called Quark-Gluon Plasma, is important in several areas of Physics. Examples are the evolution of the early Universe [1], heavy ion collisions at RHIC (Brookhaven) and LHC (CERN) [2]. A major problem that spurred progress in the late 1980's was the apparent gauge dependence of the one-loop order quasiparticle dispersion relations, most notably the gluon damping rate. The problem was resolved in [3]. It turns out that in order to calculate consistently at high temperature, we have to use an effective perturbation that sums the so-called hard thermal loops (HTL) into dressed propagators and vertices [3, 4]. The first next-to-leading order physical quantity that has been determined in the framework of the HTL program is the zero-momentum transverse gluon damping rate [5]. It was shown to be finite and positive. Subsequent studies of the behavior of the gluon and quark damping rates in the imaginary-time formalism have indicated that there are difficulties in the infrared sector [6-12]. A similar observation has been done in the context of scalar electrodynamics [13]. To look further into the infrared behavior, we propose to calculate the next-to-leading order dispersion relations for slow-moving Longitudinal Photons at high-temperature scalar quantum electrodynamics (Scalar QED), using the real time formalism (RTF) in physical representation. We derive the analytic expressions of hard thermal loop (HTL) contributions to propagators to determine the expressions of the effective propagators in RTF that contribute to the complete next-to leading order contribution of retarded Longitudinal photons self-energy. The



longitudinal retarded photons self-energy is related to the next-to-leading order dispersion relations.

Effective expansion

In the Landau gauge, the effective photon propagator followed from the resummation of the HTL photon self energy. To leading order the effective photon propagator is given by:

$$\Delta_{ra/ar}^{\mu\nu}(K) = P_T^{\mu\nu} \frac{1}{\delta\Pi_T^{r/a} - K^2 \mp i\text{sgn}(k_0)\varepsilon} + P_L^{\mu\nu} \frac{1}{\delta\Pi_L^{r/a} - K^2 \mp i\text{sgn}(k_0)\varepsilon}, \quad (1)$$

where $P_T^{\mu\nu}, P_L^{\mu\nu}$ are the usual transverse and longitudinal projectors respectively and

$$\begin{aligned} \delta\Pi_L^{r/a}(K) &= -3m^2 \left[1 - \frac{k_0}{2k} \ln \frac{k_0 + k \pm i\varepsilon}{k_0 - k \pm i\varepsilon} \right] \\ \delta\Pi_T^{r/a}(K) &= \frac{3}{2} m^2 \frac{k_0^2}{k^2} \left[1 - \left(1 - \frac{k^2}{k_0^2} \right) \frac{k_0}{k} \ln \frac{k_0 + k \pm i\varepsilon}{k_0 - k \pm i\varepsilon} \right] \end{aligned} \quad (2)$$

with $m = \frac{1}{6} e^2 T^2$ the photon thermal mass.

The HTL contribution to the scalar self-energy is obtained by summing the one loop diagrams and it is given by:

$$\delta\Sigma_{hl}(K) = m_s^2, \quad (3)$$

with $m_s = eT/2$ the scalar thermal mass.

The HTL resummed scalar propagator is given by

$$\begin{aligned} \Delta_{R,A}^{-1}(K) &= K^2 - m_s^2 \pm i\text{sgn}(k_0)\varepsilon \\ \Delta_F^{-1}(K) &= -2\pi i [1 + 2n_B(|k_0|)] \delta(K^2 - m_s^2), \end{aligned} \quad (4)$$

where $K = (k_0, k)$ and $n_B(k_0) = 1/(\exp(k_0/T) - 1)$ the Bose distribution function.

The dressed vertices are equal to the tree amplitudes, i.e., unaffected by the hard thermal loops.

The vertex with one photon and two scalar external lines undressed (Q incoming, P outgoing) is:

$$\Gamma^\mu(P, Q) = -e(P + Q)^\mu, \quad (5)$$

and the vertex between two photons and two scalars is momentum independent and writes:

$$\Gamma^{\mu\nu}(P, Q) = -ie^2 g^{\mu\nu}, \quad (6)$$

Damping rate and energy for photons in hot SQED

The dispersion relations are defined by:

$$p^2 - \delta\Pi_{ra/ar}^l(\Omega_l, p) - {}^*\Pi_{ra/ar}^l(\Omega_l, p) = 0, \quad (7)$$

where ${}^*\Pi^l$ is the next-to-leading order longitudinal photon self-energy. The next-to-leading-order energy of the slow-moving longitudinal photons is:

$$\text{Re}\Omega_l(p) = \omega_l(p) - \frac{\text{Re} {}^*\Pi_{ra/ra}^l(P)}{\left. \frac{\partial}{\partial\omega} \delta\Pi_{ra/ar}^l(P) \right|_{\omega=\omega_l}} \quad (8)$$

and the damping rate is given by:

$$\gamma_l(p) = - \frac{\text{Im} {}^*\Pi_{ra/ra}^l(P)}{\left. \frac{\partial}{\partial\omega} \delta\Pi_{ra/ar}^l(P) \right|_{\omega=\omega_l}} \quad (9)$$

where ω_{s_0} is the leading-order scalar energy. So, to obtain the next-to leading-order dispersion relations for slow moving longitudinal photons, we have to determine the next-to leading-order 'NLO' longitudinal photons self-energy. The diagrams that contribute to next-to-leading-order longitudinal photons self energy are the following two diagrams, in which the internal momenta are soft.

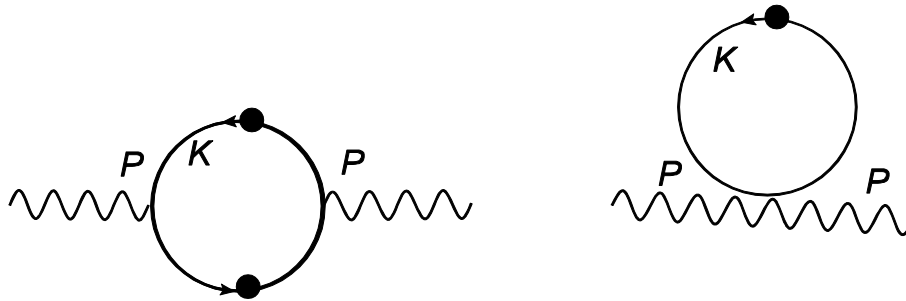


Figure1: NLO HTL-summed longitudinal photons self-energy

The contribution of the two diagrams in the Keldysh basis is given by:

$$\begin{aligned} {}^*\Pi_{ab}^l(P) = & \int \frac{d^4 K}{(2\pi)^4} \left[\Gamma_{ab\alpha\beta}^{\mu\nu}(Q, -Q, K, -K) {}^*\Delta_{\alpha\beta}(K) \right. \\ & \left. + {}^*\Gamma_{\alpha\alpha'}^\mu(K, K-Q) {}^*\Delta_{\alpha\alpha'}(K) {}^*\Gamma_{\alpha'\beta\beta'}^\nu(K-Q, K) {}^*\Delta_{\beta\beta'}(K-Q) \right] \end{aligned} \quad (10)$$

where K is the soft internal momentum and $Q=P-K$.

In Keldysh representation the retarded, advanced and symmetric resummed (effectif) propagator are given by:

$$\begin{aligned} {}^*\Delta_{r,a}(K) &= \frac{1}{K^2 - m_s^2 \mp i \text{sgn}(k_0) \epsilon}, \\ {}^*\Delta_s(K) &= -2\pi \left(1 + 2n_B(|k_0|) \right) \delta(K^2 - m_s^2) \end{aligned} \quad (11)$$

where we have used the notation $K = (k_0, \vec{k})$, $k = |\vec{k}|$ and $n_B(x) = 1/(\exp(x/T) - 1)$ denotes the Bose

distribution function. The effective temperature dependent scalar mass is given by $m_s = \frac{eT}{3}$. The contribution of the first term using the real time formalism to the retarded self energy can be written as:

$${}^{tad*} \Pi_R^L(P) = -ie^2 \int \frac{d^4 K}{(2\pi)^4} \left({}^* \Delta_F(K) + {}^* \Delta_R(K) + {}^* \Delta_A(K) \right) \quad (12)$$

After integrating over k_0 by means of δ function and trivially over the angle reduces to:

$${}^{tad*} \Pi_R^L(P) = -\frac{e^2}{\pi^2} \int_0^\infty dk \frac{k^2}{\omega_k} n_B(\omega_k) \quad (13)$$

Where $\omega_k^2 = k^2 + m_s^2$

The contribution of the second term is given by:

$${}^{1*} \Pi_R^L(P) = \frac{e^2}{2} \int \frac{d^4 K}{(2\pi)^4} (2k_0 + p_0)^2 \left[{}^* \Delta_S(Q) {}^* \Delta_R(K) + {}^* \Delta_A(Q) {}^* \Delta_S(K) \right] \quad (14)$$

Conclusion

In this work, we have reported on the progress in our determination of the HTL next-to-leading Longitudinal Photons dispersion relation. We have derived a compact analytic expression for the complete next-to-leading contribution to the retarded longitudinal photons self-energy in the context of hard-thermal-loop summed perturbation of Scalar QED at high temperature using real time formalism. These expressions need to be manipulated, mainly numerically, to determine the next-to-leading order longitudinal photons dispersion relation. This work is in progress.

References

- [1] D. J. Schwarz, *Annalen. Phys.*12 (2003) 220
- [2] J. Bartke, *Relativistic Heavy-Ion Physics*, Singapore World Scientific 2003.
- [3] E. Braaten and R.D. Pisarski, *Nucl. Phys. B*337 (1990) 569.
- [4] M. Le Bellac, *Thermal Field Theory*, Cambridge University Press, 1996.
- [5] E. Braaten and R.D. Pisarski, *Phys. Rev. D*42 (1990) R2156.
- [6] A. Abada, O. Azi and K. Benchallal, *Phys. Lett. B*425 (1998) 158.
- [7] A. Abada, O. Azi, *Phys. Lett. B*463 (1999) 117.
- [8] A. Abada, K. Bouakaz and O. Azi, *Phys. Scr.* 74 (2006) 77.
- [9] A. Abada, K. Bouakaz and N. Daira-Aifa, *Eur. Phys. J. C*18 (2001) 765
- [10] A. Abada, N. Daira Aifa and K. Bouakaz, *Int.J.Mod.Phys.A*21(2006) 5317.
- [11] K. Bouakaz, A. Abada *AIP Conf.Proc.*1006:150-153,2008.
- [12] A. Abada, K. Bouakaz and D. Deghiche, *Mod.Phys.Lett.A*22 (2007)903-914.
- [13] A. Abada and K. Bouakaz, *JHEP*01 (2006) 161
- [12] A. Abada, K. Bouakaz and D. Deghiche, *Mod.Phys.Lett.A*22 (2007)903-914.
- [13] A. Abada and K. Bouakaz, *JHEP*01 (2006) 161.

Sensing Properties and Sensitivity Improvement of an Asymmetric Waveguide with Dispersive Left-handed Material

Abdellatif CHERIFI^{*1} and Benamar BOUHAFS²

Department of physics, Faculty of Sciences Theoretical Physics Laboratory, University of Tlemcen, 13000, Algeria

*Corresponding Author

ABSTRACT

Optical sensors supporting resonant phenomena have been extensively employed for characterizing surface effects manifested in the vicinity of a metallic layer and a dielectric of opposite permittivities. To get appreciable sensing performance in terms of detection accuracy and resolution highly required in various applications such as biochemical and gas sensing, various plasmonic materials were proposed in the literature. Importantly, the proper responses of possible arrangements between active layers and dielectric media when stimulated with an external incident light differ on the field profiles, energy distribution and dispersion properties. As to this, owing to their unique properties, black phosphorous, graphene and molybdenum disulfide (MoS₂) mediated silver or gold regarded as multilayer sensors, were functionalized and implemented for sensing applications. In this contribution, an asymmetric waveguide including gold (Au), left-handed material (LHM) layers and an outer medium, was designed and numerically investigated, under plane wave irradiation as a function of the incidence angle and of the polarization. The proposed configuration as schematically illustrated in Fig. 1, is a four layered media stacked along z-direction. Gold layer of thickness, d_2 is placed in contact between a sensing environment of refractive index, n_c and a left-handed material (LHM) of thickness, d_1 . The above media are coated on the base of a chalcogenide (2S2G) glass-substrate having a RI, n_p . The refractive index of the a left-handed material (LHM) n_{LHM} is given by $n_{LHM} = -\sqrt{\epsilon_{LHM} \times \mu_{LHM}}$ and we chose the experimental values of the dielectric permittivity and magnetic permeability: $\epsilon_{LHM} = -33.5$, $\mu_{LHM} = -11$ respectively¹.

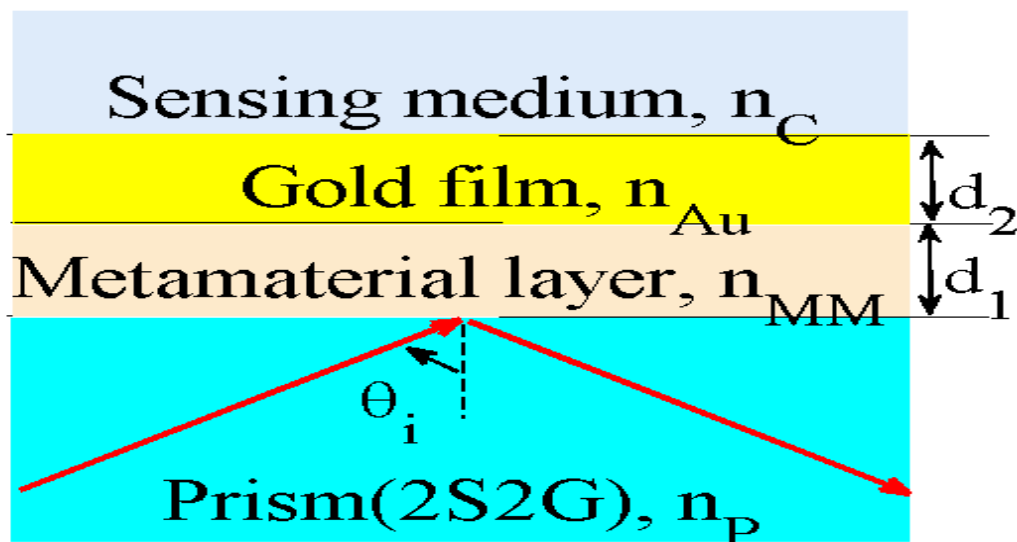


Fig.1: Schematic diagram of proposed SPR

Furthermore, we also investigate the effect of sensing environment RI, n_c on p-reflectance curve in the previous conditions. As shown in Fig. 2, when RI increases from 1.32 to 1.34, resonance condition shifts gradually from 36.15° to 36.84°.

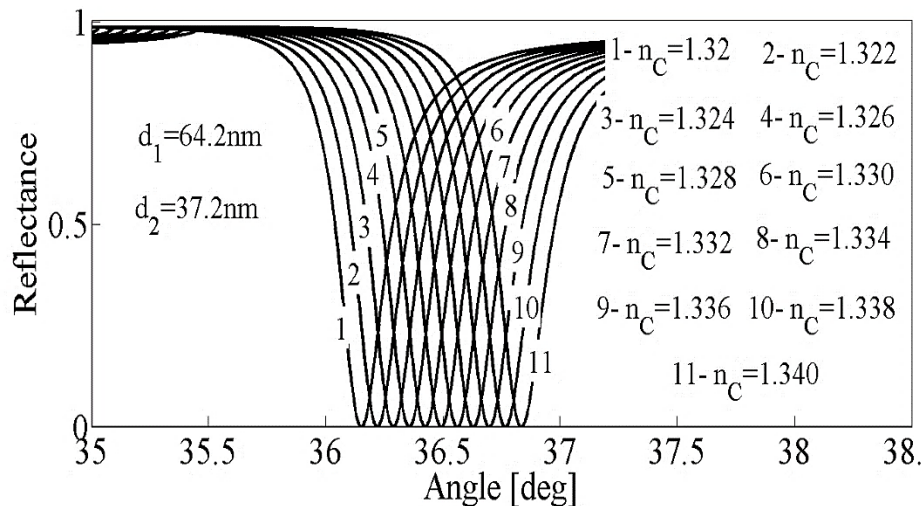


Fig. 2 Change of the reflectance spectra as a function of the incidence angle for the multilayered structure Metamaterial (64.2nm)/Au (37.2nm)/Sensing medium with increasing refractive index of inner gap, n_s from 1.320 to 1.340

As such, a small fluctuation in the RI of sensing environment reflects, how precisely the sensor detects the resonance condition and its shift, this value allows the determination of resulting sensitivity, $S_\theta = \partial\theta_{SPR}/\partial n_s$ ² and Figure of merit is $FoM = S_\theta/FWHM$ ³. Angular resonance a linear change between the refractive index of the medium to be sensitive as follows:

$$\theta_{SPR} = 34.364 \times n_s - 9.21 \pm 0.00874$$

According to this significant effect induced on SPR mode, angular sensitivity and figure of merit for the designed sensor can be evaluated as $S_\theta = 34.364$ and $FoM = 137.46$ respectively. It is matter in fact that, if the approach is used for sensing aqueous solution whose RI is close to the one of water, the closest accuracy value could be within thousandths of the reference index, hence rendering it a highly sensitive optical sensor.

Keywords: Asymmetric Waveguide, Biosensing, Left-Handed Material, Sensitivity, Sensing Characteristics.

References

1. Xiao.S M, Drachev. V. P, Kildishev. A. V, Ni. X. J, Chettiar. U. K, Yuan.H K, and al, « Loss-free and active optical negative-index metamaterials, » *Nature*, 2010, 466(7307), 735-738.
2. CHERIFI. A and BOUHAFS. B « 'Sensitivity Analysis of GaAs-metamaterial Nanocavity as a Tunable Surface Plasmon Resonance Sensor» *International Journal of Sensors, Wireless Communications and Control*, 2020, 10 (6), 00.
3. Meng. Q-Q, Zhao. X, Lin. Ch-Y, Chen. Sh-J, Ding. Y-Ch and Chen. Zh-Y « Figure of Merit Enhancement of a Surface Plasmon Resonance Sensor Using a Low-Refractive-Index Porous Silica Film» *Sensors*, 2017, 17(8), 1846: 1-11

Towards the Optimization of the Performance of N-I-P Microcrystalline Silicon nc-Si:H Flexible Solar Cells

Wafa Hadj Kouider*, Tayeb Youcef Belabbas, Abbas Belfar

Laboratoire de Physique des Plasmas, des Matériaux Conducteurs et leurs Applications (LPPMCA),
Université des Sciences et de la technologie Mohamed-Boudiaf, Oran, Algérie.

*Corresponding Author

ABSTRACT

The use of low-cost flexible substrates reduces the installation and transportation charges, thereby reducing the system price. This study focuses on the investigation and the optimization of the efficiency of a thin-film flexible microcrystalline silicon nc-Si:H solar cell by simulation tools. As a result, we could achieve the 6.37% relatively high efficiency for n-i-p single junction nc-Si:H flexible solar cell.

INTRODUCTION

Flexible thin film solar cells have received worldwide attention [1]. However, given that conversion efficiency is crucial for cost-competitiveness, it is necessary to develop devices on flexible substrates that perform as well as those obtained on rigid substrates [2]. The performances of laboratory $\mu\text{c-Si:H}$ single junction cells on plastic substrates are starting to reach values comparable with those initially obtained for $\mu\text{c-Si:H}$ cells deposited on TCO coated glass [3]. For this purpose, we have carried simulation study on nc-Si:H flexible cells. The relationship between the material properties of nc-Si:H thin film solar cell different layers and their performance cells was investigated systematically

EXPERIMENTAL/THEORETICAL STUDY

The structure of the n-i-p flexible solar cells simulated in this study was SUS substrate/Cr (20 nm)/Ag (300 nm)/ZnO:Al (100 nm)/n-nc-Si:H (30 nm)/i-nc-Si:H (1.0 μm)/p-nc-Si:H(15 nm)/ITO (80 nm)/Al grid. Which has been fabricated by Cho et al.[4].

RESULTS AND DISCUSSION

In order to figure out the effect of using nc-Si:H in flexible solar cells, we have simulated the electrical output of these devices. Fig.1: shows the photo J-V curves of the flexible nc-Si:H solar cell. The cell characteristics are also listed in Table 1.

Table 1: photoelectrical parameters of simulated solar cell

Jsc (mA/cm ²)	FF (%)	η (%)	VOC(V)
19.87	75.90	6.37	0.42

For the nc-Si:H solar cell with the narrow-bandgap p-nc-Si:H window layer, a conversion efficiency of 6.37% is obtained. This due to the higher conductivity of nc-Si:H.



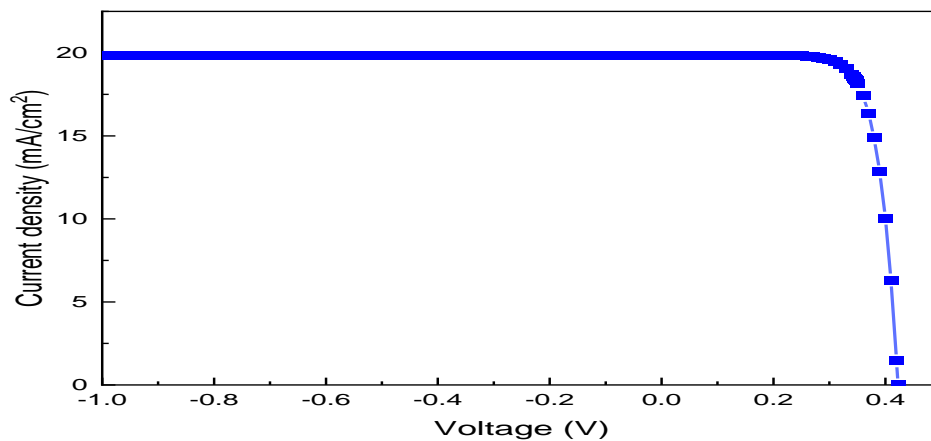


Fig. 1 : Current density-voltage characteristics of the n-i-p junction nc-Si:H device under AMI (100 mW/cm²) illumination at 300K.

CONCLUSION

Our simulation results indicated that thin microcrystalline silicon films with high quality can be used to fabricate relatively high performance and stable flexible solar cells. Also, we showed that the optimization of nc-Si:H layers parameters enhanced the simulated device power conversion efficiency to 6.37%.

REFERENCES

1. Ramanujam J, Bishop DM, Todorov TK, Gunawan O, Rath J, Nekovei R, et al. « Flexible CIGS, CdTe and a-Si:H based thin film solar cells: A review». *Progress in Materials Science*. 2020;110:1–20.
2. Chirilă A, Buecheler S, Pianezzi F, Bloesch P, Gretener C, Uhl AR, et al. «Highly efficient Cu(In,Ga)Se₂ solar cells grown on flexible polymer films». *Nature Materials* [Internet]. Nature Publishing Group; 2011;10:857–61.
3. Bassler H. « thin film solar cells fabrication, characterization and applications» . Poortmans J, Arkhipov V, editors. *Thin Film Solar Cells*. Chichester, UK: John Wiley & Sons, Ltd; 2006.
4. Cho JS, Jang E, Lim D, Ahn S, Yoo J, Cho A, et al. « Wide-bandgap nanocrystalline silicon-carbon alloys for photovoltaic applications». *Solar Energy Materials and Solar Cells* [Internet]. Elsevier B.V.; 2018;182:220–7.

(2+1) D Massless Dirac Equation in Anti de-Sitter Space

Lakhdar Sek^{1*}, Mokhtar Falek¹, Mustafa Moumni^{1,2}

¹Laboratory of Photonic Physics and Nano-Materials (LPPNNM), Department of Matter Sciences,
University of Biskra, ALGERIA

²Laboratory of Radiation and their Interactions with Matter (PRIMALAB), Department of Physics,
University of Batna1, ALGERIA

*Corresponding author

Abstract

In this study, we investigate the study of 2D graphene in the presence of external magnetic field in Anti de-Sitter space. Where the energy eigenvalues and the corresponding wave functions are obtained using Nikiforov-Uvarov method after submission this latter in the extended uncertainty principle of Heisenberg in order to show the curvature of the space. Moreover, the upper bound of the minimal uncertainty in momentum experimentally has calculate.

Keywords: Graphene, Anti de-Sitter space, Extended Uncertainty principle.

Introduction

Carbon in its allotropic forms such as graphite and diamond occupies a prominent place in various branches of science. In particular, one can imagine that graphite consists of the accumulation of thick layers of carbon in an atom, the so-called graphene. Theoretical scientific community, since experimental observations revealed the existence of electrical charge carriers that behave like massless Dirac quasi-particles [1-4]. The reason for this lies in the unusual molecular structure of graphene. Carbon atoms are arranged in a hexagonal lattice, similar to a honeycomb structure [5]. It has been observed that low-energy electronic excitations at the corners of the Brillouin zone of graphene can be described by (2 + 1) Dirac fermions with a linear scattering ratio (massless) [3, 4]. This effect offers the opportunity to test various aspects of relativistic phenomena, which generally require high energy, in experiments in condensed matter physics, such as: the chiral tunnel and the Klein paradox [6, 7]

On the other hand, among the various attempts to integrate gravity into the quantum world, there is one area that has generated great interest; it is the quantum theory of fields in curved space through generalizations of Heisenberg algebra, such as the extended uncertainty principle (EUP). The purpose of this extended principle is to account for the quantum fluctuations of the gravitational field in order to include gravity in the quantum mechanics domain. One of the consequences of this standardization is the existence of a minimal length scale of the Planck order [8]. We can combine this minimum length with a modification of Heisenberg's standard algebra by adding small corrections to the canonical commutation relations and thus changing their standard algebra; we quote here the work of Mignemi [8], who showed that Heisenberg relations in the (anti-) deSitter space are modified by adding corrections that are proportional to the cosmological constant. These modifications were also motivated by Doubly Special Relativity (DSR) [9, 10], string theory [11], non-commutative geometry



[12] and black hole physics [13, 14]. Effects of Newtonian gravity in quantum systems [15] and that the modification of inertia, which is predicted by some alternative theories of gravity on cosmic scales, can be derived naturally within the framework of the EUP [16].

In recent years, a large part of the research work has been devoted to the study of relativistic quantum mechanics with the EUP [17-19]. Some problems have also been solved in non-relativistic quantum mechanics; this happened despite the fact that we cannot derive any non-relativistic Schrödinger-like covariant equations from the Klein-Fock-Gordon covariant equation in the traditional field theoretical method of the deSitter (dS) models and anti-deSitter (AdS) [20-22].

In this work, we are interested in phenomenological models of quantum gravity. We study analytically in 2D spaces, the massless dirac equation in the position space representation for deformed quantum mechanics with EUP in an interaction with an external uniform magnetic field for this system.

The paper is organized as follows: In Sec.2, we provide an analysis of the AdS model while in Sec.3; we introduce the Nikiforov–Uvarov (NU) method used to solve the equation of our system. We expose in Sec.4 the explicit calculations of both eigenfunctions and eigenvalues of the deformed 2D graphene in a uniform magnetic field with AdS algebra. To sum up with a conclusion in Sec.5.

Review of the deformed quantum mechanics relation

The deformed Heisenberg algebra, which leads to the EUP model in AdS, is defined in 3D spaces by the following commutation relations [23, 24]:

$$[\mathbf{X}_i, \mathbf{X}_j] = \mathbf{0}; [\mathbf{P}_i, \mathbf{P}_j] = -i\hbar\lambda\epsilon_{ijk} \mathbf{L}_k; [\mathbf{X}_i, \mathbf{P}_j] = i\hbar(\delta_{ij} - \lambda\mathbf{X}_i\mathbf{X}_j) \quad (1)$$

where λ is a small positive deformation parameter. In the sense of quantum gravity, this parameter λ is calculated as the fundamental constant associated with the scaling factor of the expanding universe and is proportional to the cosmological constant $\Gamma = -3\lambda = -3a - 2$ where a is the radius of AdS [25]. L_k are the usual components of angular momentum and are expressed as follows:

$$\mathbf{L}_k = \epsilon_{ijk}\mathbf{X}_i\mathbf{P}_j \quad (2)$$

These components follow the usual momentum algebra;

$$[\mathbf{L}_i, \mathbf{P}_j] = i\hbar\epsilon_{ijk}\mathbf{P}_k; \quad (3)$$

$$[\mathbf{L}_i, \mathbf{X}_j] = i\hbar\epsilon_{ijk}\mathbf{X}_k;$$

$$[\mathbf{L}_i, \mathbf{L}_j] = i\hbar\epsilon_{ijk}\mathbf{L}_k$$

The AdS deformed algebra (1) gives rise to modified Heisenberg uncertainty relations:

$$\Delta\mathbf{X}_i\Delta\mathbf{P}_i \geq \frac{\hbar}{2}(1 + \lambda(\Delta\mathbf{X}_i)^2) \quad (4)$$

Where we have chosen the states for which $\langle X_i \rangle = 0$.

It also generates a minimum uncertainty in momentum. For simplicity, if we assume isotropic uncertainties $X_i = X$, we get:

$$(\Delta\mathbf{P}_i)_{\min} = \hbar\sqrt{\lambda} \quad (5)$$

So the noncommutative operators X_i and P_i satisfy the AdS algebra (1) with the rescaled uncertainty relations in position space (4). In what follows, we represent these operators as functions of the usual x_i and p_i operators fulfilling the ordinary canonical commutation relations in position space; this is done with the following transformations:

$$X_i = \frac{x_i}{\sqrt{1 - \lambda r^2}} \quad (6)$$

$$P_i = -i\hbar\sqrt{1 - \lambda r^2}\partial x_i \quad (7)$$

Here the variable r vary in the domain $\left] -\frac{1}{\sqrt{\lambda}}, \frac{1}{\sqrt{\lambda}} \right[$.

Nikiforov-Uvarov method

NikiforovUvarov's (NU) approach is mainly based on the hypergeometric differential equation. The formulas used in the NU method reduce the differential equations of the second order with a suitable coordinate transformation to the hypergeometric type (note that $s \equiv s(x)$ and the prime numbers denote the derivatives):

$$\psi''(s) + \frac{\tilde{\tau}(s)}{\sigma(s)}\psi'(s) + \frac{\tilde{\sigma}(s)}{\sigma^2(s)}\psi(s) = 0 \quad (8)$$

Where $\sigma(s)$ and $\tilde{\sigma}(s)$ are at most polynomials of the second degree [26, 27], while the degree of the polynomial $\tilde{\tau}(s)$ is strictly less than

$$\psi(s) = \phi(s)y(s) \quad (9)$$

Eq. (8) becomes [27]:

$$\sigma(s)y''(s) + \tau(s)y'(s) + \Lambda y(s) = 0 \quad (10)$$

Where

$$\pi(s) = \sigma(s) \frac{d}{ds}(\ln\phi(s)) \text{ and } \tau(s) = \tilde{\tau}(s) + 2\pi(s) \quad (11)$$

Moreover, Λ defined by;

$$\Lambda_n + n\tau' + \frac{n(n+1)}{2}\sigma'' = 0 \text{ and } n = 0, 1, 2, \dots \quad (12)$$

The energy eigenvalues of the system are determined from the previous equation, to find them we need to evaluate $\pi(s)$ and identify them first:

$$k = \Lambda - \pi'(s) \quad (13)$$

We get the solution of the quadratic equation for $\pi(s)$, which is a polynomial of s :

$$\pi(s) = \left(\frac{\sigma' - \tilde{\tau}}{2}\right) \pm \sqrt{\left(\frac{\sigma' - \tilde{\tau}}{2}\right)^2 - \tilde{\sigma} + \sigma k} \quad (14)$$

It should be noted that in computing $\pi(s)$ the determination of k is critical point and it is reached by indicating that the expression under the square root in (14) must be a square polynomial; this gives us a general quadratic equation for k . We use (11) and the Rodrigues relation to evaluate the polynomial solutions $y_n(s)$:

$$y_n(s) = \frac{C_n}{\rho(s)} \frac{d^n}{ds^n} [\sigma^n(s)\rho(s)] \quad (15)$$

Where C_n are constants that used to normalize the solutions, the weighted function satisfy the following relationship:

$$\frac{d}{ds} [\sigma(s)\rho(s)] = \tau(s)\rho(s) \quad (16)$$

This last equation relates to the classical orthogonal polynomials and we write the orthogonality relations for the polynomial solutions as follows:

$$\int_a^b y_n(s)y_m(s)\rho(s)ds = 0 \text{ if } m \neq n \quad (17)$$

2D Massless Dirac Equation in Anti de-Sitter Space

The electron in quantum theory of graphene is a massless fermion that moves at a velocity $V_F = (1.12 \pm 0.02) \times 10^6 \text{ ms}^{-1}$, called the Fermi velocity verify the relativistic massless Dirac equation. The discovery of graphs gives us the opportunity to test various effects of QED, such as the “small paradox”, since this effect cannot be observed in particle physics [28]. In this section, we are interested in solving the Dirac equation without dimensional mass (1 + 2) in the presence of a constant external magnetic field $\vec{A} = \frac{B}{2} (-y, x, 0)$. The Hamiltonian of the massless (2+1)-dimensional Dirac equation is [29];

$$(\hat{\alpha} \cdot \mathbf{p})\Psi(\mathbf{r}) = \frac{E}{V_F}\Psi(\mathbf{r}) \quad (18)$$

Where $\hat{\alpha}$ is the usual Dirac matrices and we may assume that the four-component spinor Ψ is of the form $\Psi(\mathbf{r}) = (\Psi_a(\mathbf{r}), \Psi_b(\mathbf{r}))$.

We use the AdS algebra definition (eqs.6 and 7) and involving the spinor above, to rewrite this equation in the deformed momentum space:

$$\hat{\sigma} \cdot (\mathbf{p} - e\mathbf{A})\Psi_b(\mathbf{r}) = \frac{E}{V_F}\Psi_a(\mathbf{r}) \quad (19-a)$$

$$\hat{\sigma} \cdot (\mathbf{p} - e\mathbf{A})\Psi_a(\mathbf{r}) = \frac{E}{V_F}\Psi_b(\mathbf{r}) \quad (19-b)$$

With $\hat{\sigma}$ designates the Pauli matrices. Then, we eliminate $\Psi_b(\mathbf{r})$ in favor of $\Psi_a(\mathbf{r})$, to obtain the following equation:

$$[\hat{\sigma} \cdot (\mathbf{p} - e\mathbf{A})]^2\Psi_a(\mathbf{r}) = \frac{E^2}{V_F^2}\Psi_a(\mathbf{r}) \quad (20)$$

According to the following relations:

$$(\hat{\sigma} \cdot \mathbf{A})(\hat{\sigma} \cdot \mathbf{B}) = \mathbf{A} \cdot \mathbf{B} + i\hat{\sigma} \cdot (\mathbf{A} \times \mathbf{B}) \quad (21)$$

The eq (20) becomes:

$$(\mathbf{p}^- \cdot \mathbf{p}^- + i\hat{\sigma} \cdot (\mathbf{p}^- \times \mathbf{p}^-))\Psi_a(\mathbf{r}) = \frac{E^2}{V_F^2}\Psi_a(\mathbf{r}) \quad (22)$$

Where $\mathbf{p}^- = \left(\sqrt{1 - \lambda r^2} \mathbf{p} - \left(\frac{eB}{2} \right) \left(\frac{-y}{\sqrt{1 - \lambda r^2}} \vec{i} + \frac{x}{\sqrt{1 - \lambda r^2}} \vec{j} \right) \right)$.

After a straightforward calculation of eq (22), we obtain:

$$\left[(1 - \lambda r^2) \mathbf{p}^2 + \alpha \frac{r^2}{1 - \lambda r^2} + i\hbar \lambda \mathbf{r} \cdot \mathbf{p} - \gamma L_z - eB\hbar \sigma_z - \frac{E^2}{V_F^2} \right] \Psi_a(\mathbf{r}) = 0 \quad (23)$$

Here the parameters;

$$\alpha = \frac{e^2 B^2}{4} - \frac{eB}{2} \lambda \hbar \sigma_z \quad (24)$$

$$\gamma = eB + \lambda \hbar \sigma_z \quad (25)$$

To solve the eq.(23), we introduce the polar coordinates in position space (r, ϕ) , and we use the following ansatz $\Psi_a(\mathbf{r}) = \exp(i m_l \phi) R_{n,l}(r) \chi_\tau$, where n is the radial quantum number, m_l and $\tau = \pm 1$ are, respectively, the eigenvalues of angular momentum and spin operators, and $\chi_{+1}^T = (1, 0)$, $\chi_{-1}^T = (0, 1)$ are the spin functions; to obtain

$$\left[(1 - \lambda r^2) \left(\frac{d}{dr} \right)^2 - \frac{m_l^2 (1 - \lambda r^2)}{r^2} - \frac{\eta r^2}{\hbar^2 (1 - \lambda r^2)} + \varepsilon \right] R_{n,l}(r) = 0 \quad (26)$$

With

$$\eta = \frac{\hbar^2}{4l_B^4} - \frac{\lambda\hbar^2}{2l_B^2}\tau \quad (27)$$

$$\varepsilon = \frac{E^2}{\hbar^2 v_F^2} + \frac{\tau}{l_B^2} + m_1 \left(\frac{1}{l_B^2} + \lambda\tau \right) \quad (28)$$

Where $l_B = \sqrt{\frac{\hbar}{eB}}$ is the fundamental length scale in the presence of a magnetic field.

We consider the transformations and the proceeding steps to follow by using the Nikiforov-Uvarov (NU) in order to obtain the energy spectrum and the corresponding wave function as in Ref [30].

Until we get the energy spectrum in the form:

$$E_{n,m_1,\tau}^\lambda = \pm \frac{\hbar v_F}{l_B} [(2n + m_1 + 1) \sqrt{(1 - 2\lambda l_B^2 \tau + \lambda^2 l_B^4) + \lambda l_B^2 (4n(n + m_1 + 1) + (2 - \tau)m_1 + 1) - (m_1 + \tau)}]^{1/2} \quad (29)$$

We notice that the energy spectrum of our system has n^2 dependence of the energy levels, which corresponds to a confinement at the high-energy area; our result is equivalent to the energy of a spinless relativistic quantum particle in a square well potential.

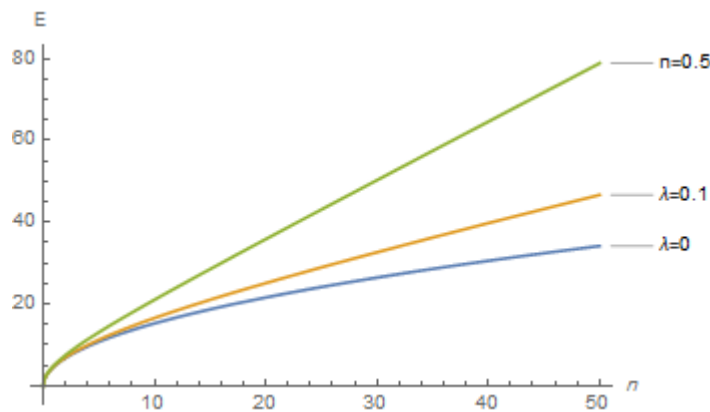


Figure.1: Energy spectrum as a function of n for the different values of the parameter λ

In **Fig. 1**, We represent the energy level as a function of the quantum number n for different values of λ , we have chosen $\lambda = 0, 0.1, 0.5$ and $m_1 = 0$, $s = 1/2$. As a result, we observe that for a fixed value of n, the energy E increases monotonically with increasing parameter EUP. The effect of the EUP parameter on the energy levels can be observed, where $\lambda = 0$ corresponds to the case of normal quantum mechanics.

Now, let us conclude the corresponding wave function after employing and following the steps as NU method to get that form;

$$\Psi_n(r, \phi) = C_n 2^{\frac{m_1}{2}} \exp(i m_1 \phi) (1 - \lambda r^2)^{\mu/2} (\lambda r^2)^{\frac{m_1}{2}} P_n^{(m_1, \mu-1/2)}(1 - 2\lambda r^2) \quad (30)$$

Where C_n is the normalization constant.

We can test this finding in many ways such as; if we put $\lambda = 0$, we obtain the ordinary expression of the spectrum in the usual space [31]

$$\mathbf{E}_{n,0,1}^0 = \pm \frac{\hbar \mathbf{V}_F}{l_B} \sqrt{2n} \quad (31)$$

In order to get the upper limit of the deformation parameter λ and to output it up to the first order, we use the s-states of the energy eigenvalues

$$\mathbf{E}_{n,0,1}^\lambda = \mathbf{E}_{n,0}^{\lambda=0} + \mathbf{E}_{n,0}^{\lambda=0} \left(\frac{l_B^2 (2n+1)}{2\sqrt{2n}} \right) \lambda \quad (32)$$

$$\mathbf{E}_{n,0,1}^\lambda = \pm \frac{\hbar \mathbf{V}_F}{l_B} [2n(1 + \lambda l_B^2 (2n+1))]^{1/2} \quad (33)$$

Where $\mathbf{E}_{n,0}^{\lambda=0}$ defined in eq (31).

The deviation from the usual case caused by the modified commutation relations (1) of the nth energy level is provided by:

$$\Delta \mathbf{E}_{n,0,+1}^\lambda = \mathbf{E}_{n,0}^{\lambda=0} \left(\frac{l_B^2 (2n+1)}{2\sqrt{2n}} \right) \lambda \quad (34)$$

We use the experimental results of the relativistic Landau levels in graphene [32]. In the absence of deformation, the energy for the Landau levels $n = 1$, for a magnetic field of strength $B = 18\text{T}$ is $\mathbf{E}_{n,0} = (172 \pm 3)\text{meV}$. At this point, if we put $n = 1$ in the s-states of the energy eigenvalues (31) and considering that the uncertainty in the energy is $\Delta \mathbf{E}_{n,0,+1}^\lambda < 6\text{meV}$, we get the following constraint:

$$\lambda < 25 \times 10^6 \text{m}^{-2} \quad (35)$$

This leads to the following upper bound of the minimal uncertainty in momentum $\Delta P_{\min} = \hbar \sqrt{\lambda} < 2.64 \times 10^{-27} \text{kg m s}^{-1}$.

Conclusion

In this paper, we investigated the exact solutions of the 2D massless Dirac equation with a uniform external magnetic field in the context of deformed quantum mechanics with anti-deSitter commutation relationships. These AdS deformations lead to a minimal non-zero uncertainty in the measurement of the momentum. The NikiforovUvarov method was used and thus we get the analytical expressions of the bound state energies and the wave functions of the system, in this case, we express the functions analytically in terms of the system in relation on Jacobi's polynomials and the corresponding eigenenergies with additional corrections depending on the deformation parameter λ . Our results show that the deformed spectrum remains discrete even with large values of the principal quantum number and thus the EUP deformation eliminates the degeneracy of the spectrum (no deformations) found in the normal case. We have thus obtained an experimental parameter of the limit deformation. Finally, a satisfactory upper limit for the EUP was determined in order to see the effect of the deformation in physical systems and to compare it with the experimental results of the relativistic Landau levels in graphene.

References

- [1] K.S. Novoselov, et al. Science 306 (2004) 666.
- [2] K.S. Novoselov, et al. Proc. Natl. Acad. Sci. 102 (2005) 10451.
- [3] A.H. Castro Neto, F. Guinea, N.M.R. Peres, K.S. Novoselov, A.K. Geim, Rev. Modern Phys. 81 (2009) 109.

- [4] N. Peres, *Rev. Modern Phys.* 82 (2010) 2673.
- [5] Charles L. Fefferman, Michael I. Weinstein, *J. Amer. Math. Soc.* 25 (2012) 1169.
- [6] M.I. Katsnelson, K.S. Novoselov, A.K. Geim, *Nat. Phys.* 2 (2006) 620.
- [7] M.I. Katsnelson, *Mater. Today* 10 (2007) 20.
- [8] S. Mignemi. *Mod.Phys. Lett. A* 25, 1697 (2010) 17
- [9] G. Amelino-Camelia. *Phys. Lett. B* 510,255 (2001)
- [10] G. Amelino-Camelia. *Int. J. Mod. Phys. D* 11, 35 (2002)
- [11] S. Capozziello, G. Lambiase, G. Scarpetta. *Int. J. Theor. Phys.* 39, 15 (2000)
- [12] M.R. Douglas and N.A. Nekrasov. *Rev. Mod. Phys.* 73, 977 (2001)
- [13] F. Scardigli. *Phys. Lett. B* 452, 39 (1999)
- [14] F. Scardigli and R. Casadio. *Class. Quant. Grav.* 20, 3915 (2003)
- [15] V.E. Kuzmichev and V.V. Kuzmichev. *Eur. Phys. J. C* 80, 248 (2020)
- [16] J. Gin' e and G. G. Luciano. *Eur. Phys. J. C* 80, 1039 (2020)
- [17] B. Hamil and M. Merad. *Eur. Phys. J. Plus* 133, 174 (2018)
- [18] W.S. Chung, H. Hassanabadi and N. Farahani. *Mod. Phys. Lett. A* 34, 1950204 (2019)
- [19] M. Hadj Moussa and M. Merad. *Few-Body Syst.* 59, 44 (2018)
- [20] B. Hamil, M. Merad and T. Birkandan. *Eur. Phys. J. Plus* 134, 278 (2019)
- [21] S. Ghosh and S. Mignemi. *Int. J. Theor. Phys.* 50,1803 (2011)
- [22] M. Falek, N. Belghar and M. Moumni. *Eur. Phys. J. Plus.* 135, 335 (2020)
- [23] S. Mignemi. *Class.Quant. Grav.* 29, 215019 (2012)
- [24] M.M. Stetsko. *J. Math. Phys.* 56, 012101(2015)
- [25] B. Bolen, M. Cavagli`a. *Gen. Relativ. Gravit.* 37, 1255–1262 (2005)
- [26] H. Egrifes, D. Demirhan, F. Buyukkili,c. *Phys. Scripta* 59, 195–198 (1999)
- [27] A.F. Nikiforov, V.B. Uvarov, *Special Functions of Mathematical Physics* (Birkhauser, Basel, 1988).
- [28] A.D. Guclu, P. Potasz, M. Korkusinski, P. Hawrylak, *Graphene Quantum Dots* (Springer, Berlin, 2014)
- [29] Hamil, B., & Merad, M. *Few-Body Systems*, 60(2), 36. (2019)
- [30] Sek, Lakhdar, Mokhtar Falek, and Mustafa Moumni. *Int. J. Mod.Phys.A.*2150113 (2021)
- [31]V. Santos, R.V. Maluf, C.A.S. Almeida, *Ann. Phys.* 349, 402 (2014)
- [32] Z. Jiang et al. *Phys. Rev. Lett.* 98, 197403 (2007)

Spin-polarized DFT Calculation of the Magneto-electronic Properties Under Pressure of the YCrSb Half-heusler Alloy

Ilhem BENAISTI¹, Nacir GUECHI², and Mourad DEHBAOUI^{3*}

¹Laboratory of Energy and Smart Systems, Faculty of Science and Technology, University of Khemis Miliana, Algeria

²Laboratoire d'Etudes des Surfaces et Interfaces des Matériaux Solides, University Ferhat Abbas Setif 1, Algeria

³Laboratoire de Physique des Techniques Expérimentales et ses Applications, Université de Médéa, Algeria

*Corresponding author

Introduction

Half Heusler materials XYZ are typically consisting of transition metals (X,Y) and an sp-element (Z). These materials are important in spintronics¹. Half heuslers crystallize in a cubic structure with the space group no.216.

Experimental/Theoretical Study

The spin-polarized electronic structure calculations are performed using the ultrasoft PP-PW method as applied in the CASTEP code³. The exchange-correlation potential is described using the generalized gradient approximation GGA-PBEsol⁴. The considered valence states are: Y: 4d¹5s², Cr: 3d⁵4s¹, Sb: 5s²5p³. A plane-wave basis set cut-off of 380 eV and a 10×10×10 *k*-points⁵ grid for the integration over the Brillouin zone (BZ) are selected to guarantee sufficiently accurate total energy calculations.

Results and Discussion

A geometry optimization is performed by computing the total energy of the unit cell at each fixed pressure for the type I structure with spin polarized configuration. The calculated total energies versus unit-cell volumes have been fitted to the Birch-Murnaghan equation of states⁶ as displayed in Fig.1.(a). The calculated equilibrium lattice parameter (a_0) and bulk modulus (B) at zero pressure are 6.3 Å and 72 GPa, respectively. These findings agree very well with those reported in Ref. [2].

As shown in Fig.1.(b) at 0 GPa, the spin-down bands (in red color) have a metallic behaviour with a nonzero density of states at the Fermi level, while, the spin-up bands (in black color) shows a semiconducting nature with an indirect gap Γ -X of 0.93 eV. As a result, YCrSb can be considered as a perfect half-metallic alloy. The variations of valence band maximum VBM and conduction band minimum CBM as functions of pressure for the spin-up states is shown in Fig.1.(c). One can see that the variation of pressure from -9 GPa to 25 GPa do not affect the spin-down bands. Therefore, YCrSb behaves like a metal along this spin channel. Furthermore, from Fig.1. (c), one can also see that VBM is slightly decreases and both CBM and the band gap increase with the increasing of pressure, so we deduce for pressure values less than -3 GPa, YCrSb has a metallic nature, and for pressures range from -3 to 25 GPa, YCrSb has a half metallic nature. The calculated total magnetic moment (M_t) of YCrSb is equal to $4\mu_B$ which agree very well with the " $M_t=18-Z_t$ " Slater Pauling rule [1]. For YCrSb, the spin-up bands contain 9 electrons and the total number of valence electrons per unit cell (Z_t) is equal to 14. From Fig.1.(d) it is worth to note that the variation of pressure does not affect the total magnetic moment of YCrSb.



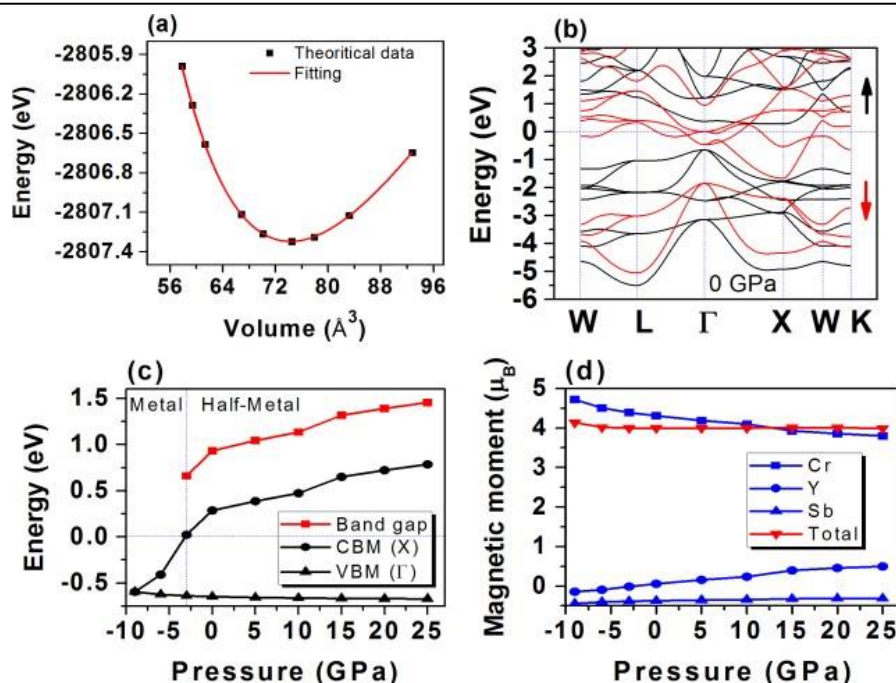


Fig.1. (a) Total energy versus volume per unit cell, (b) spin-polarized band structure at 0 GPa, (c) pressure effect on the spin-up band gap, and (d) pressure effect on the magnetic moments of YCrSb.

Conclusion

In summary, the magneto-electronic properties of the YCrSb Half-Heusler under pressure effect were investigated by using the PP-PW method with the GGA- PBEsol approximation. The calculated band structures indicate that the YCrSb material is a perfect ferromagnetic half metal for a wide range of pressure with a total magnetic moment of $4 \mu_B$. This value is in good agreement with the “ $M_t=18-Z_t$ ” Slater-Pauling rule.

References

1. Graf T, Felser C, & Parkin S S. « Simple rules for the understanding of Heusler compounds » *Prog. Solid State Chem.*, 2011;39(1): 1-50.
2. Sattar M A, Rashid M, Hashmi M, Ahmad S A, Imran M, & Hussain F. « Theoretical investigations of half-metallic ferromagnetism in new Half-Heusler YCrSb and YMnSb alloys using first-principle calculations » *Chin. Phys. B*, 2016;25(10), 107402.
3. Payne M C, Teter M P, Allan D C, Arias T A, & Joannopoulos A J. « Iterative minimization techniques for ab initio total-energy calculations: molecular dynamics and conjugate gradients » *Rev. Mod. Phys.*, 1992;64(4), 1045.
4. Perdew J P, Burke K, & Ernzerhof M. Generalized gradient approximation made simple, *Phys. Rev. Lett.*, 77(18), 3865.
5. Monkhorst H J, & Pack J D (1976), « Special points for Brillouin-zone integrations » *Phys. Rev. B*, 1996;13(12), 5188.
6. Birch F. « The effect of pressure upon the elastic parameters of isotropic solids, according to Murnaghan's theory of finite strain » *J. Appl. Phys.*, 1938;9(4), 279-288.

Mechanical Characteristics of Polyester Filled with Palm Fibers and Ash Particles

Zahi Souilah

Centre for Development of Advanced Technologies (CDTA), City 20 August 56, Baba Hassen, Algiers, Algeria

ABSTRACT

This study investigated the mechanical properties of polyester matrix reinforced with surface-modified fibers derived from oil palms and surface-modified fly ash particles obtained from a coal-fired powerplant. Two different composite materials were made: the first composite was made with only an increased percentage of fibers, and the second composite contained both a constant amount of fly ash and the different fiber content. The investigation of the mechanical properties included hardness, tensile strength, impact strength and corresponding fractographic analysis of the composites. It has been shown that the composites containing fly ash are superior in hardness and tensile strength, but lower in toughness. Factorography and image processing further demonstrated and explained the behavior of palm oil fibers and fly ash particles within the polyester matrix.



Superstatistical Properties of Ionization Rates of Li⁺

SAMIA DILMI^{1*}, Fadhila KHALFAOUI²

¹University of El Oued, Fa. Exact Sciences, Lab in Operator Theory and PDE, 39000, W. El-Oued, Algeria,

²University of El Oued, Fa. Exact Sciences, Lab in Operator Theory and PDE, 39000, W. El-Oued, Algeria

*Corresponding Author

ABSTRACT

Electron-impact ionization (EII) can also have a significant effect on the charge state distribution for plasmas with a non-thermal electron energy distribution. We demonstrate the connection between the Maxwellian distributions and the Beck-Cohen superstatistics and the influence of superstatistics on nonthermal and suprathemic distributions on the calculation of ionization rates for Li⁺.

INTRODUCTION

The electron impact ionization (EII) is a cause of generated collisional plasma. In the ionization state can be limited by ionization rates [1]. Where we depend on the Maxwellian distributions and the Beck-Cohen Superstatistics, Then we study the influence of superstatistics on nonthermal and suprathemic distributions by calculation of ionization rates for Li⁺.

THEORETICAL ASPECT

Cohen and Beck introduced superstatistics [2] (in 2003), which are shown in nonequilibrium and stable states. Where they are described by effective Boltzmann factor $B(E)$ as:

$$B(E) = \int_0^{\infty} f(\beta) e^{-\beta E} d\beta$$

where: $f(E)$ is probability distribution, E is an energy.

Then it becomes into general form as [3]:

$$B(E) = e^{-\beta_0 E} \left(1 + \frac{1}{2} (q-1) \beta_0^2 E^2 + g(q) \beta_0^3 E^3 \dots \right)$$

where the factor $g(q)$ refers to:

$$g(q) = \begin{cases} =0 & \text{(Uniform and 2-level)} \\ =-\frac{1}{3} (q-1)^2 & \text{(Gamma)} \\ =-\frac{1}{3} (q^3 - 3q + 2) & \text{(log-normal)} \\ =-\frac{1}{3} \frac{(q-1)(5q-6)}{3-q} & \text{(F-distribution)} \end{cases}$$

In the case of direct ionization, the coefficient of the ionization rates is given by:

$$\tau = \int v \sigma(E) F(E) dE, \quad (cm^3 s^{-1})$$

Where M and $v = \sqrt{\frac{2E}{M}}$ are mass and velocity of electron, $\sigma(E)$ is the cross section and it was calculated by the Flexible Atomic Code (FAC) [4] and $F(E)$ is a Maxwellian distribution function.

In our work, we replace $F(E)$ with effective Boltzmann factor $B(E)$ to using superstatistics.



So, the formula of the coefficient of the ionization rates becomes:

$$\tau = \int v\sigma(E)e^{-\beta_0 E} \left(1 + \frac{1}{2}(q-1)\beta_0^2 E^2 + g(q)\beta_0^3 E^3\right) dE$$

RESULTS AND DISCUSSION

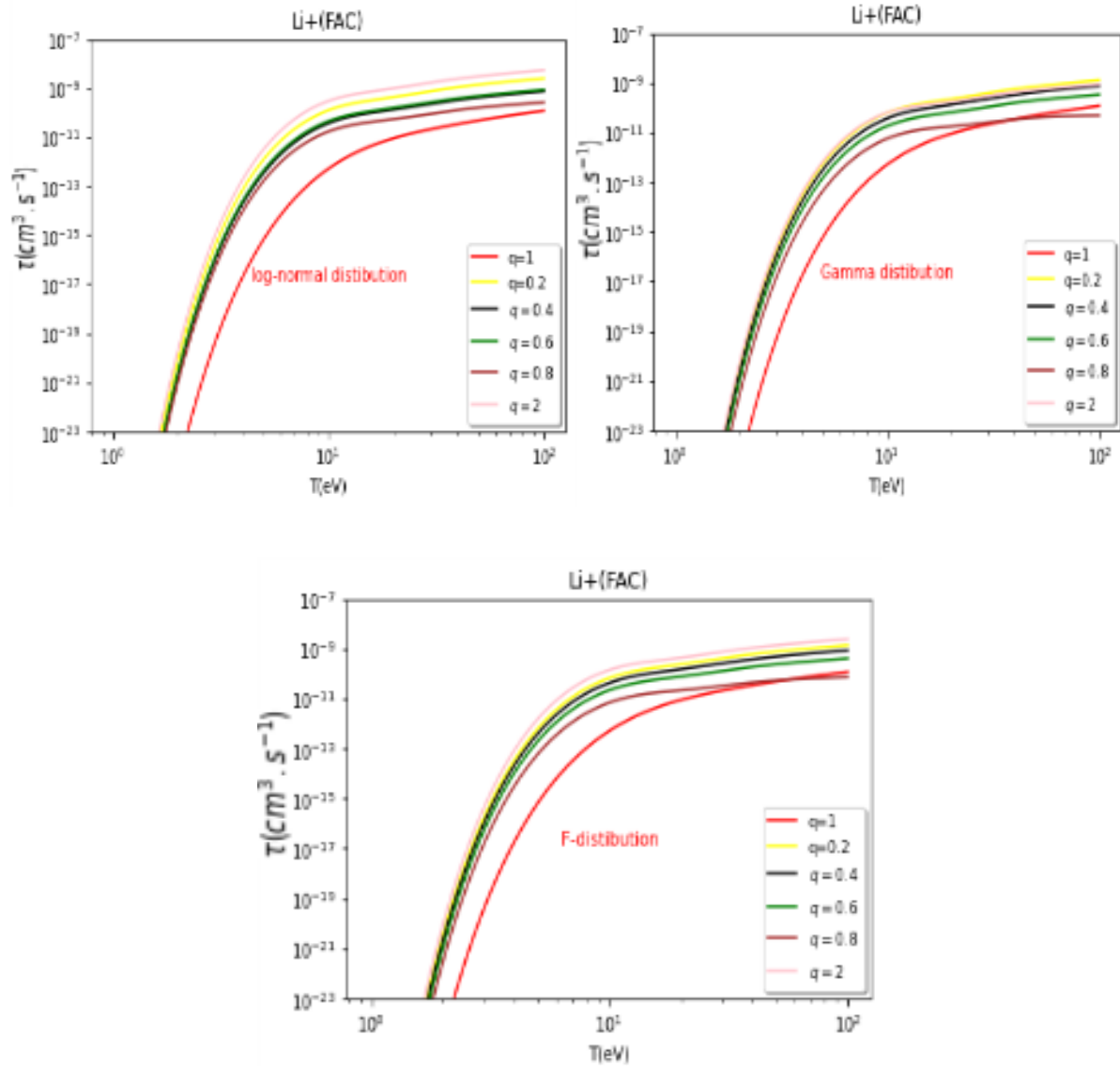


Figure 1: Coefficients of the ionization rates of Li^+ : obtained using different forms of distribution functions and of various values from q .

The ionization rates are obtained using the various $g(q)$ functions of superstatistic. It is noted that the superstatistics approach in the calculation of the rates for Li ions, there is nice coordination between the curves of the three functions especially for the low values of q .

CONCLUSION

We can remark the connection between the Maxwellian distributions and the Beck-Cohen superstatistics where we have shown the relation between the superstatistics approach as well as the low values of q less than 1 on the calculation of ionization rates of Li^+ .

REFERENCES

1. Sergio Davis, Jalaj Jain, Diego Gonz'alez, Gonzalo Guti'errez, Implications Superstatistics for steady-state plasmas, IOP Conf. Series: Journal of Physics: Conf. 1043 , 012011, (2018).
2. C. Beck and E.G.D. Cohen, Physica 322A, 267 (2003).
3. A. Boumali , F. Serdouk, S. Dilmi, J.Phys.A: Statistical Mechanics and its Applications (2020).
4. S. Dilmi, AM. Boumali, Ukr. J. Phys. Vol. 66, No. 8, (2021)

Raman and IR Spectroscopy of SnO₂ Nanostructures with Oxygen Vacancies: An Ab-Initio Calculations

Faiza Bouamra^{1*}, Michel Rérat²

¹Department of physics, LASICOM Laboratory, University of Blida 1, Algeria.

²E2S UPPA, CNRS, IPREM, Université de Pau et des Pays de l'Adour, France

*Corresponding Author

Abstract

Recent trend and opportunity in the field of transparent and conducting oxides (TCO) based on creation of gaz sensors devises boosted the research to study the large band gap semiconductors like SnO₂, TiO₂ and ZnO. In particularity, tin oxide SnO₂ semiconductor is an important material of transparent and conducting oxides (TCO). has been studied intensively experimentally and theoretically by many researchers, because of its sensitivity and transparency. Tin oxide SnO₂, in his anatase phase, is a large band gap semiconductor (E_g=3.6eV), with space group $P4_2/mnm$ [1]. It has been demonstrated that the presence of oxygen vacancy (VO) has an important effect on the electronic, magnetic and spectroscopic properties. In this context, our investigation subscribed. We present an ab-initio study of Raman and IR spectrum of SnO₂ nanostructures with oxygen vacancies.

Method of calculation and models

Using SCF-LCAO-DFT periodic method at the level of B3LYP exchange and correlation pseudopotentials, implemented in the CRYSTAL17 program [2], we performed effective core pseudo-potential calculations. The basis sets used are: DB-41G for O and DB-21G* for Sn. Configurations adopted for different elements are 4d¹⁰ 5s² 5p² for Sn and 2s² 2p⁴ for O. Supercell of 2x2x2 who contain 48 atoms (Sn₁₆O₃₂) is used to create 2(VO) Figure1, with cell parameters: a=b=9.57Å and c=6.38Å.

Results and Discussion

many tests are released to obtain the most energetically stabilized structure of SnO₂ with 2(VO). Obtained structure is represented in figure2. For tetragonal structure of perfect SnO₂ crystal, the irreducible representation of normal vibration modes at the center of the Brillouin zone is given by:

$$\Gamma_{RR} = A_{1g} + A_{2g} + B_{1g} + B_{2g} + E_g + A_{2u} + 2B_{1u} + 3E_u$$

Where Raman active modes are represented by: A_{1g}, B_{1g}, B_{2g} (nodegenerated), and E_u (doubly degenerated), and infrared active modes: A_{2u} and E_u(triply degenerated), A_{2g} and B_{1u} modes are silent.

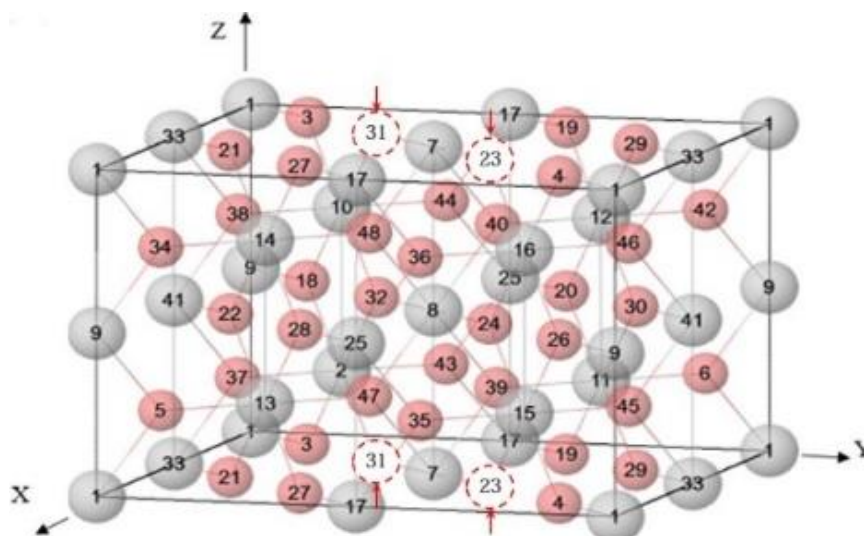
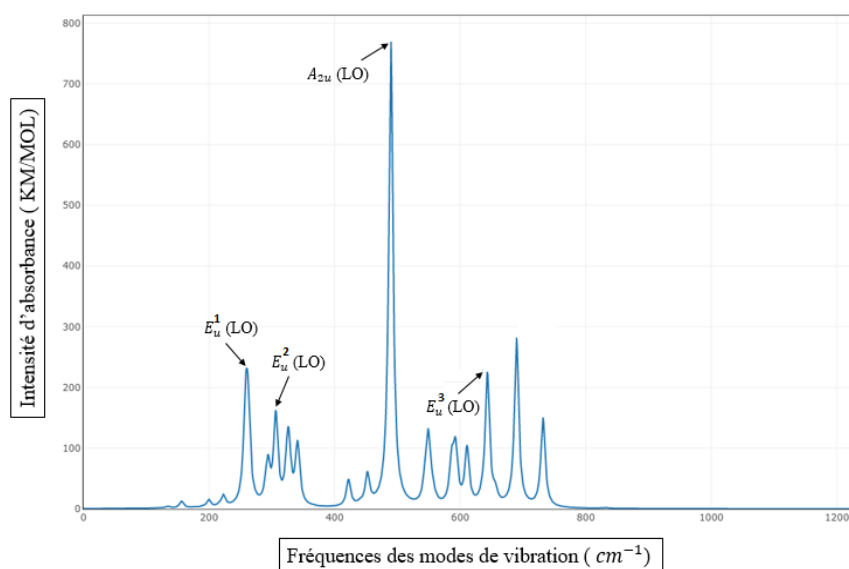
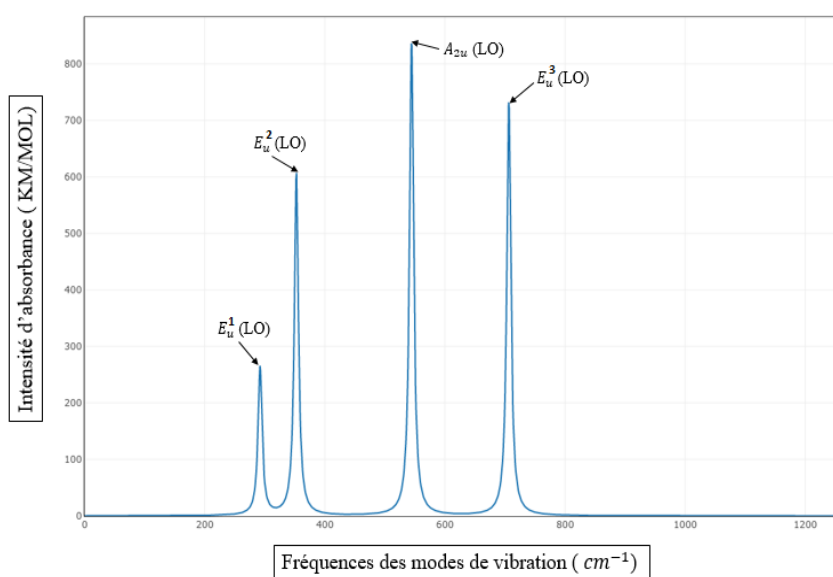
Assignment of (VO)s Raman mode is the aim of this theoretical study.

Raman and IR spectrum of stoichiometric and defected SnO₂ structures are represented in Figure2. Vibration Modes of Sn₁₆O₃₂ cell structure with 2(VO), are represented in table1.

Table1: vibrational mode of Raman and IR for Sn₁₆O₃₂ cell with 2(VO).

Raman vibrationnel mode	B _{1g}	E _g	A _{1g}	B _{2g}
Frequencies (cm ⁻¹)	177	482	707	827
IR vibrationnel mode	E _u ² (LO)	E _u ³ (LO)	A _{2u} (TO)	E _u ¹ (LO)
Frequencies (cm ⁻¹)	294	351	498	706



Figure1: Sn₁₆O₃₂ cell structure with 2(VO).Figure2: IR and Raman spectrum of Sn₁₆O₃₂ cell with 2(VO)

Acknowledgements

The authors gratefully acknowledge Chemical-Physics group of IPREM of Pau University.

References

1. M. Batzill, U. Diebold, "Surface studies of gas sensing metal", *Surf. Sci.*, 79 (2005) 47-154.
2. R. Dovesi et al., "User's Manual of CRYSTAL17", code available from <http://www.crystal.unito.it>

O19

Numerical Simulation of the Influence of an Sb layer on a Cu (In,Ga)Se₂ Solar Cells Performance

Abdelghani Bouabdallah

LMSM, Univerité de Biskra, Biskra, Algeria

ABSTRACT

A comprehensive study of adding an antimony (Sb) layer on top of the Mo layer in a low cost CIGS solar cell is presented. It was found that adding Sb layer improves the solar cell efficiency which was attributed to the reduction of defects at the CdS/CIGS interface. To elucidate this phenomenon, numerical simulation is used to evaluate a CIGS thin film solar cell figures of merits with and without an Sb layer. The cell performance is evaluated by introducing defects at the interface CdS/CIGS. An improvement of the conversion efficiency from 12,08 to 13,6% is reached. The short circuit current density J_{sc} improved from 25,74 to 26,46 mAcm^{-2} , the open circuit voltage V_{OC} is reduced from 0.674 to 0.670 V and the fill factor FF increases from 69.57 to 77.13%. The calculated figures of merit are in good agreement with the measurement.



O20

Mechanical and Anisotropy Properties of SrCdPt Compound under Pressure

Abla GUECHI^{1*}, Mohamed Chegaar²

¹Institute of Optics and Precision Mechanics, Laboratory of Optoelectronics and Components Setif-1 University, 19000, Setif, Algeria

²Laboratory of Optoelectronics and Components, Department of Physics, Faculty of Science, Setif-1 University, 19000, Setif, Algeria

*Corresponding author

ABSTRACT

The first principle calculations are performed to investigate the mechanical and anisotropy properties under the pressure of intermetallic compound SrCdPt by using density functional theory (DFT) through the PBEsol-GGA scheme. Our calculations for the elastic constants support the required stability conditions of the SrCdPt compound over the pressure range of 0 GPa to 100 GPa. The study of the shear modulus, bulk modulus, Cauchy pressure, Poisson's ratio, Pugh's ratio, and the hardness reveals that this compound is hard. Furthermore, the anisotropy properties of SrCdPt were visually illustrated and discussed by analyzing the anisotropy indexes (A1, AU, A3) and directional young's modulus, which suggesting that SrCdPt is a relatively anisotropic material and strongly pressure dependent. Additionally, the SrCdPt compound can be regarded as a candidate of incompressible and hard material. Furthermore, the Debye temperatures are also discussed by investigating the elastic constants and moduli.

1 Crystal Structure

SrCdPt crystallizes in the TiNiSi structure type. The titanium, nickel, and silicon sites are occupied by strontium, cadmium, and platinum, respectively, in the structure of the title compound. Although platinum and nickel are in the same group in the periodic table, the platinum in SrCdPt occupies the silicon site and not the nickel site because platinum is the most electronegative metal in this structure, just like silicon in TiNiSi. The atomic structure of this compound is presented in Fig. 1

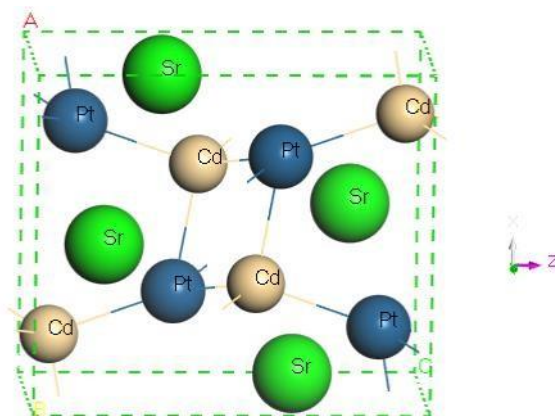


Fig. 1. Atomic structure of the intermetallic compound SrCdPt

Results and Discussion

The elastic constants of solids provide a link between the mechanical, physical, and dynamical behavior of crystals and give important information concerning the nature of the forces operating in solids. Our results of mechanical properties under pressure are summarized in this Table as follow:

SrCdPt compound	0 GPa	100 GPa
Bulk modulus	67.146 GPa	475.844
Compressibility	0.0148	0.0021
Young modulus (GPa)	74.883 59.605 69.934	297.541 573.642 247.697
Shear modulus (GPa)		
Poisson ratio	0.298	0.392
Hardness	4.403	4.90734
Universal anisotropy index	0.359	3.551
Debye temperature (K)	212.040	363.146

References

1. Gulo, F., Samal, S. L. & Corbett, J. D. (2013). *Inorg. Chem.* 52, 10112– 10118.
2. Villars, P. & Cenzual, K. (2011). *Pearson's Crystal Data–Crystal Structure Database for Inorganic Compounds*, Release 2010/11. ASM International, Materials Park, Ohio, USA.
3. F. Guloa, J. Köhler, Crystal structure of the intermetallic compound SrCdPt,, *Crystallographic Communications*, 70, 2014, 590-592.

O21

Effect of Annealing Time on Electrodeposited ZnS Thin Films

Amria Bencherif^{1*}, Ahmed Baari², Essaid Bousbiat³, Abdelyamine Naitbouda⁴ and Assia Bouraiou²

^{1*} Département de Physique, Université de Boumerdes, Algerie, (a.bencherif@univ-boumerdes.dz)

²Laboratoire des Sciences et Informatique des Matériaux, Université de Djelfa, Algérie,

³ LSIC, ENS Kouba, Alger, Algérie

⁴Centre de Développement des Technologies Avancées, Baba Hassen

*Corresponding Author

INTRODUCTION

ZnS is a direct band gap semiconductor with a wide band gap (3.68-3.80 eV)¹. It is generally observed in two phases: cubic or zinc blende and hexagonal or Würtzite. The cubic phase is the most stable at low temperatures and low pressure¹. Due to its physical properties, high chemical stability to processing and photoelectric properties, ZnS is well suited for various applications such as catalysts, gas sensors and photovoltaic applications. Today, ZnS is one of the materials considered as an alternative for buffer layers in solar cells. Compared to CdS, ZnS is a non-toxic and an environment friendly material². In the present work, we will elaborate series of ZnS samples, using electrodeposition method to study the effect of the annealing time on their structural and optical properties.

EXPERIMENTAL STUDY

In this work, we studied the effect of annealing time on the structural and optical properties of zinc sulfide (ZnS) thin films growth by electrodeposition method. The ZnS films were deposited on ITO substrate at 65°C during 45 min from an aqueous solution of (ZnSO₄.7H₂O). We have elaborated two samples; each of the as-deposited films was locked up with 30 mg of sulphur powder into a glass capsule (**Fig.1**), filled with argon-neon gas mixture (75% argon and 25% neon) at a fixed pressure of 10 mbar. In order to investigate the effect of annealing time, the two capsules were annealed in the furnace at 550 °C during 60 and 120 min.

RESULTS AND DISCUSSION

The structural and optical properties of the elaborated films were studied, respectively, using X-ray diffraction (XRD) and Raman spectroscopy methods. After annealing, the XRD diagrams of the films present one phase; ZnS under its hexagonal Würtzite structure (File N°: 01-089-2194)³. The average grain size is estimated using Scherrer's formula; and it is equal to 20.6 and 23.6 nm for the films annealed respectively during 60 and 120 min (**Fig.2 (a) and (b)**).

The Raman spectra of the films present the lines situated at 275, 344, 414, 627, 694, 981, 1042 and 1389 cm⁻¹, (**Fig.2 (c)**) which are the modes observed for ZnS under its hexagonal structure⁴.

We have found that the intensities of the characteristic peaks of the ZnS phase increased as the annealing time increased.





Fig.1: Photography images of (a): the films in the capsule, and (b): sample after annealing under sulfur atmosphere.

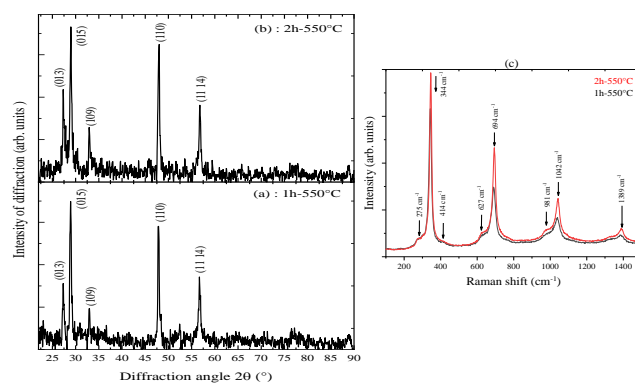


Fig. 2: X-ray diffraction patterns of ZnS films after thermal annealing at 550 °C during (a): 60 and (b): 120 min, (c): Raman spectra of the two films.

CONCLUSION

The XRD investigation indicated that the second film (annealed during 120 min) presents the best crystallinity. Raman spectroscopy shows that all the ZnS films synthesised in this work possess a hexagonal structure. The obtained results suggest that the elaborated ZnS films have suitable properties for used as a buffer layer in solar cells.

ACKNOWLEDGMENTS

The authors thank Dr. Ali Sari for his contribution to this work.

REFERENCES

1. Ali S, Saleem S, Salman M, Khan M. « Synthesis, structural and optical properties of ZnS–ZnO nanocomposites». Mater. Chem. Phys. 2020;248:122900.
2. Hong J, Lim D, Eo YJ, Choi C. « Chemical bath deposited ZnS buffer layer for Cu(In,Ga)Se₂ thin film solar cell». Appl. Surf. Sci. 2018;432:250-254.
3. International Center for Diffraction Data, ICDD, file number 01-089-2194 for ZnS.
4. Fairbrother A, Izquierdo-Roca V, Fontané X, Ibáñez M, Cabot A, Saucedo E, Pérez-Rodríguez A. « ZnS grain size effects on near-resonant Raman scattering: optical non-destructive grain size estimation». R. Soc. Chem. 2014. 2014;16(20):4047–4340.

Effect of Electric and Magnetic Field on the Transport Coefficients of a Non-Equilibrium Gas by the Monte Carlo Method

Benbaier Kouider*, Bedrane Zeyneb and Liani Bachir

Theoretical Physics Laboratory, Physics Dpt., Sciences Faculty, Tlemcen University, Algeria

*Corresponding author

Introduction

This work is devoted to the calculation of the transport parameters of electrons subjected to the action of an electric field and a uniform magnetic field, in a weakly ionized gas to better understand the kinetics of electrons in an electric discharge. We've chosen the Monte Carlo method, which tracks electrons one by one as they travel through the gas from their emissions to their extinction, at any time and at any point of the discharge. In this work we are interested to the study and simulation of electronic transport parameters in oxygen O_2 and carbon dioxide CO_2 under the effect of a uniform electric and / or magnetic field and electron-molecular collisions (solving the Boltzmann equation). The calculation procedure takes into account the random walk of the electrons and the influence of the transport parameters expressed as a function of time, as a function of the reduced electric field E/N (E : applied electric field, N : the density of the gas), and as a function of the magnetic field E/N (B : the magnetic field applies). Monte Carlo simulation consists in simulating the movement of a large number of electrons one by one, thus followed from its emission until its disappearance. During the simulation, the flight position and speed are recorded for each flight time and for each electron. The knowledge of these magnitudes allows using the appropriate static averages and using the sampling methods to calculate the electronic transport parameters in the gas under consideration, taking into consideration the collision processes involved.

Modelisation Procedure

In this work we are interested in the estimation of transport parameters in a weakly ionized gas, under the action of a uniform electric and / or magnetic field, using the Monte Carlo method. We will present the different results obtained by our Fortran program. We will treat in this program all the real electron-molecule collision processes (elastic, inelastic, excitation, ionization and attachment), and fictitious which occur in a discharge plasma (or weakly ionized gas), and we will store the speed, and the energy of each electron at a given time, to calculate the electronic transport parameters (average energy E_{moy} , the drift speed $V_z moy$, the transverse diffusion coefficient ND_T , the longitudinal diffusion coefficient ND_L , the coefficient of ionization N and the attachment coefficient). We will run the program for an electron beam $n_0 = 15000$ (the number of primary electrons), is free with a maximum energy large enough to deal with all the following situations $\epsilon_{max} = 120$ eV, a gas density N_{gaz} at the temperature being equal to $3.293 \times 10^{22} \text{ m}^{-3}$, and a maximum simulation time $t_{max} = 8$ ns (was chosen always greater than the relaxation time), in what follows all the transport parameters are calculated under the same conditions. Transport parameters were calculated for two gases,



oxygen, and carbon dioxide, in the following three cases:

- Under the unique action of an electric field anti-parallel to the axis Oz
- Case of a magnetic field parallel to the electric field, *i.e.* $B \parallel (Oz)$
- Case of a magnetic field perpendicular to the electric field, *i.e.* $B \perp (Oz)$

Results and Discussion

Under the effect of a uniform electric and / or magnetic field, electrons are animated between two collisions, with a uniformly accelerated movement following the direction of the fields. In general, all the transport parameters (average energy, drift speed, transverse diffusion coefficient, longitudinal diffusion coefficient, ionization coefficient, attachment coefficient, etc.) increase with the field (electric and / or magnetic), and the nature of the gas.

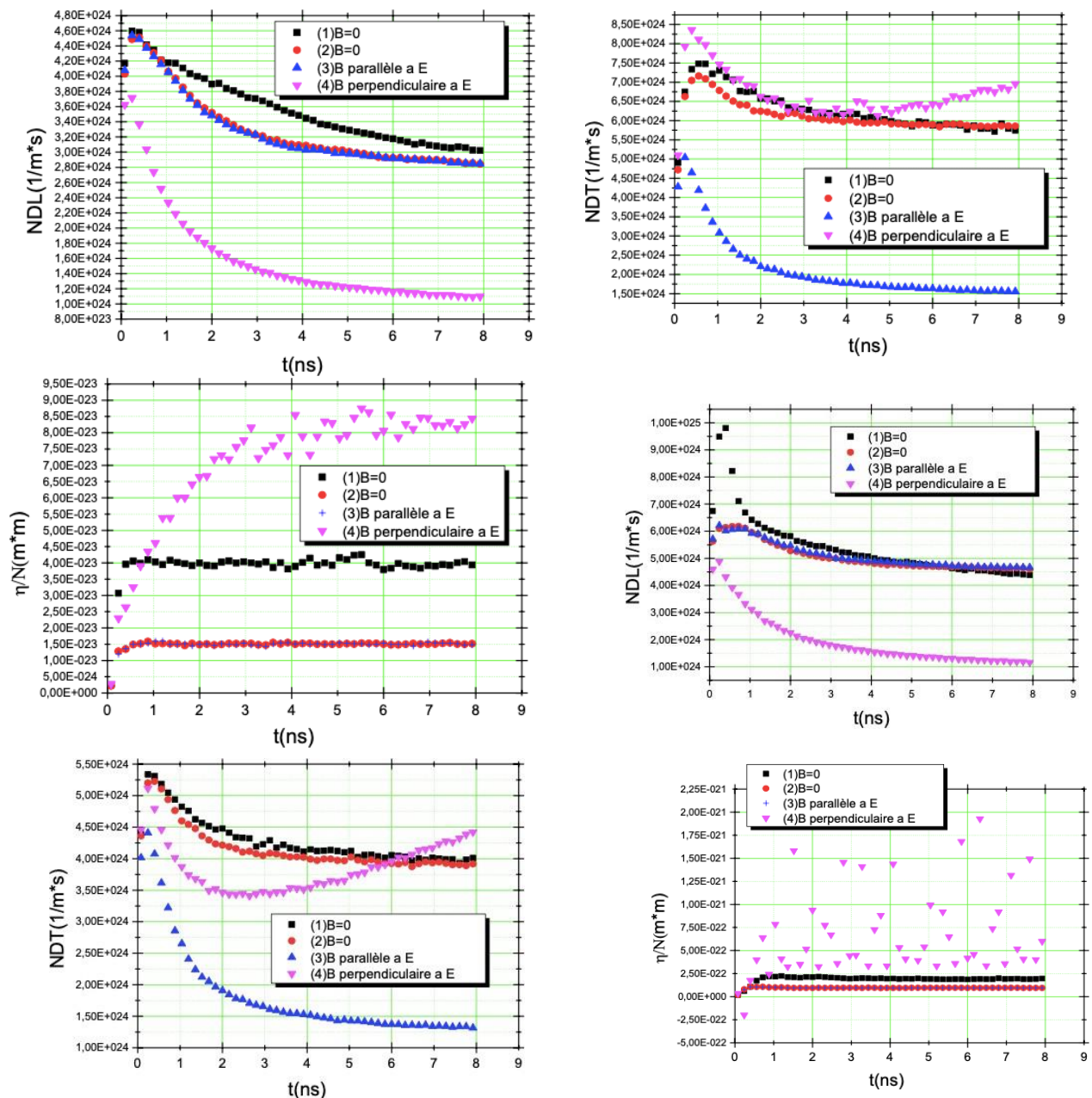


Fig1: longitudinal diffusion coefficient, transverse diffusion coefficient and attachment coefficient Vs time. First row for O_2 and the second row for CO_2

Conclusion

In this work we were interested in determining the various parameters that can displace or modify the state of equilibrium (the evolution time, the electric field and the longitudinal and transverse magnetic field). We can say that the Boltzmann equation can only be solved if and only if the transport parameters are in a state of equilibrium.

References

1. Longo S, "Monte Carlo models of electron and ion transport in non-equilibrium Plasmas", *Plasma Sources Sci. Technol.*, 9(4):468-476, 2000.

Po02

Comparative Simulation of the Perovskite Solar Cell

Nawal Benyahia*, H. Mazari, A. Boumesjed, K. Ameer, N. Benseddik, Z. Benamara

Applied Micro-Electronic Laboratory, electronics' department, DjillaliLiabès University

*Corresponding author

Introduction

Photovoltaic solar cells are the most important device of renewable energy, Silicon based junction solar cells present efficiency lower than 25%. Therefore, researchers switch to new materials to improve the solar cell performance. In recent years perovskite materials have aroused great interest in optoelectronic and microelectronic devices because of their excellent performance, Low production cost and high absorption. Among these materials, the methylammonium tin triiodide $\text{CH}_3\text{NH}_3\text{SnI}_3$, and: the Methylammonium lead halide $\text{CH}_3\text{NH}_3\text{PbI}_3$ which are considered to be ones of the best choices for photovoltaic applications, the efficiency of perovskite solar cell has been significantly enhanced from 5.44 % in 2014 [1] to 23.36 % in 2016 [2,3].

In this work, we simulated the characteristic of perovskite solar cells; we studied the effect of the buffer layer thickness and doping on the photovoltaic parameters such as open circuit voltage, short circuit current, fill factor and efficiency.

Theoretical Study

The simulation was performed using SCAP's 1D simulator.

Results and Discussion

The simulated structure is illustrated in Figure 1, the cell is consisting of TCO (transparent conductive oxide)/ZnO/perovskite on the top of HTM (Hole Transport Material) substrate.

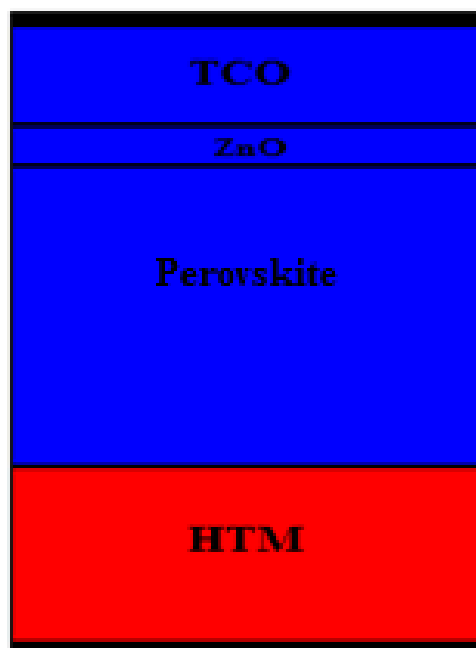


Fig1: Simulated solar cell structure.



Conclusion

In summary, we have investigated simulation of perovskite solar cell, we have studied the effect of thickness and N-concentration of the active layer on the photovoltaic parameters such as open-circuit voltage V_{oc} , short-circuit current J_{sc} , efficiency η and fill factor FF , and we compared the performances of solar cells based on $CH_3NH_3SnI_3$ and that based on $CH_3NH_3PbI_3$.

Acknowledgments

The authors thank Professor Marc Burgelman for his SCAPs software freely available for research.

References

1. F Hao, C- C Stoumpos, R Chang, M G. Kanatzidis, Anomalous Band Gap Behavior in Mixed Sn and Pb Perovskites Enables Broadening of Absorption Spectrum in Solar Cells, Journal of American Chemical Society, April 2, 2014.
2. H-J Du, W-C Wang, J-Z Zhu, Device simulation of lead-free $CH_3NH_3SnI_3$ perovskite solar cells with high efficiency, Chinese Physical Society and IOP Publishing Ltd. 2016, Vol. 25, No. 10 (2016)108802.
3. A Hima, N Lakhdar, B Benhaoua, A Saadoune, I Kemerchou, F Rogti, An optimized perovskite solar cell designs for high conversion efficiency, Superlattices and Microstructures Journal, 129 (2019) 240–246.

Buckling Analysis of Carbon Nanotube-Reinforced Composite Plates Resting on Elastic Foundation

Boumediene Bakhadda*^{1,2*}, Mohamed Bachir Bouiadjra^{1,6}, Fouad Bourada³,
Abdelmoumen Anis Bousahla⁴, Abdelouahed Tounsi^{2,5,7}, and S.R. Mahmoud⁶

^{1*}Laboratoire des Structures et Matériaux Avancés dans le Génie Civil et Travaux Publics, Université de Sidi Bel Abbès, Faculté de Technologie, Département de génie civil, Algeria. presenting author

²Material and Hydrology Laboratory, University of Sidi Bel Abbès, Faculty of Technology, Civil Engineering Department, Algeria

³Département de Génie Civil, Institut des Sciences et de la Technologie, Centre Universitaire de Ain Témouchent, Algérie

⁴Laboratoire de Modélisation et Simulation Multi-échelle, Département de Physique, Faculté des Sciences Exactes, Département de Physique, Université de Sidi Bel Abbés, Algeria

⁵Department of Civil and Environmental Engineering, King Fahd University of Petroleum & Minerals, 31261 Dhahran, Eastern Province, Saudi Arabia

⁶Department of Mathematics, Faculty of Science, King Abdulaziz University, Jeddah, Saudi Arabia

⁷Algerian National Thematic Agency of Research in Science and Technology (ATRST), Algeria

*Corresponding author

ABSTRACT

The buckling behavior of carbon nanotube-reinforced composite (CNTRC) plates resting on the Pasternak elastic foundation is investigated in this study. To strengthen the plates, four types of uniaxially aligned single-walled carbon nanotube (SWCNTs) distributions are investigated. This paper presents analytical answers derived from a mathematical formulation based on hyperbolic shear deformation plate theory. The suggested theory's accuracy is numerically tested by comparing the obtained results to some existing ones in the literature. The current study takes into account a number of important characteristics such as carbon nanotube volume fraction, spring constant factors, plate thickness and aspect ratios, etc. New buckling evaluations of CNTRC plates are provided and analyzed in depth using numerous higher-order shear deformation theories.

Keywords: Buckling analysis; CNTRC plate; Elastic foundation; Plate theory.



Study of n/p solar cell based on ITO/Si Heterojunction

Rima CHERROUN¹, Afak MEFTAH¹

¹Laboratory of semiconducting and metallic materials (LMSM), University Mohamed Khider-Biskra, Biskra Algeria

*Corresponding author

Introduction

Transparent conductive oxides (TCO) are remarkable materials in many fields. The existence of their dual property, electrical conductivity and transparency in the visible, in addition to mechanical durability, including flexibility, makes them ideal candidates for applications in optoelectronics, photovoltaic or even as electro-chromic windows¹. They can become conductive (of type n for example: ZnO, ITO..and type p: NiO, SnO)²The use of TCO in heterojunction C-Si solar cells as transparent electrodes, and as n or p type layers in a solar cell is an economically viable photovoltaic technology³. Among n type TCO are tin doped Indium oxide (ITO is formed from indium oxide (In₂O₃) and a few atomic percentages in tin (Sn), generally 10 %), which is the most used on an industrial large scale since it is non-toxic, good cost and abundance⁴. In this paper presented the study simulation of ITO /Si heterojunction solar cells using the simulation program Silvaco-Atlas that are used as optical window also used as electrodes for a solar cell.

Theoretical Study

The ATLAS device simulator, by Silvaco international, is a computer program, which uses solid-state physics and numerical analysis to simulate the behavior and characteristics of electrical devices⁵. In this chapter, the ATLAS simulator is used to study n/p solar cells based on conductive oxide /Si heterojunction. The studied cell is ITO/Si. Figure.1:

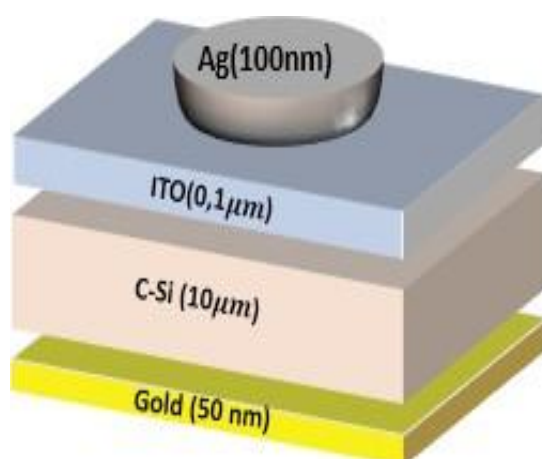


Figure.1: The structure of ITO/Si solar cell.

Results and Discussion

We notice that this study is carried out in the ideal case by omitting defects in the ITO (n-type)/Si (p-type) solar cell. The first structure named structure 1 is presented, in which the cathode material is the silver. We have tried to improve structure 1 to structure 2 in which a SiO₂ anti-reflecting (AR) layer is added on the top of the cell and the silver cathode is replaced by three transparent conductor ITO



cathode .by comparing the two structures indeed there is improvement in J_{sc} unlike V_{oc} and FF that increase a little. Structure 2 exhibits a conversion efficiency of 3.14% better than 0.85% of structure 1. These values are in the experimental range (early measurement without any optimized conditions). In second section, we study the thickness effect of the C-Si p-layer. The layer thickness is varied from 10 μm to 500 μm using structure 2. Significant increase is noticed in J_{sc} . All the other parameters also increase the significant increase in J_{sc} is related to the absorption with the augmentation of the p-layer thickness but without exceeding the free carrier diffusion length and the efficiency increase from 3.14% to 7.9 %. The p-type C-Si layer thickness is kept at 500 μm and thickness of ITO ranges from 0.1 to 1 μm it is observed that V_{oc} remains constant during the simulation process the efficiency enhances from 7.9% to 9.45%. The little increase remarked in it is because the ITO is characterized by transparency and then absorbs in the UV and generates few carriers. In third section, the doping of the two layer of the cell is augmented and in addition, a back doping in the Si region is inserted. A benefit effect of the doping is observed in FF and V_{oc} . The best efficiency is 17.24 % using a back doping. In section fourth the effect of anode work function is studied the work function anode contact is changed from 5.23 eV to 5.8 eV, taking into account the precedent optimum parameters of thicknesses and doping. It is observed that all outputs improve little a bit with the increase of the anode and the reached efficiency is 18.39%. In final section, we suggest the formation of a buffer layer between the ITO and Si region little amelioration is noticed in all outputs parameters of the solar cell are summarized: $J_{sc}=35.01 \text{ mA.cm}^{-2}$, $V_{oc}=0.665\text{V}$, $FF=0.832$, $\eta =19.39 \%$.

Conclusion

In this paper, we have successfully simulated solar cells based on ITO /Si using Silvaco-Atlas software. Many improvements have been made (thickness, doping, work function of anode, buffer layer). Before optimizations, the conversion efficiency was 0.85% optimization process efficiency reached 19.39%.

References

- 1 G. V. Samsonov, *The oxide handbook*: Springer Science & Business Media, 2013.
- 2 I.Jellal, H. Ahmoum, Y. Khaissa, K. Nouneh, M. Boughrara, M. Fahoume, S. Chopra, J. Naja4, "Experimental and ab- initio investigation of the microstructure and optoelectronic properties of FCM–CVD- prepared Al- doped ZnO thin films", *Applied Physics A* 125:650, 2019.
- 3 M. Ouafa and C. Amar, "Etude et simulation des cellules solaires à hétérojonctions de type ITO/Si," Université Mouloud Mammeri, 2016.
- 4 B. Chavillon, "Synthèse et caractérisation d'oxydes transparents conducteurs de type p pour application en cellules solaires à colorant," 2011.
- 5 A. Labouret and M. Viloz, *Energie solaire photovoltaïque* vol. 4: Dunod, 2006.

Synthesis and Characterization of Layered Double Hydroxide Based on Zn and Cr Used for Anion Exchange

Boudjenane F Z^{1*}, Chouaih. A¹, Bahmani. A², Belakfouf. N¹, Boukabcha N¹, Megrouss. Y¹

¹Laboratory of technology and solid properties, Abdelhamid Ibn Badis University of Mostaganem, 27000 Mostaganem, Algeria

²Laboratory of inorganic materials chemistry and application, university of science and the technology of Oran (USTOM.B), 31000 Oran, Algeria

*Corresponding author

ABSTRACT

Layered double hydroxides (LDHs) have a layered structure with a host layer of octahedrally coupled metalcations and a guest layer (interlayer) of anions, which have recently been actively explored for their anion exchange capabilities. In this study, we used an anion exchange method to synthesize a LDH based on zinc and chrome $ZnCr-CO_3$ ($Zn_{0.6}Cr_{0.4}(OH)_2(CO_3)_{0.2}.nH_2O$) with different anions to deal with the exchange whereas the use of infrared spectroscopy and X-ray diffraction was essential to characterise, confirm the stability into LDH interlayers and the success of the anion exchange.

Keywords: LDH, anion exchange, X-ray diffraction, infrared spectroscopy.

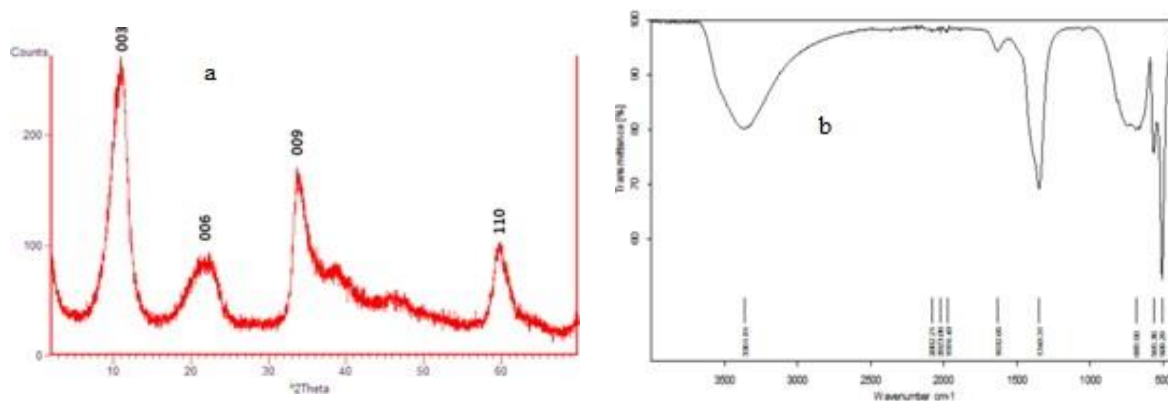


Fig a,b. Characterization by X-ray diffraction and infrared spectroscopy for the $Zn_{0.6}Cr_{0.4}(OH)_2(CO_3)_{0.2}.nH_2O$

References

1. D.L. Bish, " Anion exchange in the pyroaurite group mineral takovite. Applications to other hydroxide minerals ", Bull. Minéral., 103 (1980) 170- 175.
2. A. De Roy, C. Forano, K. El Malki, J.P. Besse, " Anionic clays: Trends in Pillaring chemistry. In Synthesis of microporous materials ", (M.L.Occelli, H.E. Robson. Eds). Van Nostrand Reinhold, New-York, (1992) 108-169.
3. J. Wang, A.G. Kalinichev, R.J. Kirkpatrick, X. Hou, " Molecular modeling of the structure and energetics of hydrotalcite hydration ", Chemistry Materials, 13 (2001) 145-150.



Theoretical Study of the Structural Electronic Properties of half-Heusler RbInSn Alloy

Kara Ilham^{1*}, Mostefa Zahira² and Mahi fattima²

¹ Department of Physics, University of Oran1 Ahmed Ben Bella, theoretical and simulation laboratory of materials

² Department of Physics, University Abd Hamid ben badis, Mostaganem, Laboratoire de Structure, Elaboration et Application des Matériaux

*Corresponding author

Introduction

The aim of the searchers is to find multifunctional materials which combine many physical properties in order to assure a various technological functionality. All these characteristics can be found in half-Heusler with topological behavior [1]. We frequently concentrate on investigating the properties of previously reported compound RbInSn [2].

Experimental/Theoretical Study

Here we present ab initio study of RbInSn half Heusler alloy with 8-valence electrons in the quest to discover its thermoelectric skills. We use the full-potential linearised augmented plane-wave (LAPW) method, implemented in the WIEN2K code and the GGA exchange correlation functional including the spin orbit coupling (SOC) effect to predict its structural and electronic properties.

Results and Discussion

Our results show that this compound exhibit a topological behaviour signed by the inversion between the states s and p. The stability of our compound is confirmed by computing phonon dispersion and mechanical calculations. After having performing the elastic constants (Cij) we theoretically calculate the lattice thermal conductivity Kl its absolute value decreases rapidly with increasing temperature and reached 0.14 W/m°K at 1200 °K.

Conclusion

Our finding can be useful for tuning thermoelectric devices.

Acknowledgments

Authors can acknowledge any person, or funding agency that has made a significant contribution to the work.

References

1. Feng. W, Xiao. D, Zhang. D and Yao. Y, "Half-Heusler topological insulator: A first-principles study with the Tran-Blaha modified Becke- Johnson density functional," *Physical Review* 2010 B 82, 235121.
2. Zhang. X.M, Xu. X.G, Du. Y, Liu. E. K, Liu. Z. Y and Wang. W. H, "A new class of topological insulators from I-II-IV half-Heusler compounds with strong band inversion strength," *Journal of Applied Physics*, 2014 .115, 083704.
3. Feng. W, Xiao. D, Zhang. D and Yao. Y, "Half-Heusler topological insulator: A first-principles study with the Tran-Blaha modified Becke- Johnson density functional," *Physical Review* 2010 B 82, 235121.



Po08

Study of Microstructural and Electrical Properties of the (P)A-Si : H/(N)C-Si Heterojunction: Uncooled Microbolometer Application

Khadidja KETROUSS^{1*}, Rabah CHERFI¹ HadjYahia SEBA^{1,2}, Sonia TATA¹, Lamia CHABANE¹, Abba RAHAL¹.

¹Departement de physique, Université des Sciences et de la Technologie Houari Boumediene Algérie.

²Departement de technologie des systèmes énergétiques et environnement, Université Ourgla, Algérie.

*Corresponding author

Introduction

Recently, outstanding achievements have been made in the development of a novel class of uncooled microbolometer infrared (IR) focal plane arrays (FPAs), the ones based on Si diodes as temperature sensors [1-2]. The previous achievements in this field [1-4], stimulates the search for simple complementary metal-oxide semiconductor (CMOS) compatible technological solutions based on diode bolometers which would be suitable for mass production of IR FPAs with adequate performance for many civilian applications [4]. Indeed, to achieve high temperature resolution, the thermodiode must have a high temperature sensitivity and a linear dependence of the output over a wide temperature range. In this work, lightly hydrogenated a-Si:H(B) based heterojunction diodes are proposed as uncooled microbolometer IR FPA elements [5]. Our approach followed our previous study, in which we made a case that lightly hydrogenated a-Si:H(B) films prepared by DC magnetron sputtering promise high manufacturability, including the ease of incorporating its formation process into the CMOS production cycle, in combination with low process cost. We study the interfacial electrical and bolometric properties of the (p)a-Si:H/(n)c-Si heterojunction for different boron concentrations in the a-Si:H layer.

Experimental Study

In this work, p-type a-Si:H was deposited by DC magnetron sputtering technique for different doping concentrations. Double side polished n-type float zone c-Si (100) wafers were used as substrates. The boron concentration on the a-Si:H(B) was estimated by energy dispersive X-ray (EDS). Ellipsometric measurements were carried out (p)a-Si:H/(n)c-Si structure using spectroscopic ellipsometer (Sopra, GES5). (I-V-T) measurements were performed at a temperature range between 290 K and 370 K. In our measurement, which is based on the variation of current with temperature at a fixed voltage, the sensitivity of the heterojunction diode is expressed by the temperature coefficient of the detector current: $TCS = d[\ln S(T)]/dT$, where $S = I$

Results and Discussion

Tauc-Lorentz (T-L) optical model is used to estimate the thickness, bandgap, structural properties of the films, whereas Bruggeman effective medium approximation (BEMA) is applied to find the thickness of the top rough layer. The thickness of the a-Si:H layers remains almost constant around a value of 700 nm, with the addition of boron. The band gap decreases with WB from 1.34 eV to 1.1 eV. The observations suggest an increase in structural disorder in the a-Si:H(B) layer deposited at higher boron concentrations. Varying the doping concentration of the (p) a-Si:H layer from 1.5% to 43% largely influences the properties of the (p)a-Si:H/(n)c-Si heterojunction. The samples prepared at the average boron



concentration show the best rectification factor of about three orders at 0.75 V, the smallest series resistance and the lowest ideality factor. On the other hand, the sample prepared at the highest doping concentration shows poor rectification quality and high ideality factor of about 5, which is related to the increase of structural disorder in the interface. I-V-T measurements show excellent linearity, with R^2 often greater than 0.9998, and a sensitivity always greater than $0.06\text{ }^{\circ}\text{C}^{-1}$. Indeed, the sensitivity obtained for this heterojunction is better than that reported in recent work on thermodiodes for bolometry applications [1-3].

Conclusion

The results obtained in this study indicate that (p)a-Si:H/(n)c-Si is a potential material for thermodiodes in uncooled microbolometers. Future efforts should be directed towards the fabrication of a-Si:H/(n)c-Si thermodiode in complete detector configurations.

Acknowledgments

The authors gratefully acknowledge the financial support from General Direction of Scientific Research and Technological, Development, Algeria (DGRSDT/MESRS).

References

1. Chizh, K. V., Chapnin, V. A., Kalinushkin, V. P., Resnik, V. Y., Storozhevykh, M. S., and Yuryev, V. A., "Metal silicide/poly-Si Schottky diodes for uncooled microbolometers," *Nanoscale Res. Let.* 8, 177 (2013).
2. T. Yamada, N. Inomata, T. Ono, Sensitive thermal microsensor with pn junction for heat measurement of a single cell, *Jpn. J. Appl. Phys.* 55 (2016).
3. V.A. Yuryev, K. V. Chizh, V. V. Chapnin, V.P. Kalinushkin, Metal silicide/Si thin-film Schottky-diode bolometers, *Nanotechnol.* VII. 9519 (2015)
4. M. Mansoor, I. Haneef, S. Akhtar, A. De Luca, F. Udrea, Silicon diode temperature sensors - A review of applications, *Sensors Actuators, A Phys.* 232 (2015) 63–74.
5. K. Ketrroussi, R. Cherfi, H. Yahia Seba, S. Tata, L. Chabane, L. Ozyuzer, A. Rahal, Study of boron doped amorphous silicon lightly hydrogenated prepared by DC magnetron sputtering for infrared detectors applications, *Infrared Phys. Technol.*

Po09

DCF Method for Dispersion Compensation in Optical Fiber Link for LongHaul Communication

KHERIS (Saliha)^{1*}, BOUABDALLAH(Badra)²

¹Department of Electronics / Faculty of Electrical Engineering, University of Djillali Liabès, Sidi Bel Abbès, Algeria

² Department of Materials and Sustainable development/ Faculty of Exact Sciences. University of Djillali Liabès, Sidi Bel Abbès Sidi Bel Abbès , Algeria

*Corresponding author

ABSTRACT

To improve the overall performance of the high speed transmission system, and reduce losses as much as possible, several dispersion compensation techniques are used. In this article, we proposed a model of the compensation schemes which performed according to the position of the DCF. In pre-compensation, the DCF is placed before the SMF. In post-compensation, the DCF is placed after the SMF. In symmetrical (pre-post), that is to say that the DCF is placed before and after SMF, with bit rates 10 Gbit /s having SMF of length 100km and DCF of length 21.25 km. The performances have been compared on the basis of parameters such as Q factor and bit error rate (BER). All the simulation work is done with the help of Optisystem Software version 7.0. It is concluded from the results that the symmetrical compensation technique shows performs better than pre and post compensation technique in the system for long haul.

Table.1. Comparison of three different techniques at different frequency at 193.1 THz, 193.3THz and 193.5 THz

f= 193,1THz			
	Pré	Post	Symmetrical
Q-Factor	16.7698	25.729	53.7365
BER	1.2365e ⁻¹¹⁴	2.916675e ⁻¹¹⁹	3.2569e ⁻²¹¹

f= 193,3 THz			
	Pré	Post	Symmetrical
Q-Factor	14.2010	23.4222	48.6325
BER	1.2365e-90	8.3886e ⁻¹¹¹	2.2362 e ⁻¹²⁵

f= 193,5 THz			
	Pré	Post	Symmetrical
Q-Factor	13.9568	22.3698	45.7218
BER	6.227 e-70	1.97269 e ⁻⁸⁹	1.6034e ⁻¹¹³

Keywords: Dispersion Compensation DCF, BER, Q factor, Pre, Post, and Symétrique Compensation..



Po10

First-Principles Predictions of the Electronic, Optical and Thermoelectric Properties of the New Zintl-Phase Sr_2CdAs_2

A. Khireddine, B. Tahir, A. Bouhemadou*

Laboratory for Developing New Materials and Their Characterizations, Department of Physics, Faculty of Science, University Ferhat Abbas Setif 1, Setif, 19000, Algeria

*Corresponding author

ABSTRACT

In this paper, we report results of a detailed first-principles study of physical parameters related to electronic and thermoelectric properties of the ternary distronium cadmium diarsenide Sr_2CdAs_2 . This compound crystallizes in the orthorhombic space group, $Cmc2_1$ (No. 36, $Z=4$). The equilibrium structural parameters are determined by CASTEP code, while the electronic structure and related properties are investigated using Wien2k package. The energy band structure $E_g = 1.44$ eV with a direct bandgap. The thermoelectric parameters are investigated using the semi-classical Boltzmann transport theory.

Introduction

Zintl phases compounds have a wide variety of interesting physical properties, such as photovoltaics and thermoelectricity, where the thermoelectric materials can be generating the electricity from the thermal energy (Heat) with high efficiency. In this paper, we report results of a detailed first-principles study of physical parameters related to electronic and thermoelectric properties of the ternary distronium cadmium diarsenide Sr_2CdAs_2 . This compound crystallizes in the orthorhombic space group, $Cmc2_1$ (No. 36, $Z=4$) 1.

Theoretical Study

The determined equilibrium structural parameters through the pseudopotential plane wave method within the density functional theory framework with the GGA-PBEsol functional are in excellent agreement with the available experimental counterparts, providing proof of the reliability of the reported results. The electronic structure and related properties are investigated using the full-potential linearized augmented plane wave plus local orbitals with the TB-mBJ potential. The microscopic origins of the electronic states involved in the direct interband optical transitions are identified. Dependencies of temperature and charge carrier concentrations of the thermoelectric parameters are investigated using the semi-classical Boltzmann transport theory.



Results and Discussion Electronic Properties

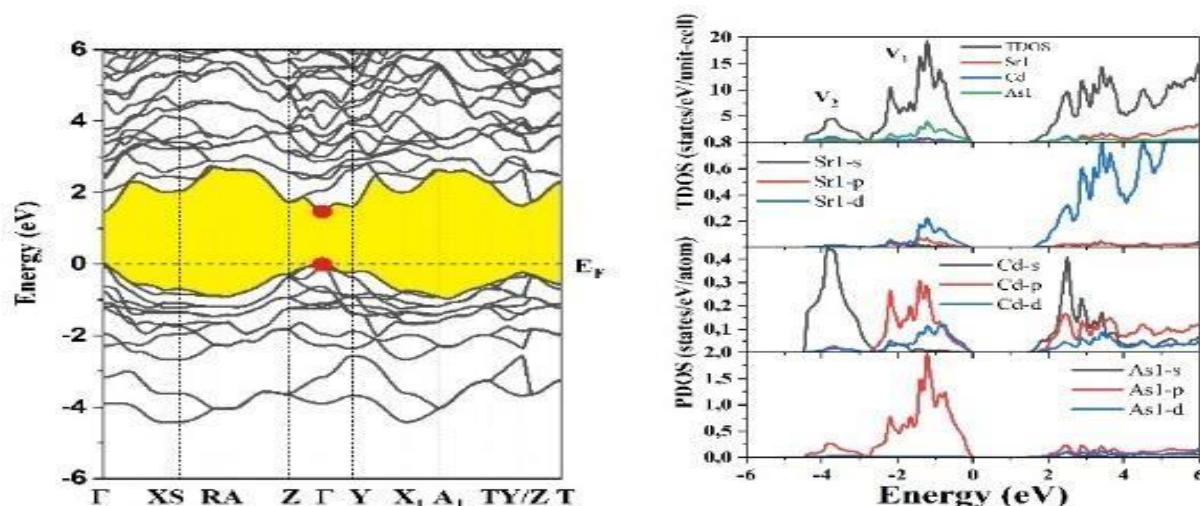


Fig. 1. Band structures calculated (left), the total density of states (TDOS) and its projections on orbitals and sites (PDOS) of Sr₂CdAs₂ (right) using the TB-mBJ potential. The Fermi level is set to zero.

Calculated energy band dispersions of Sr₂CdAs₂ along a selected high symmetry path that connects points of high symmetry in the BZ is depicted in Fig. 1. Both VBM and CBM occur at the BZ center; Γ -point, indicating that investigated compound is direct bandgap material $E_g = 1.44$ eV. The GGA-PBEsol bandgap was the unique reported theoretical result for Sr₂CdAs₂ compound; $E_g = 0.6$ eV, calculated using PAW pseudopotentials 2 (See supporting information).

Optical Properties

Frequency-dependent optical parameters are determined in an energy range 0-6 eV for incident electromagnetic radiation.

Thermoelectric Properties

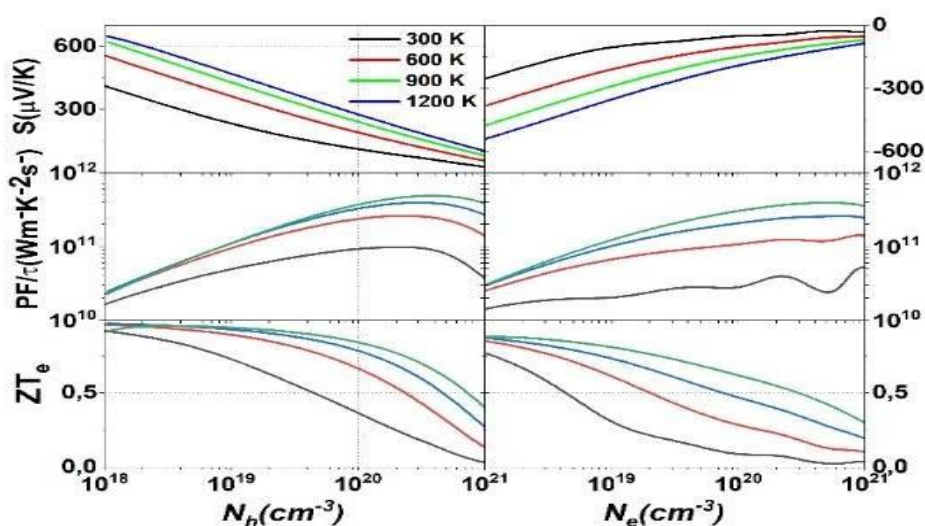


Fig. 2. Transport coefficients of the Seebeck coefficient (S) power factor ($PF = S^2 \sigma$) and figure of merit (ZT) as a function of carrier concentration 10^{18} cm^{-3} and 10^{21} cm^{-3} for the n -type and p -type doped

Sr₂CdAs₂ compound at 300, 600, 900 and 1200 K.

According to Fig. 2, we can note the figure of merit ZT reaches a maximum of ~1 for hole concentration of 10¹⁹ cm⁻³ at 1200k.

Conclusion

In summary, using the FP-LAPW method, it is found that Sr₂CdAs₂ compound is semiconductor with direct band gap at the Γ -point, positioned in the visible sunlight spectrum. Calculated thermoelectric properties proves that p-type title compound is more favorite for thermoelectric performance than the n-type one. Seebeck coefficient of p-type title compound of 650 μ V/K at 1200 K and the carrier concentration equal to 10¹⁸ cm⁻³.

References

1. J. Wang, M. Yang, M. Y. Pan, S. Q. Xia, and X. T. Tao, Synthesis, Crystal and Electronic Structures, and Properties of the New Pnictide Semiconductors A₂CdPn₂ (A = Ca, Sr, Ba, Eu; Pn = P, As), *Inorg. Chem.*, (2011) 50, 8020–8027.
2. A. Balvanz, J. Qu, S. Baranets, E. Ertekin, P. Gorai, and S. Bobev, New n-Type Zintl Phases for Thermoelectrics: Discovery, Structural Characterization, and Band Engineering of the Compounds A₂CdP₂ (A = Sr, Ba, Eu), *Chem. Mater.* (2020) 32, 24 10697–10707.

Po11

Solvent Effect on Hyper-Rayleigh Scattering (HRS) First Hyperpolarizability of Substituted Polyene: Ab Initio Study

N.S.LABIDI

Faculté des Sciences et de la Technologie, Département des Sciences de la Matière, Université de Tamanrasset.11000 Tamanrasset, Algérie

ABSTRACT

The first hyperpolarizabilities β_{HRS} of substituted hexatriene molecules have been carried out to assess the effects of the bridge length, of the frequency dispersion as well as the solvent polarity. These calculations confirm the particular behaviour of the first hyperpolarizability β_{HRS} , depolarization ratio and the anisotropy factor as a function of the incident light frequency and solvent polarity. The impact of the solvent and expanding the π -conjugated limit to improve the β_{HRS} . Finally, the interplay between β_{HRS} and $\beta_{//}$, β_{vec} , $d_{\text{N...N}}$, E_{gap} and the Kirkwood–Onsager factor $[(\epsilon-1)/(2\epsilon + 1)]$ was established.

Keywords: First hyperpolarizability; Hyper-Rayleigh scattering (HRS); push-pull; solvent

INTRODUCTION

This study deals with the solvent effects on the NLO responses in a series of push-pull polyenes [D- π -NO₂] that have been proposed in view of achieving large second-order NLO responses. Here, we present the results, starting with an investigation of the bridge lengths effects, the frequency dispersion for the selected system as well as the effects of the solvent polarity on the first hyperpolarizability (β_{HRS}) responses, energy gap and bond length alternation (BLA). Finally, the relationships between the first hyperpolarizability (β_{HRS}) and $\beta_{//}$, β_{vec} , separation distance ($d_{\text{N...N}}$), energy gap (E_{gap}) and the Kirkwood–Onsager factor $[(\epsilon-1)/(2\epsilon + 1)]$ are established^{1,2}.

COMPUTATIONAL DETAILS

The dynamic $\beta_{\text{HRS}}(-2\omega; \omega, \omega)$ and static $\beta_{\text{HRS}}(0; 0, 0)$ first hyperpolarizabilities were evaluated with the time-dependent Hartree–Fock (TDHF) and the coupled perturbed Hartree–Fock (CPHF) schemes^{3,4}. To take into account the solvent effects the polarizable continuum model within the integral equation formalism (IEF-PCM) was employed at 6-31+G* and 6-311+G* basis sets³. Champagne and co-workers³ developed an effective method to evaluate the hyper-Rayleigh scattering (HRS) response $\beta_{\text{HRS}}(-2\omega; \omega, \omega)$, which is described as:

$$\beta_{\text{HRS}}(-2\omega; \omega, \omega) = \sqrt{(\langle \beta_{\text{ZZZ}}^2 \rangle + \langle \beta_{\text{ZXX}}^2 \rangle)} \dots \dots (1)$$

$\langle \beta_{\text{ZZZ}}^2 \rangle$ and $\langle \beta_{\text{ZXX}}^2 \rangle$ are the orientational averages of the molecular β tensor components. All calculations were performed using the Gaussian 09 program⁵.

RESULTS AND DISCUSSION

To model the effect of the solvent polarity, the static and dynamic β_{vec} , $\beta_{//}$, β_{HRS} and depolarization ratio (DR) of all-trans α, ω -nitro, dimethylamino-hexatriene in a variety of solvents ranging dielectric



constants from $\epsilon = 2.27$ to $\epsilon = 46.83$, are calculated at the TDHF level of approximation with 6-311+G* basis set and presented in Fig. 4a and Fig.4b. The solvent enhances the first hyperpolarizabilities (β_{HRS}) significantly by amplitude depending on the polarity of the solvent and the strength of the substituted groups.

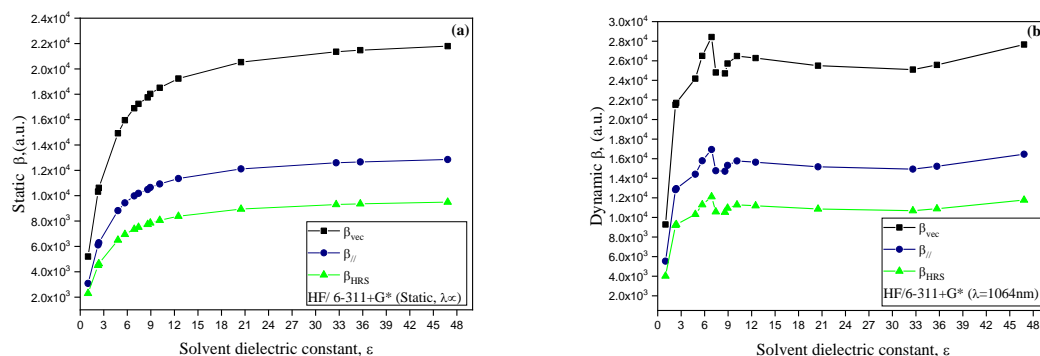


Fig. 1: Solvent polarity effects on calculated static (a) and dynamic (b): β_{vec} , $\beta_{//}$, β_{HRS} for all-trans α,ω -nitro, dimethyl amino-hexatriene at the HF/ 6-311+G* level.

CONCLUSION

Our calculations allow us to identify the main observations: i) The solvent enhances the first hyperpolarizabilities (β_{HRS}) significantly by amplitude depending on the polarity of the solvent and the strength of the substituted groups; ii) The specific behavior of the HRS first hyperpolarizability with its anisotropy factor and depolarization ratio as a function of the incident light frequency. iii) A quantitative relationship was established between the first hyperpolarizability β_{HRS} and the separation distance $d_{\text{N}\dots\text{N}}$, energy gap (E_{gap}) and the Kirkwood–Onsager factor $[(\epsilon - 1)/(2\epsilon + 1)]$.

ACKNOWLEDGEMENTS

I would like to thank Professor Benoit Champagne from Namur University -Belgium for his help (Laboratoire de chimie theorique appliquee. Unité de recherche en chimie physique, théorique et structurale. LCTA-Namur).

REFERENCES

1. Clays K, and André.P. «Handbook of advanced electronic and photonic materials and devices» H.S.Nalwa (Eds.), Hyper-rayleigh scattering: Opportunities for molecular, supramolecular, and device characterization by incoherent second-order nonlinear light scattering. San Diego: Academic Press, 2001; pp. 229-266.
2. Stegeman G.I, Stegeman R.A. «Nonlinear Optics: Phenomena Materials and Devices». New York: Wiley. 2012; pp.15–39.
3. Tomasi J, Mennucci B, Ammi R. «Quantum Mechanical Continuum Solvation Models. Chem Rev. 2005 ; 105 : 2999–3094.
4. Champagne B, Plaquet A, Pozzo J.L, Rodriguez V, Castet F. «Nonlinear Optical Molecular Switches as Selective Cation Sensors». J. Am. Chem. Soc. 2012 ; 134 : 8101–81033.
5. Frisch M.J. et al. 2010. Gaussian 09, Revision C. 01. Wallingford CT.

Po12

Ab-initio Investigation of Structural, Electronic and Topological Properties of Half- Heusler Compounds: TiRh_z (Z=Sb,Bi).

Yamina Lakred^{1*}, Mokhtar Elchikh² and Soumia Bahlouli²

¹LPMF laboratory, Department of physics, University of sciences and technology of Oran-USTO, Algeria

²LPMF laboratory, University of sciences and technology of Oran-USTO, Algeria

*Corresponding author

Introduction

Topological insulator (TI) is a new class of materials discovered recently, which has a insulating gap in the bulk and metallic surface states ¹. In recent years, TIs have generated a great interest in view of their great potential technological for spintronic and quantum computing applications ^{1,2}. Currently, the search for TIs is extended to the Heusler family ^{3,4} due to their various interesting physical properties such as magnetism, spintronics, superconductivity, half-metallicity and thermoelectricity. In this work, we have investigated the structural, electronic and topological properties of half- Heusler compounds TiRhZ(Z=Sb,Bi) in order to discuss the topological band structure behavior.

Computational Details

In this study, we perform our calculations using FP- LAPW method implemented in Elk code ⁵ with the exchange and correlation energy of GGA-PBE. Spin-orbit coupling is essential for calculating the electronic band structure, is included in our calculations by second- variational procedure. The SCF calculations is achieved by demanding the convergence of the total energy is smaller than 10⁻⁶ eV.

Results and Discussion

Structural Optimization

Generally, the half-Heusler compounds crystallize in a face-centered cubic (fcc) with space group F43m (no.216). There are three different configuration: α -phase, β - phase and γ - phase. According to Gautier et al. ⁶, α -phase is more stable.

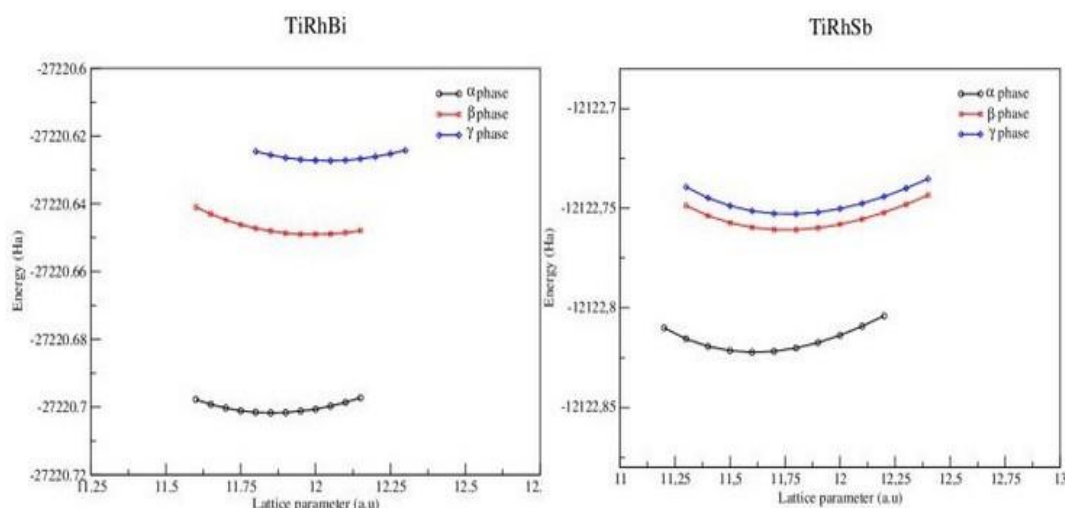


Figure 1: Structural optimization of half-Heusler compounds TiRhBi and TiRhSb in three configurations.



Table 1: Parameters optimization of stable phase; i.e; α -phase.

Compounds	a_0 (Å)	E (Ha)	B_0 (GPa)	B_0'
TiRhSb	6.143	-12122.822	142.879	4.811
TiRhBi	6.273	-27220.701	123.628	4.791

ELECTRONIC AND TOPOLOGICAL PROPERTIES

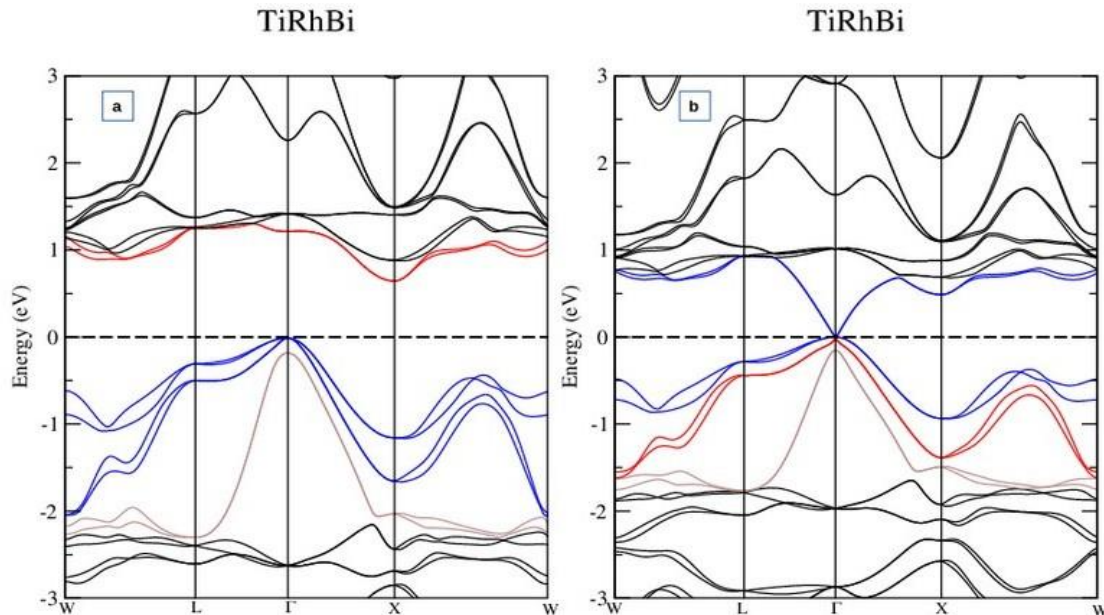


Figure 2: Band structure of TiRhBi, (a) at equilibrium lattice parameter and (b) with hydrostatic strain in order to find a topological semimetal.

Conclusion

In this work, we have study the topological band structure of new half-Heusler and we summarize in few points:

- Our half-Heusler compounds TiRhZ are more stable in α -phase and we have a good agreement with others results.
- The two compounds are trivial semiconductors with indirect band gap, that means they used in several applications.
- In this study, we have confirmed that the band topology is sensitive with lattice parameter that made us apply a hydrostatic strain to find a new topological material with inverted band structure⁷.

Acknowledgments

Part of the calculations were conducted on ENPO UCI AI- Farabi Supercomputer

References

1. Moore Joel E. « The birth of topological insulators» Nature 2010;464 ;194.
2. Fu L, Kane C.L, and Mele E.J. « Topological insulators in three dimensions» Phys.Rev.Lett 2007;98 ;106803.
3. Al-Sawi W, Lin Hsin, Markeiwicz R.S et al. «Topological electronic structure in half-Heusler topological insulators» Phy.Rev.B 2010 ; 82 ;125208.

4. Khirat M, Lazab M, Bettahar N and Rached D «First- principles calculations of the band ordering conversion in the $\text{La}_x\text{Sc}_{2-x}\text{RuPb}$ compounds» *Solid State Communications* 2018; 276 ;14-18.
 5. Dewhurst K, Sharma S, Norstrom L, Cricchio F, Bultmark F, Gross H, Ambrosch-Draxl C, Persson C, Brouder C, Armiento R, et al., ELK, <http://elk.sourceforge.net> (2016).
 6. Gautier R, et al. «Prediction and accelerated laboratory discovery of previously unknown 18-electron ABX compounds» *Nature chemistry* 7.4 (2015): 308.
 7. Lared Y, Elchich M, Bahlouli S, «Electronic and topological properties in heavy element based Heusler compounds X_2RhPb ($\text{X}=\text{Sc}, \text{Y}, \text{La}$):first-principle method» *Eur.Phys.J.B* 2021;94:135.
- .

Po 13

Thermal And Dynamic Study of Confluent Round Jet of Different Diameters

Samira Hamaili louaifi*, Amina Mataoui and Mohamed Aksouh

Laboratoire de mécanique des fluides théorique et appliquée, LMFTA-USTHB, ALGER

*Corresponding author

ABSTRACT

The interaction between two axisymmetric jets of different diameters is examined in this study in order to perform a dynamic and thermal description. The various results of the three-dimensional configurations allowed to evaluate the influence of the velocities ratio and the temperature ratio on the flow structure resulting from the interaction in convergence, merging and fully developed regions. Throughout this study the maximum heat exchange point was located for a given velocities ratio and for different temperature ratios of the two jets. In addition, we find that the velocities ratio affects the distribution of temperature particularly its thermal expansion rate. This study permitted us to propose correlations predicting both the velocities and temperature ratios of the two jets.

Introduction

Free jets have been widely studied for their various industrial and environmental applications. In order to improve their efficiency, the application of multiple jets has been the subject of a considerable number of studies. This configuration is encountered in several industrial applications such as: cooling systems, combustion and dispersion of pollutants. The objective of this contribution is to study the interaction between the main jet and the secondary jet, in order to analyze the effect of the velocities ratio and the temperature ratio on the flow structure after the mixing.

Theoretical Study

The flow studied is fully turbulent and the fluid is Newtonian. The considered configuration consists of two aligned round jets. The calculations are performed using 3D-RANS modeling. The averaged equations for incompressible fluid, translate from the principles of conservation equations of the mass, momentum and energy, coupled with the equations of the turbulence model.

Results and Discussion

This study considers numerically several velocity ratios λ and several temperature ratios T ranges. The two unequal jets are round of diameters D and d , parallel. For a given strong jet velocity U_0D , the weak-jet is varied such as: $0 \leq \lambda \leq 1$; where. For the thermal study, the strong jet is heated and the cold jet is varied from ambient temperature T_0d to the strong jet temperature, corresponding to temperature ratio. The velocity contours and particle trajectories predicted by the k -Realizable model are shown in Figures 1, which describe the structure of the 3D flow produced by the interaction of the two jets. These contours show that the longitudinal velocity component is always positive, which justifies the absence of a recirculation zone. Contrary to the cases of plane jet configurations that induce recirculation zones. These contours illustrate the interaction between the two jets and the



important curvature of the secondary jet towards the primary jet, due to the Coanda effect where a favorable pressure gradient is produced. We note that the two jets meet at a point called the confluence point. We also observe that for low velocities of the secondary jet, its deviation is more important towards the strong jet.

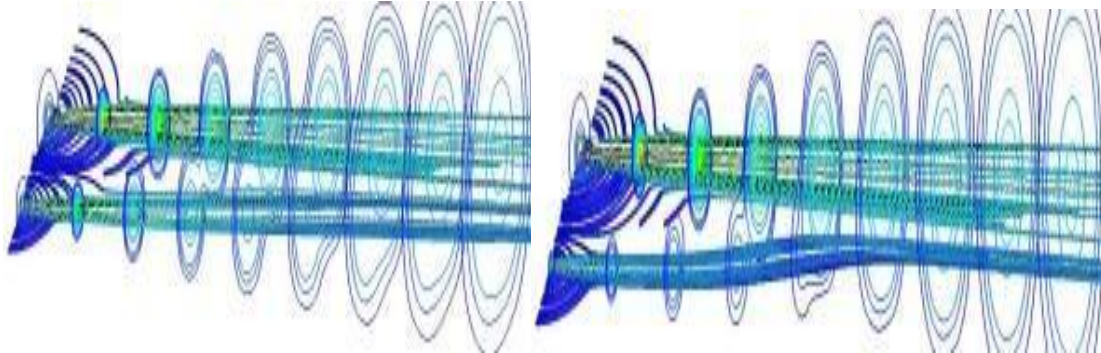


Figure 1: Trajectories of the particles of the interacting jets, and magnitude contours velocity. Figure 2 shows that the position of the maximum temperature of the jet (y_{Tmax}) varies linearly with the velocity ratio λ , for T between 0.88 and 1 and $0.25 \leq \lambda \leq 1$. The slope of this line decreases when the velocity ratio decreases. y_{Tmax} is correlated from the speed and temperature ratios.

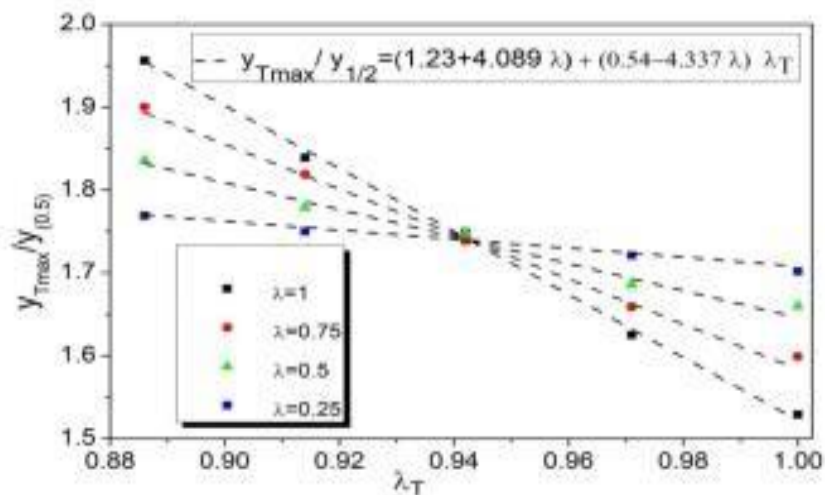


Figure 2: Position of temperature maxima.

Conclusion

Through this study the maximum heat exchange point was located for a given velocity ratio and for different temperature ratios of the two jets, the growth of the dynamic expansion rate with the increase in velocity. In addition, we note that the velocity ratio affects substantially all the quantities of the flow resulting from the interaction of the two jets, more particularly the temperature distribution, in particular its thermal expansion rate. Therefore, the effect of the secondary jet plays an effective role in the cooling of a strong jet.

References

1. Vouros, A., & Panidis, T. (2008). Influence of a secondary, parallel, low Reynolds number round jet on a turbulent axisymmetric jet. *Experimental Thermal and Fluid Science*, 32(8), 1455-1467.
2. Louaifi-Hamaili, S., Mataoui, A., & Aksouh, M. Effect of a Weak Jet on a Strong Jet. *Journal of Applied Fluid Mechanics*, 12(6), 2083-2093, 2019.

Po14

First Principles Investigation of Structural and Electronic Properties of AlN/GaN Superlattices Growth Along Various Crystallographic Axes

Mimouna Oukli*, Nouredine Mehnane, Hafida Belghoul

Applied Materials Laboratory (A.M.L), Faculté de Genie Electrique, University Djillali Liabes of Sidi Bel Abbes, 2200 Sidi Bel Abbes Algeria

*Corresponding author

Introduction

The group III-nitrides semiconductors, InN, GaN and AlN and their alloys are of continuing great interest due to their vast technical application as design of Laser Diodes and Light-Emitting Diodes (LED's) operating in the short-wavelength from blue-green [1-5], ranging from 0.667 to 4.904 eV. The AlN and GaN lattice parameters are approaching each other, and significantly smaller than that of InN [6], the challenge of the lattice mismatch between the epitaxial layers and substrates can be solved by introducing a small amount of InN [7].

While AlGaIn is attracting all the attention, the AlN/GaN SL's with various growth axis directions have not received a particular attention. Especially, it has been shown that SL systems can be very useful for theoretical investigation to the determination of their electronic properties. The reason for that is that atomic layers of GaN and AlN in AlN/GaN SL's are (artificially) grown separately and with the desired width for each layer

Theoretical Study

For binaries, a primitive cell is considered. Each position contains two atoms, the first one being (Ga or Al) and the second one being (N). The second atom is obtained from the first atom by a shift of $(1/4, 1/4, 1/4)$. a_0 in the zinc blende phase, a_0 being the lattice parameter of the binary (AlN or GaN). The investigated structures consist of ideal quantum well superlattices made of a periodic sequence of monolayers of AlN and monolayers of GaN. On the other hand, we adopted the notation $SL(m, n)$ for SL's with m monolayers of AlN and n monolayers of GaN, each monolayer contains one cation and one anion. We consider the SLs with the growth axis along the three directions. We restrict ourselves to the case for which $(m + n)$ is even.

Results and Discussion

We have calculated the band structures of both binaries AlN and GaN. That is, the valence band (VB) maximum and conduction band (CB) minimum are found at the Γ point. Comparison with previous experimental results reveals that the present calculated bandgaps of 3.406 eV for AlN and 1.916 eV for GaN are underestimated compared to the experimental values of 6.28 eV for AlN and 3.20 eV for GaN [35], but this will not alter the conclusions of the present work since they are not related to the quantitative estimation of gaps.

For the growth axis (001), the high symmetry points B and Y do not exist in the (001), because in



this case, they are identical to R and X respectively. Thus, we have just represented R and X but we labelled them B and Y to allow comparison. In all cases, the gap remains directly with the top of VB and the bottom of CB both at Γ and is about 2.495 eV with $m = n = 3$. However, we remark that the Γ - Γ gap decreases with thickness from $m = n = 1$ to $m = n = 2$ by 0.084 eV, and when n increases, the Γ - Γ gap becomes smaller: it decreases from $m = n = 2$ to $m = n = 3$ by 0.112 eV. The same remark holds in the case of the Γ - X , Γ - M , Γ - Z and Γ - A gap which follows similar variations (but remain greater than the Γ - Γ gap). In the case of Γ - R , we note that the gap increases from $m = n = 1$ to $m = n = 2$, and decreases more for $m = n = 3$. We remark also that this Γ - Γ direct gap is lower than the fundamental gaps of AlN, and thus is not obtained from interpolation of both parents AlN and GaN.

An interesting feature is obtained in the SLs from (110) and (111) growth axis is found to have a indirect bandgap with $m = n = 1, 2, 3$, the top of the valence band (VB) being at Y from (110) SL and R from (111) SL and the bottom of the CB located at Γ and Z respectively. When $m = n = 3$ the indirect bandgap for the (110) SLs is about 2.437 eV which is close to the direct Γ - Γ bandgap of 2.453 eV. However, the indirect bandgap for the (111) SLs is about 0.386 eV (an Γ - Γ bandgap of 0.576 eV), where it shifts towards lower energy when compared to both directions (001) and (110) SLs. Furthermore, the Y - Γ and R - Z gaps decreases with thickness from $m = n = 1$ to $m = n = 3$ by 0.254 eV and 0.042 eV from (110) and (111) growth axis. We notice also significant changes in the CB behaviour near M , A and X become non-linearly varying, Γ - M and Γ - A (Γ - X) increases (decreases) than decreases (increases) for (110) compared with (001).

Conclusion

The most important results are that all these systems exhibit direct or indirect band gap, and that (AlN) n /(GaN) n superlattices are energetically more stable with increasing n . However, it is shown that the band structures of (001) is different from (110) and (111) SL's. We believe that a larger influence of sp and pd coupling between Ga and N atoms modify the nature of the gap and reduce here value.

References

1. S. Nakamura, M. Senoh, S. Nagahama, N. Iwasa, T. Yamada, T. Matsushita, Y. Sugimoto, H. Kiyoku, Appl. Phys. Lett. 70 (1997) 1417.
2. M.G. Cheong, E.K. Suh, H.J. Lee, J. Lumin. 99 (2002) 265.
3. H.P. Zhao, G.Y. Liu, X.H. Li, R.A. Arif, G.S. Huang, J.D. Poplawsky, IET Optoelectron. 3 (2009) 283

Dangling Bonds Parameters Effect on Dark and Illuminated Conductivity in a-Si:H Absorber Layer for Solar Cells Applications

Ilias Sbahi^{1*}, Baya Zebentout¹, Raouia Djemai², Zineb Benamara¹ and Kamel Khirouni²

¹Laboratoire de MicroElectronique Appliqué, Faculté de Génie Electrique, Université de Sidi Bel Abbes (Algérie).

²Laboratoire de Physique des Matériaux et des Nanomatériaux appliquée à l'Environnement (LaPhyMNE), Faculté de Gabès (Tunisie).

*Corresponding author

Introduction

In this paper, a contribution is made to study the impact of the DOS (Density of States) defects in undoped a-Si:H on the conductivity in the dark and under solar illumination. The quality of this material is the key to the best PV efficiencies reached in the solar cells based on a-Si:H, used as an absorbing layer between two heavily doped regions. There is a strong correlation between the PV output and the quality of this region for an optimal thickness. It has been widely shown that PECVD and HWCVD techniques lead to a growth of silicon with a high density of defects in its forbidden band and usually described by two decreasing exponential distributions for the valence and the conduction band tail (BT) and two correlated Gaussian distributions for deep defects introduced by dangling bonds (DB). In this perspective, we shall investigate the contributions of certain types of DOS defects with direct impact on undoped a-Si:H conductivity by means of computer modeling schemes requesting the solution of the basic semiconductor equations which are the hole and electron continuity equations and Poisson's equation according to the Schrafetter and Gummel model scheme [1].

Theoretical Study

The density of states (DOS) is important for the calculation of the electrical and optical properties of the material. The usual DOS model in the amorphous silicon shown in figure 1 is used to describe the U-shape distribution of the states inside the forbidden band-gap [2,3]:

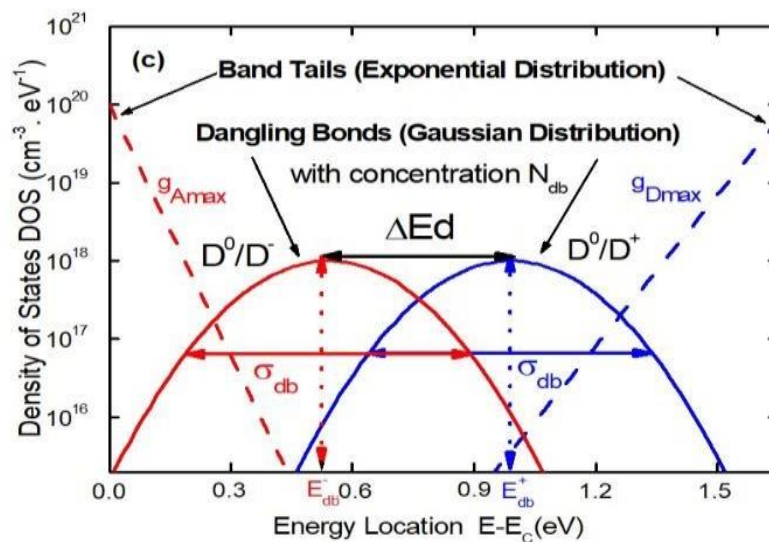


Fig. 1 Density of States (DOS) in the gap of the a-Si:H.



Results and Discussion

The dark or illuminated conductivity (Fig.2) is at a minimum when the overlap is total with the smallest standard deviation value of 0.05 eV which is relative to the largest value of the total density N_{db} equal to $5 \cdot 10^{16} \text{ cm}^{-3}$ of DB resulting in a high trapping efficiency. This conductivity increases with the increase of ΔE_d and then in this case the states D^+ and D^- moved away from the middle of the gap.

For $0 \leq \Delta E_d \leq 0.4$ we remark a proportional evolution of σ_{db} and ΔE_d which led to an increase of conductivity this increase can be interpreted by two simultaneous phenomena the recovery of the distributions of the dangling bonds states N_{DB}^- acceptors and N_{DB}^+ donors when σ_{db} increases the increase in the energy difference between the centers D^+ and D^- which is ΔE_d has led the traps to move away from the middle of the forbidden band and the probability of capture of an electron or a hole by a center D^0 decreases, it follows that the level of fermi E_f is pushed back to the E_c level.

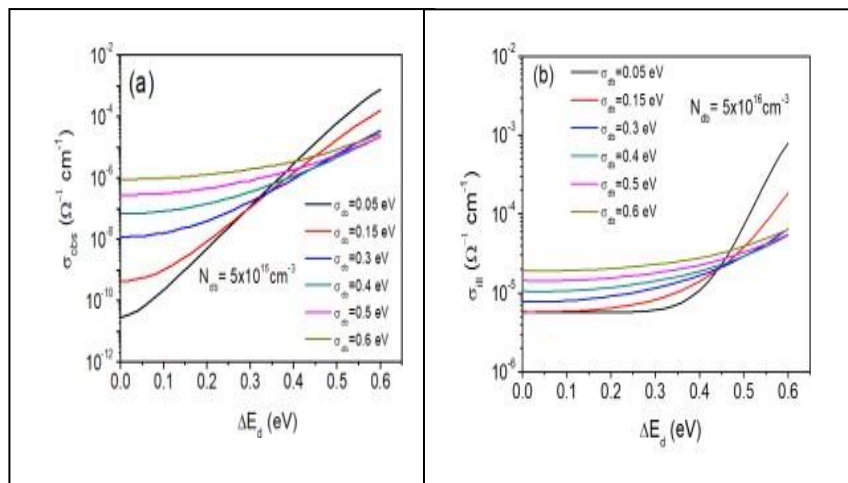


Fig.2. Variation of the conductivity as function of correlation energy for different standard deviations σ_{db} : (a) without illumination. (b) under illumination.

Conclusion

The parameters of the dangling bonds have a direct impact on the quality of a-Si:H layer for PV applications.

References

1. D.L. Schrafetter, H.K. Gummel, IEEE Trans. Electron. Dev. 16 (1969)64.
2. H. Flietner, "U-Shaped distribution at semiconductors interfaces and the nature of the related defect centers", Phys. Stat. Sol. (a). Vol. 91, 153, 1985.
3. G.L. Gray, "Computer model for the simulation of thin-film silicon-hydrogen alloy solar cells", IEEE Transactions on Electron Devices, vol. 36, N°5, May 1989.

The Window Layer Doping Effect on the Performance of a SiO_x:H Based Solar Cells

Tayeb Youcef Belabbas*, Wafa Hadj Kouider and Abbas Belfar

Laboratory of plasma physics, Conductor Materials and their Applications, Faculty of Physics, Oran University of Sciences and Technology Mohamed Boudiaf. Oran, Algeria.

*Corresponding author

ABSTRACT

In this work, the conversion efficiency of hydrogenated amorphous silicon oxide (a-SiO_x:H) based solar cells was analyzed and designed by SCAPS-1D software. So, we have investigated by numerical simulation the influence of the p-nc-SiO_x:H window layer doping concentration (Na) on the performance of the n-i-p single junction solar cell. However, our calculation was carried out by varying the doping concentration (Na) between 10¹⁸ and 3×10¹⁹ cm⁻³. The best results obtained with the Na optimized value are VOC = 989 mV, JSC = 13.9 mA/cm², FF = 77.6 % and a conversion efficiency value equal to 10.67%.

Introduction

Because of their diverse microelectronic uses, hydrogenated amorphous silicon oxygen alloy films (a-SiO_x:H) are of great interest [1,2]. We aim in this work to study the impact of doping Na of the window layer on a-SiO_x:H based solar cells.

Simulation

The simulated a-SiO_x:H based solar cell structure is illustrated schematically in (Fig. 1). We analyze this cell using the Solar Cell Capacitance Simulator structures (SCAPS-1D). SCAPS solves the fundamental semiconductor equations in one dimension and under steady-state conditions [3,4].



Fig.1: Schematic structure of a-SiO_x:H based thin film solar cell.

Results and Discussion

Fig. 2 plots the different output parameters of the cell, namely the short circuit current JSC, open circuit voltage VOC, form factor FF and efficiency (Eff) as a function of Na doping of the p nc-SiO_x:H window layer. The best values for the output parameters of the cell (JSC = 13.9 mA.cm⁻², VOC = 989 mV, FF = 77.6% and Eff = 10.67%) are obtained for a doping Na= 3×10¹⁹ cm⁻³.



This is explained by the fact that the increase of the doping of the window layer will increase the space charge area and the improvement of the collection of photogenerated carriers.

To better understand the origins of these improvements in the solar cell output parameters as a function of the simultaneous variation of Na, we have plotted the energy band diagrams (Fig. 3).

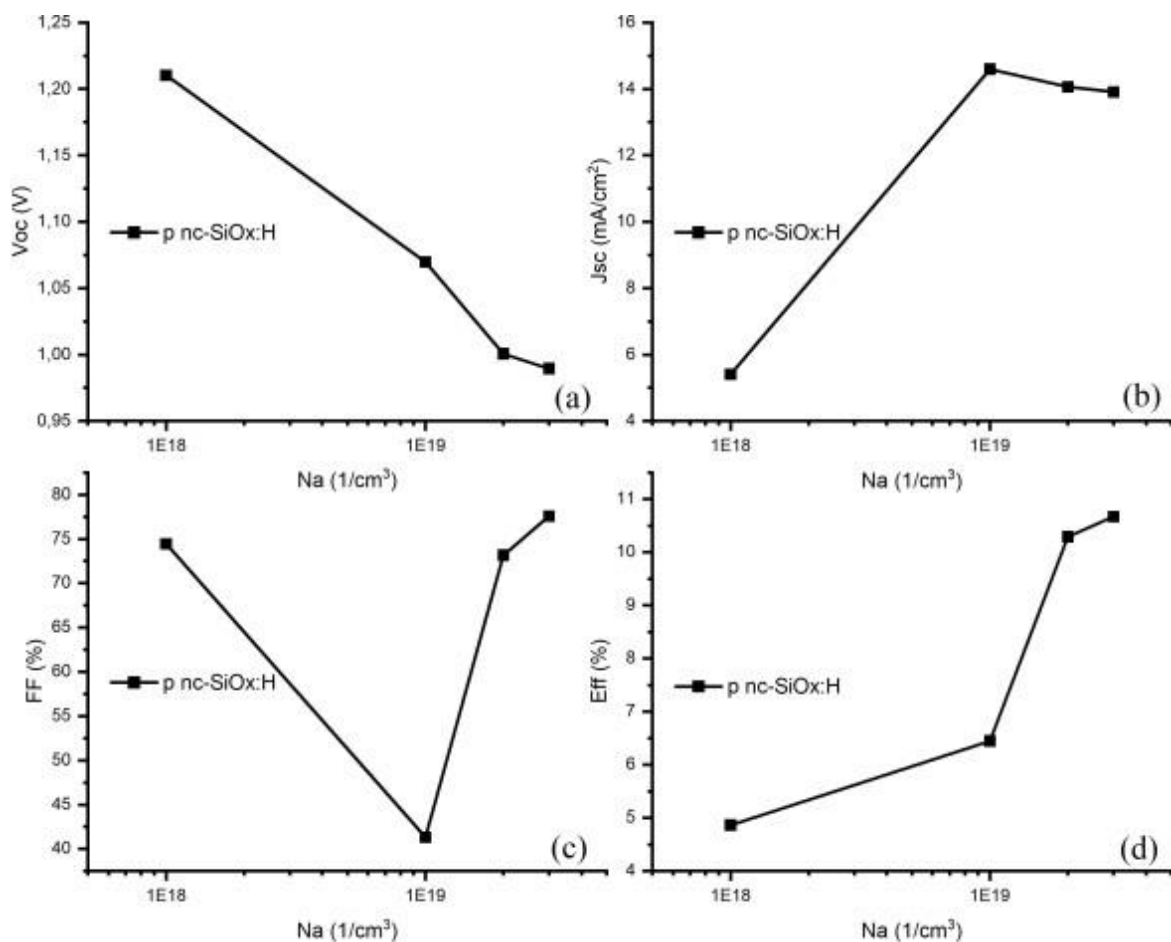


Fig.2: Variations of (a) VOC (b) JSC (c) FF and (d) efficiency with various dopant concentration Na of the window layer and optimized solar cells.

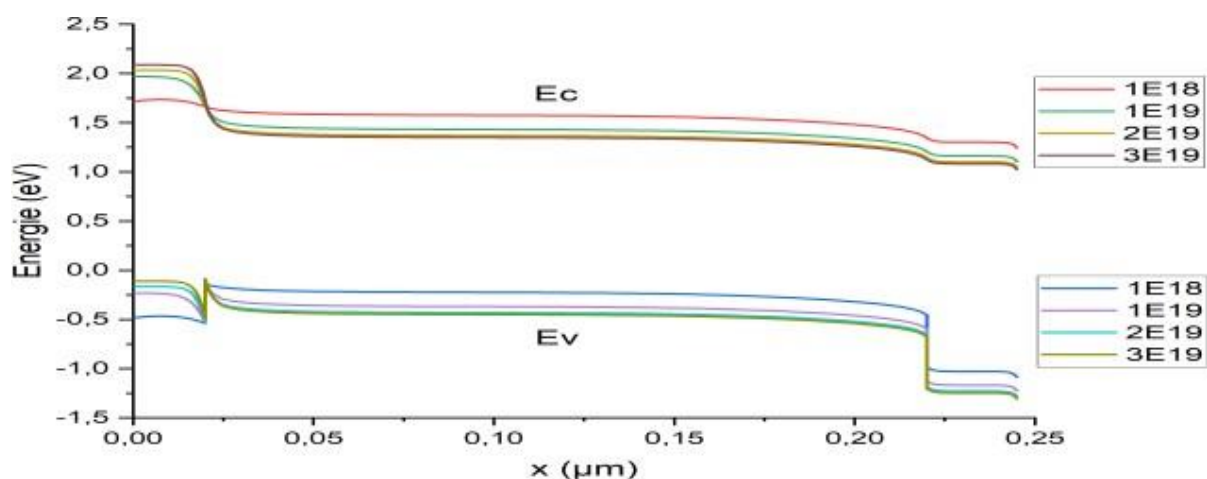


Fig. 3 Band diagram of the solar cell with various dopant concentration (Na) of the p window layer.

Conclusion

In this investigation, we have studied the performance of the a-SiO_x:H-based solar cells. The photovoltaic parameters (J_{sc}, η, Voc and FF) have been calculated by using SCAPS-1D .It was found that the optimal value of the doping concentration is 3×10¹⁹ cm⁻³ for p nc- SiO_x:H window layer. The obtained results are Voc = 989mV, Jsc = 13.9 mA/cm², FF = 77.6 % and the power conversion efficiency is 10.67 %.

References

1. Tsu D V., Kim SS, Theil JA, Wang C, Lucovsky G. Preparation and properties of SiO₂ –SiO_x heterostructures formed by uninterrupted processing by remote plasma enhanced chemical vapor deposition. *Journal of Vacuum Science & Technology A: Vacuum, Surfaces, and Films.* 1990;8:1430–6.
2. Ohmori K. Tachyonic kink and lump-like solutions in superstring field theory. *Journal of High Energy Physics.* 2001;5.
3. Decock K, Khelifi S, Burgelman M. Modelling multivalent defects in thin film solar cells. *Thin Solid Films.* 2011;519:7481–4.
4. Burgelman M, Verschraegen J, Degraeve S, Nollet P. Modeling thin- film PV devices. *Progress in Photovoltaics: Research and Applications.* 2004;12:143–53.

Study of Ultra-Fast Phenomena Generated in Femtosecond Laser-material Interactions

Zerradi Amal*, Abdelmalek Ahmed and Bedrane Zeyneb*

Theoretical Physics Laboratory, Physics Dpt., Sciences Faculty, Tlemcen University, Algeria

*Corresponding author

Introduction

The great technological progress in the field of pulsed lasers and in particular femtosecond lasers attracts a lot of attention whether for academic research or in industry because of the interest of its justified applications in multiple fields. The interaction of light with matter is very different for these pulses compared to longer pulses. The matter is almost instantly changed and then evolves as the laser pulse is terminated; the thermal effects are profoundly changed. These mechanisms are of course studied for themselves, but already it is possible to understand that many new applications are accessible. The innovative applications of laser technology are linked to the advancement of knowledge of the mechanisms of laser-matter interaction. The aim of this work is to understand the ultra-fast phenomena generated during the interaction of ultrashort lasers with metallic surfaces such as gold for thermal machining.

RESULTS AND DISCUSSION

The two-temperature model (TTM) was used for modeling the laser-gold interaction. TTM offers the possibility of describing heat transfer and energy exchange between the ion network and the electrons in the material. It also allows us to properly analyze the spatial and temporal distribution of the energy flow from hot electrons to the cold ionic network where each of these two subsystems is supposed to be in thermodynamic equilibrium [1,2]. Fig 1 shows the evolution of the electronic temperature T_e and of the network temperature T_i as a function of time on the gold surface, in the case of the three pulsed regimes: fs, ps and ns.

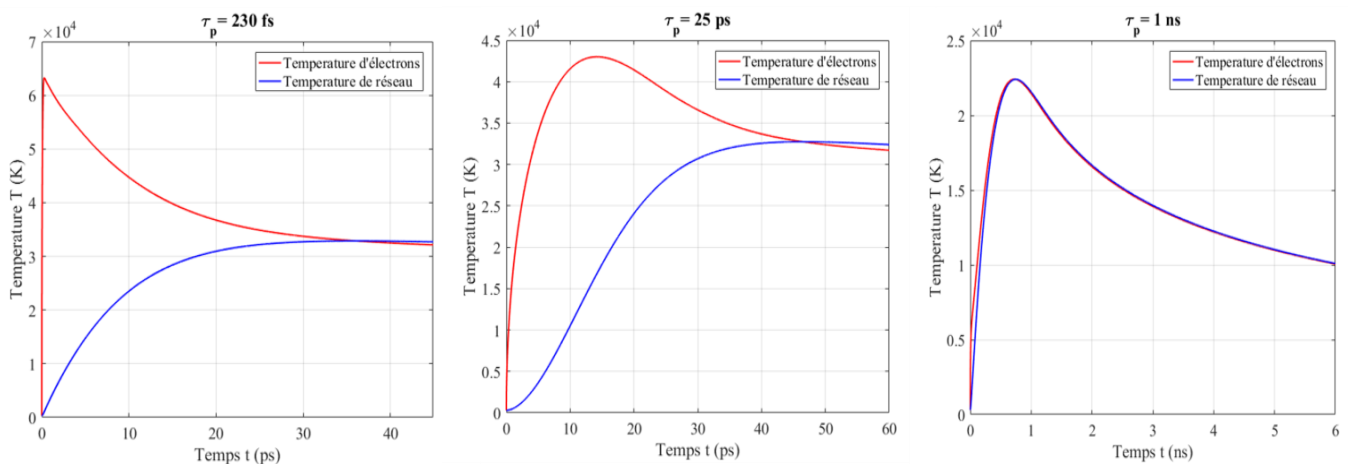


Fig 1: Evolution of the electronic temperatures T_e (red line) and of the T_i network (blue line) as a function of time on a gold surface irradiated with fluence $F = 10 \text{ J/cm}^2$ and laser wavelength = 800 nm. (a) a femtosecond laser with a pulse duration of 230 fs, (b) by a picosecond laser with a pulse duration of 25 ns, (c) irradiated for 1 ns.



We have found that one can achieve purely thermal fusion and ablation accompanied by the ejection of the molten material during the ns laser and ps laser interaction with the material, but with an amount of scattering lower in the case of a picosecond laser. Whereas in the case of femtosecond pulses, the tearing of the material is very fast and takes place before the thermalization of the energy and the propagation of the heat, which makes it possible to confirm that fusion is non-thermal and the ablation occurs by ejection of the material in the form of plasma.

CONCLUSION

The time required to effect a change in a material during the ablation is a factor of great importance, in this respect we have studied the evolution of the temperatures of the network and of the electrons as a function of the time at the sequence of nanosecond and picosecond pulses in order to compare them with the femtosecond pulse rate. It can be concluded that, from the point of view of precision, fs lasers have very specific characteristics due to the ultra-fast mechanisms which govern the interaction of the laser with the material are non-thermal producing.

REFERENCES

1. A. Abdelmalek *et al.*, *Appl. Sci.* 2018, 8(10), 1826.
2. A. Abdelmalek *et al.*, 2018 *J. Phys.: Conf. Ser.* 987 01201

Po19

Special Finite Element Modeling for Predicting the Mechanical Properties of Carbon Nanotubes at the Atomic Scale

Abdellah Reguieg Yssaad^{1*}, Krour Baghdad¹ and Laib Salah Eddine¹

¹Structurs and Advanced Materails in Civil engineering and Public Works Laboartory, Sidi Bel Abbés, Algeria

*Corresponding author

ABSTRACT

Due to the difficulties of experimental methods, computational methods are considered to be powerful tools to predict the mechanical properties of carbon nanotubes. In this paper a special finite element model based on harmonic inter-atomic potential is carried out in order to predict the elastic properties of nanotubes at atomic scale. The importance of contribution of the bond dihedral element in the modeling is studied, its results have shown that it stabilize the calculation. Moreover, the effect of length, diameter and chirality on the mechanical properties are also studied and discussed. The obtained results show good agreement with other results in the literature and they have proved the importance of this method in the rapid prediction of the elastic behavior of the CNT compared to the molecular dynamic method (MD).

Keywords—Atomic scale, Carbon nanotube, Finite element method, Harmonic inter atomic potential, Mechanical properties.



Improvement of Positron Annihilation Lifetime Spectrometer Resolution: A Comparative Study

Djamila Kebci^{1*}, Abderrahim Guittoum², Messaoud Hemmous² and Nouredine Bendjedda²

¹Physics Department, Faculty of Science, M'hamed Bougara University, Avenue de l'Indépendance, 35000 Boumerdes Algeria

²Nuclear Research Centre of Algiers, 2 Bd Frantz Fanon, Bp 399, Alger-Gare, Algiers, Algeria

*Corresponding author

Introduction

Positron life time spectroscopy (PALS) is a variant of positron annihilation spectroscopy (PAS), which is of great interest to researchers for a wide range of applications such as medical sciences: Molecular imaging by positron emission tomography¹, tumors², as it can also provide a plus regarding the harmfulness of a new drug³, or biology⁴. It is also used in astrophysics⁵, development and manufacturing of telecommunication equipments⁶ for high reliability critical service applications. The objective of my work is to improve the PALS coincidence system, to have a better instrumental (temporal) resolution combined with a high count rate. For this purpose, we opted for a FAST-FAST system.

Experimental Study

The FAST-FAST device with only one circuit (anode). For this system the pulses coming out of the photomultiplier (PMT) are selected in amplitude and shaped in time at the CFDD (Constant Fraction Differential Discriminator). The temporal signals coming from the START and STOP channels are then injected into the TAC (Time-Amplitude Converter). The amplitude of the electrical signal at the output of this module is proportional to the time interval between the two START and STOP events. The signal is finally digitized using the ADC (Analog to Digital Converter). The accumulation of a large number of events allows obtaining a temporal spectrum of positron annihilation. This system allows obtaining better statistics and a good resolution at the level of two scintillator detectors.

Results and Discussion

Different combinations (scintillator + photomultiplier + base) have been chosen and tested on polymer CR39 and silicon samples. We have shown that for the study of polymers (lifetime > 2 ns), all combinations (scintillators + PMT + base) can be used. However, in the case of metals and semiconductors which are known to have low lifetimes (< 0.22 ns), the most suitable combinations are: BC418 scintillator + H3378-51 and BC418 scintillator + R329-02 + ORTEC265. These combinations give resolution values of 0.2390 ns and 0.266 ns, with high count rates. The preferred combination for studying various types of materials is BC418 + H3378-51 which give better resolution with a higher count rate in addition to its low cost compared to other combinations.

Conclusion

Our work is part of the improvement of the instrumental resolution of a positron lifetime spectrometer (comparative study of coincidence systems). Several combinations have been chosen



based on the characteristics of the different parameters that constitute them. Indeed, a study has been initiated on the different parameters such as (rise time, refractive index, wavelength of the maximum response and decay time). In our study and with regard to the obtained results, we can say that, for the study of polymers (CR39) which are characterized by high values of the positron lifetime (>2 ns), all the combinations (scintillators + photomultiplier + base) can be used. However, in the case of metals and semi conductors which are known to have small lifetimes (<0.22ns), the most suitable combinations are: BC418 + H3378-51 and BC418 + R329-02 + ORTEC265. These combinations offer us small resolution values which are respectively 0.23890 ns and 0.26601 ns with highcounting rates equal to 20.5 and 11.35 counts/second. On the other hand, the preferred combination for the study of various types of materials is BC418 + H3378-51 which offers a better resolution with the highest count rate in addition to its low cost compared to the other combinations.

References

1. Phelps, Michael.E. «Molecular imaging with positron emission tomography, Annu». *Annu. Rev. Nucl. Part. Sci.* 2002; 52:303-338.
2. Jean.Y, Li.Y, Liu.G, Chen.H, Zhang.J, Gadzia .J. E, « Applications of slow positrons to cancer research: Search for selectivity of positron annihilation to skin cancer ». *APPL.SURF. SCI.* 2006; 252: 3166-3171.
3. Moskal.P, Jasinska.B, Stepien.S.D, Bass.S.D. « Positronium inmedicine and biology ». *Na. Rev. Phys.* 2019; 1: 527-529.
4. Sakurai.H, Itoh.F, Hirano.Y, Nitta.M, Suzuki.K, Kato.D, Yoshida.E, Nishikido.F, Wakizaka.H, Kanai.T. « Positron annihilation spectroscopy of biological tissue in 11C irradiation». *Phys. Med. Biol.*2014; 59:7031.
5. Siegert.T, Crocker.R.M, Diehl.R, Krause.M.G, Panther F. H, Plei.M. M.Weinberger.C. « Constraints on positron annihilation kinematics inthe inner Galaxy». *Astrophys.* 2019; 105: 014312.
6. Heng.C, Chelomentsev.E, Peng.Z, Mascher.P, Simpson.P. «Photoluminescence and positron annihilation spectroscopy investigation of (ge, er) codoped si oxides deposited by magnetronsputtering». *J. Phys.* 2009; 105: 014312.

Thermal Properties of the Klein-Gordon Oscillator in Deformed Space

M'hamed HADJ MOUSSA

Department of physics, Faculty of Sciences, Saad Dahlab-Blida-1 University, BP 270, 09000, Blida

ABSTRACT

Different methods used Heisenberg's generalized uncertainty principle (GUP) and the extended uncertainty principle (EUP) that allows the generalization of physical quantities in relativistic or non-relativistic quantum mechanics. In this work, we have treated the problem of the thermal physical properties of the Klein Gordon oscillator in the deformed space within the framework of the minimum length with the generalized uncertainty principle (GUP). This study provides a precise vision of the behavior of particles in the deformed space depending on whether the temperature value is high or low.

Keywords: Minimum length, Klein Gordon Oscillator.

INTRODUCTION

In recent years, there is a studies carried out in the chosen space such the phase space, non-commutative space and deformed space ... etc, to improve physical properties. In this work we interest in the deformed space by using the minimum length with a deformation parameter Beta (β) [1-2] . Where the uncertainty of Heisenberg is generalized. Our objective is to calculate the physical properties for understanding the behavior of the particles in high or low temperature.

THEORETICAL STUDY

The one dimensional Klein–Gordon oscillator equation is given by "we put $\hbar = c = 1$ "

$$[(\hat{p} + im\omega\hat{x})(\hat{p} - im\omega\hat{x}) + m^2 - (E - q\varepsilon\hat{x})^2]\psi(p) = 0$$

Where ε is the intensity of electrical field and q is the electrical charge. Our algebra is defined as [1-2]:

$$\hat{x} = i(1 + Bp^2) \frac{d}{dp}$$

$$\hat{p} = p$$

Where \hat{x} is The position coordinates operator and \hat{p} is the operator of the momentum coordinates

RESULTS AND DISCUSSION

After to calculate the spectrum energy in the case $\varepsilon=0$ we calculate the partition function z as follows:

$$Z = \sum_{n=0}^{\infty} \exp\left\{-\left(\frac{E_n - E_0}{K_B T}\right)\right\}$$

We use the Taylor-Maclaurin developments, and by the necessary approximations, we obtain

$$Z \approx \frac{1}{2} - \frac{1}{2} \sqrt{\frac{\pi}{\beta\omega^2\mu^4}} \left(\left(\frac{T}{T_0}\right)^{\frac{1}{2}} + U \left(\frac{T_0}{T}\right)^{\frac{1}{2}} + \frac{U^2}{2} \left(\frac{T_0}{T}\right)^{\frac{3}{2}} + \dots \right)$$



Where

$$\lim_{\varepsilon \rightarrow 0} \mu = 1 - \frac{1}{\beta m \omega}$$

and

$$U = \frac{\beta \omega^2 \mu^2}{2} + \frac{1}{2\beta m^2}$$

Now, we can deduce the other thermal properties free energy F , mean energy U , specific heat C and entropy S by the following relations.

$$F = -K_B T \ln Z, \quad U = K_B T^2 \frac{\partial \ln Z}{\partial T},$$

$$C = \frac{\partial U}{\partial T} \quad \text{and} \quad S = -\frac{\partial F}{\partial T}$$

CONCLUSION

The analysis of the physical properties of thermodynamics, allows seeing these thermal properties depend on beta deformation parameter as well as the variation according to the high or low temperature within the formulas calculated analytically and their graphical representation.

REFERENCES

1. Achim Kempf, Gianpiero Mangano, Robert B. Mann. << Hilbert space representation of the minimal length uncertainty relation >> *phys. Revi. D.* 1995; 52.1108-1118.
2. T.V. Fityo , I.O. Vakarchuk, V.M. Tkachuk.: <<One-dimensional Coulomb-like problem in deformed space with minimal length >>. *J. Phys. A: Math. Gen.*, 2006; 39.2143—2149
3. N.P.Landsman.: Deformations of Algebras of observables and the classical limit of quantum mechanics. *Rev.math.phys.* 1993. 05, 775-806.

Role of Hydroxyl Group in CO Adsorption on SnO₂ (110) Surface Investigated by a First-principle Study

N. Bouchelarem*, F. Bouamra¹ and M. Derbal¹

Department of physic, LASICOM Laboratory, University of Blida 1, Algeria

*Corresponding author

ABSTRACT

Tin dioxide SnO₂ is a wide band gap (3.6 eV) n-type semiconductor with rutile bulk structure¹. It has a wide application in solar cells, catalysis and gas sensors^{2,3}. SnO₂ (110) surface is the most stable one thermodynamically among the low-index surfaces, which is usually covered with hydroxyl groups (OH) formed by dissociative chemisorption of H₂O. Their presence on the surface influences the adsorption of molecules such as CO,⁴ NO₂,⁵ etc. The aim of this work is to investigate the adsorption of CO on SnO₂ (110) surface in the presence of hydroxyl group.

Density functional theory (DFT) calculations were performed using the program CRYSTAL09 package⁶, which employ the LDA and the hybrid B3LYP exchange- correlation functionals. Pseudo-potential (ECP) of Durand-Barthelat's⁷ were used to describe the Sn, O, and C centers, and those proposed by Otero-de-la Roza et al.⁸ for H center. The stoichiometric SnO₂ (110) surface has a rectangular structure, corresponding to the Pmm2 (C_{2v}) space group with lattice parameters a=3.186Å and b=6.69Å. The SnO₂ (110) surface is represented by *p*(4x1) supercell with a periodic slab of three layers (3L), as shown in Fig. 1(a). CO molecule was adsorbed on two different sites (O_{2c}, Sn_{5c}) to determine the favorable site, while the H atom was adsorbed on bridging oxygen O_{2c} atom thus modeling quarter monolayer coverage (1/4 ML), as shown in Fig. 1(b-d). The cut-off energy is fixed at 10⁻⁸ Hartree. The Brillouin zone integrations were performed with a 6x6x1 Monkhorst-Pack grid, corresponding to 16 k-points in the irreducible part of the first Brillouin zone (IBZ).

Calculation of CO adsorption on SnO₂ (110) surface was studied firstly to determine favorable site of adsorption. Two possible adsorption sites are considered: bridging oxygen (O_{2c}) and 5-fold tin (Sn_{5c}) as shown in Fig. 1(b) and Fig. 1(c), respectively. When CO is adsorbed on top of O_{2c} atom site, the adsorption energy is positive at about 1.44 eV, which indicate energetically disfavored adsorption site. Our results indicate that the CO molecule preferentially adsorbs with the C end on a Sn_{5c} atom site, and the adsorption energy is -0.79 eV. The following calculations only focus on this stable configuration (Fig. 1(c)).

In the presence of the hydroxyl group on the SnO₂ (110) surface, where the H atom is adsorbed on O_{2c} site resulting bridging hydroxyl group (OH_b), the adsorption energy is calculated to be -3.42 eV. The absolute value of adsorption energy increases by 2.63 eV in the presence of OH_b. This indicate that the hydroxyl group is present to facilitate CO adsorption on Sn_{5c}. Band structures, total and projected density of states and Mulliken charge were investigated to discuss our results.

Finally, we concluded that the hydroxyl group plays a significant role in the adsorbed CO molecule and its reactivity on SnO₂ (110) surface.



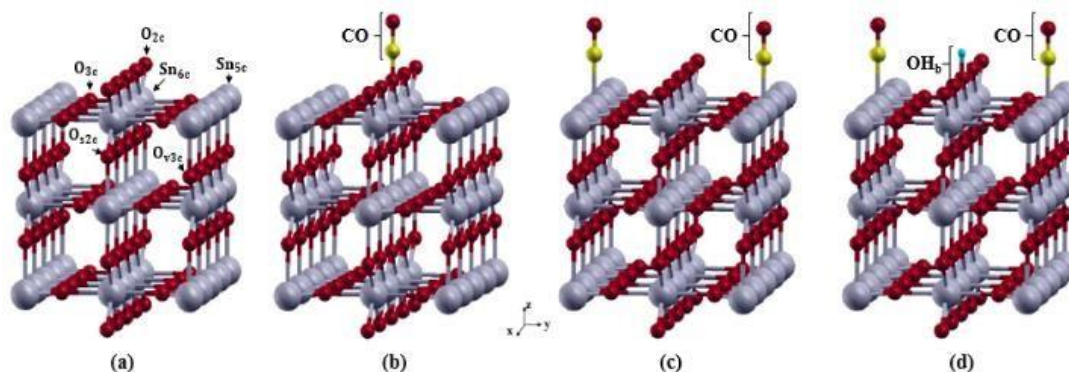


Fig. 1: stoichiometric SnO₂ (110) surface (a) before and after adsorption of CO on (b) O_{2c} site and (c) Sn_{5c} site, adsorption of both CO and H on Sn_{5c} and O_{2c}, respectively.

References

1. V. E. Henrich, P. A. Cox, "The surface chemistry of metal oxides", Cambridge University Press, Cambridge, UK (1994).
2. M. Batzill, U. Diebold, "Surface studies of gas sensing metal", *Surf. Sci.*, 79 (2005) 47-154.
3. G. S. Devi, S. Manorama, V. J. Rao, "High sensitivity and selectivity of an SnO₂ sensor to H₂S at around 100°C", *Sen. Actua.*, 28 (1995) 31-37.
4. N. Barsan and U. Weimar, "Understanding the fundamental principles of metal oxide based gas sensors; the example of CO sensing with SnO₂ sensors in the presence of humidity", *J. Phys. Cond. Matter* 15 (2003) R813–R839.
5. C. Liu et al., "Structure-activity relationship of surface hydroxyl groups during NO₂ adsorption and transformation on TiO₂ nanoparticles", *Environ. Sci. Nano.*, 4 (2017) 2388–2394.
6. R. Dovesi et al., "User's Manual of CRYSTAL09", code available from <http://www.crystal.unito.it>
7. P. Durand and J.-C. Barthelat, "A theoretical method to determine atomic pseudopotentials for electronic structure calculations of molecules and solids", *Theo. Chem. Acta*, 38 (1975) 283–302.
8. A. Otero-de-la-Roza and G. A. DiLabio, "Transferable Atom-Centered Potentials for the Correction of Basis Set Incompleteness Errors in Density-Functional Theory", *J. Chem. Theo. Comp.* 13 (2017) 3505–3524.

The Effect of Aluminum Sources On $(\text{Gd}_{0.7}\text{Lu}_{0.3})_3\text{Al}_5\text{O}_{12}$ Cubic Garnet Structure Synthesized by Co Precipitation Method

Imane LANEZ, Brahim Rekik, Amina Kezzim, Mourad Derbal, Boudjemline Ihcen, Lydia Chabane
LASICOM Laboratory, Department of physics, Saad Dahleb Blida 1 University, ALGERIA

*Corresponding author

Introduction

The multi-component cubic garnet $(\text{Gd}_{1-x}\text{Lu}_x)_3\text{Al}_5\text{O}_{12}$ structure attracts a lot of attention, making it the most popular in fields including as optics electronics. The one with the large Ln^{3+} cations is $(\text{Tb}_3\text{Al}_5\text{O}_{12})$. For eight fold coordination, the radius of the Tb^{3+} cation is 1.040. Because of its small ionic size (0.977 Å), lutetium is thought to be a stabilizer for the metastable $(\text{Gd}_3\text{Al}_5\text{O}_{12})$. According to the previous studies, GAG garnet can be stable at 1300°C when Gd is replaced with roughly 10% Lu and the radius of Ln : (Gd+Lu) is 1.0454. The Ln_2O_3 – Al_2O_3 system is widely known to exist in three crystal phases: LnAlO_3 (LnAP with a perovskite structure), $\text{Ln}_4\text{Al}_2\text{O}_9$ (LnAM with a monoclinic structure), and $\text{Ln}_3\text{Al}_5\text{O}_{12}$ (LnAG with a cubic garnet structure) [1]. In conventional solid-state reactions, LnAG is far more stable than the other two intermediate phases. Chemical methods such as co-precipitation have been shown in numerous investigations to be effective in lowering the sintering temperature and obtaining pure LnAG powders [1]. The complicated structure and homogeneity of Gd^{3+} , Lu^{3+} , and Al^{3+} in the precursor for the synthesis of the pure (Gd,Lu)AG phase [1] at different temperatures with two different precipitation processes normal and reverse strike with two different aluminum sources $\text{Al}(\text{NO}_3)_3$ and $\text{NH}_4\text{Al}(\text{SO}_4)_2 \cdot 12 \text{H}_2\text{O}$ are discussed in this study.

EXPERIMENTAL SECTION

The samples $(\text{Gd}_{0.7}\text{Lu}_{0.3})_3\text{Al}_5\text{O}_{12}$ were synthesized by co-precipitation method with normal (NS) and reverse strike (RS) processes, with aluminum nitrate $\text{Al}(\text{NO}_3)_3 \cdot 9\text{H}_2\text{O}$ and aluminum ammonium sulfate $\text{NH}_4\text{Al}(\text{SO}_4)_2 \cdot 12\text{H}_2\text{O}$ as aluminum sources. As a precipitant, ammonium hydrogen carbonate (AHC, NH_4HCO_3) was utilized. Concentrated rare-earth nitrate solutions were obtained by dissolving Ln_2O_3 (Ln: Gd and Lu) in hot nitric acid. Under room temperature, 100 mL of the nitrate solution (Gd+Lu+ Al) was added to 160 mL of the AHC precipitant solution. A stock solution of mother salts was produced from the nitrate solutions and aluminum using the formula $(\text{Gd}_{1-x}\text{Lu}_x)_3\text{Al}_5\text{O}_{12}$ ($x=0.3$). XRD is used to characterize $(\text{Gd}_{0.7}\text{Lu}_{0.3})_3\text{Al}_5\text{O}_{12}$ nanoparticles in order to prove pure phase under various conditions.



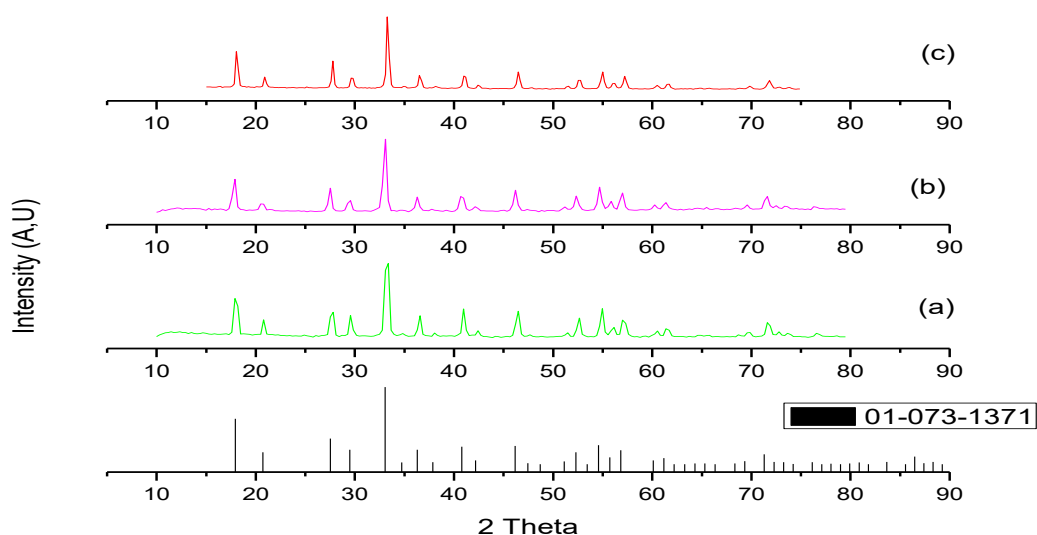


Fig.1: XRD patterns of $(\text{Gd}_{0.7}\text{Lu}_{0.3})_3\text{Al}_5\text{O}_{12}$ calcined at , (a) 1150°C Nitrate ($_{\text{RS}}$), (b) 1150°C sulfate ($_{\text{NS}}$) and (c)1150°C sulfate ($_{\text{RS}}$)

RESULTS AND DISCUSSION

At various calcinations temperatures, XRD data indicate the pure phases of $(\text{Gd}_{0.7}\text{Lu}_{0.3})_3\text{Al}_5\text{O}_{12}$ cubic garnets synthesized by co-precipitation. The pH values are the main difference between the two processes, normal and reverse strike. The powder X-ray diffraction data of $(\text{Gd}_{0.7}\text{Lu}_{0.3})_3\text{Al}_5\text{O}_{12}$ reveals a near match with calculated patterns after Rietveld refinement. Because of the difference in crystallite size, we observed a minor shift in the lattice parameter. In order to reduce powder agglomeration, the sulfate aluminum source had a substantially lower agglomeration strength than the nitrate aluminum source [1,2].

CONCLUSION

$(\text{Gd}_{0.7}\text{Lu}_{0.3})_3\text{Al}_5\text{O}_{12}$ pure phases have been successfully synthesized used co-precipitation method. According to XRD analysis of the samples structures, the results achieved by $\text{Al}(\text{NO}_3)_3$ are better than NH_4AlSO_4 employed as an aluminum source for the preparation of GdLuAG precursor. The precipitates are completely different, when the cations are precipitated in both normal and reverse strikes processes of co precipitation method.

REFERENCES

1. Jinkai Li, Ji-Guang Li, Zhongjie Zhang, Xiaoli Wu, Shaohong Liu, Xiaodong Li, Xudong Sun, and Yoshio Sakka. « Gadolinium Aluminate Garnet ($\text{Gd}_3\text{Al}_5\text{O}_{12}$): Crystal Structure Stabilization via Lutetium Doping and Properties of the $(\text{Gd}_{1-x}\text{Lu}_x)_3\text{Al}_5\text{O}_{12}$ Solid Solutions ($x = 0-0.5$)» J. Am. Ceram. Soc., 95 [3] 931–936 (2012).
2. C.C. Chiang, M.S. Tsai, C.S. Hsiao, M.H. Hon. « Synthesis of YAG:Ce phosphor via different aluminum sources and precipitation processes » Journal of Alloys and Compounds 416 (2006) 265–269

Structure Properties of LiAl (WO₄)₂ Solid Solution

N. NAIMI*, B. REKIK, M. DERBAL

LASICOM Laboratory, Faculty of sciences, Saad Dahleb Blida1 University

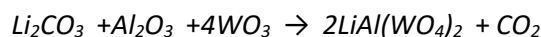
*Corresponding author

Introduction

Tungstate crystals with the general formula AB (WO₄)₂, where A=Li is the alkaline element; the B=Al is trivalent element have attracted a great attention, for their great optical properties and high performance for many applications, such as optical fibers [1], scintillator materials [2], humidity sensors [3], catalysis [4], phosphor's and laser's light, [5]. For this study we analyzed by X-ray diffraction the crystalline structures of our compounds. The use of Xpert HighScore Plus identification. Due to the large difference in ionic radius between Li and Al, the formation of the LiAl (WO₄)₂ phase is incomplete, the goal of this work is to see what is the limit of this phase to see the majority of the LiAl(WO₄)₂ phase, regarding temperature point of view, using the solid state reaction method.

Experimental

The synthesis of the compounds studied was carried out by solid-state reaction of Li₂CO₃, Al₂O₃ (Philips, 99.99%) WO₃ (Philips, 99.97%). They were weighed in stoichiometric molar proportions. Single phases were obtained through the following chemical reaction:



In this work we have studied the structural properties of LiAl(WO₄)₂. After the elaboration of powders ceramics, the phases were identified by X-ray diffraction which they were obtained with a Bragg-Brentano Bruker D8 Advance diffractometer working with the Cu K α radiation, thanks to a backward monochromator. The use of XPert High Score Plus identification software allowed us to find the most probable structure of the synthesized compound.

Results and Discussion

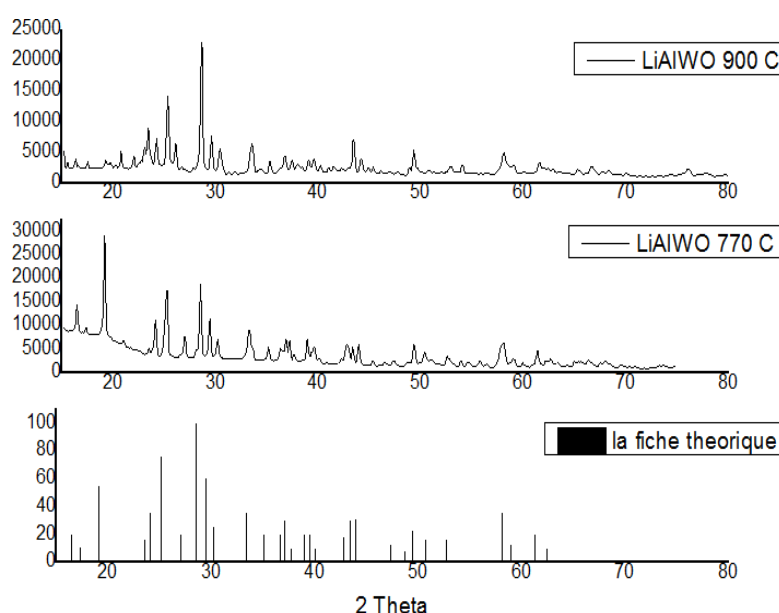


Fig.b: Powder LiAl (WO₄)₂ X Ray Diffraction at t= 770 . 900° C.



The phase identification by the High ScorPlus software makes it possible to the presence of the crystalline phase $\text{LiAl}(\text{WO}_4)_2$ as a function of heat treatment. for a thermal treatment of 770°C on a $92\% \text{LiAl}(\text{WO}_4)_2$ and the rest Li_2WO_4 .

Conclusion

materials of alkaline Li element and trivalent element Al have become compound actively studied for their remarkable optical properties.

References

- [1] A.M. Kaczmarek, R. Van Deun, Chem. Soc. Rev. 42 (2013) 8835e8848.
- [2] S. Dutta, S. Som, J. Priya, S. Sharma, Solid State Sci. 18 (2013) 114e122.
- [3] L. You, Y. Cao, Y. Sun, P. Sun, T. Zhang, Y. Du, G. Lu, Sensor. Actuator. B Chem.161 (2012) 799e804
- [4] B. Karami, S. Khodabakhshi, Z. Haghighijou, Chem. Pap. 66 (2012) 684e690.
- [5] V. Petrov, M.C. Pujol, X. Mateos, O. Silvestre, S. Rivier, M. Aguil_o, R.M. Sol_e,J. Liu, U. Griebner, F. Díaz, Laser Photon. Rev. 1 (2007) 179e212

The Influence of Preparation Parameters on Structural and Optical Properties of n-Type Porous Silicon

Kawther M'HAMMEDI^{1,2*}, Noureddine GABOUZE¹

¹ Couches Minces, Surfaces et Interfaces' Division – Centre de Recherche en Technologie des Semi-conducteurs pour l'Energétique (CRTSE), 02 Bd. Frantz Fanon, B.P. 140, Alger 7-merveilles, Algiers, Algeria

² Laboratoire surfaces, *Interfaces et couches minces*, Faculté des Sciences, Département de Physique, Université Blida 1

*Corresponding author

Introduction

The interest in macroporous silicon has increased greatly over the two last decades mainly due to its several potential applications as capacitors [1], membrane (pump of particles) [2], solar cell [3], Metallic barcodes [4]. etc. Macroporous silicon (MPS) can be fabricated with straight pores and smooth pore walls by using back side illumination of n-type Si which is widely used in macropore formation on n-type silicon (n-Si) by photoelectrochemical anodization in aqueous HF containing electrolytes. Anodic oxidation of silicon is connected with the consumption [5] of holes at the surface. Holes can be generated by illumination. However few results are available on macropores formed under front-side illumination. In this work, we describe the formation of macroporous silicon (MPS) formed on n-type Si (100) substrates at a constant current density under front side illumination using two electrolytes. The first electrolyte consisted on HF/Ethanol used to prepare porous samples for 30min. The second electrolyte containing HF/Ethanol/H₂O₂ was used to prepare porous samples substrates for different etching time 10, 20 and 30 min.

Experimental Study

Macroporous silicon samples were obtained from n-type silicon (100) and resistivity (1-10 Ω.cm). The macroporous silicon samples were etched via electrochemical etching process in a Teflon cell using two electrolytes. The first electrolyte was composed to a mixture of HF/Ethanol to prepare porous samples for 30min. The second electrolyte was composed of HF/Ethanol/H₂O₂ used to prepare macroporous Si for different etching times (10, 20 and 30 min) at a constant current density under front side illumination so that to create more electron-hole pairs on the surface. After the etching process, macroporous samples were rinsed with ethanol and dried by nitrogen.

Results and Discussion

Effect of electrolyte

The SEM surface images of Si etched in HF/Ethanol/H₂O₂ (sample b), top view after etching under front side illumination for 30 min, shows that the pores size is larger than the sample etched without H₂O₂.

Effect of etching time

The results indicated that the pore density and the pore size of the macroporous silicon samples increased with the etching time. The infrared absorption spectrum (FTIR) has been carried out to verify that the freshly prepared MPS contains Si-H bonds. Finally, we found that the oxidant agent give a new



type of the macropores morphology, of which the shape of pores changes with the increases of etching time.

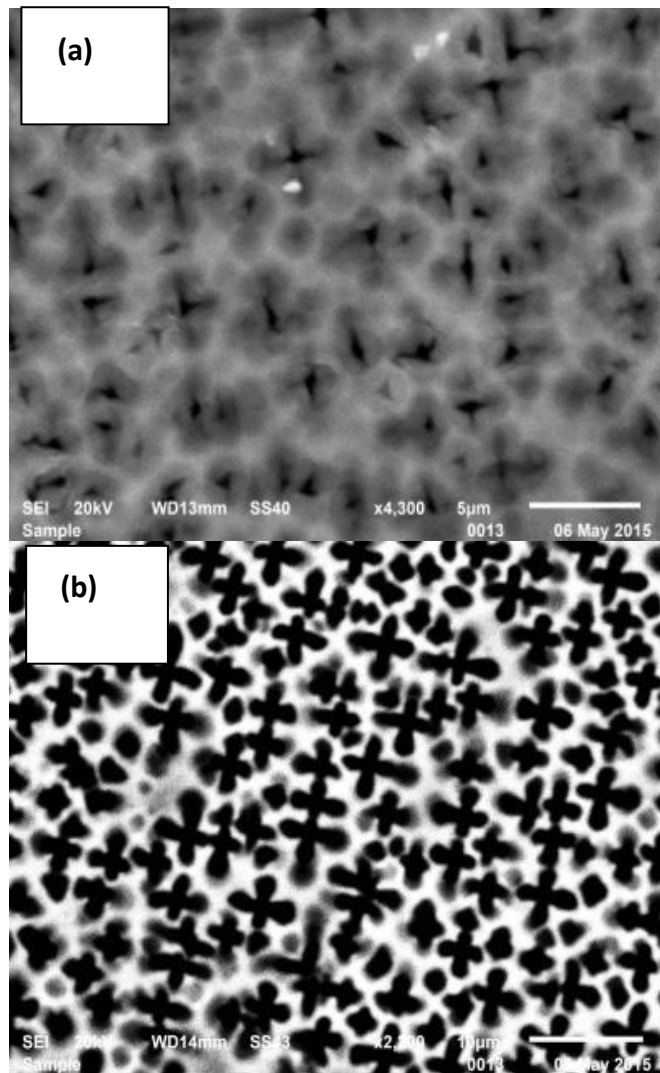


Fig.1: SEM images for MPS with etching time of 30 min for different samples (a) without H₂O₂ (b) with H₂O₂.

Conclusion

This work was focused on the macropores formation in n-Si (100) using front-side illumination using two electrolytes the first without H₂O₂ and the second containing an oxidizing agent H₂O₂. It is found that the oxidant agent give a new type of the macropores morphology, of which the shape and the size of pores change with the increases of etching time.

References

- [1] Lehmann, V. Journal of the Electrochemical Society, 146 (8) 2968-2975 (1999)
- [2] Kettner et al. Phy. Stat. Sol (a) 182, 585 (2000)
- [3] Lipinski et al. Phy. stat. sol. (a) 197, No. 2, 512–517(2003)
- [4] Nicewarner-Pena et al. Submicrometer Metallic Barcodes. Science, 294(5540), 137–141(2001).
- [5] A. Cojocaru et al. Phy, Status Solidi C6, No. 7, 1571-1574 (2009)

Study the Structural Properties of WO₃:Fe Thin Films Elaborated by Spray Pyrolysis Technique at 450 °C

Elaid OUADAH¹, Nasr-Eddine HAMDADOU² and Abdelkader AMMARI^{3*}

¹Laboratory of Micro and Nanophysics (LaMiN), National Polytechnic School of Oran (ENPO) Maurice AUDIN, BP 1523

²Oran, Algeria Laboratory of Micro and Nanophysics (LaMiN), National Polytechnic School of Oran (ENPO) Maurice AUDIN, BP Algeria

³Department of Physics, Faculty of Material Science, Ibn-Khaldoun University, Tiaret, Algeria

*Corresponding author

ABSTRACT

In this work, we have deposited Fe-doped WO₃ thin films using the reactive chemical spray in liquid phase technique (spray pyrolysis) from an aqueous solution based on ammonium tungstate (NH₄)₁₀H₂(W₂O₇)₆ at a concentration of 0.005M on glass substrates heated to a fixed temperature of 350°C. The obtained thin films were heat-treated at 450 °C for 4 hours. Our objective is to study the influence of doping on the morphological and structural properties of these films. The latter have been analyzed by the Dektak XT profilometer and the grazing incidence X-ray diffraction (GIXRD) respectively. Dektak XT analysis revealed that the WO₃:Fe thin film thickness varies between 2362 nm at 3123 nm and increasing in doping can improve the quality of the surface. The XRD analysis shows that the WO₃:Fe thin films obtained by annealing at 450 °C for 4 hours are of polycrystalline nature with monoclinic structures, identified using the JCPDS (Joint Committee of Powder Diffraction Standards) sheet No. 431035. The average grain size was 271 nm, 97 nm and 170 nm for a doping concentration of 1%, 3% and 5%, respectively.

Keywords: WO₃ Thin films, Pyrolysis Spray, heat treatment, Dektak XT profilometer, GIXRD.



Calculation of the Structural Properties of GdBO_3 by the Theoretical Method *ab-initio*

Leghigane Billel¹, Guerbous Lakhthar², Taibeche Mohammed,³ and Diaf Madjid^{4*}

^{1,4}Department of Physics, University Badji Mokhtar of Annaba, Algeria

^{2,3}Department of electronic and photonic spectroscopy, Algiers nuclear research center, Algeria

*Corresponding author

Introduction

Actually, the industry demand is still very important in this field of advanced innovative materials due to their potential applications in many luminescent devices. Until now, rare earth ions doped inorganic luminescent nanomaterials with controllable, very clear morphologies has been an important challenge of modern materials physics and chemistry. Actually, it is well established that the properties of such luminescent nano-crystals depend on their structure, phase, shape, dimensionality, and size distribution in addition to their chemical composition, the luminescence quenching due to these defects will be significant. Borate of gadolinium (GdBO_3) is an important class of host materials because of their high vacuum ultra-violet (VUV) transparency and exceptional optical damage thresholds. These properties make them good candidates for scintillators, flat displays and mercury-free fluorescent tubes. Primarily, the GdBO_3 and YBO_3 orthoborates are isostructural. They own a " YBO_3 " type structure derived from the vaterite structure

Theoretical Study

In this work we will calculate the structural properties of GdBO_3 after the system relaxation and the optimization of some parameters such as cut-off energy and the volume of the elementary cell which corresponds to the most basic energy by method *ab-initio*.

Results and Discussion

Details of structure and calculation of GdBO_3

Pure GdBO_3 crystal crystallizes in the vaterite (Hexagonal structure) space group $p63/mmc$ [1], No 194. In the hexagonal mesh, trivalent rare earth cations (TR^{3+}) occupy two sites different crystallographic. The first is an octahedral site and the second is coordination twelve.

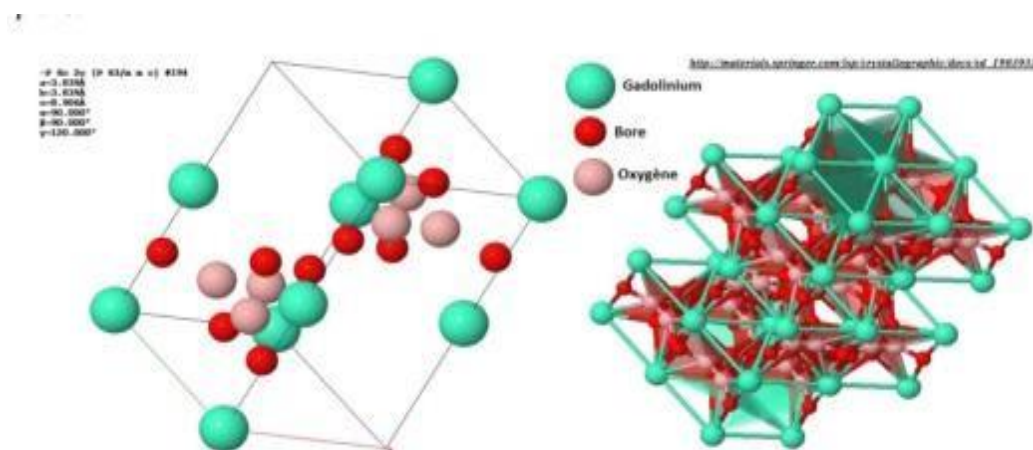


Fig 1 : the structure of GdBO_3

The constant anion model of the GdBO₃ structure was firstly considered, GdBO₃ has a Hexagonal structure space group p63/mmc, lattice constants $a = b = 3.83 \text{ \AA}$, $c = 8.90 \text{ \AA}$, and crystal plane angles $\alpha = \beta = 90^\circ, \gamma = 120^\circ$ [2]. As shown in Fig. 1

Relaxation structure

Optimization of Cutt-of energy and volume

After determining the number of points k , we set the latter to the value of $2 \times 2 \times 2$ and we vary the breaking energy between 300 and 700 eV, for each of these values, the total energy is calculated and the curve (Figure III.6) of variation of the total energy according to the E_{cut} values. This curve shows us that the energy total converges within the limits of 450 eV. (Fig 2)

We have optimized and relaxed the structure of Y₂O₃, seeking to minimize energy and canceled out the Hellmann-Feynman forces [3], which act on atoms, we calculated the mesh parameter of the equilibrium state then the modulus of compression, which gives the lowest total energy value (the state fundamental). The mesh parameter values are varied from -10% to 10% of the value of experimental lattice parameter

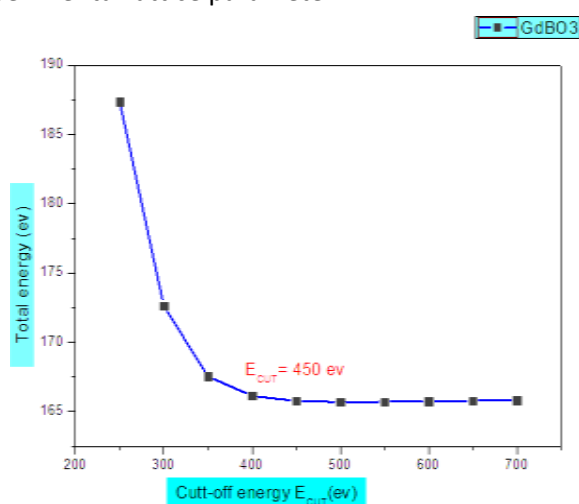


Fig 2 : Optimization of Cutt-of energy

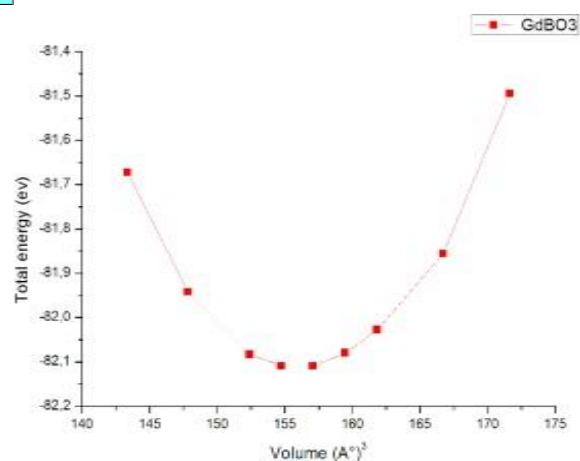


Fig 3 : Optimization of volume

Conclusion

In all cases the calculation of the optimized structure and properties were performed until the above given convergence limits were reached the obtained results are discussed in this work

Acknowledgments

I thank all the researchers at the Nuclear Research Center who contributed to the achievement of this work.

References

- [1] Y.C. Wu, S. Parola, O. Marty, M. Villanueva-Ibanez, J. Mugnier, *Optics Mater*, 27, 471–1479 (2005)
- [2] Y. Lv, W. Zhang, H. Liu, Y. Sang, H. Qin, J. Tan, L. Tong, *Techno*, 217, 140–147 (2012)
- [3] P. Dorenbos, *Journal of Luminescence*. 91, 155 (2000)

Computational Determination of the Magneto-electronic Properties of $Ce_{1-x}Cu_xO_2$ ($x=12.5\%$): Emerging Materials for Spintronic Devices

Aicha.BOUHLALA*, Sabah CHETTIBI

Laboratoire de Physique des Matériaux, Université 8mai 1945, Guelma, Algérie

*Corresponding author

Introduction

Ceria (CeO_2) is used in a wide range of applications, it has many interesting physical properties like its high oxygen storage capability; consequently, this material has a wide range of applications covering catalytic industry, superconductivity and solid oxide fuel cells [1,2]. It is a promising component in catalytic converters to reduce harmful emissions from automobile exhausts [3]. In the present work, we investigated the structural, electronic and magnetic properties of copper-doped CeO_2 . The Cu transition metal is used as a dopant agent to persuade spin polarization in CeO_2 compound.

Simulation Methodology

Doping CeO_2 with transition metals is an effective way of tuning its properties. In the present work we have performed self-consistent ab-initio calculation using the full-potential linearized augmented plane-wave method (FP-LAPW), based on the density functional theory (DFT) as implemented in the Wien2k simulation code [4] to study the structural, electronic and magnetic properties of the compound $Ce_{1-x}Cu_xO_2$ ($x=12.5\%$) fluorite type oxide and to explore the effects of dopant Cu in ceria. The exchange correlation potential has been treated using the Perdew-Burke-Eenzerhof revised of solid (PBEsol).

Results and Discussion

In structural properties, the equilibrium lattice constant is observed for the compound, which exist within the value of 5.382 \AA . To calculate the electronic nature of this compound, the band configuration of $Ce_{1-x}Cu_xO_2$ ($x=12.5\%$) for both spin-up and spin-down configuration are simulated, and elucidates the semiconductor nature of material. It has indirect band gap for both spin channels as represented in figure 1 with the compound was observed to have a narrow band gap on the spin-down configuration (0.162 eV) and band gap on the spin-up (2.067 eV). Hence, the doped atom Cu play a vital role in increasing the magnetic moments of the super cell and the value of the total magnetic moment is found to be $2.99438 \mu_B$.



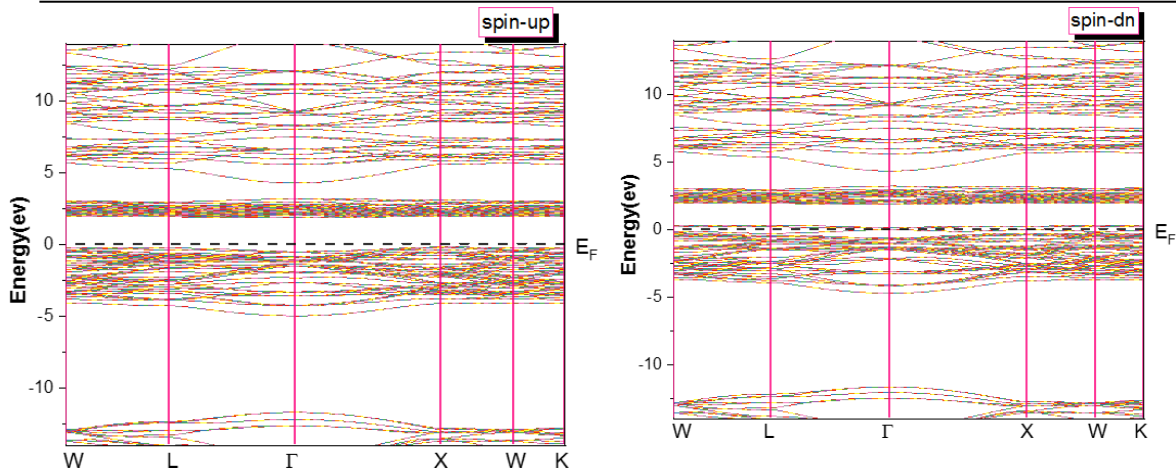


Fig. 1. Spin-polarized energy band plots of Cu-doped CeO₂.

Conclusion

Structural, electronic and magnetic properties of Ce_{1-x}Cu_xO₂ (x=12.5%) examined by using the Wien2K code via DFT computations. Cu doping in CeO₂ has confirmed the semiconductor ferromagnetism. The predicted results propose the compound could be a good candidate for spintronic applications.

References

- [1] H Inaba, H Tagawa «Ceria-based solid electrolytes». Solid State Ion. 83 (1996).
- [2] M.S. Dresselhaus, I.L. Thomas. «Alternative energy technologies». Nature 414 (2001) 332.
- [3] Y. Al-Douri, M. Gharaibeh, B.A. Albiss, A.H. Reshak. «Investigated stiffness of high performance superconductivity with nanoceria incorporated into polycrystalline magnesium diboride». Micro Nano Lett. 7(2012) 867.
- [4] P. Blaha, K. Schwarz, G.K.H. Madsen, D. Kvasnicka, J. Luitz, WIEN2k: an Augmented Plane Wave Local Orbitals Program for Calculating Crystal Properties, Karlheinz Schwarz/Techn. Universität Wien, Austria, 2001.

Po30

First-Principles Calculations of Structural, Elastic, and Electronic Properties of Antiperovskites Ca_3SiO and Ca_3GeO

Fatiha SAADAOU^{*}, Mostefa ZEMOULI, Fatima-Zohra DRISS-KHODJA, Tayeb DJAAFRI,
Mohammed DRISS-KHODJA

Laboratoire d'Etudes Physico-Chimiques, Université de Saïda, 20000 Saïda, Algérie

^{*}Corresponding author

ABSTRACT

In this work, we investigated the structural, elastic, and electronic properties of antiperovskites Ca_3SiO and Ca_3GeO , with the full-potential linearized augmented plane wave (FP-LAPW) method. To treat the exchange- correlation potential, we used the local density approximation (LDA) as well as the GGA-PBE and GGA-PBEsol schemes of the generalized gradient approximation (GGA). We employed the Tran-Blaha modified Becke-Johnson generalized gradient approximation (GGA-PBE-mBJ) to perform the calculations of the electronic properties.

Introduction

Antiperovskites M_3XY (M = metal; X =metalloid; Y = B, C, N, O) attracted a great attention of researchers due to their interesting properties such as superconductivity, giant magnetoresistance, metal-insulator transition, and magnetism¹⁻⁵. Antiperovskites show an inverted occupation of cationic and anionic sites, compared to perovskite materials. Antiperovskites Ca_3SiO and Ca_3GeO crystallize in the cubic $Pm\bar{3}m$ space group (#221). Si or Ge atoms occupy the corners of the unit cell, O lies at the body center, while Ca atoms are located at the face centers of the unit cell.

Theoretical Study

The structural, elastic, and electronic properties of Ca_3SiO , and Ca_3GeO were investigated with FP-LAPW method by using Wien2k package. The cutoff energy, which defines the separation of valence and core states, was chosen as -6 Ry. The Muffin-tin sphere radii were selected as 2.07 a.u. for Ca and O atoms and 2.5 a.u. for Si and Ge atoms. The convergence of the basis set was controlled by a cutoff parameter $R_{\text{mt}} * K_{\text{max}} = 8$.

Results and Discussion

The lattice parameters obtained with the GGA-PBE approximation are in good agreement with experimental data⁶. By using the GGA-PBE approximation, we investigated the elastic properties of Ca_3SiO and Ca_3GeO . We found that both materials are mechanically stable, elastically anisotropic, and brittle. Calculated Cauchy pressure is negative which indicates that the directional bonding is predominant in Ca_3SiO and Ca_3GeO . This tendency is confirmed by our calculations of electronic properties which show that Ca_3SiO and Ca_3GeO are narrow-gap semiconductors. Both materials have direct $\Gamma-\Gamma$ gap, equal to 0.15 and 0.22 eV, respectively.



Conclusion

The investigation of structural, elastic, and electronic properties of Ca_3SiO and Ca_3GeO show that these antiperovskite materials are narrow-gap semiconductors, mechanically stable, elastically anisotropic, and brittle.

Acknowledgments

We thank the DGRSDT (Directorate-General of Scientific Research and Technological Development - Algeria) for its support.

References

1. Joshi D.A, Kumar N, Thamizhavel A, Dhar S.K. Phys. Rev. B 2009;80:224404.
2. Shein I.R, Bannikov V.V, Ivanovski A.L. Physica C 2008;468:1.
3. Mattesini M, Magnuson M, Tasnádi F, Höglund C, Abrikosov I.A, Hultman L. Phys. Rev. B 2009;79:125122.
4. Magnuson M, Mattesini M, Höglund C, Abrikosov I.A, Birch J, Hultman L. Phys. Rev. B 2008;78: 235102.
5. Mikhailushkin A.S, Höglund C, Birch J, Czigány Zs, Hultman L, Simak S.I, Alling B, Tasnádi F, Abrikosov I.A. Phys. Rev. B. 2009;79:134107.
6. Nuss J, Mühle C, Hayama K, Abdolazimi V, Takagi H. Acta Crystallogr. B 2015;71:300-312.

Po31

Hyperfine Structures ab-initio Calculations of the $2p^4(^3P)3d^{2S+1}L_J$ States in the Fluorine Atom

Fatima Zahra Boualili^{1*}, Messaoud Nemouchi¹, Michel Godefroid², and Per Jönsson³

¹Laboratoire d'Électronique Quantique, Faculté de Physique, USTHB, BP32, El-Alia, Algiers, Algeria

²Spectroscopy, Quantum Chemistry and Atmospheric Remote Sensing (SQUARES), CP160/09, Université libre de Bruxelles, 1050 Brussels, Belgium

³Department of Materials Science and Applied Mathematics, Malmö University, SE-20506 Malmö, Sweden

*Corresponding author

ABSTRACT

In previous work devoted to ab initio calculations of hyperfine structure constants in nitrogen and fluorine atoms, we observed sizeable relativistic effects, a priori unexpected for such light systems, that can even largely dominate over electron correlation. We observed that the atomic wave functions calculated in the Breit-Pauli approximation describe adequately the relevant atomic levels and hyperfine structures, even in cases for which a small relativistic LS-term mixing becomes crucial. In the present work we identify new levels belonging to the spectroscopic terms $2p^4(^3P)3d^{2,4}(P; D; F)$ of the fluorine atom, for which correlation effects on the hyperfine structures are small, but relativistic LS-term admixtures are decisive to correctly reproduce the experimental values. The Breit-Pauli analysis of the hyperfine matrix elements nails cases with large cancellation, either between LS pairs for individual hyperfine operators, or between the orbital and the spin-dipole contributions. Multiconfiguration Dirac-Hartree-Fock calculations are performed to support the Breit-Pauli analysis.

Introduction

In previous work [1,2] devoted to ab-initio calculations of hyperfine constants of certain states of nitrogen and fluorine atoms, the authors concluded that there were anomalously large effects of relativity on the hyperfine interaction. In the present work, we have taken the opportunity of new experimental measurements [3] of hyperfine constants in the fluorine atom to study the influence of relativistic effects. The states concerned by this study are all the states of the $2p^4(^3P)3d$ configuration.

Theoretical Study

We used three methods to evaluate relativistic effects. The nonrelativistic multiconfigurational Hartree-Fock (MCHF) approach combined with the Breit-Pauli (BP) approximation to introduce relativistic effects. The second approach, purely relativistic, is the Dirac Hartree-Fock multiconfigurational method (MCDHF) combined with a relativistic configuration interaction (RCI) calculation. The third approach is the Pauli approximation (RCI-P) which is the non-relativistic limit of the Dirac theory.

Results and Discussion

In this table we reports only the case of the hyperfine structure constants (in MHz) of $2p^4(^3P)3d^4D$



for the Actif space [9f] calculated with (SD)-MR-MCHF by using the simultaneous optimization strategy, (SD)-MR-BP and (SD)-MR-RCI-P methods. These values are compared with fully relativistic results calculated with the (SD)-MCDHF-RCI method, and with observation. We notice the large differences between the nonrelativistic and Breit-Pauli results are most likely due to the strong relativistic interaction between the terms, and the good agreement between the Breit-Pauli and the other relativistic results.

J	1/2	3/2	5/2	7/2
MCHF	3472	1453	813	190
BP	4646	2262	1461	852
RCI-P	4640	2258	1458	850
MCDHF-RCI	4608	2257	1463	855
Exp[3]	4541±50	2290±50	1481±20	793 ± 20

Conclusion

In this work, we present the results of elaborate ab initio variational calculations of hyperfine constants for 17 levels in fluorine, all arising from the 6 terms $2p^4(^3P)3d^4D$, 2D , 4F , 2F , 4P and 2P . The global theory-observation agreement is very good.

Acknowledgments

F.Z.B. and M.N. acknowledge financial support from the Direction Générale de la Recherche Scientifique et du Développement Technologique (DGRSDT) of Algeria. M.G. acknowledges support from the FWO & FNR Excellence of Science Programme (EOS-O022818F). P.J. acknowledges support from the Swedish research

References

- [1]-N. Aourir, M. Nemouchi, M. Godefroid and P. Jönsson, Phys. Rev. A 97 032506-10. (2018)
- [2]-T. Carette, M. Nemouchi, J. Li and M. Godefroid, Phys. Rev. A 88 042501-9. (2013)
- [3]-X. Huo, L. Deng, L. Windholz, X. Mu, H. Wang, J. Quant. Spectrosc. Radiat. Transf. 205 1-6 (2018).

Po32

Synthesis of Zeolites from Pure and Natural Products, Modification and Application in Wastewater Treatment

Ikram Yssaad*, Fatiha Hamidi

¹Laboratory of Functional and Nano-structured Eco-materials (LEMFN), Department of Chemistry, Faculty of Sciences, University of Science and Technology of Oran Mohamed Boudiaf USTO-MB, B.P.1505 Elmenaouar, Oran, Algeria

*Corresponding author

ABSTRACT

Introduction

Zeolites are microporous solids with a structure based on a rigid anionic framework with channels and cavities of well defined dimensions. They are perfectly crystallized aluminosilicates of general formula $M_2/nO, Al_2O_3, zSiO_2$ where n is the valence of the cation M^1 . Their structure is based on a three-dimensional arrangement of TO_4 tetrahedra (SiO_4 or AlO_4^-) linked by oxygen atoms to form subunits and then large networks of identical blocks (the elementary meshes). The microporous structure of zeolites gives them properties that allow them to find applications in adsorption as well as in catalysis². Our choice is the mordenite type zeolite which presents remarkable properties, thanks to a microporous structure with large pores allowing the conversion of organic molecules and a great thermal stability in acidic media and at high temperatures. In our work, we have studied the synthesis and characterization of mordenite by proceeding to variations of the synthesis conditions and to the optimization of the preparation methods of this zeolite in order to obtain solids with the properties sought for catalytic applications.

Experimental/Theoretical Study

In this work, we examined the effect of temperature and curing time of the reaction mixture on the properties of the synthesized mordenites. The synthesis method we employed is based on the hydrothermal crystallization of a sodium aluminosilicate gel of stoichiometric composition: $5.8 Na_2O: Al_2O_3: 30 SiO_2: 780 H_2O$, prepared from aluminum and silicon sources: sodium aluminate (Riedel de Haën) and aerosil silica (Dégussa). Crystallization of the synthesis gels was performed at 160 °C and 170 °C, under autogenous pressure. The synthesized materials were characterized by X-ray diffraction, infrared spectroscopy, scanning electron microscopy and volumetric nitrogen adsorption analysis.

Results and Discussion

The experimental results showed that the sample obtained at 160 °C after 96 hours of crystallization corresponds to a pure and well-crystallized mordenite and that the crystallization time of the sample synthesized at 170 °C is 48 hours. The X-ray diffraction spectra of these solids reveal intense peaks that correspond entirely to those of a mordenite-type zeolite.



Conclusion

The increase in temperature favors the crystallization of mordenite but leads to the formation of undesirable phases. The results obtained also showed that gel ripening before hydrothermal treatment improves the selectivity of the mordenite synthesis.

Acknowledgment

I want to thank all my colleagues who helped me, even modestly, to accomplish this work.

References

1. Guisne.M, and Ribeiro.F. « Les zéolithes, un nanomonde au service de la catalyse ».France
2. Hamidi.F, Bengueddach.A, Di Renzo.F, Fajula.F. « Control of size and morphology of mordenite, catalysis Letters, Vol.87,3-4 (2003) 149-152.»

Po33

Characterization (FT-Raman, FT-IR Spectra) of 3.5-Dimethoxybenzaldehyde C₉H₁₀O₃ and Compared with Density Functional Theory (DFT)

Bouraoui Hazem^{1,2*}, Benmilat Ahmed¹, Benouatas Assia¹, Boudjada Ali¹

¹Laboratoire de Cristallographie, Université Mentouri, Constantine, Algérie

²Univ. Ouargla, Fac. des Mathématiques et Sciences de la Matière, route de Ghardaia, Ouargla 30000, Algeria

*Corresponding author

ABSTRACT

The FT-IR and FT-Raman spectra of 3.5-dimethoxybenzaldehyde C₉H₁₀O₃ molecule have been recorded in the range of 4000–400 cm⁻¹ and 3500–50 cm⁻¹ respectively. The molecular geometry and vibrational frequencies in the ground state are calculated using the DFT/B3LYP method with 6-311G++(d,p) basis sets and assuming C_s symmetry. The computed values of frequencies are scaled using a suitable scale factor to yield good coherence with the observed values.

Keywords: FT-Raman, FT-IR, DFT, 3.5-dimethoxybenzaldehyde

Introduction

This work is a part of a systematic study about the molecular conformation and the spectroscopic behavior of the methylbenzene in the solid state. One of the interests of these materials lies in the fact that they allow to study in details the influence of the molecular environment to perturb their symmetry and in particular the consequences on the spectroscopic properties.

Experimental/Theoretical Study

FT-IR SPECTROSCOPY

The FT-IR spectra (500-3500 cm⁻¹ region) were recorded on the Jasco (FT/IR-6300) spectrometer at room temperature with 4.0 cm⁻¹ resolution. Each band is characterized by its value of ν at the maximum of absorption.

RAMAN SPECTROSCOPY

The Raman spectra were made with μ -Raman Bruker Senterra in the range of 3500 to 100 cm⁻¹, equipped with a 100 mW laser source operated at $\lambda = 785$ nm, and aperture setting about 20 × 1000 μm .

QUANTUM CHEMICAL CALCULATIONS

The geometry of bromodurene was fully optimized using the DFT/B3LYP [1] method with 6-311G++(d,p), which has proven to give a very good ground state geometry.

Results and Discussion

From an overall point of view, three frequency domains can be distinguished: 16 frequency modes below 600 cm⁻¹, 34 between 600 and 1700 cm⁻¹, and 10 frequency modes above 1700 cm⁻¹. Among the 60 modes of vibration, 41 modes are active in FT-IR and Raman, 6 are active only in Raman, 10 are



active only in IR and the other 3 modes are not active. In the Raman spectrum, the extremely intense line at 991 vs cm^{-1} calculated at 1002 cm^{-1} from DFT is generated by the phenyl ring vibrations (Breathing ring). In the IR spectrum two strong bands at 1163 vs and 1200 vs cm^{-1} arise from the mixed (ip C–H) in- plane bending vibrations.

The agreement between the calculated and experimental frequencies is very good: always better than 97% for the observed skeletal vibrations. The calculations overestimate the methyl frequencies by 7%, and experiment shows only broad features for these excitations.

Conclusion

The vibrational frequencies, infrared intensities, and the Raman activities of the compound are calculated by DFT/B3LYP and compared with experimental data. The small difference between calculated and experimental wave numbers could be a consequence of the presence of vibrations of the intermolecular interactions in the crystals that were completely missing in the DFT calculation.

Acknowledgments

This work was supported by the Laboratoire de Cristallographie, Departement de Physique, Universite' Constantine1. Algeria.

References

1. A..D. Becke, J. Chem. Phys. 98 (1993) 5648.

Po34

Cathodoluminescence Calculation of AlGa_xN/GaN Quantum-Wells by Monte Carlo Model: Effect of Compositional and Temperature

Redha. Aouati^{*1,2}, A. Nouiri², H. Djaaboube¹, A. Bouabellou¹

¹Departement of physics, Laboratoire Couches Minces et Interfaces (LCMI), University Frères Mentouri
Constantine1,25000 Constantine, Algeria

²Department of Physics, Laboratoire des Matériaux et Structures des Systèmes Electromécaniques et Leurs
Fiabilités, University of Oum-El-Bouaghi, Oum-El-Bouaghi, 04000, Algeria

*Corresponding author

ABSTRACT

In this paper, a AlGa_xN/GaN multi-quantum wells (MQWs) with Al_xGa_{1-x}N barriers and GaN quantum wells have been studied using Monte Carlo calculations and cathodoluminescence (CL) technique, in this study we demonstrate the influence of important parameters such as Al mole content (x) and temperature (T) in AlGa_xN/GaN. The cathodoluminescence signal CL is calculated in AlGa_xN/GaN taking into account compositional, temperature and confinement phenomenon of electrons within the quantum well of GaN.

Keywords: Monte Carlo, Cathodoluminescence, AlGa_xN/GaN, quantum well.

INTRODUCTION

The III–V nitride materials are very important due to their wide band gap [1], in addition Monte Carlo methods are widely used for complex physical problems. This numerical method can be used to simulate electron trajectories. Cathodoluminescence is a very useful tool for the characterization of low-dimensional structures. In this paper, cathodoluminescence model of AlGa_xN/GaN multi quantum wells has been studied by Monte Carlo calculation method to describe the interaction of electron beam with Al_xGa_{1-x}N/GaN nanostructure. This model takes into account the x mole content of aluminium and temperature variation. The radiative recombination of electron-hole pairs is collected as a light (CL signal).

MODEL

The electron hole pair creation energy is given by [2]:

$$E(e-h) \approx 3Eg \quad (1)$$

Eg: Band gap energy, the step distance S is written as :

$$s = -\lambda \ln(R) \quad (2)$$

Where R is a random number between 0 and 1. The mean free path λ can be obtained from the total scattering cross section as :

$$\lambda = \frac{A}{N_A \rho \sigma} \quad (3)$$



Where A is the atomic weight (83.73 g for GaN), N_A is the Avogadro's number, ρ is the density of the material ($\rho=3.5 \text{ g/Cm}^3$). The total relativistic Rutherford scattering cross section is given by:

$$\sigma = 5.21 \times 10^{-21} \cdot \frac{Z^2}{E_e^2} \cdot \frac{4\pi}{\delta(1+\delta)} \cdot \left(\frac{E_e + m_0 c^2}{E_e + 2m_0 c^2} \right)^2 \quad (4)$$

Where Z is the atomic number of the scattering atom ($Z=19$ for GaN), E_e is the energy of electron in keV, C is the speed of light, m_0 is the mass of electron, and δ is a screening parameter.

The band gap of $\text{Al}_x\text{Ga}_{1-x}\text{N}$ has been described by [3]:

$$E_g(x, T) = E_g(x, 0) - \frac{\alpha(x) T^2}{\beta(x) + T} \quad (5)$$

The measured compositional dependence of α and β in $\text{Al}_x\text{Ga}_{1-x}\text{N}$ alloys for $0 \leq x \leq 1$ is based on experimental data,

The CL signal (I_{CL}) is given by [4]:

$$I_{CL} \propto \int_0^{\infty} \frac{\Delta n(y)}{\tau_n} \exp(-\alpha' y) dy \quad (6)$$

RESULTS AND DISCUSSIONS

The calculated CL signal of sample is presented in Fig. 1 for $\text{Al}_{0.25}\text{Ga}_{0.75}\text{N}/\text{GaN}$ at 300 K, the CL intensity presents a maximum at quantum wells regions. A good correlation between our calcul and other result [5], we can calculate the minority carrier diffusion length L_d of $\text{Al}_{0.25}\text{Ga}_{0.75}\text{N}/\text{GaN}/\text{Al}_{0.25}\text{Ga}_{0.75}\text{N}$ quantum well using $I_{QW} \sim I_{\max} \cdot \exp(-x/L_d)$ [5], CL measurements are fitted by Monte Carlo curve with L_d of 23 nm, this value is comparable to that of As et al[5] which was 20 nm.

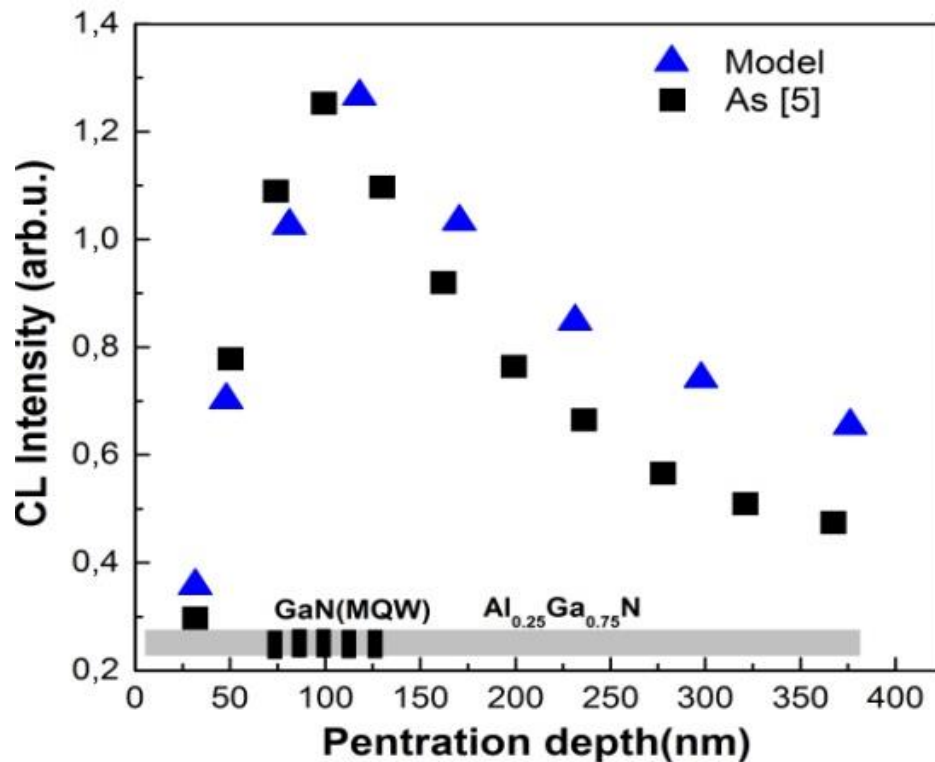


Fig. 1. Cathodoluminescence signal: comparison between our calculation model and other experimental model [5]

CONCLUSIONS

In summary, we have calculated the signal CL of $\text{Al}_x\text{Ga}_{1-x}\text{N}/\text{GaN}$ nanostructure. Cathodoluminescence spectra as a function of x mole fraction and temperature was calculated in multi-quantum wells. A comparative fitting between experimental and our simulated CL signal in the case of GaN/AlGaN sample permitted a validation of our model. The diffusion length of AlGaN/GaN/AlGaN has been calculated.

REFERENCES

1. Talele K, Samuel E. P, Patil D. S. *Optik*. 2011; 122: 626-630.
2. Alig R. C., Bloom S, *Phy. Rev. Lett.* 1975; 35: 1522-1525.
3. Nepal N, Li J, Nakarmi M. L, Lin J. Y, Jiang H. X, *Appl. Phys. Lett.* 2005; 87:242104–1-242104–3.
4. Nouri A, Chaguetmi S, Belabed N, *Surf. Interface Anal.* 2006; 38:1153 -1157.

Po35

Bloch Surface Waves Based Biosensor Using a Ternary Photonic Crystal

Ahlem Boukhenfous*¹, Malika Chikhi¹, Nadia Benseddik², Amina Louhadj¹, Fouzia Boukabrine¹

¹Laboratoire d'Étude des Matériaux et Instrumentations Optiques, Université Djillali Liabes, Sidi Bel-Abbès, BP 89
22000 Sidi-Bel-Abbès, Algeria

²Laboratoire de microélectronique appliqué, Université Djillali Liabes, Sidi Bel-Abbès, BP 89 22000 Sidi-Bel-Abbès, Algeria

*Corresponding author

ABSTRACT

We proposed a ternary photonic crystal (TPC) sustaining Bloch Surface Waves (BSWs) for biosensing. The photonic structure is three alterations of GaN/PPMA/Si. We use the Kretschmann coupling technique and p polarized incident light for Bloch surface wave excitation. The biosensor performance is simulated using the transfer matrix method (TMM).

Introduction

Bloch surface waves (BSW) are evanescent electromagnetic waves propagating on the surface of a truncated periodic one-dimensional dielectric photonic crystal (PC) [1].

Experimental/Theoretical Study

For a wavelength used is $\lambda = 633 \text{ nm}$, the refractive indices of the prism as well as the GaN and PMMA layers are respectively $n_p = 1.8449$, $n_H = 2.38475$ and $n_L = 1.4887$. The thicknesses of the layers are respectively $d_H = 66 \text{ nm}$ and $d_L = 106 \text{ nm}$

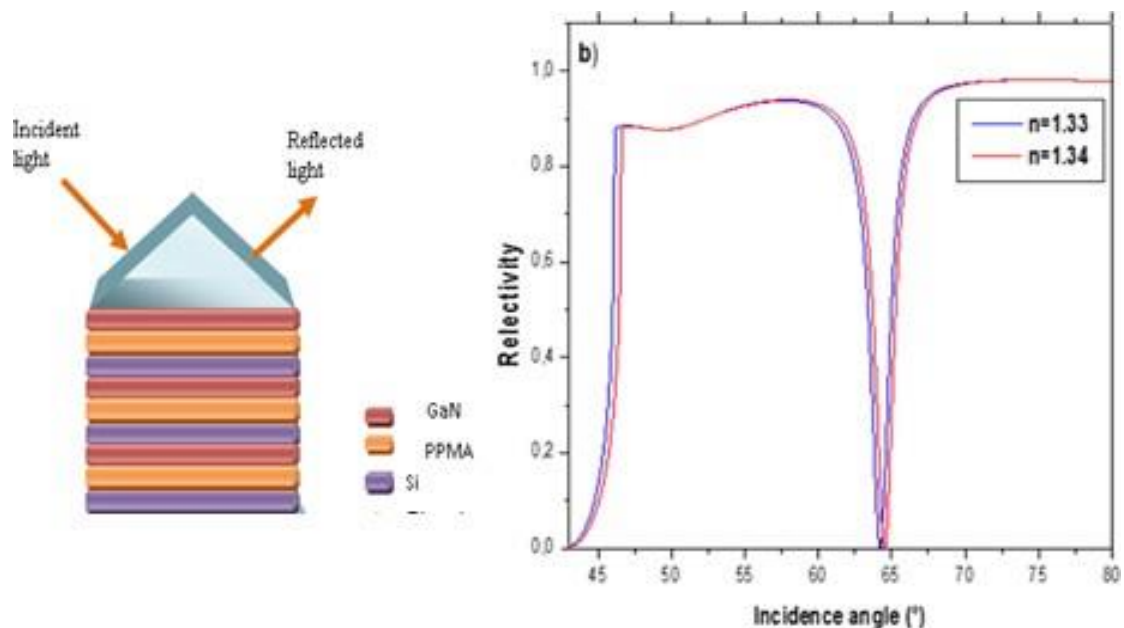


Figure 1: Angular reflectance as a function of the refractive index of the medium to be detected 1.33 (water) and 1.34. $d_{Si} = 62 \text{ nm}$

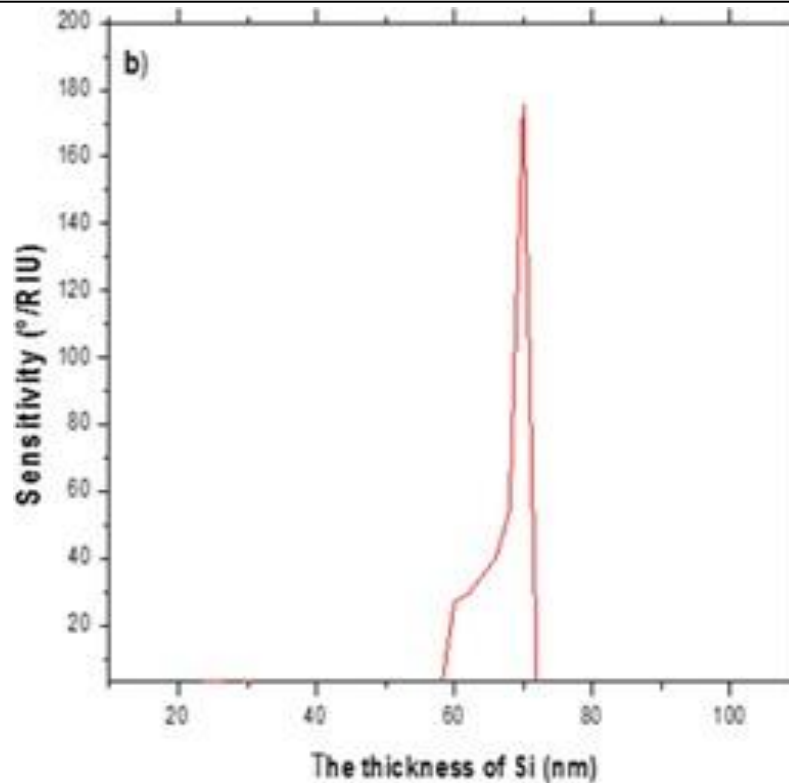


Figure 3: the variation of the sensitivity to different thicknesses of the Si layer of the structure ternary

The Ternary ePC-based biosensor are shown in Fig.1. P-polarized incident light and prism coupling in the Kretschmann configuration are used for the structure. The comparison of the performance of biosensors is carried out by the transfer matrix method (TMM) [2]

Results and Discussion

Comparison of the sensitivity of the bio detector according to the thickness of the silicon layer Si

Conclusion

Optimization of the thickness of the Si layer makes it possible to control the sensitivity of the biodetector

References

- [1] P. Yeh, A. Yariv, A.Y. Cho, Optical surface waves in periodic layered media, Appl. Phys. Lett 32 (1978) 104
- [2] X. Li, K. Xie and H. Jiang, Properties of defect modes in one –dimensional photonic crystal, Proc. SPIE, Advanced Sensor Systems and Applications, 7853 (2010).

Hyperfine Structure of the $3p^4 4s^4 p$ State of the Chlorine Atom

Amirouche TOUAT¹, Messaoud NEMOUCHI¹, Michel GODEFROID²

¹ Laboratoire d'Electronique Quantique, Faculté de Physique, USTHB, Alger, Algérie

² Service de Chimie Quantique et Photophysique, ULB, Brussel

*Corresponding author

Introduction

This work followed upon preceding work^{1, 2, 3} devoted to calculations *ab-initio* of hyperfine constants of certain atomic states of nitrogen and fluorine. The interest caused by these elements was due to experimental work of spectroscopy to very high resolution completed by the same laboratory and measuring hyperfine spectra several elements of which nitrogen, fluorine, oxygen and chlorine^{4, 5, 6, 7}. The multi-configuration nonrelativistic Hartree-Fock method combined with the approximation of Breit-Pauli⁸ to take account of the relativistic effects was used successfully in calculation of the hyperfine constants. This same method was also employed successfully in the hyperfine structural analysis of the fundamental state of chlorine⁹. We use it in this work to calculate the hyperfine structures of the excited state $3p^4 4s^4 P$ of the atom of chlorine.

Theoretical Study

We used the ATSP code to calculate the energy of hyperfine levels of our state. The wave functions associated with the state are calculated using the nonrelativistic method 'Multiconfigurationnelle Hartree-Fock' (MCHF), whereas the influence of the relativistic effects on the hyperfine structures of the state are analyzed through the approximation of Breit-Pauli (BP). We carried out several types of calculations MCHF with the purpose of highlighting the nature of the effects of correlation that describe correctly the hyperfine interaction in this atomic state of chlorine.

Results and Discussion

The results of calculations corresponding to the approaches described above are given in the table 1 and are compared with the experiment⁴. The comparison of the single-configuration Hartree-Fock computation (HF) with that of the multi-configuration Hartree-Fock (MCHF) shows the importance of the electronic correlation in the determination of the hyperfine constants. The comparison of the SR-C-MCHF and SR-C-BP approaches show that relative variations related to the relativistic effects on the magnetic constants do not exceed 2% whereas they are respectively about 12% and 5% on $A_{1/2,3/2}(^4P)$.

The effect of the electronic correlation is very remarkable on the constant $A_{1/2}(^4P)$ whereas it is not negligible on the two others constants $A_{3/2,5/2}(^4P)$. Broadly our values for these three last constants are in concord with the experiment. The most remarkable result is that of the MR2-BP calculation which is in very good agreement with the experiment.

With regard to constant B, our results show that the interaction of the electronic electric field with the nuclear quadrupole moment is insensitive with the effects of correlation and relativity.



Hyperfine constants	A _{1/2}	A _{3/2}	A _{5/2}	B _{1/2}	B _{3/2}	B _{5/2}
HF	-26.6	52.6	72.1	0.0	47.4	-59.2
SR-	31.4	74.5	284.7	0.0	50.2	-62.7
MCHF						
SR-C-	51.5	84.5	289.3	0.0	50.2	-62.8
MCHF						
MR2-	57.9	85.9	293.9	0.0	49.9	-62.4
MCHF						
MR4-	61.0	87.1	293.9	0.0	49.9	-62.4
MCHF						
MR2-BP	65.2	89,5	301.0	0.0	50,2	-64,4
Exper-	67.0 ±09	101.1 ±0.2	299.6 ±0.2	0.0	47.3 ±0.3	-62.5 ±0.5

Conclusion

In the context of nonrelativistic MCHF approach, the study of the properties in general of the atom of chlorine is complex because of the sizes, very large, of configuration spaces. This with for effect to make difficult the treatment of the correlation electronic. However, preliminary results, relating to the hyperfine constants, which we obtained are satisfactory. We think that we can improve our results within the framework of a calculation MR2-BP for the state ⁴P. The variation which still remains between these results and the experiment possibly requires to consider a calculation of the type multi-configuration Dirac-Fock (MCDf).

References

- ¹T. Carette, M. Nemouchi, P. Jönsson, and M. Godefroid, Eur. Phys. J. D 60, 231–242 (2010)
- ²P. Jönsson, M. Nemouchi, T. Carette, and M. Godefroid, J. Phys. B: At. Mol. Opt. Phys. 43 (2010) 115006 (6pp).
- ³Thomas Carette, Messaoud Nemouchi, Jiguang Li, and Michel Godefroid, Physical Review A 88, 042501 (2013).
- ⁴D.A. Tate and J.P. Walton, Phys. Rev. A 59, 1170 (1999).
- ⁵R.M. Jennerich, A.N. Keiser, and D.A. Tate, Eur. Phys. J. D 40, 81–89 (2006)
- ⁶R. M. Jennerich and D. A. Tate Physical Review A, Volume 62, 042506.
- ⁷D. A. Tate and D. N. Aturaliye, Physical Review A 56, (29 January 1997), (10pp).
- ⁸C. Froese Fischer, T. Brage, P. Jönsson, Computational Atomic Structure. An MCHF Approach,
- ⁹T. Carette and M. R. Godefroid, J. Phys. B: At. Mol. Opt. Phys. 44 (2011) 105001 (9pp) Institute of Physics Publishing, Bristol/Philadelphia, 1997.

First-principles Calculations of the Physical Properties and Stability of ScN

Asma KADRI*, Soumia BAHLOULI, Said HIADSI, Mokhtar ELCHIKH

Department of engineering physics, University of Science and Technology of Oran -USTO- Mohamed Boudiaf, Algeriaemail

*Corresponding author

Introduction

Today, the world is widely interested in studying the rare earth nitride materials due to their important physical properties. The hardness of most rare earth nitrides are usually unstable at ambient conditions [1], therefore, we employed the theoretical calculation represented by the first principle technique for discover more properties about the rare earth nitrides. The goal of the present work is using the ab initio calculation to reveal more information and details of the compound ScN stability and properties.

Theoretical Study

These calculations have been performed using the full-potential (linearized) augmented plane wave (lapw+local orbital)^{2,3} approach to the density functional theory⁴ implemented in WIEN2k code⁵, within the Generalized Gradient Approximation through Perdew-Burke-Ernzerhof(GGA-PBE), which is used for treatment the electronic exchange-correlation energy function⁶.

Results and Discussion

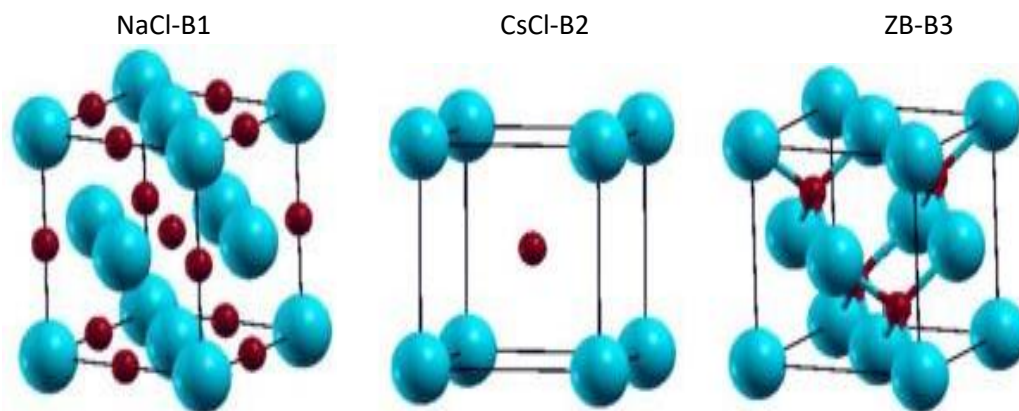


Fig.a: Unit cell of different cubic phases of rare earth nitrides ScN, the blue circles represent the Sc and red one represent the Natom.

Structural properties: The structural stability of the compound of rare earth nitride is analyzed among the three considered NaCl (B1), CsCl (B2), and ZB (B3) (figure b) and it observed that B1 structure is the most stable for the three cubic structures at the ambient conditions.

Electronic properties: It can be seen from the figure c that band gap exists for the two structures B1 and B3, for the B1 structure there two bandgap direct 2.721eV and 1.2eV at Γ and X respectively, also there is a smaller indirect Γ -X bandgap with the Fermi level, about the B2 structure we can observed the are two direct band gap 2.68 eV at X and 2.45eV at W, and no bandgap in B2 structure.

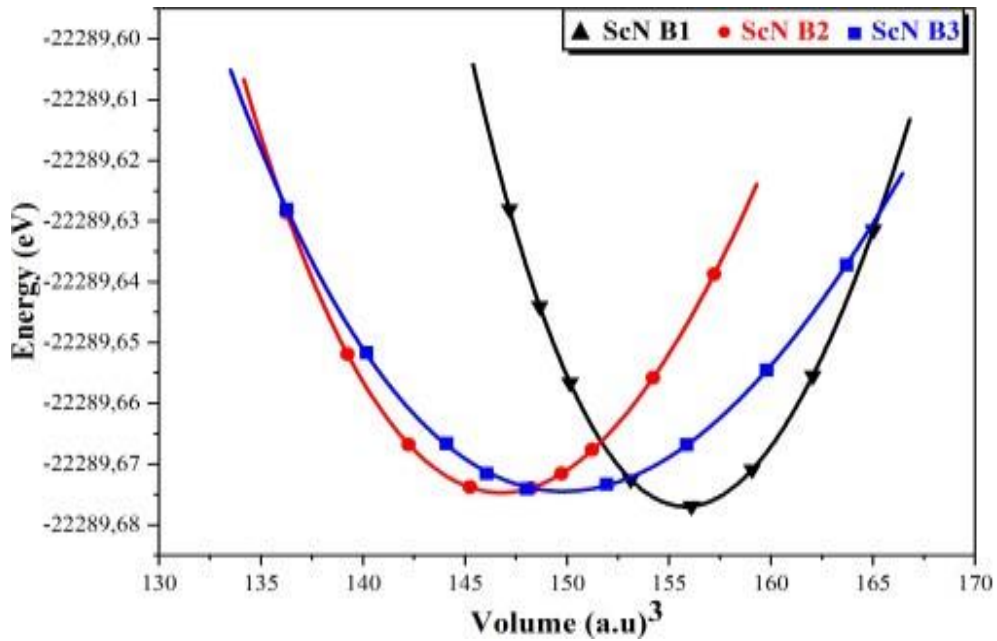


Fig.b Total energy (in eV) versus reduced volume for the three cubic phases of rare earth nitride ScN.

Table 1. Calculated lattice parameter a (Å), total energy E (eV), elastic constants C_{11} , C_{11} , C_{44} (GPa), bulk modulus B (GPa), Shear modulus B' (GPa), Young's modulus E (GPa), Poisson's ratio ν , for ScN in B1, B2 and B3 structures.

	B1	B2	B3
a (Å)	4.52	2.79	4.91
E_0 (eV)	-22289.61	-22287.51	-22288.98
C_{11}	393.59	523.4258	175.994
C_{12}	104.02	10.69	122.976
C_{44}	165.88	-118.32	95.329
B (GPa)	200.55	181.60	140.615
B' (GPa)	157.09	-126.66	54.303
E (GPa)	373.70	-495.07	151.349
ν	0.189	0.954	0.320

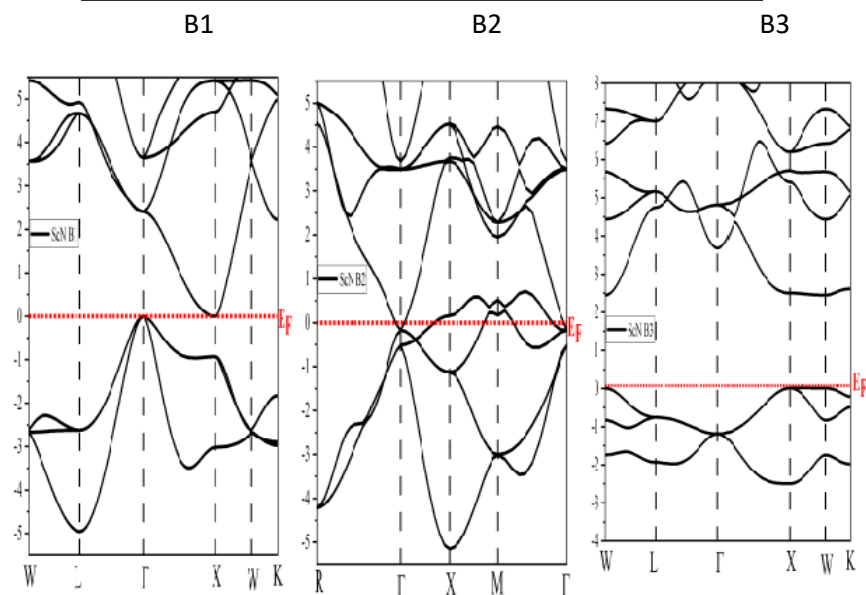


Fig.c: Electronic band structure of ScN in the NaCl(B1), CsCl (B2) and ZB (B3) cubic phases.

Conclusion

In conclusion, the structural, electronic properties of rare earth nitride ScN with three cubic possible structures are analyzed. ScN exhibit a semiconductor nature in B1 and B3 structures, and metallic behavior in B2 structure. The rare earth nitride ScN is found to be stable structurally and mechanically in NaCl (B1) structure. The calculated results are in good agreement with the available results.

References

1. J. Yang, F. Gao, H. Wang, H. Gou, X., Z. Li, *Materials Chemistry and Physics* 119 (2010) 499–504.
2. E. Sjöstedt, L. Nordström, D. J. Singh, *solid state communication* 114, 15 (2000).
3. G. K. H. Madsen, P. Blaha, K. Schwarz, E. Sjöstedt, L. Nordström, *Phys. Rev B* 64, (2001) 195134
4. W. Kohn, L. J. Sham, *Phys. Rev.* (1965)140, A1133.
5. P. Blaha, K. Schwarz, G. K.H. Madsen, D. Kvasnicka, and J. Luitz, “WIEN2k, an augmented plane wave ++ local orbitals program for calculating crystal properties,” Karlheinz Schwarz, Techn. Universität Wien, Austria, 2001, ISBN 3-9501031-1-2.
6. J. P. Perdew, K. Burke, M. Ernzerhof, *Phys. Rev. Lett.* 77, 3865.

Surface Metal Effect on I(V) Characteristics Ti/6H-SiC Schottky Diode at Room Temperature

Abderrahmane Bekaddour*, Schahrazade Tizi, Baya Zebentout, Zineb Benamara, Boudali Akkal

Laboratoire de MicroElectronique Appliqué, Faculté de Génie Electrique, Université de Sidi Bel Abbes (Algérie)

*Corresponding author

Introduction

The semiconductor industry is interested in materials that can fulfill the required conditions in the areas where silicon cannot fulfill the specifications such as for example applications in power electronics and microwave and applications in the field of photovoltaics. Thanks to its wide bandgap, good thermal conductivity and high chemical and physical stability, as well as a higher breakdown field than Si, solid silicon carbide SiC is an innovative success in components that operate at high temperatures. SiC also has interesting mechanical properties due to its hardness, its high resistance to heat^{1,2,3,4}.

Experimental/Theoretical Study

After the chemical cleaning process, the surface of SiC device was thermally oxidized. The oxide was removed at high frequency. Schottky Titanium contact was deposited till the layer formed a square contact of variable side: big, medium and small (1.6×1.6 , 0.04×0.04 , 0.16×0.04 mm²). The active layer was n-doped with $N_D = 8.8 \times 10^{15}$ cm⁻³ with a thickness of 7 μm. I(V) measurements are taken at room temperature and plotted in Fig.1. We used several mathematical models (graphical and LMS methods) to extract the electrical parameters: saturation current (I_s), ideality factor (n), series resistance (R_s) and shunt resistance (R_{sh}) which are presented in table.1.

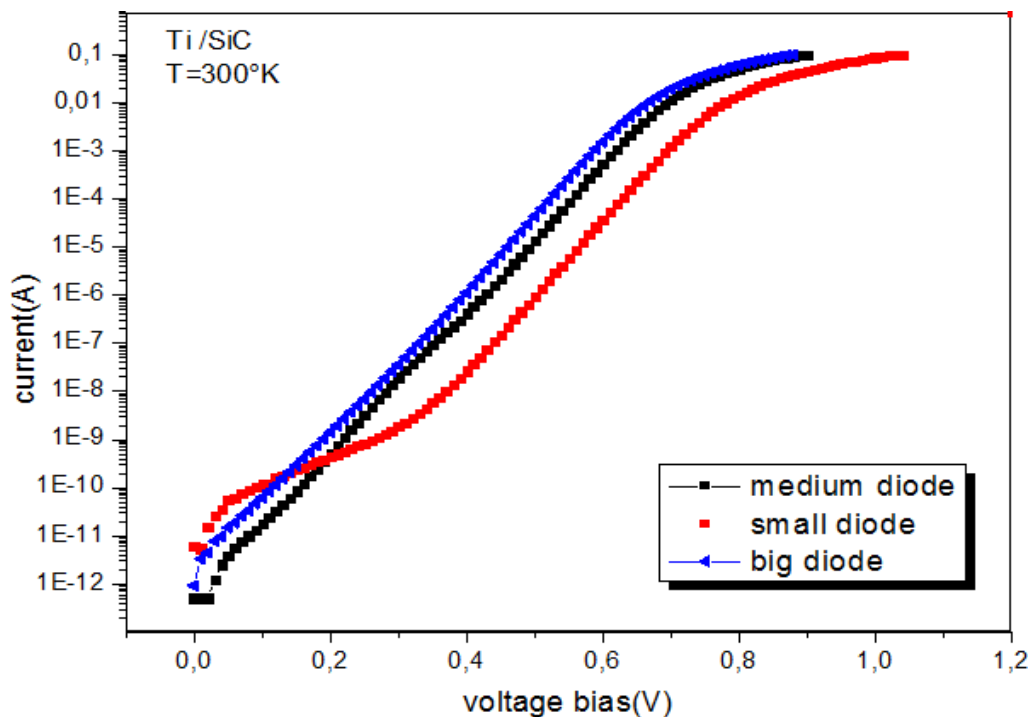


Fig.1: Experimental characteristics I (V) of Ti/SiC-6H Schottky diode.



Results and Discussion

The I(V) characteristics shows two types of diodes, big and medium diodes present a normal behavior; for the small diode, the I(V) characteristics show a double-barrier phenomenon, one high (n^H , R_s^H , I_s^H) and the other low (n^L , R_s^L , I_s^L).

Table .1: Extraction of the electrical parameters for the samples by the graphical and LMS methods.

	Parameters	Big diode	Medium diode	Small diode
Ln(I)-V	I_s^H (A)	5.60 E-13	1.38 E-13	1.54 E-14
	n^H	1.12	1.12	1.07
	R_s^H (Ω)	3	4.2	3.8
	R_{sh} (Ω)	9.5 E9	5.9 E9	4.7 E9
	I_s^L (A)	-	-	2.01 E-14
	n^L	-	-	0.69
	R_s^L (Ω)	-	-	4.3 E8
Cheung	n	1.04	1.08	1.12
	R_s (Ω)	1.51	1.61	2.03
Werner	n	1.04	1.06	1.11
	R_s (Ω)	1.58	1.67	2.05
	I_s^H (A)	5.33 E-13	1.55 E-13	2.63 E-14
	n^H	1.12	1.13	1.10
	R_s^H (Ω)	1.89	2	2.44
	R_{sh} (Ω)	2.77 E10	2.27 E10	6.63 E8
	I_s^L (A)	-	-	1.06 E-11
	n^L	-	-	1.25

Conclusion

The analysis of the I(V) characteristics at various forward voltage bias is showing a double-barrier phenomenon in the small diode. It is an inhomogeneity characterized by two independent diodes in parallel, one high and the other low. I(V) characteristics at different temperatures were used to investigate the active defects in the epitaxial layer.

References

1. A. A. Lebedev, Heterojunctions and superlattices based on silicon carbide, *Semicond. Sci. Technol.*, 21 R17 (2006), doi.org/10.1088/0268-1242/21/6/R01.
2. Tsunenobu Kimoto, Material science and device physics in SiC technology for high-voltage power devices, *Jpn. J. Appl. Phys.* 54040103(2015), doi.org/10.7567/JJAP.54.040103.
3. homogeneous barrier height for Au/n-type 6H-SiC Schottky diodes in a wide temperature range, *Superlattices and Microstructures* Volume 124, Pages 30-40, (2018), https://doi.org/10.1016/j.spmi.2018.10.004.
4. J. Weber, H. B. Weber, ja M. Krieger, On deep level transient spectroscopy of extended defects in n-type 4H-SiC, *Mater. Sci. Forum*, kd 897 MSF, lk 201–204, (2017).

Po40

Adsorption of Anticancer Drug Molecule on Single Wall Carbon Nanotube: An ab-initio Study

Lina Linda Bechohra^{1*}, Roya Majidi², Safia Kellou-Tairi¹

^{1*}Laboratoire de Physico-Chimie Théorique et Chimie Informatique, USTHB, BP 32 Bab Ezzouar, Algérie

²Department of Physics, Shahid Rajae Teacher Training University, Iran

*Corresponding author

Introduction

Curcumin is a natural compound known as a potent antioxidant, anti-tumor and anti-inflammatory agent with nontoxic side effects compared to chemotherapeutic agents [1]. However, curcumin has low bioavailability and solubility due to its hydrophobic nature. Hence Single Walled Carbon NanoTubes (SWCNTs) have been utilized experimentally as nanocarriers to overcome these issues due to their nano-hollow-tubular structure and high surface area [2]. In this work, we are interested in the theoretical insights of (n,0) zigzag SWCNTs as delivery systems in attempt to get around the curcumin biodisponibility problems. The binding energies, electronic properties, and nature of interaction were carried out using Density Functional Theory (DFT).

Theoretical Study

All simulations were done based on DFT as implemented in the OpenMX 3.8 package [3]. The exchange-correlation was described with the Perdew- Burke-Ernzerhof (PBE) within the generalized gradient approximation (GGA). The energy cutoff for the plane waves was set to 100 Ry. Along the Γ -Z direction in the Brillouin zone, 11 k-points were considered. The van der Waals interactions were included by the DFT-D2 approach proposed by Grimme. The periodic boundary conditions were applied to simulate infinitely long tubes.

Results and Discussion

Side view of curcumin @ (10,0) CNT is shown in figure 1. The binding energy value for the most stable complex is -18.93 eV. The energy band gap for isolated (10,0) CNT is 1.15 eV meanwhile the energy band gap of (10,0) CNT after functionalization with curcumin is 1.00 eV. We can notice that the energy band gap decreased with adsorption of the molecule but that doesn't affect the semiconducting behavior of the nanotube.

From the total density of state (DOS) spectra, (The Fermi level was set at 0 eV) in the presence of adsorbed molecule, an occupied state and DOS peak appears below the Fermi level.



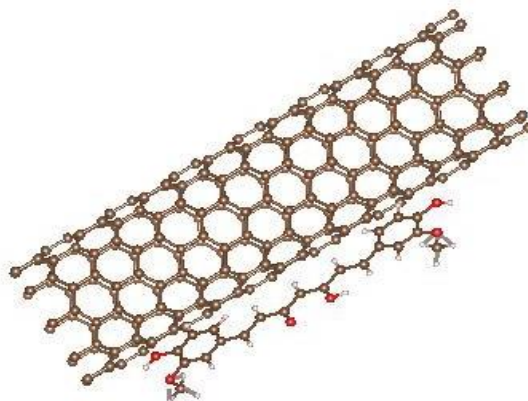


Fig1: Atomic structures of curcumin @ (10,0) CNT.

Conclusion

We can conclude that the curcumin weakly binds to the outer surface of the SWCNTs and the small interaction obtained quantitatively in terms of binding energies. However, our research is still ongoing to identify the most stable systems and to get more accuracy results when the diameter of CNTs increases.

References

1. Z. Hussain, H. E. Thu, M. W. Amjad, F. Hussain, T. A. Ahmed, S. Khan, *Mater. Sci. Eng. C*, **77** 1316 (2017).
2. S. Mahajan, A. Patharkar, K. Kuche, R. Maheshwari, P. K. Deb, K. Kalia, R. K. Tekade, *Int. J. Pharm*, **548** 540(2018).
3. T. Ozaki, H. Kino, J. Yu, M. J. Han, M. Ohfuchi, F. Ishii, et al. User's manual of OpenMX version 3.8. http://www.openmx-square.org/openmx_man3.8/openmx.html.

Po41

First Principal Study of Physical Properties of Rare Earth Based Heusler Compounds X_2RuPb ($X= Sc, Y$ and La)

Asmaa Bahlouli¹, Mokhtar Elchikh²¹Physical engineering department, University of sciences and technology of Oran, Algeria²Physical engineering, University of sciences and technology of Oran, Algeria

*Corresponding author

Introduction

Heusler compounds are a class of ternary intermetallics, including full Heusler X_2YZ with L_2 structure, Inverse Heusler with XA structure and Half Heusler XYZ with $C1b$ structure. The remarkable material class comprises a vast collection of more than 1000 compounds with interesting properties and applications in spintronics, quantum information and many other fields. In this work we study the structural, elastic and electronic properties of rare earth based Heusler compounds X_2RuPb while $X= Sc, Y$ and La .

Computational details:

In this work we perform first-principle calculation based on the full-potential linearized augmented plane wave (FP-LAPW) method within the density functional theory (DFT) implemented in the package WIEN2K [28]. The exchange and correlation potential is treated using the generalized gradient approximation (GGA) of Perdew-Burke-Ernzerhof [28].

Results

Structural properties:

To investigate the structural properties, we proceed a total energy minimization. The obtained structural properties are regrouped in tab1. The procedure shows that the three compounds are more stable in the full Heusler structure than in Inverse Heusler structure. However, the Inverse Heusler type structure still holds more interesting physical properties and the negative calculated value of the formation energy shows that the three compounds are still mechanically stable in the Inverse Heusler type structure.

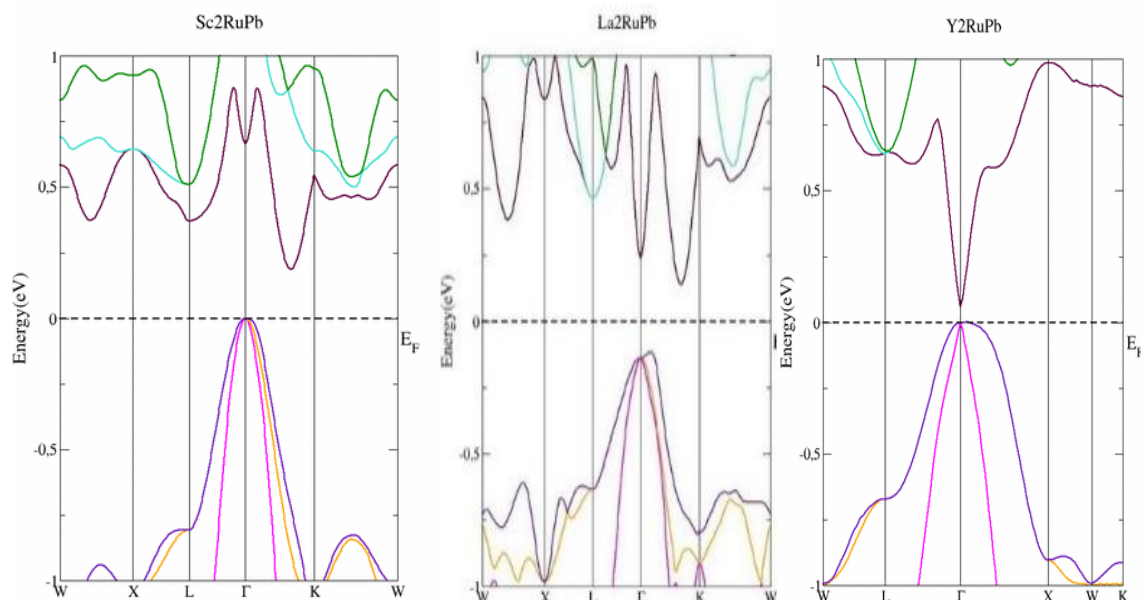
Elastic properties:

The elastic properties describe the response of a material to macroscopic applied stress. This response gives information about the elasticity matrix which is described in cubic systems by only three constants: C_{11} , C_{12} and C_{44} . We elastic constants C_{ij} , shear modulus G , Young modulus E , poisson ratio ν , Zener anisotropic factor A and Pugh ratio B/G in both structure types.

Electronic properties:

To investigate the electronic nature of our inverse Heusler compounds, we present the band structure at the theoretical equilibrium lattice constant along the high symmetry directions of the first Brillouin zone. The calculation shows that the band structure of Y_2RuPb has a direct band gap of 0.058 eV at Γ point while the band structures of Sc_2RuPb and La_2RuPb have indirect band gaps of 0.193 eV and 0.164 eV respectively which is in good agreement with previous calculations.



Fig 1: Band structure of Sc₂RuPb, Y₂RuPb and La₂RuPbTable 1: calculated lattice parameters a_0 , corresponding total energies and Bulk modulus for Sc₂RuPb, Y₂RuPb and La₂RuPb in both regular and inverse structure types.

a: [3]

b: [4]

compound		Sc ₂ RuPb		Y ₂ RuPb		La ₂ RuPb	
		Regular Heusler	Inverse Heusler	Regular Heusler	Inverse Heusler	Regular Heusler	Inverse Heusler
a_0 (Å)	Our cal.	6.8405	6.7531	7.2496	7.0871	7.6219	7.3417
	other	6.835 ^a	6.746 ^a 6.670 ^b	7.245 ^a	7.082 ^a 7.085 ^b	7.630 ^a	7.376 ^a 7.347 ^b
Total Energy (Ry)	Our cal.	-53978.045	-53978.026	-64463.975	-64463.935	-84911.727	-84911.720
	other	-53978.066 ^a	-53939.810 ^b	-64463.992 ^a	-64463.952 ^a	-84911.736 ^a	-84911.718 ^a
Bulk modulus (GPa)	Our cal.	101.96	106.74	83.393	87.461	65.422	76.003
	other	101.688 ^a	106.221 ^a	82.519 ^a	85.647 ^a	67.475 ^a	77.435 ^a

Conclusion

the study of structural and elastic properties has shown that the compounds Sc₂RuPb, Y₂RuPb and La₂RuPb stabilize in both full and inverse heusler type structures. However, the inverse heusler type is more suitable to hold interesting electronic properties. The band structure of the three compounds in inverse heusler type shows a semiconductor behavior that can be useful in thermoelectricity and radiation semiconductor detectors.

References

- [1] P. Blaha, K. Schwarz, G. Madsen, D. Kvaniscka, J. Luitz, Wien2k, An Augmented Plane Wave Plus Local Orbitals Program for Calculating Crystal Properties, Vienna University of Technology, Vienna, Austria, 2001.
- [2] J.P. Perdew, K. Burke, M. Ernzerhof, Phys. Rev. Lett. 77 (1996) 3865.
- [3] Y.Lakred, S.Bahlouli, M.Elchikh, Eur. Phys. J. B (2021) 94,135
- [4] X. Zhang, E. Liu, Z. Liu, G. Liu, G. Wu, W. Wang, Comput. Materials Sci. 70, 145(2013)

Elaboration and Characterization of Black Silicon for Photovoltaic Solar Cells

Leila Harkat^{1,2,*}, Nabil Khelifati², Ghania Fortas², Seddik-El-Hak Abaidia¹, Boudjemaa Bouaouina¹,
Faouzi Kezzoula²

¹Departement de Physique, Faculté des Sciences, Université M'hamed Bougara de Boumerdes (UMBB),
Boumerdes, Algeria

²Division DDCS, Centre de Recherche en Technologie des Semi-conducteurs pour l'Energétique (CRTSE), Algiers,
Algeria

*Corresponding author

ABSTRACT

In this work, the optical and morphological properties of black silicon (b-Si) have been investigated. The b-Si was fabricated by Metal-Assisted Chemical Etching (MACE) method. Two-step MACE process was deployed to produce b-Si nanostructures by using silver (Ag) as a catalyst. The b-Si was elaborated with and without KOH post-etching, and the samples prepared without KOH treatment exhibited the lowest average weighted reflectance (AWR) and the highest absorption, especially in violet and near infrared wavelength regions. The SEM images of samples post-etched by KOH solution show the formation of square-like nanostructures with a size varies in the range 20 - 200 nm. While the samples containing b-Si without treatment by KOH solution showed nanostructures with other shapes and different sizes.

Introduction

As a widely used semiconductor material, silicon has been extensively used in many areas, such as a photodiode, photodetector, and photovoltaic devices. However, the high surface reflectance and large bandgap of traditional bulk silicon restrict the full use of the solar spectrum, especially in photovoltaic application. To solve this problem and improve the photon absorption of this material, many methods have been developed. Among them, nanotextured silicon surface, so-called black silicon (b-Si), is an excellent path to minimize the light losses in the front of solar cells. It absorbs light very efficiently for a wide range of wavelengths, and as a result, it appears black to the naked eye. In this work, we investigated the surface morphological and the optical properties of b-Si wafers fabricated by the MACE technique by using Ag as a catalyst^{1,2}.

Experimental

The black silicon was fabricated by the Metal-Assisted Chemical Etching (MACE) technique. The two-step MACE process was deployed to produce nanostructures through silver (Ag) used as a catalyst. The MACE etching process duration has been optimized to be 60 min. After the fabrication of b-Si, some samples were treated by their immersion in KOH solution for 10 s and 50 s, and the obtained results were discussed according to the effect of KOH and the immersion time. The samples characterization was carried out by high resolution Scanning Electron Microscope (SEM) as well as by UV-Vis Spectrophotometer.



Results and Discussion

Fig.1 illustrates an example of the findings. It shows that b-Si without KOH treatment exhibits nanostructures with the lowest reflectance especially in violet and near infrared regions, with an average weighted reflectance(AWR) of 8.32%. The use of KOH increases AWR value to 8.98% and 10.97% when the immersion time is 10 s and 50 s, respectively. The improved light absorption for the samples prepared without KOH treatment can be explained by the refractive index gradient yields from the changing of material density in nanometric scale. On the contrary, the samples treated by KOH solution demonstrated the creation of square-like holes as shown in the right inset of Fig.1 (i.e. MEB image). The size of these holes varies between 20.5 nm and 208 nm, and their light absorption is less efficient than that associated to the samples without KOH treatment.

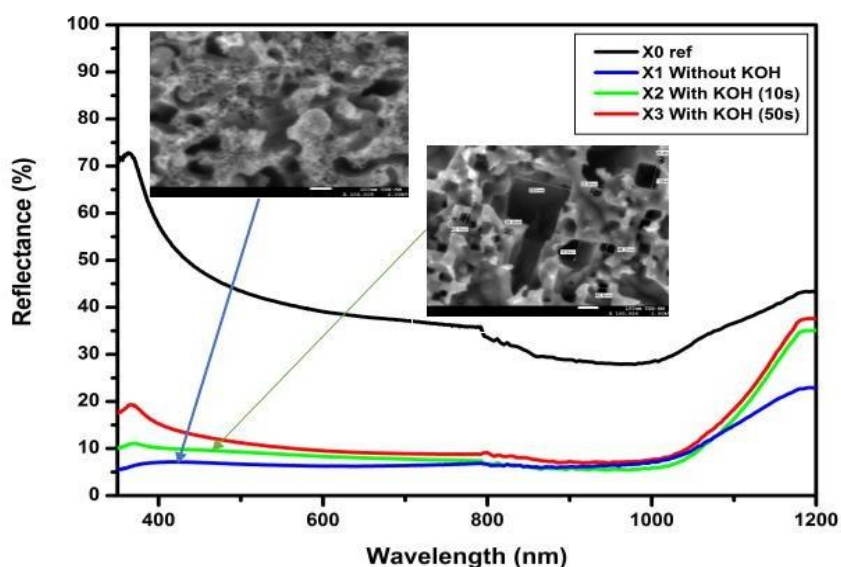


Fig.1: Reflection spectra of black silicon (b-Si) without and with KOH treatment for 10 s and 50 s, compared to the spectrum of silicon with plan surface. The insets are the SEM images of b-Si without and with KOH treatment.

Conclusion

This investigation showed the effect of KOH etching on the properties of b-Si and its importance to control the size of the nanostructures. This control is an important step in the photovoltaic technology, because it leads to an efficient light management in the solar cells.

Acknowledgments

This work was supported by General Directorate for Scientific Research and Technological Development (DGRSDT/Algeria).

References

1. Cheng, S.; Cai, B.; Zhu, Y. «Black Silicon as Absorber for Near-Infrared Photo-Thermal Conversion». In Proceedings of the 2015 Opto- Electronics and Communications Conference (OECC), Shanghai, China, 28 June–2 July 2015; pp. 1–3.
2. Yang, X.; Liu, B.; Liu, J.; Shen, Z.; Li, C. «A novel method to produce black silicon for solar cells». Sol. Energy 2011, 85, 1574–1578.

Structural Investigations Studies of Antimony-Tungsten and Sodium Metaphosphate Glass Systems with NaPO₃ as Additive

Guesmia Nesrine, Hamzaoui Majda, Beghdadi Lina

Department of physics /laboratory of photonic physics and nanomaterials multifunctional, University of Biskra, Algeria

*Corresponding author

ABSTRACT

Sb₂O₃-based heavy metal oxide glasses in the Sb₂O₃– WO₃–NaPO₃ ternary system were prepared. The physical properties and structural properties of the glasses have been investigated. From Raman and FTIR spectroscopy, the average cross-link density and number of network bonds per unit volume have been increased and discussed according to the create P-O-W strong linkage. The optical and structural properties of these glasses were found to be generally affected by the chemical changes in the glass composition due to the formation of linear chain of phosphate, that increase the connectivity and rigidity of the glass network. This work demonstrates that our glasses can be used for produce optical fiber application.

KEYWORDS: Sb₂O₃– WO₃–NaPO₃ ternary system, FTIR and Raman spectroscopy.

INTRODUCTION

Antimony oxide based glass has attracted extensive investigation in recent years; Since these glasses possess a large nonlinear optical susceptibility (χ^3) coefficient¹ making them suitable for potential applications in nonlinear optical devices². Phosphate-based glasses are among the most researched for potential applications in optical fields because they exhibit unusual physical properties when compared to silicate glass. In order to improve the chemical durability of these NaPO₃ based bottles, the formulations should be improved by adding the selected elements^{3, 4}. WO₃ are of particular interest and have undergone several studies since controlling the molar composition can lead to specific optical properties⁵. In this paper, we report on the physical and structural properties of glasses in the Sb₂O₃–WO₃–NaPO₃ ternary system.

RESULTS AND DISCUSSION

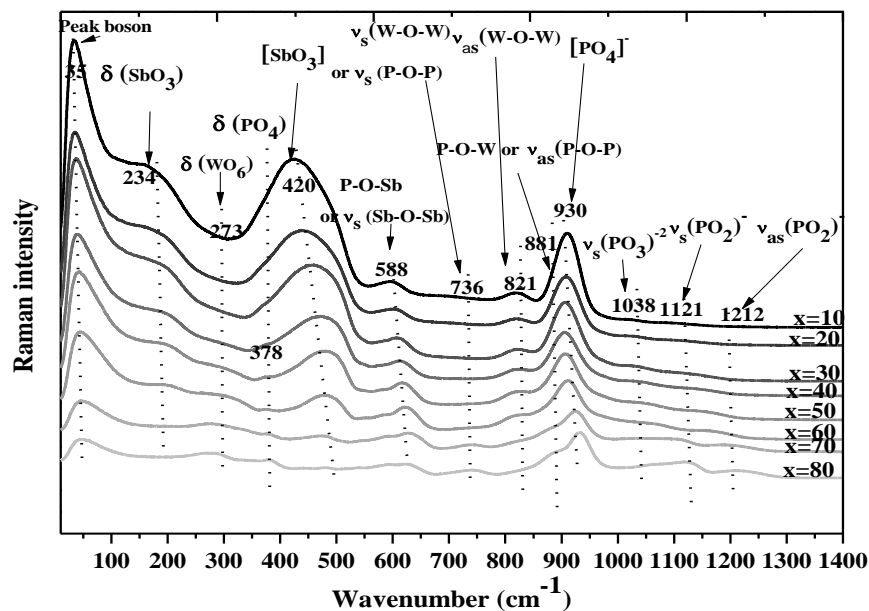
We calculated the \bar{n}_c and n_b of our SWN glasses by using the formula in⁶. The mean cross-link density, \bar{n}_c , is rise from 1.26 to 2, while the number of links per unit volume, n_b , is increased from 40,37 to $64.01 \times 10^{21} \text{cm}^{-3}$. Since Antimony oxide is substituted with another glass former (NaPO₃), which has a higher cationic coordination number than Sb₂O₃ ($n_{f(\text{NaPO}_3)} = 4$) and therefore creates a BO sites, the network has become stiffer and more linked in SWN glasses. With the increase in NaPO₃ concentration, both \bar{n}_c and n_b values an improve enhancement (Table 1).



Table 1: Values of density (ρ), molar volume (V_m), average cross-link density (\bar{n}_c) and number of bonds per unit volume (n_b) of glasses in the SWN systems.

S.n°	ρ (g/cm ³)	V_m (cm ³ /mol)	\bar{n}_c	$n_b(\times 10^{21}\text{cm}^{-3})$
SWN10	5.256	50,722	1,26	40,37
SWN20	4.975	49,777	1,37	42,35
SWN30	4.827	47,376	1,47	45,77
SWN40	4.580	45,792	1,58	48,67
SWN50	4.325	44,109	1,68	51,89
SWN60	4.068	42,236	1,79	55,62
SWN70	3.725	41,037	1,89	58,71
SWN80	3.471	38,578	2,00	64,01

The Raman spectra of the vitreous samples of system (90- x) Sb₂O₃-10WO₃-xNaPO₃ with x varying from 10 to 80, is shown in Fig.1.

**Fig.1:** Raman absorption spectra of SWN glasses.

In conclusion, the stiff vitreous of the SWN samples is responsible for the formation of W-O-W, P-O-W, and P-O-Sb bonds. As a result of the increased NaPO₃ and the glass transition temperature rising, the NBO atoms are reduced⁷.

CONCLUSION

In conclusion, the introduction of NaPO₃ into the SWN glass led to the formation of more linear chains, which reduced the number of NBOs and an increase in the structural compactness of these glasses. The structural studies of SWN glass supported this hypothesis by the formation of phosphate obeyed Q² with some modes of Q¹ and P-O-W linkage with the addition of NaPO₃. In general, these new glasses showed good behavior for producing optical fibers applications.

References

1. K. Terashima, T. Hashimoto, T. Uchino and T. Yoko, *J. Ceram. Soc. Jpn.* 104 (1996), p. 1008.
2. G. Poirier, M. Poulain and M. Poulain, *J. Non-Cryst. Sol.* 284 (2001), p. 117.
3. A. Mori, Y. Ohishi, M. Yamada, H. Ono, Y. Nishida, K. Oikawa and S. Sudo, *Proc. OFC 97* (1997), p. 1.
4. Ducl J.F, Videau J.J., 'Physical and chemical characterizations of sodium borophosphate glasses', *Matter. Lett.*, 13 (1992) p271-274
5. G Poirier, Y Messaddeq, S J L Ribeiro, M. Poulain, *Non-Cryst. Solid* 351 (4) (2005) 293.
6. M.Çelikbilek,A.E.Ersundu,S.Aydin,J. *Non-Cryst. Sol.* 378 (2013) 247-253.
7. G. Poirier, Y. Messaddeq, S. J.L. Ribeiro, M. Poulain, *J. Sol. State Chem*, 178, (2005) 1533–1538.

In-depth Analyses of P-type Silicon Solar Cells by Laser-Induced Breakdown Spectroscopy (LIBS)

Mohamed Amine Benelmouaz^{1*}, Sid Ahmed Beldjilali¹, Sabrina Messaoud Aberkane²,
Kenza Yahiaoui², Djoudi Bouhafis³ and Nabila Belkhir¹

¹Laboratoire LPPMCA, Université des Sciences et de la Technologie d'Oran Mohamed Boudiaf USTO-MB, BP
1505 EIM'naouer, 31000 Oran, Algérie

²CDTA, Centre de Développement des Technologies Avancées, Cité 20 Aout 1956. BP 17. Baba Hassen Alger,
Algérie

³CRTSE, Centre de Recherche en Technologie des Semi-conducteurs pour l'Énergétique, 16038, Alger, Algérie

*Corresponding author

Introduction

Following the rapid development in the field of renewable energy, the photovoltaic industry is rushing to meet the growing demand and is investing in processes, materials and research to achieve the necessary scale to reduce the cost of electricity produced by photovoltaic panels. Polycrystalline silicon photovoltaic cells are the most popular and economical cells in the market due to their cost-effective manufacturing methods and cheap substrates, with factories incorporating production quality control systems to continuously optimize the manufacturing process to maintain their efficiency and performance¹. In this context, we have analyzed polycrystalline silicon solar cells by LIBS laser induced breakdown spectroscopy to characterize the nature and determine the content of impurities present in these cells².

Experimental

A Q-switched Nd-YAG laser source (Quantel YG 980) operating at its fundamental wavelength (1064 nm) with a pulse width of 7 ns is used in the ablation process with 20 mJ of laser energy focused onto the sample surfaces in air. The plasma emission light recorded by Echelle spectrometer (Aryelle 200, LTB Lasertechnik Berlin) coupled with a gated intensified charge coupled detector ICCD (iStar, Andor). Data acquisition and analysis were performed using Sophi software (LTB).

Results and Discussion

Using the NIST database, the position of the lines allows us to identify the elements present in the solar cell; we will first look for the most intense lines of all the elements present in the periodic table. After an analysis of the spectrum emitted from 200 to 790 nm (fig. 1) and hundreds of lines identified, we found eight elements: silicon, silver, aluminum, calcium, sodium, carbon, magnesium and potassium. Most of the emission lines lie in the UV region and the visible region. The temperature of the plasma is deduced from these Boltzmann plots and the condition of the ETL (local thermodynamic equilibrium) is verified by the McWhirter criterion. The impurities found in metallurgical silicon come mainly from raw materials processing during wafers fabrication.



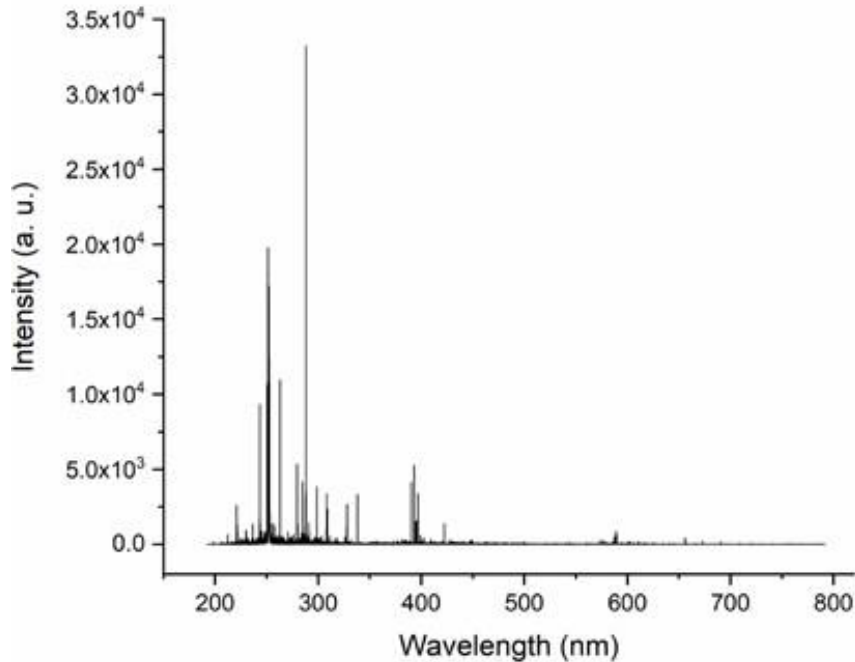


Fig.1: Solar cell emission spectrum recorded during LIBS analysis.

By applying the CF-LIBS approach, the mass fractions of the elements detected in the solar cell were measured with a CF-IRSAC correction of the self-absorbed lines. In-depth profiling is investigated to follow in depth the concentration of elements detected in the solar cell.

Conclusion

A spectroscopic study was made to analyze the photovoltaic cells based on polysilicon. The goal was to investigate the distribution of elements detected in the sample. Eight elements were detected in this analysis, which are: Silicon, Silver, Aluminum, Calcium, Magnesium, Sodium, Potassium and Hydrogen. The depth profiling allowed us to follow the distribution of the elements detected in the volume of the solar cell.

References

1. Ratanaphan, S., Yoon, Y. & Rohrer, G.S. «The five parameter grain boundary character distribution of polycrystalline silicon. *J Mater Sci.* 2014: 49- 4938.
2. Hamdani, F. Z., Beldjilali, S. A., Benelmouaz, M. A., Aberkane, S. M., Yahiaoui, K., & Belasri, A. « Depth Profiling of Solar Cells Using Laser- Induced Breakdown Spectroscopy (LIBS) ». *ICREEC 2019 Proceedings of the 1st International Conference on Renewable Energy and Energy Conversion, Springer Proceedings in Energy*, ISSN: 2352-2534, Springer Nature Singapore Pte Ltd. 2020, <https://doi.org/10.1007/978-981-15-5444-5>.

Po46

Diagnosis of an Unknown Solar Cell by Electrical Characterization

¹Benslafa Nacera, ¹Belmekki Mohamed, ²Diallo Mouhammad Affoh Ahmad Moctar

¹ Université des Sciences et de la Technologie d'Oran, Faculté de Physique BP1505 El Mnaouer Bir El Djir Oran
Algérie

² Magnambougou Projet Rue :420; Porte :221 Bamako Mali

*Corresponding author

ABSTRACT

The diagnosis of a solar cell whose composition and electrical characteristics are unknown is carried out by an electrical characterization. The procedure used is based on the exploitation of the experimental results of the current-voltage variations for different light intensities. This study will then make it possible to define mathematical series of the behavior of the cell which will be used to optimize the choice of the cell for different percentage of lighting using CAD techniques.

I-Measurement of the electrical characteristics of the solar cell in the dark

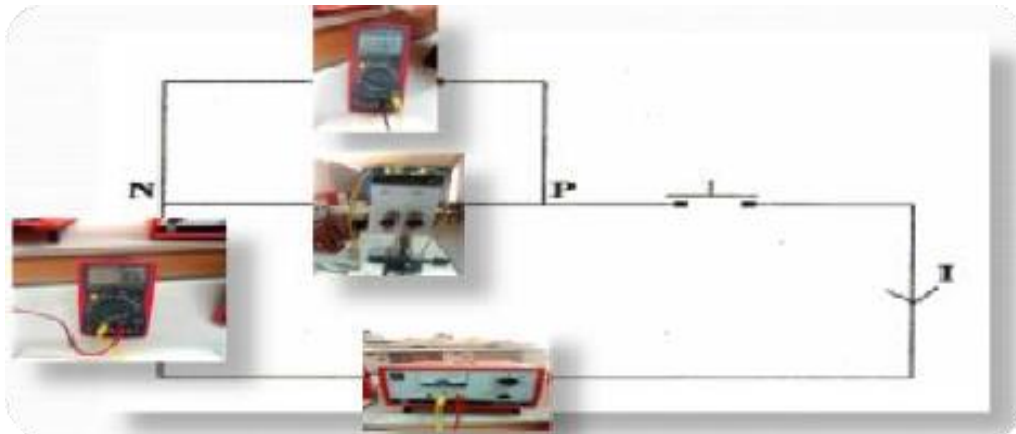


Figure 1: Measuring circuit

The current-voltage variation curve is determined experimentally using the circuit given in figure 1. The solar cell is in the dark and its connection in direct polarity, the generator voltage varies from a low voltage close to zero to an infinite limit value. Polarity reversal is done by reversing the polarity of the generator. The results obtained are given in figure 2.

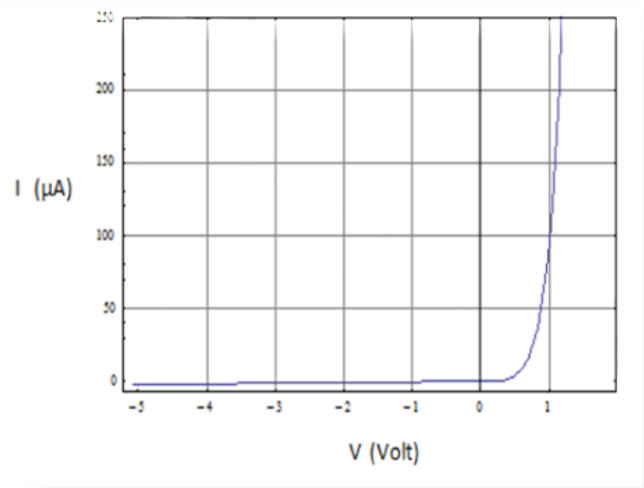


Figure 2: Dark current-voltage characteristics



The electrical behavior of the solar cell in the dark is similar to that of the conductivity of a diode, which allows us to justify the modeling methods used subsequently.

II-Modeling methods

There are 3 models for modeling a solar cell in the dark: The one-diode model, The two-diode model, The similar model. The one-diode model: This is the most widely used analytical model to obtain the unmeasured quantities shown in the circuit in Figure 3.

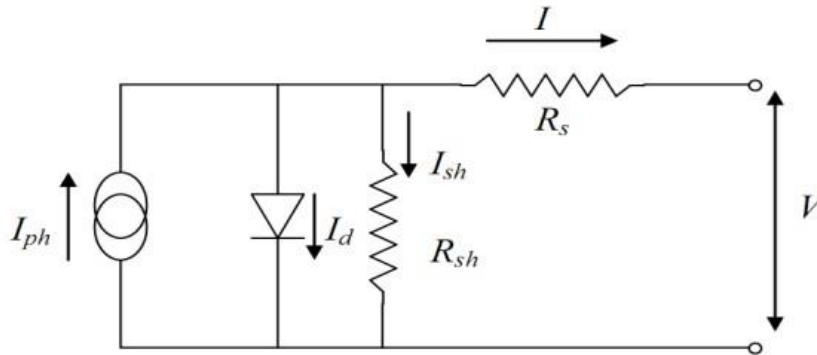


Figure 3: Equivalent diagram of a cell

Conclusion

The setting up of the experimental procedure is simple and does not require heavy equipment and gives good quality results for the objective which has been set. In addition, the numerical simulation does not present any difficulties since the models based on the similarity with the diodes exist. It is the mastery of the physical phenomena that are linked to the design of the solar cell that eventually cause the latter to have a low efficiency.

Affecting Parameters on Polymers Surface Treatment by Atmospheric Pressure Plasma Jets

Fatma Bedrouni^{1*}, Mohamed Ouchabane² Nadia Saidi-Amroun¹, Fateh Almabouada²

¹Department of physics, University of Science and Technology Houari Boumediene, Algeria

²Center for Development of Advanced Technologies, Algeria

*Corresponding author

ABSTRACT

Low-temperature atmospheric pressure plasma jet (APPJ) is a new technology that proves their effectiveness in the field of polymer surface treatment. It used to improve wettability and adhesion property of the surface. These modifications are affected by the treatment time, source- surface distance, the discharge gas and the type of polymer. The aim of this study is to reach a deeper understanding about the influence of these parameters on the surface modification of different polymer through review of research paper published during the past years.

Introduction

Due to their ease of installation and the absence of vacuum chamber the atmospheric pressure plasma jets (APPJs) at low-temperature take the attention of modern research, especially in the surface treatment and modification of polymer [1,2]. There are various methods to generate APPJ, such as radio frequency (RF) discharge, alternative current discharge (AC) and direct current (DC) discharge. All of these methods are used to modify the property of polymer surface like the wettability or the adhesion strength paint and coatings to polymer surface. Given the variety of parameters that are involved in APPJ treatment, a comprehensive understanding of the effect of these factors will aid in better utilization of this methods. This study focuses on the effect of the important parameters; treatment time, distance of the surface from the source and the gas used, already published by researchers.

Treatment time

During the exposition to the jet, the surface properties change with treatment time then remain unchanged when the time is greater than a critical value depending on the type of polymers [3,4], due to the saturation of active sites.

Surface-source distance

The concentration of the plasma species decreases along the jet, this axial gradient is due to the short lifetime of the reactive species and their reaction with atmospheric space or recombination processes in the plasma bulk. As a result, the modification of surface is important when the surface is near from the source [5,3].

Discharge gas

The energetic species of the plasma such as ions, electron, excited atoms or molecules are depending on the discharge gas, consequently the change will be different. It was found that in the case of air or a mixture of oxygen and argon O₂/Ar plasma, the modification of contact angle is more important than Argon plasma. This result could be attributed to the formation of high concentration of polar groups produced by air and oxygen [5].



Type of polymer

The chemical composition of the polymer affects significantly the degree of change that the plasma induces on its surface. Aromatic polymers are more resistant than other polymers to plasma modification, because of their aromatic groups, such as phenolic compounds [6].

Conclusion

The treatment time, the source-surface distance, the discharge gas and the type of polymer are among factors that affect modification of polymer surface properties with atmospheric pressure plasma jet. Such a review study will contribute to master all parameters behind the desired properties and then aids to set and develop this technology to specific application.

References

- [1] A. Van Deynse, P. Cools, C. Leys, R. Morent, et N. De Geyter, « Surface modification of polyethylene in an argon atmospheric pressure plasma jet », *Surf. Coat. Technol.* 2015; 276: 384- 390.
- [2] K. Michał, T. Piotr, M. Paweł, et P. Joanna, « Wettability of Polymeric Materials after Dielectric Barrier Discharge Atmospheric-pressure Plasma Jet Treatment », *Sens. Mater.* 2018;1207.
- [3] A. Vesel et G. Primc, « Investigation of Surface Modification of Polystyrene by a Direct and Remote Atmospheric-Pressure Plasma Jet Treatment », *Materials.* 2020;13: 2435.
- [4] H. B. Baniya, R. P. Guragain, B. Baniya, et D. P. Subedi, « Cold Atmospheric Pressure Plasma Jet for the Improvement of Wettability of Polypropylene », *Int. J. Polym. Sci.* 2020;2020:1-9.
- [5] R. Kawakami *et al.*, « Effects of air-based nonequilibrium atmospheric pressure plasma jet treatment on characteristics of polypropylene film surfaces », *Appl. Surf. Sci.* 2020;509:144910.
- [6] K. Fricke, H. Steffen, T. von Woedtke, K. Schröder, et K.-D. Weltmann, « High Rate Etching of Polymers by Means of an Atmospheric Pressure Plasma Jet », *Plasma Process. Polym.* 2011;8:51-58.

Crystal Structure and Comparative Study via Hirshfeld Surface Analyses of Charge Transfer Compounds Based on Anthranilic Acid

Fatima Allouche*, Tahar Benlecheb, Nabil Benyza

Department of Material Science/ Laboratory of Sensors, Instrumentations and Process (LCIP),
University of Abbes Laghrour, Khenchela, Algeria

*Corresponding Author

INTRODUCTION

Studies of organic-inorganic hybrid materials, including aminoacids and various inorganic acids^{1,2}, have received a great deal of attention in recent years. The need to use these materials is permanently increasing³. Hence, this symbiosis can lead to new rich structure, chemical and physical properties and has secured a good place in various fields of application such as biomolecular science^{4,5}, electronic⁶, nonlinear optics^{7,8}. In order to enrich the varieties in such kinds of hybrid materials and to investigate the influence of hydrogen bonds on the structural features, they have synthesized a new compound; this kind of hydrogen bonding is observed in similar previously studied hybrid compounds¹⁰.

EXPERIMENTAL AND THEORETICAL STUDY

This present work undertakes the crystal structure and comparative study via Hirshfeld surface (HS) analyses of charge transfer of two organic-inorganic hybrid material based on anthranilic acid, which has been obtained by the single crystal X-ray diffraction method. Hirshfeld surface analysis is a powerful tool used to quantify the intermolecular interactions of molecular crystals. The HS⁹ and fingerprint plots¹⁰ presented here are carried out using Crystal Explorer 17.1¹¹.

RESULTS AND DISCUSSION

The structure of the title compound o-carboxyanilinium dihydrogenphosphate, (C₇H₈NO₂⁺, H₂PO₄⁻) (I)¹² crystallizes in the centrosymmetric space group P-1, describes the in-depth structural analysis thereof shows that a single proton transfer occurs. The analyses of the hydrogen bonds of the two compounds (C₇H₈NO₂⁺, H₂PO₄⁻) (I) and (C₇H₈NO₂⁺, H₂AsO₄⁻) (II)² show that the anions and cations are held together via strong and short O—H...O hydrogen bonds, in addition to N—H...O interactions. Complementary Hirshfeld surface analysis was carried out to investigate and quantify the contributions of the different intermolecular interactions of the two compounds. The normalized contact distance (d_{norm}) (Fig. 1), based on d_e (d_e de (distance from a point on the surface to the nearest nucleus outside the surface) and d_i (distance from a point on the surface to the nearest nucleus inside the surface), was calculated via the following expression:

$$d_{norm} = \frac{d_i - r_i^{vdw}}{r_i^{vdw}} + \frac{d_e - r_e^{vdw}}{r_e^{vdw}} \quad (1)$$

Where r^{vdw} is the van der Walls radius of the atom that lies inside the surface of Hirshfeld, while r_e^{vdw}



is the van der Waals radius of the atom that lies outside of the surface of Hirshfeld.

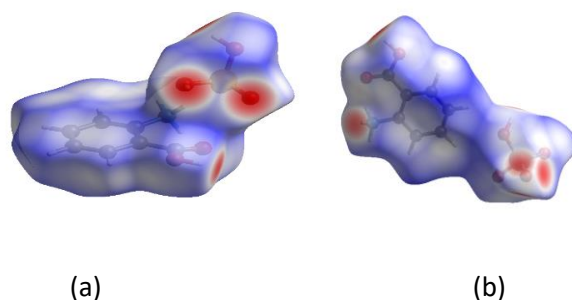


Fig.1. Hirshfeld surface analysis d_{norm} of o-carboxyanilinium dihydrogenphosphate (a) and o-carboxyanilinium dihydrogenarsenate (b).

CONCLUSION

The Single crystal XRD analysis established the supramolecular nature of the two crystals structures. The comparative study via 3D Hirshfeld surface and 2D fingerprint plots of the two compounds (I) and (II) reveal that the structure is dominated by O...H/H...O (52.9,50.3) %, the H...H contacts as the second dominant interactions with (28.2, 25.3) % and C—H... π (11.6,10.5) % contacts successively. Hydrogen bond interactions are the primary contributors to the intermolecular stabilization in the crystal.

REFERENCES

1. Kagan C. R., Mitzi D. B., Dimitrakopoulos C. D., Science, 286, (1999) 945- 947.
2. Tordjman, I.; Masse, R.; Guitel, J. *Acta Crystallogr., Sect. C*, 44, (1988) 2055–2057.
3. Y. Oueslati, S. Kansız, A. Valkonen, T. Sahbani, N. Dege, W. Smirani. *J. Mol. Struct.* 1196 (2019) 499-507.
4. R. Fezai, A. Mezni, M. Kahlaoui, M. Rzaigui, *J. Mol. Struct.* 1119 (2016) 54-63.
5. S. Sleyimi, K. Lahbib, N. Rahmouni, M. Rzaigui, S. Besbes-Hentati, S. Abid, *J. Mol. Struct.* 1144 (2017) 406-414.
6. S. Kamoun, A. Daoud, R. Von Der Muhll, J. Ravez, *Solid State Commun.* 85 (1993) 661-664.
7. J. Zyss, J. Pecaut, J.P. Levy, R. Masse, *Acta Cryst.B* 49 (1993) 334-342.
8. J. Pecaut, R. Masse, *J. Mater. Chem.* 4 (1994) 1851-1854
9. J.J. McKinnon, M.A. Spackman, A.S. Mitchell, *Acta Cryst. B* 60 (2004) 627-668.
10. M.A. Spackman, P.G. Byrom, *Chem. Phys. Lett.* 267 (1997) 215-220.
11. M. J. Turner, J. J. McKinnon, S. K. Wolff, D. J. Grimwood, P. R. Spackman, D. Jayatilaka and M. A. Spackman, *CrystalExplorer17*. University of Western Australia. 2017.
12. Benali-Cherif, N., Allouche, F., Direm, A., Boukli-HBenmenni, L., Soudani, K. *Acta Cryst. E* 63, (2007) o2643—o2645.

Effect of Various Auxiliary Acceptors on the Optical and Photovoltaic Properties of a D-A'- π -A Sensitizing Dye. DFT and TD-DFT Study

Manal GOUDJIL¹, Djaffar KHEFFACHE^{1,2}, Maammar REKIS¹

¹Theoretical Chemistry and Computational Photonics Laboratory, Faculty of Chemistry, USTHB, BP 32, Algiers, 16111, Algeria.

²Chemistry Department of the Faculty of Sciences, University M'Hamed Bougara (UMBB), 35000 Boumerdes, Algeria

*Corresponding author

ABSTRACT

The introduction should be simple and easy to understand. Our theoretical study aims to modulate the electronic and photovoltaic properties of a sensitizing dye developed by Marder's team [1] having a D-A'- π -A configuration [1]. To achieve this goal, we examined the effect of various auxiliary acceptors "A" on the spectroscopic and photovoltaic properties of the reference dye [1]. Computational tools based on density functional theory "DFT" and its time dependent variant "TD-DFT" were implemented to determine the optoelectronic and photovoltaic characteristics of the series of sensitizing dyes considered in this study. The optoelectronic and photovoltaic properties including absorption spectra, energy levels (HOMO and LUMO), light harvesting efficiency (LHE), electronic injection driving force (ΔG_{inj}), dye regeneration energy (ΔG_{reg}), and open circuit voltage VOC were determined theoretically to identify the right sensitizer dyes for photovoltaic use.

Keywords: DSSC; Auxiliary acceptor; TD-DFT; UV-visible.

Acknowledgments

Authors can acknowledge any person, or funding agency that has made a significant contribution to the work.

References

- [1] Gao, Y., Li, X., Hu, Y., Fan, Y., Yuan, J., Robertson, N., Hua, J., Marder, S. R. (2016). *Journal of Materials Chemistry A*, 4(33), 12865-12877.



Preparation and Characterizations of MgFe₂O₄ Spinel Semiconductor

Maroua BENLEMBAREK^{1*}, Ali BOULAHOUACHE^{1,2}, Zoubir BENMAAMAR³, Mohamed TRARI⁴,
Rafik BENRABAA^{5,6}, Nassima SALHI^{1,2}

¹Laboratoire de Chimie du Gaz Naturel, Faculté de Chimie, USTHB, BP32, El-Alia, 16111 Bab Ezzouar, Alger, Algérie

²Laboratoire LCPMM, Faculté des Sciences, Université BLIDA1, B.P 270, Route de Soumaa, BLIDA, Algérie

³Laboratoire de Procédé Energétique et Nanotechnologie, Faculté des Sciences, Université BLIDA1, B.P 270, Route de Soumaa, BLIDA, Algérie

⁴Laboratoire de Stockage et valorization de l'énergie renouvelable, Faculté de Chimie, USTHB, BP32, El-Alia, 16111 Bab Ezzouar, Alger, Algérie

⁵Laboratoire de Matériaux Catalytiques et Catalyse en Chimie Organique, Faculté de Chimie, USTHB, BP32, El-Alia, 16111 Bab Ezzouar, Alger, Algérie.

⁶Département de Pétrochimie & Génie des Procédés, Faculté de Technologie, Université 20 Août-Skikda, BP 26, route Al-Hadaiek, 21000 Skikda, Alger, Algérie.

*Corresponding author

ABSTRACT

Introduction

The attention in the synthesis of magnetic nanocomposites has been developed enormously in recent years owing to the unique properties of these materials, such as crystallinity, crystallite size, specific surface area, particle size, morphology and catalytic activity [1]. They have great potential for applications in various fields such as engineering, physics, chemistry, biology and medicine. Nanosized spinel ferrite composites exhibit significant photocatalytic properties to be applied in the solar energy conversion and water purification [2]. As application, these oxides were successfully tested for the degradation of dyes [3], H₂ production and metal reduction [4] under solar light.

Experimental/Theoretical Study

In the present research, MgFe₂O₄ oxide synthesized by nitrate route via nitrates precursors salts, is a narrow band gap semiconductor crystallizing in spinel structure. Various techniques including: X-Ray fluorescence (XRF), TG-analysis, X-ray diffraction (XRD), Fourier Transform Infrared Spectroscopy (FTIR), UV-Visible Spectroscopy and Scanning Electron Microscopy (SEM-EDX) are used to characterize the material.

Results and Discussion

The XRD analysis of the so prepared powder indicates a cubic symmetry spinel structure with an average crystallite size of 13nm. The direct optical band gap E_g (1.91 eV), determined from the diffuse reflectance, is due to the lifting of degeneracy of Fe $3d$ orbital octahedrally coordinated. The SEM analysis of MgFe₂O₄ surface shows a uniform morphology with regular grain size in the range of 0.1- 0.5 μ m. The EDX elemental analysis supports the presence of only Mg, Fe and O without any other polluting element. The electrochemical analysis is also undertaken.



Conclusion

This work was devoted to the preparation of the spinel MgFe_2O_4 by nitrate route and the physical and electrochemical properties, which have been combined to establish the potential / energy diagram. Various techniques were used for the characterization of synthesized sample. The crystalline size of the MgFe_2O_4 as calculated by XRD pattern was 13 nm. The mixed oxide has an optical gap of 1.91 eV.

Keywords: Spinel MgFe_2O_4 , Nitrate route, Semiconductor.

References

- [1] F. Tavangarian and R. Emadi, "Synthesis and characterization of spinel-forsterite nanocomposites," *Ceram. Int.*, vol. 37, no. 7, pp. 2543–2548, 2011.
- [2] H. Lahmar, M. Benamira, F. Z. Akika, and M. Trari, "Reduction of chromium (VI) on the hetero-system $\text{CuBi}_2\text{O}_4/\text{TiO}_2$ under solar light," *J. Phys. Chem. Solids*, vol. 110, no. Vi, pp. 254–259, 2017.
- [3] N. Eskandari, G. Nabiyouni, S. Masoumi, and D. Ghanbari, "Preparation of a new magnetic and photocatalyst $\text{CoFe}_2\text{O}_4\text{-SrTiO}_3$ perovskite nanocomposite for photo-degradation of toxic dyes under short time visible irradiation," *Compos. Part B Eng.*, vol. 176, no. July, p. 107343, 2019.
- [4] Z. Boukhemikhem, R. Brahimi, G. Rekhila, G. Fortas, L. Boudjellal, and M. Trari, "The photocatalytic hydrogen formation and NO_2 -oxidation on the hetero-junction $\text{Ag}/\text{NiFe}_2\text{O}_4$ prepared by chemical route," *Renew. Energy*, vol. 145, pp. 2615–2620, 2020.

Po51

Numerical Thickness Optimization Study of CIGS Based Solar Cells with SCAPS-1D

Ikram Bellouati^{1*}, Houda Bakhchi¹, Samia Bahlouli¹, Houaria Riane^{1,2} and Fatima Hamdache¹

¹Laboratoire de Physique des plasmas, Matériaux Conducteurs et leurs Applications LPPMCA, Université des Sciences et de la Technologie d'Oran Mohamed Boudiaf USTO-MB, BP 1505 El M'naouer, 31000 Oran, Algérie

²Département LMD-SM, Faculté des Sciences et Technologie, Université de Mascara, Route de Mamounia, Mascara 29000, Algérie.

*Corresponding author

Introduction

The photovoltaic market knew a strong growth in the last few years. Although various sectors and technologies split the market, the cells containing Silicon dominate it with more than 85%, this is due primarily to the maturity of the nanoelectronic industry which uses massively the Silicon and good performance of the cells [1]. However, the many steps of production make this material technology expensive and tedious, which justifies the interest to develop the cells in less expensive thin layers. Chalcopyrite Cu(In,Ga)Se (CIGS) is a very promising material for thin film photovoltaics and offers a number of interesting advantages compared to the bulk silicon devices. In addition, CIGS cells offer many advantages: Cells CIGS are fabricated sonochemically [1], offer a significant absorption capacity which requires 100 times less material ($\sim 1\mu\text{m}$) than the Silicon cells ($\sim 100\mu\text{m}$), and they can be deposited on various types of substrates (flexible or rigid) of large [2].

In this work, we present numerical simulation results of a heterojunction cell based on CIGS (i-ZnO / CdS / OVC / CIGS) using the SCAPS-1D simulation code.

Theoretical Study

The studied HIT cell is represented in the figure below.

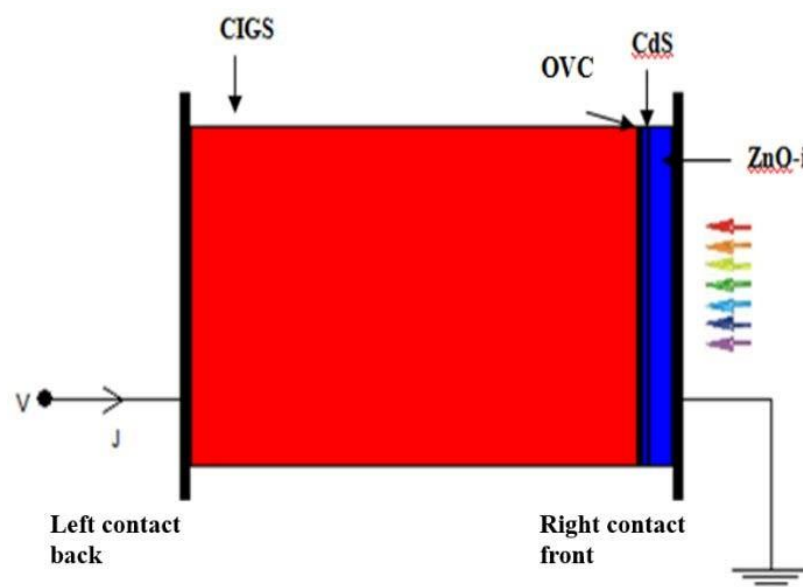


Fig. 1: Heterojunction cells based on CIGS (i-ZnO / CdS / OVC / CIGS).

CIGS, is the absorber of the P-type cell. The junction is formed with CdS / ZnO, n-type semiconductors. ZnO is called a window layer because it has to pass radiation to the absorber. The CdS buffer, traditionally used, is optimal when combined with a CIGS with a gap of 1.15eV but less optimal when the latter's gap is higher.

Results and Discussion

This theoretical study is carried out in order to study the effect of the variation in thickness and doping of the p- CIGS layer, which represents the window layer in the heterojunction (i-ZnO / CdS / OVC / CIGS) on the performance of solar cells. In figure 2, we have reported the results of calculation of the efficiency as a function of the thickness of the absorbent layer with a thickness varying between 100 to 3500 nm.

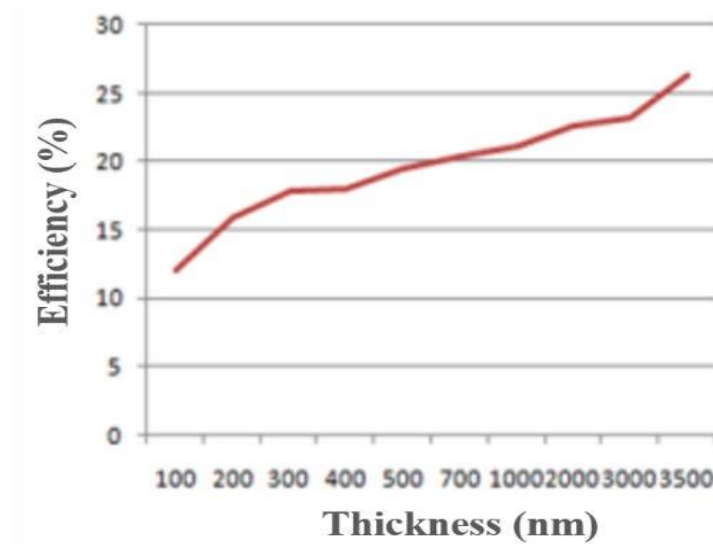


Fig. 2: Influence of CIGS thickness on the efficiency.

Conclusion

In this work we have used a numerical simulation to study the characteristics of these devices. We have also optimized the physical and electrical parameters of a specific CIGS-based solar cell structure to achieve maximum electrical conversion efficiency. Modeling and simulation were done by SCAPS software, to study the performance of CuInGaSe-based solar cells. We can say that the parameters of the CIGS absorber layer play a very important role in improving the efficiency of heterojunction solar cells and the characteristics of the cells are closely dependent on those of the individual layers.

References

1. Movla H. «Optimization of the CIGS based thin film solar cells: Numerical simulation and analysis», *Optik*. 2014:125- 67.
2. Poortmans J and Arkhipov V. Eds. «Thin Film Solar Cells: Fabrication, Characterization and Applications», John Wiley and sons, Ltd. 2006.

Po52

Influence of Porosity on the Structural and Electronic Properties of Porous Silicon

Hanane. Lachenani^{1*}, Souad.Ouir², Nourdinne. Gabouze³

¹.Laboratoire de Physique des Techniques Expérimentales et ses Applications de Médéa LPTEAM, Département Science de la Matière, Faculté des Sciences, Université de Médéa Algérie

².Laboratoire de Surfaces, Interface et Couches Minces, Département de Physique, Facultés des Sciences, Université Blida1, Algérie.

Address B.P 270, Route de Soumaa, Blida, Algeria

³.Centre de Recherche en Technologie des Semi-conducteurs pour l'Énergétique (CRTSE), 02 Bd, Frantz Fanon, B.P. 140, Alger, Algérie

*Corresponding author

INTRODUCTION

Porous silicon (PSi) is a promising material for several applications in significant and varied fields photoluminescence (PL), electroluminescence (EL) and gas and (bio) sensing, etc. In this work we have studied the influence of porosity on the structural and electronic properties of porous silicon and comparing them to those of the solid (c-Si) in order to understand changes in these properties when it is reduced to nanometric sizes.

THEORETICAL STUDY

In this work, structural and electronic properties investigations of PSi were performed using ab-initio pseudo potential plane wave (PP-PW) method founded on DFT. The exchange correlation energy is treated within the generalized gradient approximation of Perdew-Burke-Ernzerhof (GGA-PBE) included in the CASTEP program (Cambridge Serial Total Energy Package) [1]. The pseudopotential of Vanderbilt-type ultra-soft was utilized to compute the potential seen by the valence electrons. Supercell model was used to simulate porous silicon structures with four porosities (P = 3.12, 15.62, 28.12 and 40.62%) respecting the same space group P4 2 m (No.111). Hydrogen atoms were used to passivate all surfaces dangling bonds in silicon pores.

RESULTS AND DISCUSSION

Optimized structural parameters of all studied structures were obtained by geometry optimization step. For all porosities, the PS structures expand when compared to that of c-Si due to the hydrogen-hydrogen interaction. The electronic properties of PSi were studied by calculating the band structures, densities of states and electron density distributions. The electron band structures show for the different porosity, in contrary to the silicon crystal (c-Si) which possesses an indirect band gap, the feature of direct band gap. Otherwise, as shown in Fig. 1, The values of the gap of porosities 3.12, 15.62, 28.12, 40.62% are respectively 0.735, 1.196, 1.792, 2.090 eV unlike c-Si which has an indirect gap of 0.622 eV. There is a widening in the forbidden band which varies as a function of the porosity. This broadening is due to the increase in quantum confinement in the resulting structure and the increase in specific surface area as a function of porosity [2]. The densities of states and the electron



charge maps of all PSi structures show that covalent bond Si-Si is conserved as in the case of c-Si.

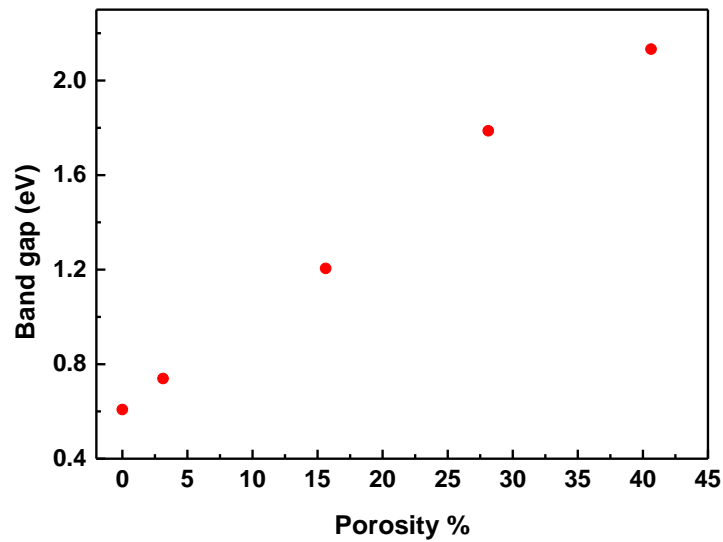


Fig 1: Evolution of band gap energy with porosity

CONCLUSION

Geometric optimization indicates expansion of the supercells, described by an increase in lattice parameters as a function of porosity. In addition, the electronic band structure of all PS structure shows direct band gap semiconductors for all studied porosities.

References

- [1] Clark SJ, Segall MD, Pickard CJ, Hasnip PJ, Probert MIJ, Refson K, Payne MC (2005) First principles methods using CASTEP. *Z Kristallogr* 220:567–570.
- [2] Canham LT (2014) Mechanical properties of porous silicon. *Handbook of porous silicon*, pp 213–220.

Label-free Biosensor Based on Photonic Crystal Microcavity for Malaria Detection with High Sensitivity

Bounaas Faiza*, Labbani Amel

Laboratory of Hyperfrequency and Semiconductors, Department of Electronics Faculty of Science and Technology, University of Frères Mentouri Constantine1, Constantine Algeria

*Corresponding Author

INTRODUCTION

The majority of deaths occur in tropical countries is due to Malaria disease. The people infected by this malady caused by a parasite will have severe complications like anemia, cerebral Malaria, organ failure, etc. Several technologies have been developed for detecting Malaria. Label-free optical biosensors have received considerable attention due to their contribution to significant advances in medical diagnostics and chemical and biochemical applications. One-dimensional photonic crystal (1D PC) optical biosensors have attracted the most interest of many researchers because they open the possibility of controlling and manipulating light in confined space. In addition, they have received significant attention owing to their high sensitivity, reliability, and short detection time. For this reason, we have investigated a highly sensitive biosensor based on a 1D PC platform for detecting Malaria disease at an early stage. The proposed device comprises an endlessly repeating stack of silicon (Si) and water layers with one defect cell containing the sample to be monitored. The obtained structure has the following sequence (Si) (water/Si)^N D(Si/water)^N(Si), where D and N are the cavity layer and the period number, respectively. The sensing principle is based on varying the refractive index of the analyte. When the blood sample is infiltrated into the cavity, the spectral position of the wavelength peak shifts to the shorter wavelength.

THEORETICAL STUDY

We have theoretically analyzed the defect mode transmission properties of the suggested biosensor design using the transfer matrix method (TMM). The TMM of a single layer is expressed as:

$$M_i = \begin{bmatrix} \cos d_i \rho_i & -\left(\frac{i}{P_i}\right) \sin d_i \rho_i \\ -i P_i \sin d_i \rho_i & \cos d_i \rho_i \end{bmatrix} \quad (1)$$

where i represents the Si layer, water layer and D microcavity cell. The matrix of the entire structure is the product of such matrices $M_{Si}(M_{water}/M_{Si})^N M_D(M_{water}/M_{Si})^N M_{Si}$

The transmittance coefficient t can be given as:

$$t = \left| \frac{2P_0}{(Q_{11}+Q_{12}P_0)P_0+Q_{21}+Q_{22}P_0} \right|^2 \quad (2)$$

RESULTS AND DISCUSSION

In this section, we present the numerical results of our biosensor design. The structure is expressed as $M_{Si}(M_{water}/M_{Si})^N M_D (M_{water}/M_{Si})^N M_{Si}$. The refractive indices of Si and water are 3.4 and 1.33, respectively. The thicknesses of all the layers are given to be quarter-wavelength ($\lambda_0/4$), which λ_0 is



equal to 1550nm. In our model, the defect layer's thickness is assumed to be 550 nm. Such defect is filled with blood samples with a different refractive index of the healthy and infected person corresponding to different stages of malaria infection. Fig. 1 depicts the transmission spectra for normal and infected cells at different stages of Malaria. From this figure, we noticed that as the refractive index (RI) decreases, the resonant peak shifts towards a shorter wavelength. The refractive index and the resonant peak position calculated by TMM are shown in Table 1.

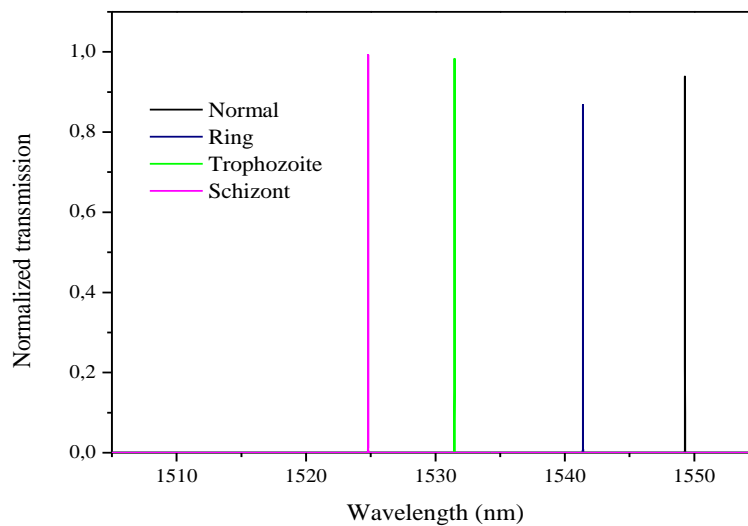


Fig. 1 transmission spectra at different stages of Malaria

Table 1. The refractive index of Malaria stage and the resonant wavelength

Malaria stage	RI	Wavelength(nm)
Normal stage	1.408	1549.283
Ring stage	1.396	1541.398
Trophozoite stage	1.381	1531.466
Schizont stage	1.371	1524.8

CONCLUSION

This paper investigates a highly sensitive refractive index for Malaria diagnosis based on the 1D-PC platform. TMM method is used to demonstrate the performance of the presented device. From the result of the numerical simulations, it is found that the variation of the analyte's refractive index leads to the shift of the resonant mode. The shift in the transmittance peaks varies from 1549.283 nm to 1524.8 nm. Therefore, the proposed biosensor offers a high sensitivity of 657.083 nm/RIU, the quality factor of 7.17×10^5 and detection limit of 2.72×10^{-7} . The obtained results are much better than similar devices¹. Therefore, they can be used to design highly sensitive PC biosensors. In addition, the suggested device is easy to fabricate with low operating costs.

REFERENCES

1. Ankita, Suthar B, Bhargava A, Biosensor Application of One-Dimensional Photonic Crystal for Malaria Diagnosis, Plasmonics. 2021; 16: 59–63.

Ab-Initio Study of the Ferromagnetic Half-Metallic Perovskite KMgO₃

Amina HAQUI*, Mokhtar ELCHIKH and Asmaa HIRECHE BAGHDAD

Département of Engineering Physics, USTO-Oran, Algeria

*Corresponding author

ABSTRACT

In this work, we investigated the structural, electronic, magnetic and elastic properties of Pérovskite KMgO₃, using the Linearized Augmented Plane Wave Method with Total Potential (FP-LAPW) as part of the density functional theory implemented in Wien2k code.

INTRODUCTION

The recent years has seen a lot of research on Pérovskites for potential applications in electronics, photovoltaics, renewable energy and innumerable other industries¹. The optimized structural parameter of KMgO₃ at equilibrium obtained is in good agreement with the results found by other authors; The results show that these compound is stable in the ferromagnetic phase and he has character half-metallic.

THEORETICAL STUDY

To study the properties of KMgO₃ which is interest in spintronic applications, we performed quantum simulation of first principles “ab-initio” using the formalism of the theory of the functional density² to determine with precision a large range of properties of matter. Our DFT calculations are based on full potential linearized augmented plane wave (FP-LAPW³). The exchange and correlation potential is treated with the GGA-PBE approximations.

RESULTS AND DISCUSSION

The KMgO₃ Pérovskite in the cubic form with space group is Pm-3m (221) contains one formula unit and the K, Mg and O atoms are positioned at 1a (0, 0,0), 1b (½, ½,½) and 3c (0,½, ½) sites of Wyckoff coordinates, respectively. The equilibrium lattice parameter for this compound was obtained from the energy optimization calculations as a function of volume, to determine the structural properties such as lattice parameter a, the modulus of compressibility B and its derivative B' (shown in Table 1)

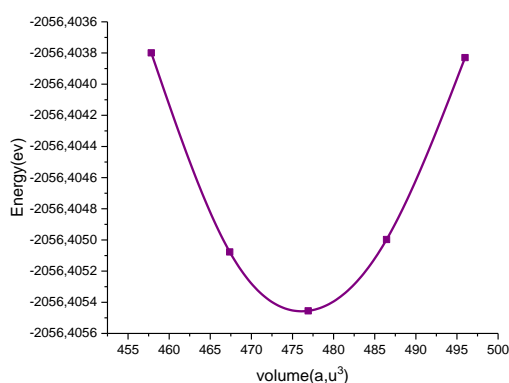


Fig1: Volume optimization of KMgO₃



To investigate the elastic properties, we use IRelast package integrated in the WIEN2k. The study of the elastic properties informs us on the behavior of this compound with regard to the ductility, brittleness and application of the external forces. For compounds that have a cubic structure the elastic constants c_{ij} are reduced to only three (c_{11} ; c_{12} ; c_{44}).

Table1: Calculated values of the lattice parameter a_0 , bulk modulus B, its pressure derivation B' and elastic constants C_{11} , C_{12} , and C_{44}

Parameters	Our calc	Other calc
a_0 (Å)	4.1325	4.1344
B(GPa)	63.0911	61.7614
B'(GPa)	4.7480	4.3491
C_{11} (GPa)	130.0052	121.5406
C_{12} (GPa)	32.7361	32.5717
C_{44} (GPa)	14.3281	9.0363

For electronic properties, it is clear in fig 2 that for spin-down states, the compound exhibits a metallic nature but, for the spin-up, the compound shows an insulating nature with half-metallic gaps of 7.285ev.

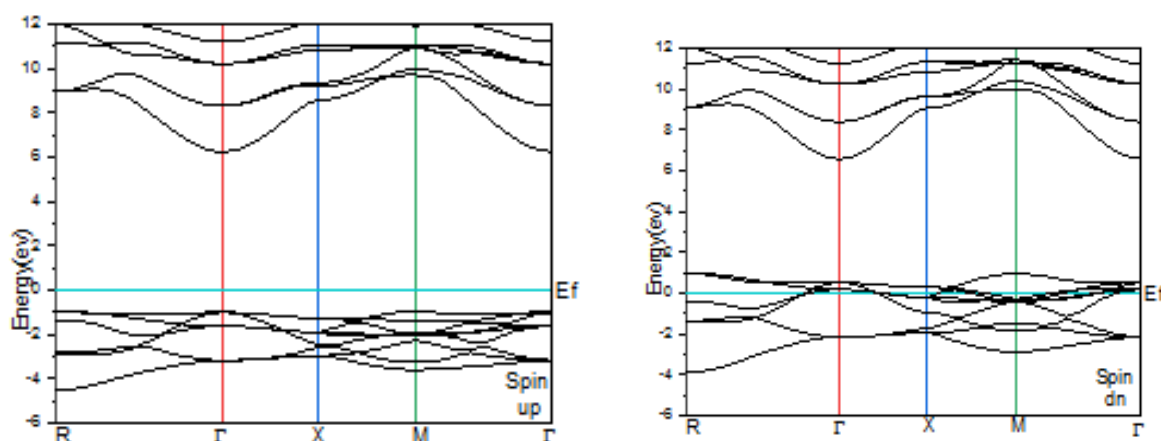


Fig2: band structure of KMgO_3 compound in both spin-up and spin-down states

CONCLUSION:

we used the FP-LAPW method founded in the DFT to calculate the different parameters of KMgO_3 . Calculations reveal that the compound KMgO_3 has a minimum energy in ferromagnetic configuration. According to results of elastic properties, we found that our material KMgO_3 shows ductile behavior and suggests a high metallic nature like inter-atomic bond. For electronic properties, it is clear that the material has a half-metallic character, this type of material can be very interesting for future spintronics applications.

REFERENCES

1. Mannhart, J. Schlom, D. G. (25 March 2010). "Oxide Interfaces--An Opportunity for Electronics". *Science*. 327 (5973):1607-1611.
2. J. Perdew, K. Burke and M. Ernzerhof, *Phys. Rev. Lett* 77, 3865 (1996)
3. P. Blaha, et al, WIEN2k, An Augmented Plane Wave. Local Orbitals Program for Calculating Crystal Properties (Vienna:Vienna University of Technology.(2001). 4. Mama Hamlat, Keltouma Boudia, Kadda Amara, Friha Khelfaoui ,Norredine Marbough ;*Computational Condensed Matter* 23 (2020) .

Ab Initio Calculations of the Structural and Electronics Properties of Double Tungstates $\text{NaY}(\text{WO}_4)_2$

Hanane Arioumlil^{1*}, Faiza Bouamra¹ and Michel Rérat²

¹Department of physic, LASICOM Laboratory, University of Blida 1, Algeria

²E2S UPPA, CNRS, IPREM, Université de Pau et des Pays de l'Adour, France

*Corresponding author

ABSTRACT

The tetragonal crystal structure of double tungstates $\text{NaY}(\text{WO}_4)_2$ has been determined. Our calculations confirm the insulating character of $\text{NaY}(\text{WO}_4)_2$, the obtained results were justified and discussed from the diagrams of bandstructures and density of states DOS and LDOS.

Introduction

Bi-tungstate materials of the general formula $\text{MT}(\text{WO}_4)_2$, where M is a monovalent alkali cation and T is a trivalent cation, the majority of these crystals have tetragonal symmetry with a random distribution of monovalent and trivalent ions¹ and they have attracted a lot of attention because of their excellent chemical stability in air and also in the field of spectroscopy specifically for the Laser. In the literature, a few theoretical researches work on double tungstates $\text{NaY}(\text{WO}_4)_2$ has been determined. The aim of this investigation, is to determine theoretically structural and electronics properties of double tungstates $\text{NaY}(\text{WO}_4)_2$.

Theoretical Study

The Bi-tungstate $\text{NaY}(\text{WO}_4)_2$ in his tetragonal phase, is characterized by space group $I4_1/a-C^6$ with lattice parameters $a=b=5.24\text{\AA}$, $c=11.38\text{\AA}$ and $\alpha=\beta=\gamma=90^\circ$. W occupies the tetrahedral sites composed by the O atoms, Na and Y cations have the same occupancy factors. An ab initio SCF-LCAO-B3LYP calculations are performed with Crystal17 program³ to determine structural and electronics properties of $\text{NaY}(\text{WO}_4)_2$.

Results and Discussion

Figure 1, show the primitive NYW cell. The W^{6+} ion is coordinated by four O^{2-} at a tetrahedral site, representations are performed with J-ice visualization program⁴.

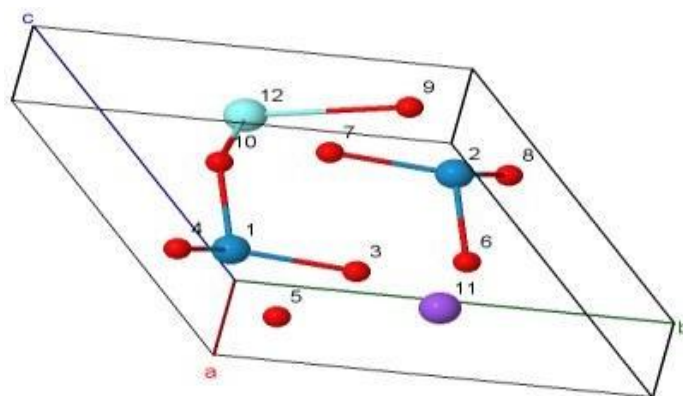


Fig.1. Elementary unit cell of $\text{NaY}(\text{WO}_4)_2$.



The band structure of $\text{NaY}(\text{WO}_4)_2$ along the high symmetry points of the irreducible Brillouin zone is shown in Figure 2a. Value of the band gap is the difference between the CBM and the VBM equal to 5.48 eV, which confirm the insulator character of $\text{NaY}(\text{WO}_4)_2$, is in good agreement with experimental results. Total density of states (DOS) and the projected on layer (LDOS) are shown in figure 2.b.

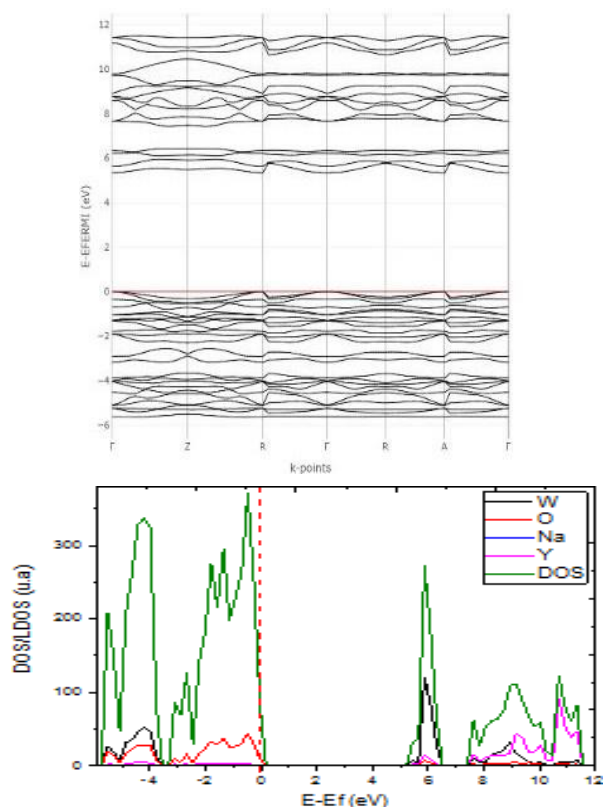


Fig.2. (a) Band structure of $\text{NaY}(\text{WO}_4)_2$, (b) DOS/LDOS

Conclusion

Double tungstates $\text{NaY}(\text{WO}_4)_2$ in his tetragonal phase has been studied at the level of SCF-LCAO-B3LYP theory. Calculations shows that is an insulator Materials with calculated band gap of 5.48 eV.

Acknowledgments

The authors gratefully acknowledge Chemical-Physics group of IPREM of Pau University.

References

- [1] L. Macalik, J. Hanuza, A.A. Kaminskii « Polarized Raman spectra of the oriented $\text{NaY}(\text{WO}_4)_2$ and $\text{KY}(\text{WO}_4)_2$ single crystals» (2000) 289–297.
- [2] HE Yizong, WANG Guofu, HUANG Xiaoying, Luo Zundu, «The Emission and Structure of a New Laser Crystal $\text{Nd}^{3+}:\text{NaY}(\text{WO}_4)_2$ » 1994, 267-271.
- [3] R. Dovesi et al., "User's Manual of CRYSTAL17", code available from <http://www.crystal.unito.it>
- [4] *J-ICE: a new Jmol interface for handling and visualizing Crystallographic and Electronics properties*, P. Canepa, R. M. Hanson, P. Ugliengo, M. Alfredsson *J. Appl. Cryst.* 44, 225 (2011)

First-principles Study of Structural, Electronic, Elastic and Thermal Properties of XPd_3 ($\text{X} = \text{Ca}, \text{Mg}$)

A. Benamer^{1,2*}, A. Roumili¹, Y. Medkour¹

¹Laboratoire d'Etudes des Surfaces et Interfaces des Matériaux Solides, Department of Physics, Faculty of Sciences, University of Setif1, 19000 Setif1, Algeria.

²Ecole normale supérieure de Bousaada

*Corresponding author

ABSTRACT

We report results obtained from first principle calculations of XPd_3 ($\text{X} = \text{Ca}, \text{Mg}$) compounds with antiperovskite structure. The estimated equilibrium lattice parameters are in agreement with the experimental ones. Elastic constants C_{ij} for single crystal are calculated, then polycrystalline elastic moduli (bulk, shear and Young moduli, Poisson ration, anisotropy factor) are presented. Based on Debye model, Debye temperature Θ_D is calculated from the sound velocities V_l , V_t and V_m . Band structure results show that the compounds under study are electrical conductors and the conduction mechanism is assured by Pd-d electrons. Bonding nature and bonds strength are discussed based on the partial densities of states, population analysis and the electronic charge distribution.

Keywords: Intermetallic compounds, Ab initio calculations, Elastic properties



Po57

Synthesis and Characterization of Polystyrene (PS)/Copper Oxide CuO Nanocomposites

Bessi Assia^{1,*}, Hamza kahina^{1,2}, Boudine Boubkeur³, Boudaren Chouki⁴

¹Laboratoire de chimie physique moléculaire et macromoléculaire « LCPMM », Saad Dahleb University, Route Soumâa BP270, Blida 09000, Algeria

²Laboratoire de recherche pour valorisation des produits bioactifs et valorisation de la biomasse, ENS Kouba, Algeria

³Crystallography Laboratory Physics Department, Faculty of Exact Sciences, Mentouri Brothers University, Route Ain ElBey, 25000 Constantine, Algeria

⁴CHEMS, Research Unit Mentouri Brothers University, Route Ain El Bey, 25000, Constantine, Algeria

*Corresponding author

ABSTRACT

In this work, copper oxide (CuO) nanoparticles were synthesized via the sol-gel process (soft chemistry), On the other hand, Polystyrene (PS) nanocomposites loaded with copper oxide (CuO) have been carried out using the solution mixing method. The effect of CuO nanoparticles on the properties of Polystyrene (PS) has been studied using a number of techniques: X-ray diffraction (XRD), Fourier transform infrared (FT-IR) and UV-Vis spectroscopy.

Introduction

Polymers are used in several sectors of human activity due to their properties and easy processing. On the other hand, nanoparticles have several advantages related to their large specific surface area. To take advantage of these two materials, the researchers thought of mixing them to take advantage of their advantages by erasing the defects. It was the birth of nanocomposites.

Experimental

Nanocomposite films loaded with different weights (5.10, 15 and 20%) of CuO nanoparticles were obtained after evaporation of the solvent. Films were deposited using spin coating.

Results and Discussion

From the analysis of the XRD Figure-1, it is observed that the average size of the CuO crystallites used in the PS / CuO nanocomposites is approximately 36 nm [1]. The results of FT-IR spectroscopy as shown in figure-2 confirm the existence of the CuO phase in the Polystyrene (PS) matrix. UV-Visible spectroscopy shows a decrease in the optical gap energy of nanocomposites [2]. In addition, it shows a significant shift in the energy of the band gap of CuO towards the blue which is attributed to the quantum confinement effect exerted by the nanocrystals.



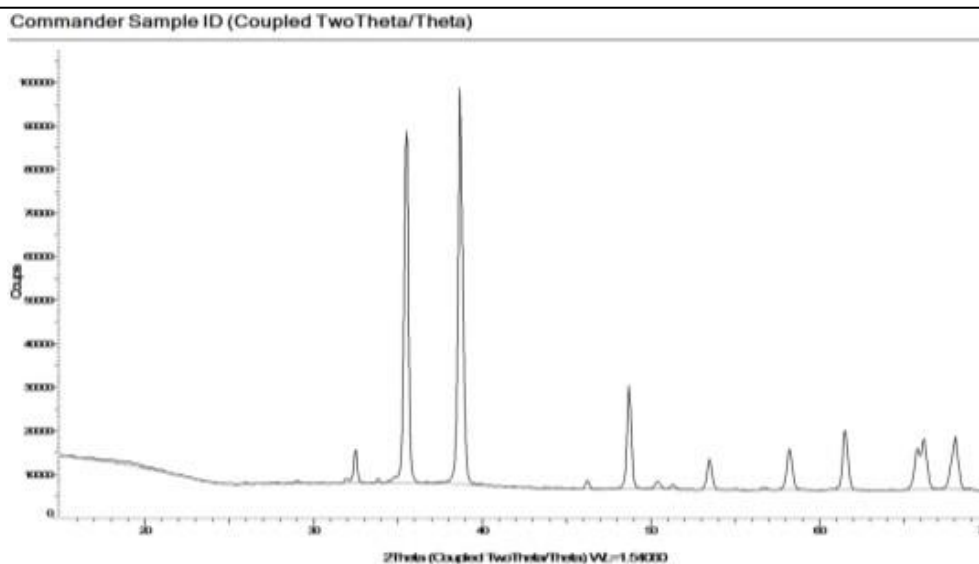


Figure-1: XRD pattern of CuO nanoparticles

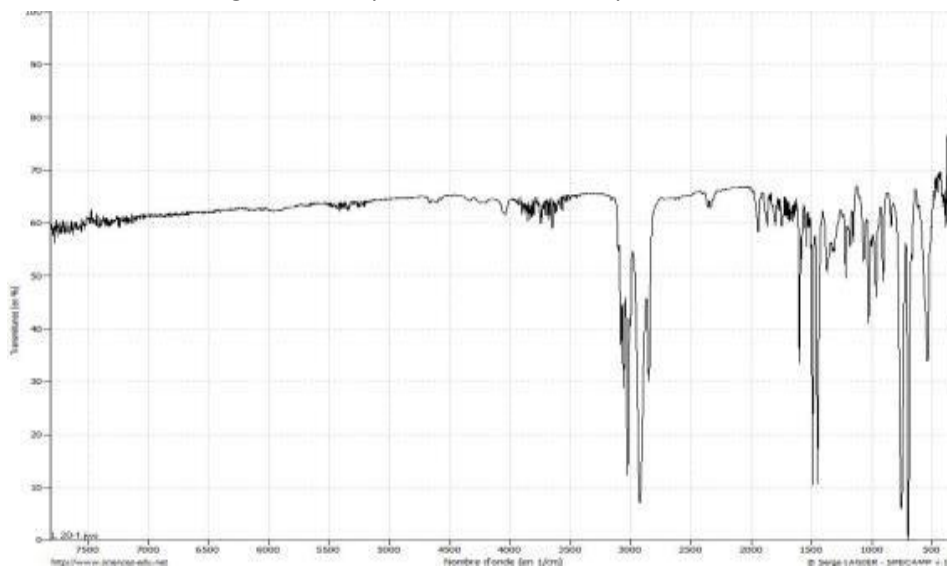


Figure-2: IF-TR spectrum of PS/CuO nanocomposite

Conclusion

The dispersion of these nanoparticles synthesized in a polymeric polysulfone matrix shows good dispersion and good homogeneity at the surface. These nanocomposites can be used in several fields, especially as packaging.

References

- [1] Das D, Nath BC, Phukon P, Dolui SK. Synthesis and evaluation of antioxidant and antibacterial behavior of CuO nanoparticles. *Colloids Surf B Biointerfaces*. 2013 Jan 1;101:430-3. doi:10.1016/j.colsurfb.2012.07.002
- [2] A. El-Trass, H. ElShamy, I. El-Mehasseb, and M. El-Kemary, "CuO nanoparticles: Synthesis, characterization, optical properties and interaction with amino acids," *Applied Surface Science* 258 (7), 2997-3001 (2012).

Po59

Theoretical Study of Structural and Electronics Properties of Lithium Niobate LiNbO_3

Nadia Hadjila¹, Faiza Bouamra¹, Michel Rérat²

¹Department of physic, LASICOM Laboratory, University of Blida 1, Algeria.

²E2S UPPA, CNRS, IPREM, Université de Pau et des Pays de l'Adour, France

*Corresponding author

ABSTRACT

The main objective of this work is to study the structural and electronic properties of Lithium niobite in his ferroelectric phase. Calculations are released using the periodic LCAO-DFT-B3LYP approximation with the program CRYSTAL17³. Analysis of band structure and density of state diagram shows that lithium niobate is an insulator.

INTRODUCTION

At the last decade, Lithium niobate (LiNbO_3 , LN) materials, has attracted a great interest as a future functional material due to their excellent ferroelectric, photorefractive, electro-optic, piezoelectric, nonlinear-optical, photocatalytic, and ion conductive properties^{1,2}. These various properties of LN open the way to various technological applications. The aim of this study is to release a calculation with Density Functional Theory (DFT) of structural and electronics properties of lithium niobate.

THEORETICAL STUDY

In the present work, structurals and electronics properties of lithium niobate (LiNbO_3) have been studied using density functional theory (DFT). Exchange and correlation functional were taken using the B3LYP approximation. The LiNbO_3 crystallizes in trigonal structure of hexagonal symmetry with ten atoms per unit cell. with space group R3c (no. 161) and change into para-electric phase (R3c) above 1480K temperature¹. Atomic positions are: Li (0, 0, 0.21956); Nb (0,0,0) and O(0.0376, 0.32347,0.1028)². The atomic configurations used are: Li $2s^1$, Nb $4d^4 5s^1$ and O $2s^2 2p^4$. Integration in the 1BZ use k-point mesh 9×9 of Monkhorst-Pack scheme.

RESULTS AND DISCUSSION

The unit cell structure of LiNbO_3 is shown in Fig.1. The optimized lattice parameters and related cell volume are presented in Table 1.

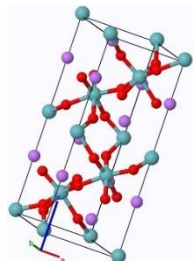


Fig 1 : Unit cell structure of LiNbO_3

a=b	c	volume	References
5.148	13.863	318.17	This work
5.159	13.869	320.18	Theor ³
5.147	13.849	317.73	Expt ⁴

Table 1 : Optimized lattice parameters and volume of unit cell of LiNbO_3



It is noted that the values of the structural parameters obtained are in good agreement and very close with the parameters of the literature.

Electronic properties

The energy bands of LiNbO₃ are along the high symmetry direction, (G-M-K) of the Brillouin zone. The Fermi level is chosen at zero value of energy Fig.2.a.

Total and local electronic density of states of LiNbO₃ are shown in Fig2. The value of the gap energy obtained is 11eV, which means that our system is an insulator. Analysis of diagram of DOS and LDOS, show that the conduction and valence band are essentially composed of the participation of niobium (Nb) and oxygen (O) atoms simultaneously. We note that the Li element has a weak participation at the CBM and VBM.

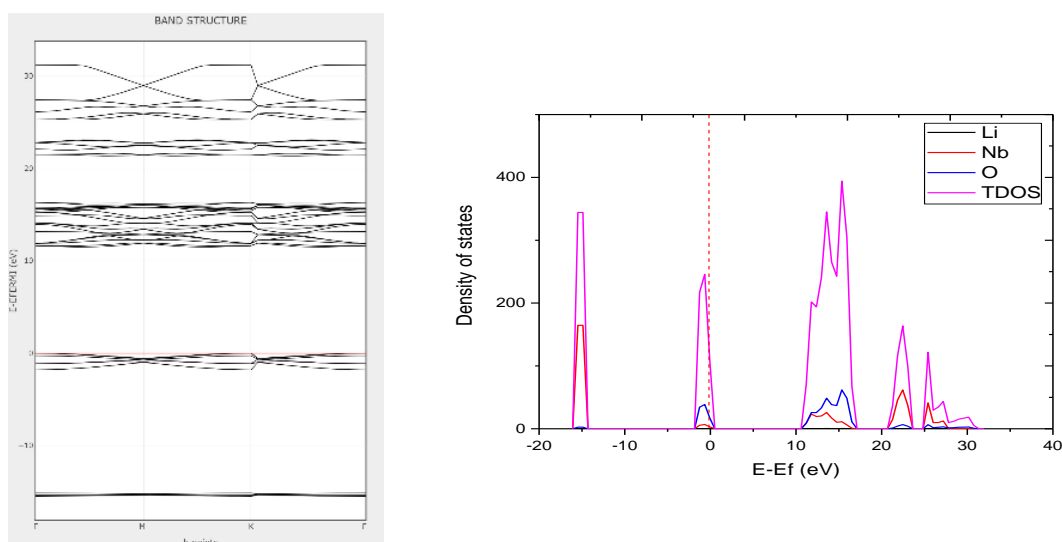


Fig.2: (a) Band Structure diagram of LiNbO₃, (b) Total and partial density of states (DOS) of LiNbO₃

CONCLUSION

Structural and electronic properties of LiNbO₃ have been studied by using SCF-LCAO-DFT-B3LYP approximation. The band gap of LN is calculated to be 11eV.

ACKNOWLEDGMENTS

The authors gratefully acknowledge Chemical-Physics group of IPREM of Pau University.

REFERENCES

- ¹K. Toyoura, M. Ohta, A. Nakamura, K. Matsunaga, J. Appl. Phys. 118 (6) (2015), 064103.
- ²S.C. Abrahams, E. Buehler, W.C. Hamilton, S.J. Lapaca, J. Phys. Chem. Solids 34 (3)(1973) 521e532.
- ³ R. Dovesi et al., "User's Manual of CRYSTAL17", code available from <http://www.crystal.unito.it>

Po61

Effect of Doping with Niobium on the Properties of Titanium Dioxide Thin Films Prepared by Sol Gel (Spin-coating) Process

Djehiche Nour el houda^{1*}, Saidi Hnane¹ and Attaf Abdallah¹

Physics of thin films and applications (LPCMA) university of Biskra Algeria

*Corresponding author

ABSTRACT

In this study we deposited undoped and Niobium doped Titanium Dioxide thin films with doping percent varied between (0% -10%) onto glass substrates by Sol-Gel spin-coating method. The films were analysed by the X-Rays diffraction (XRD), UV-Visible spectroscopy. The results obtained by the XRD showed that the prepared films are polycrystalline Titanium Dioxide with a tetragonal structure of anatase. The preferential orientation is (101). The UV-Visible spectrum indicated that the transmission of the films in the visible is about 90%.

Keywords: Thin films, Titanium Dioxide, Sol Gel (spin-coating), Niobium Doping.

Introduction

The study of matters in the form of thin films has been the subject of a growing number of studies since the second half of the 20th century due to advances technological in the development and the characterization of these layers. TCO materials are increasingly used in new applications and occupy an increasingly important place in our lives. They are at the base of a new scientific and technological revolution¹. Among the TCO, Titanium Oxide TiO₂ has an interesting properties (high chemical stability, high refractive index and transparency in the visible) that allow to use it in several applications².

Experimental/Theoretical Study

The Sol-Gel process is based on the conversion of a liquid into a solid phase by a series of chemical reactions of the hydrolysis and condensation type of the molecular solution of extreme purity³. In all samples, the starting solution contains Titanium Tetraisopropoxide used as dissolved ethanol, with a certain percentage of niobium chloride NbCl₅ as a source of doping source. The mixture is stirred by a magnetic stirrer at 50 ° C. The final solution is transparent yellowish and slightly viscous.

Results and Discussion

1: X-Ray diffraction:

The different peaks characteristic of the TiO₂ structure for different concentrations of Niobium are grouped together in Fig .1



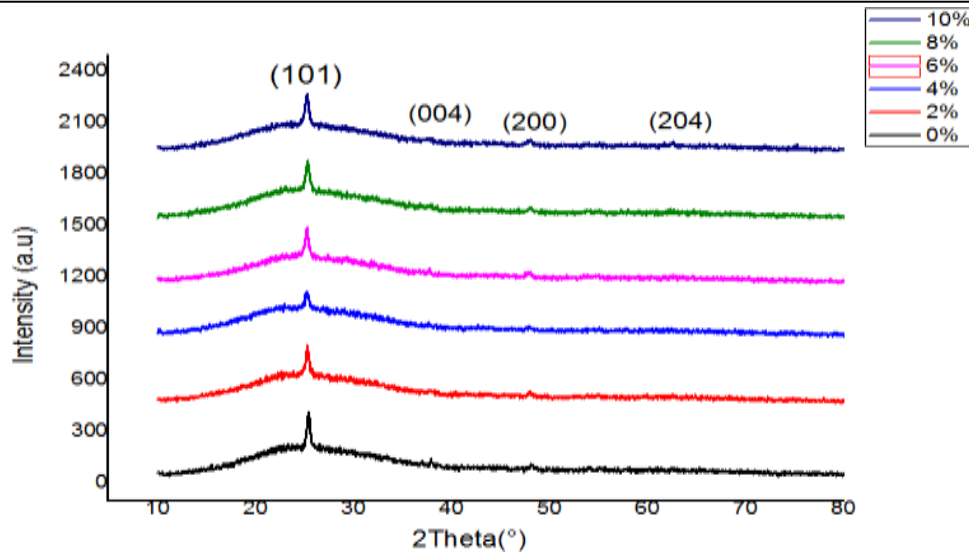


Fig.1: X-Ray diffraction patterns for Nb-doped TiO₂ thinfilms

According to the Fig.1 we observe a maximum intensity according to the plane (101), with the existence of other secondary peaks according to (004), (204) and (002) which correspond to the phase anatase^{4,5}.

2: The Optical properties:

The transmittance spectra of our samples are illustrated in the Fig.2:

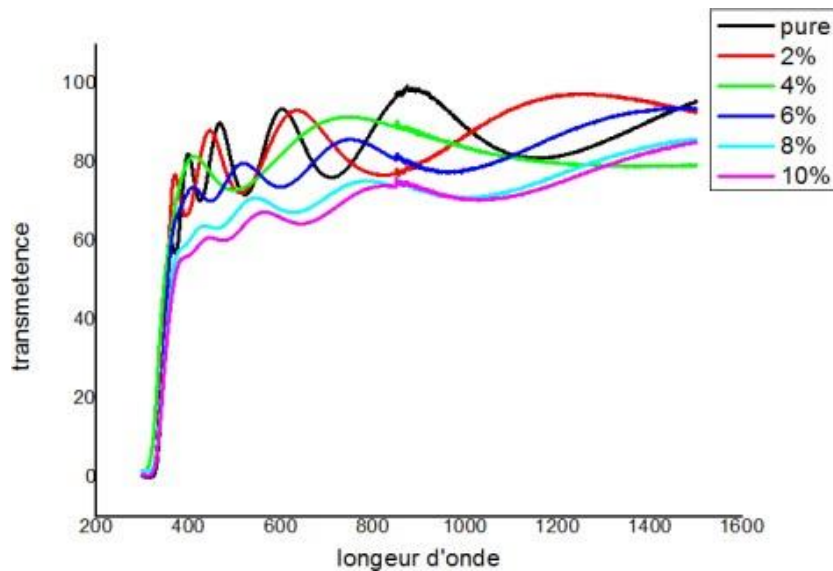


Fig.2: Optical transmittance spectra of TiO₂ thin films.

Transparent zone between 350 nm and 800 nm which makes it possible to know the transmittance value in the visible domain. We note that the transmittance value of our thin films is varied between 75% and 98%. It is also observed that the transmittance decreases with the increase of the doping concentration. This decrease is caused by the increase of the absorption due to the increase of opaque niobium atoms⁶.

Conclusion

In this paper we can say that we have succeeded in developing thin layers of undoped TiO₂ and doped with Niobium by the Sol-Gel technique (spin-coating) with good structural and optical properties

References

1. O. Bousoum, « Etude de l'effet d'une couche mince de TiO₂ sur les paramètres d'une cellule solaire au Silicium », Memory of Magister, Mouloud Mammeri University, TiziOuzou, 2011.
2. V. Trinte, « Etude de théorie des phases du titane », doctorat thesis, school polytechnique, 2007.
3. G. Granger, « Etude et développement de fibres optiques par voie sol-gel composées de nanocristaux à base d'oxydes (ZrO₂, SnO₂). Application aux sources lasers », Doctorat thesis, Limoges university, France, 2013
4. M. A. Golobostanfard, H. Abdizadeh, *Physica B*, 413(2013) 40-46.
5. M. Alzamani, A. Shokuhfara, E. Eghdama, S. Mastalib, *Materials International*, 23 (2013) 77- 84.
6. H. Su et al, *Electrochimica Acta* 182 (2015) 230–237.

Po62

Structural, Electronic, Elastic and Thermodynamic Properties of ReAuSn

Halima HAMADA*, Kadda AMARA, Friha KHALFAOUI; Fatiha SAADAUI, Samira HAMADA
Laboratoire physico-chimique Université Dr Moulay Tahar de Saïda, Saïda, Algerie

*Corresponding author

INTRODUCTION

Among Intermetallic phases, the compounds containing rare-earth atoms from numerous Class, well studied for many years in both fundamental and applied research. all known phases are binary or ternary compounds, with some general features [1]. The equiatomic intermetallic ReTX, where (Re) rare- earth element, T=transition metal and X= element of the 3 rd, 4th or 5th main group [2]. In this work, The electronic, structural properties of the Intermetallic ReAuSn (Re=Sc,Lu) have been calculated using the full potential linearized Augmented plane wave (FP-LAPW) method within GGA and LDA approximation.

EXPERIMENTAL/THEORETICAL STUDY

Full-Potential Linearized Augmented Plane Wave (FP-LAPW) method was used for the first-principles calculations within the density functional theory DFT [3-4]. using WIEN2K code [5]. We have investigated the structural, electronic, elastic and thermal properties of ReAuSn (Re=Sc,Lu). and the exchange-correlation energy was calculated using the approximation (GGA) (PBE) LDA and GGAPBsol for the calculation of structural properties. so that the electronic elastic thermal properties compute with GGA. In this calculation we have used 2000 K-point in the first Brillouin zone for the structural properties and 4000K-point for the electronic elastic properties. which marks the separation of valence and core states was chosen as -6 Ry.

RESULTS AND DISCUSSION

Table 1. The calculated values of the lattice parameter (A°), bulk modulus (GPa), and its pressure derivative of ReAuSn

compond		a (A°)	B	B'	Expt
ScAuSn	PBE	6.5187	90.0866	4.9687	6.4194
	PBEsol	6.4271	100.6010	5.0794	
	LDA	6.3672	111.1603	5.0124	
LuAuSn	PBE	6.6639	83.6716	4.8745	6.5652
	PBEsol	6.5618	95.7994	5.1533	
	LDA	6.4976	106.3989	5.0478	



Table 2: Calculated elastic constants C_{11} , C_{12} , and C_{44} (GPa); bulk modulus B (GPa); shear modulus G (GPa); Young's modulus E (GPa); Poisson's ratio ν ; for ReAuSn (Re=Sc, Lu):

Paramètres	ScAuSn	LuAuSn
C_{11}	132.8858	129.5031
C_{12}	69.3442	63.6711
C_{44}	73.1487	66.5420
B (Gp)	90.524	85.615
G (Gpa)	52.345	50.164
E (Gpa)	131.658	125.902
ν	0.257	0.254

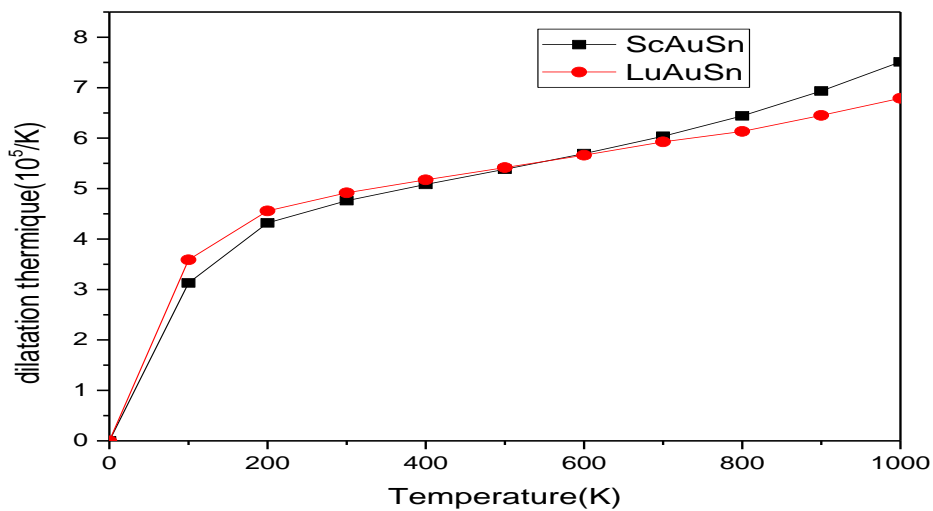


Fig1. Variation of the dilatation thermique en fonction de la temperatura at $P=0$

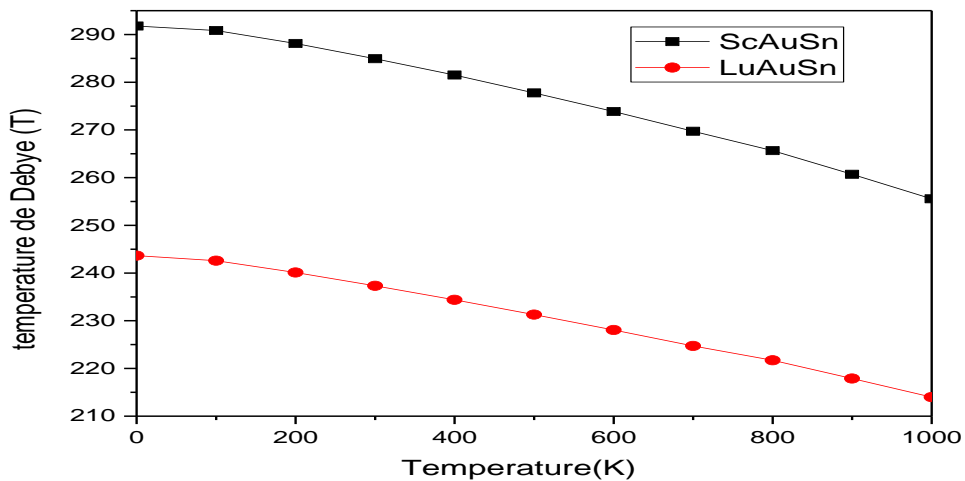


Fig 2 Variation of the Debye temperature as a function temperature at $P=0$.

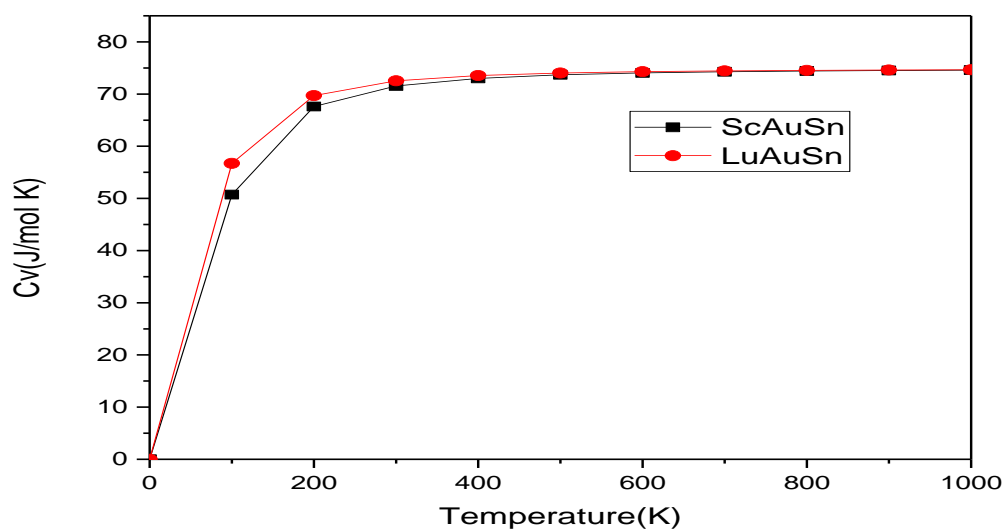


Fig 2 Variation of the CV as a function temperature at P=0

CONCLUSION

The structural, mechanical, electronic and thermal properties of ReAuSn (Re=Sc,Lu) ternaries are investigated using the FPLAPW method with PBE-GGA exchange correlation. The results reveal that ReAuSn (Re=Sc,Lu) is stable for (NM) configuration structure. According to the elastic properties results, we found that our material ReAuSn (Re=Sc,Lu) is mechanically stable. For the electronic properties, we have observed that have indirect gap.

ACKNOWLEDGMENTS

The authors acknowledge the Algerian Ministry of Higher Education and Scientific Research (MESRS)

REFERENCES

1. Sudhindra Rayaprol, C .peter Sebastian, Rainer PÖttgen, J of solid state chemistry 1979 (2006) 2014-2046.
2. P.Hohenberg and W.Kohn.phys .Rev.136(1964)B864 W.Kohn and L.JSham. phys .Rev 140(1965)A1133.
3. P. Hohenberg, W. Kohn, Density functional theory (DFT), Phys. Rev, 136 (1964) B864
4. W. Kohn, L.J. Sham, Self-consistent equations including exchange and correlation effects, Physical review, 140 (1965) A1133.
5. D. Kvasnicka, J. Luitz, wien2k, An augmented plane wave+ local orbitals program for calculating crystal properties, (2001).

Po63

Investigation of Deposition Temperature and Time Effect on the Quality of FSF in n-PERT Solar Cells Using Phosphorus Doped Paper Sheets

LABDELLI Boutaleb*¹, MEDANI Sonia², HAMIDI Samira², ABDELGHANI BOUCHEHAM¹, DJELLOUL Abdelkader¹ and BENHARRAT Lyes¹

¹Research Center in Semiconductor Technology for Energetic (CRTSE) 02 Bd. Frantz Fanon—Alger, BPN°140, Les 07 Merveilles—Algiers—Algeria

²Mouloud Mammeri University of Tizi Ouzou (UMMTO) Faculty of Electrical and Computer Engineering Department of Electronics BP N ° 17 RP, Hasnaoua I, 15000 Tizi-Ouzou Algeria

³Research Center in Semiconductor Technology for Energetic

*Corresponding author

ABSTRACT

The generation of phosphorus-diffused Front Surface Fields (FSF) is regarded as a key step in the fabrication of high-conversion-efficiency n-typePERT (passivated emitter rear fully diffused) solar cells. Experimental data show that the application of a FSF reduces the total series resistance. The penetration depths in the range of 0.50 μm and 0.81 μm , the dopants surface concentrations are $2.5 \text{ E}21 \text{ cm}^{-3}$ and $1.9 \text{ E}22 \text{ cm}^{-3}$ for n-850 and n-900 °C respectively. The passivation property was studied, and it was discovered that the effective lifetime grew considerably to 127 μs at 900 °C and a deposit period of 20 minutes, and subsequently decreased to up to 20 μs at the same temperature and a deposition time of 6 minutes.

Keywords: n-type silicon solar cells; n-PERT; front surface field (FSF); lifetime (t_{eff}).

Introduction

Because of its great efficiency, n-type crystalline silicon (c-Si) solar cells are now attracting a lot of attention. In this work, we presented front surface field (FSF) optimization for n-PERT¹ (Passivated Emitter Rear Totally-diffused). N-type silicon has longer bulk lifetimes and is less susceptible to metal impurities² and light-induced degradation³. The primary function of an FSF is to decrease the dark emitter current and therefore raise the open-circuit voltage⁴. This study presents findings for industrially optimizing diffusion (FSF), with a focus on the two parameters temperature and deposition time to obtain high FSF performance.

Experimental

We employed sheet paper (perform source) to examine the FSF quality diffusion through phosphorus source doped n-type monocrystalline silicon wafers with low resistivity (1 - 3 Ωcm). The diffusion process is carried out in the Omega Junior 3 oven of the manufacturer Tempress (Holland). The effect of diffusion temperature and deposition time is investigated.



Results and Discussion

SIMS and ECV measurements reveal that diffusion by a solid source at 900°C and a deposition period of 20 minutes yields a satisfactory result, which is consistent with minority carrier lifetime data or a good passivation of the surface. The Hall stripping technique we demonstrate that increasing the deposition temperature or duration reduces the Hall mobility, which may be explained by a high doping level. For a doping time of 10 min we have a concentration of $1.83 \times 10^{16} \text{ cm}^{-3}$, a larger fraction of substituted phosphorus.

Conclusion

Sample n-850 had a penetration depth of 0.65 μm and a concentration of $2.5 \text{ E}21 \text{ cm}^{-3}$, whereas sample n-900 had a depth of 0.81 μm and a concentration of $1.9 \text{ E}22 \text{ cm}^{-3}$. We investigated the effective lifetime of the minority charge carriers. We achieved lifetime values 127 μs and an open circuit voltage of 634.5 mV using iodine-ethanol passivation at a deposition temperature of 900 ° C and deposition duration of 20 minutes.

Acknowledgments

The author would like to thank the Research Center in Semiconductor Technology for Energetic CRTSE/ and Directorate General for Scientific Research and Technological Development.

References

1. Blevin, T., Lanterne, A., Grange, B., Cabal, R., Vilcot, J.P., Veschetti, Y., 2014. Development of industrial processes for the fabrication of high efficiency n-type PERT cells. *Sol. Energy Mater. Sol. Cells* 131, 24–29.
2. Glunz SW, Rein S, Lee JY, Warta W. Minority carrier lifetime degradation in boron-doped Czochralski silicon. *Journal of Applied Physics* 2001; 90: 2397–2404.
3. Macdonald D, Geerligs LJ. Recombination activity of interstitial iron and other transition metal point defects in p- and n-type crystalline silicon. *Applied Physics Letters* 2004; 85: 4061–4063.
4. Lindholm FA, Neugroschel A, Pao SC, Fossum JG, Sah CT, Design consideration for silicon HLE solar cells. In: *Record of the 13th IEEE Photovoltaic Specialist Conference*: 1978. p. 1300e1130.

Ab-initio Study of the Optoelectronic Properties of CsXCl₃ Perovskites (X = Pb, Sn or Ge)

Samira BOUKACHABIA*, Fatima Zohra BENTAYEB

Laboratory of Magnetism and Spectroscopy of Solids (LM2S) Badji Mokhtar University, P. O. Box 12, Annaba
23000, Algeria

*Corresponding author

Introduction

Halide perovskite-based solar cells are very attractive due to their excellent power conversion efficiency and low cost.

Experimental/Theoretical Study

In this work CsXCl₃ perovskite alloys (X = Pb, Sn or Ge) are investigated using the ab initio Quantum Espresso package, which is based on the pseudo-potential and plane wave methods.

Results and Discussion

The calculation of the electronic band structures and the density of states shows that these materials have a direct gap, which is crucial for photovoltaic applications. In addition, the light absorption domain is determined through the examination of the optical properties, allowing us to better understand the photovoltaic behavior of these compounds.

Conclusion

Our results reveal that these materials are promising photovoltaic candidates.

Keywords: Photovoltaic materials; perovskite structure; DFT; TDDFT; Quantum Espresso; Band gap.

References

1. Idrissi S, Ziti S, Labrim H, Bahmad L, « Band gaps of the solar perovskites photovoltaic CsXCl₃ (X=Sn, Pb or Ge) » Materials Science in Semiconductor Processing 122 (2021) 105484
2. Hamid M. Ghaithan, Zeyad. A. Alahmed 1, Saif M. H. Qaid, Abdullah S. Aldwayyan « Materials Structural, Electronic, and Optical Properties of CsPb(Br_{1-x}Cl_x)₃ Perovskite: First-Principles Study with PBE-GGA and mBJ-GGA » Materials 2020, 13, 4944; doi:10.3390/ma1321494
3. Muhammad Amin P, Minqiang W, Yongqiang Ji, Yun Zhou, Hengwei Qiu and Zhi Y « Stable near white light emission in CsPbCl₃ perovskite quantum dots by incorporating Al³⁺/Mn²⁺ ions » Nano Express 1 (2020) 030033



High Spin Polarization and Mechanic Stability of Half-Heusler Compounds: CrFeSn and CrFeGe as a Candidate in the Spin-FETs for Spintronic Applications

Abbès Beloufa^{1*}, Driss Bouguenna² and Khaled Hebali³

^{1*}Department ST/Faculty of Science and Technology, University Mustapha Stambouli of Mascara, Algeria

²Department ST/Faculty of Science and Technology, University Mustapha Stambouli of Mascara, Algeria

³Department of Physics/Faculty of Exact Sciences, University Mustapha Stambouli of Mascara, Algeria

*Corresponding author

ABSTRACT

In this work, we have performed self-consistent ab-initio calculation using the full-potential muffin-tin orbital method based on density functional theory (DFT), to study the electronic, magnetic and elastic properties of the half-Heusler compounds CrFeSn and CrFeGe with generalized gradient approximation (GGA+U) and mBJ- GGA+U. The magnetic proprieties of CrFeSn and CrFeGe are well defined within mBJ with an exact integer value of magnetic moment, using this approach for the total energy as a function of the strain. We calculate the elastic constants of the compounds studied in their structure which are not yet reported in the *C1b* structure, and can therefore be realized under ideal experimental circumstances. These alloys seem to be a potential candidate in the spin-FETs for spintronic applications.

Keywords: Half-Heusler, Magnetic, ab initio, Spin-FET, Spintronic.

Introduction

Several research groups have worked on the spin-field effect transistors (spin-FETs) device using semi-Heusler metals are considered to be optimal electrodes have also been employed in the spin-FETs where the spin polarized current injectors to lateral spin valves for spintronic applications [1]. The compounds (CrFeSn and CrFeGe) prove to be potential topological insulators and are promising candidates for improving the performance of microelectronics and optoelectronics [2]. A further investigation on the electronic and magnetic properties still required. In this letter, we present a computational study on the two CrFeSn and CrFeGe half-Heusler compounds using the full-potential muffin-tin orbital (FP-LMTO) method based on DFT.

Method Description

All electron full-potential linear muffin-tin orbital method as implemented in the LMTO code is used for the calculation of the physical properties of the XYZ compounds and the density of state (DOS) [4], within the DFT in the generalized gradient approximation GGA + U approach for the optoelectronic properties. The half-Heusler compounds XYZ crystallizes in the face centered cubic (fcc) (Figure 1) structure with the space group F43m (No.216). The electronic configurations with core level correction are Cr (3d44s2), Fe (3d64s2) and Ge (4s24p2) [5], respectively. The self-consistent calculations are considered to converge only when the calculated total energy of the crystal



converges too less than 0.0001Ry. The convergence was obtained using k points in the first Brillouin zone where 1500 special k points were used for CrFeSn and CrFeGe compounds. For the Hubbard parameter U employed in the GGA+U, we have used U=4 eV for Fe and U=3.5 eV for Cr [9, 10]. The exchange interaction J is set to J=0.

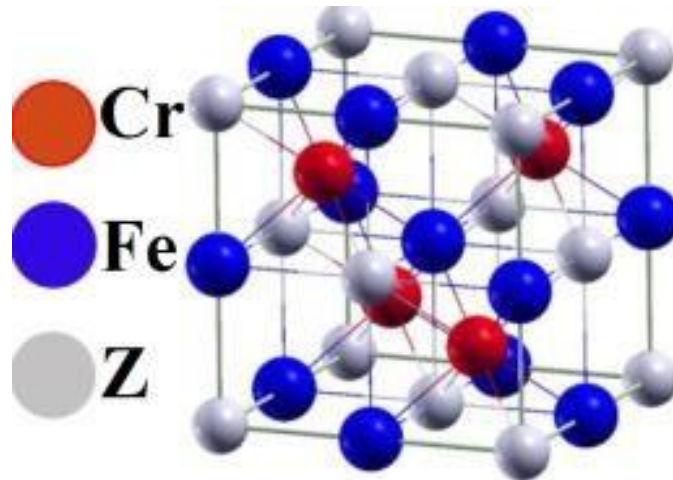


Fig.1 XYZ half-Heusler crystal structure

Results and Discussion

The two half-Heusler compounds (CrFeSn and CrFeGe) in $C1b$ phases at zero temperature. Therefore, it is possible to say that this half-Heusler compound is a metallic ferromagnetic material when GGA method is used. However, when the mBJ method was used, the band gap was seen around the Fermi energy level in spin up electrons. This showed that spin-up electrons had semiconductor properties and spin-down electrons had metallic nature. Thus, in the mBJ method, the half-Heusler compound showed half-metal ferromagnetic nature.

Conclusion

Our calculation showed that the dependence of the magnetic properties on the Sn and Ge element in the investigated half-Heusler systems using DFT based on the full-potential muffin-tin orbital (FP-LMTO) method. The half-metallicity of the two families have also been confirmed. Furthermore, the studied of CrFeSn and CrFeGe compounds have demonstrated a certain mechanical stability performance against compression. These compounds can be considered as an ideal electrode material to achieve the ohmic contacts of spin-FET devices for spintronic applications.

References

1. Bandyopadhyay S, and Cahay M., Appl. Phys. Lett. 2004; 85.
2. Kieven D, Klenk R, Naghavi S, Felser C, Gruhn T, Phys. Rev. 2010; 075208: B 81.
3. Slater J.C, Phys. Rev. 1936; 931: 49.
4. Savrasov S.Y., Phys. Rev. 1996; 16470: B 54.
5. Pauling L., Phys. Rev. 1938; 899: 54.

Investigation of an Additional Oxidation in-situ Step During Boron Diffusion Processes on P⁺ Emitter Properties

Abdelghani Boucheham*, Abbas Maref, Chahinez Nasraoui, Lyes Benharrat, Boutaleb Labdelli,
Abdelkader Djelloul

Research center in semiconductor technology for energetic, 02, Bd Frantz Fanon, les 7 merveilles, Algiers,
Algeria

*Corresponding author

ABSTRACT

Diffusion of boron in n-type silicon from preform source when using one step high temperature as drive-in temperature during the diffusion process was found to produce p⁺ emitter with relatively high surface concentration up to 1020 atoms /cm³, leading to high surface recombination, and resulting, therefore, in the formation of an undesirable boron rich layer (BRL) which is found to be responsible for the degradation of the bulk lifetime. One way to reduce the emitter boron surface concentration and to avoid the formation of the BRL is to add an additional step during the diffusion process which is the oxidation in-situ. The main purpose of the present work is to investigate the effect of a combination between an oxidation at 800°C for 30 min in oxygen ambient following a drive-in step at 910°C for 20 min in nitrogen ambient and a variable boron dose on the properties of the produced emitters. The boron dose was adjusted by varying the temperature ramp-up time from 51 min to 102 min. It was found that the boron surface concentration is reduced significantly from 1.17x10²⁰ to 2.31x10¹⁹ atoms/cm³ as measured by electrochemical capacitance voltage technique leading to an increase in sheet resistance from 45 to 65 Ω/sq as measured by four point probe after adding an oxidation in-situ step. The use of the free on line simulator EDNA 2 for plotting the variation of emitter dark saturation current density J_{0e} as a function of effective surface velocity SR_{veff} shows that adding a second step during diffusion process enhance considerably the electrical properties of the emitter.

Keywords: preform source, boron diffusion, boron rich layer, depletion zone, EDNA 2, simulation, n-type silicon, solar cells



Po67

Effect of Heat Treatment on Structural and FTIR and Lowercase

OULD ARAB Halima^{1,2}, BOUMEDDIENE Abdelkader ² and OUAGUED Abdellah³

¹Department of Material Sciences, Djilali BOUNAAMA University, Khemis Miliana

²LASICOM laboratory; Department of Physic, Blida 1 University, Blida

³*LEE laboratory, Hassiba BENBOUALI University

*Corresponding author

Introduction

Tin oxide (SnO₂) is an important oxide semiconductor with wide band gap ($E_g=3.6$ eV) exhibiting high transparency and high electrical conductivity. These characteristics make it a highly conductivity multifunctional material. Due to this, tin oxide thin films have been widely used in different application areas such as gas sensors, catalysis transparent electrode, Solar cells, spintronics and others. The most important use of SnO₂ is for gas sensors. The sensing properties of SnO₂ sensors depend on several factors, mainly crystallite size, surface structure and existing bonds. Several methods have been employed for preparing tin oxide thin films including CVD, Sol Gel, spray pyrolysis and others.

In this paper we report on the preparation and structural characterization of tin oxide. We report the effect of the heat treatment temperature on crystallinity and FTIR spectra.

Experimental

SnO₂ thin films have been prepared using Atmospheric Air Chemical Vapor Deposition (APCVD), tin Chloride SnCl₂ was employed as precursor. Thin films were deposited on glass substrate. We have used a three temperature zones horizontal tubular furnace which is attached to two separate gas sources, one for oxygen and the other for argon. The heat treatment was carried out in the same furnace. Samples were annealed for 30 minutes for 200°C and 400°C temperature. The X-ray diffraction patterns were collected using X'Pert Pro MPD of Panalytical. The FTIR spectra were drawn with an Alpha–Bruker spectrophotometer.

Results and Discussion

The XRD patterns recorded for all SnO₂ samples showed the presence of tetragonal rutile-type structure (JCPDS N°: 041-1445). However, the unheated pattern shows only three broad peaks corresponding to the more intense reflexions given a calculated crystallite size of 31,72 nm however, the weak crystallinity of unheated SnO₂ thin film have not been observed in heated samples it has been modified. Both intensity and number of peaks have been increased show that the crystallinity of samples have been improved and the crystallite size becomes 39.2 and 39.8 nm respectively for heating samples. The Scherer relation estimate the average crystallite size of the samples. Moreover, the cell parameters (a and c) of the films extracted from the relation relevant for tetragonal structure.



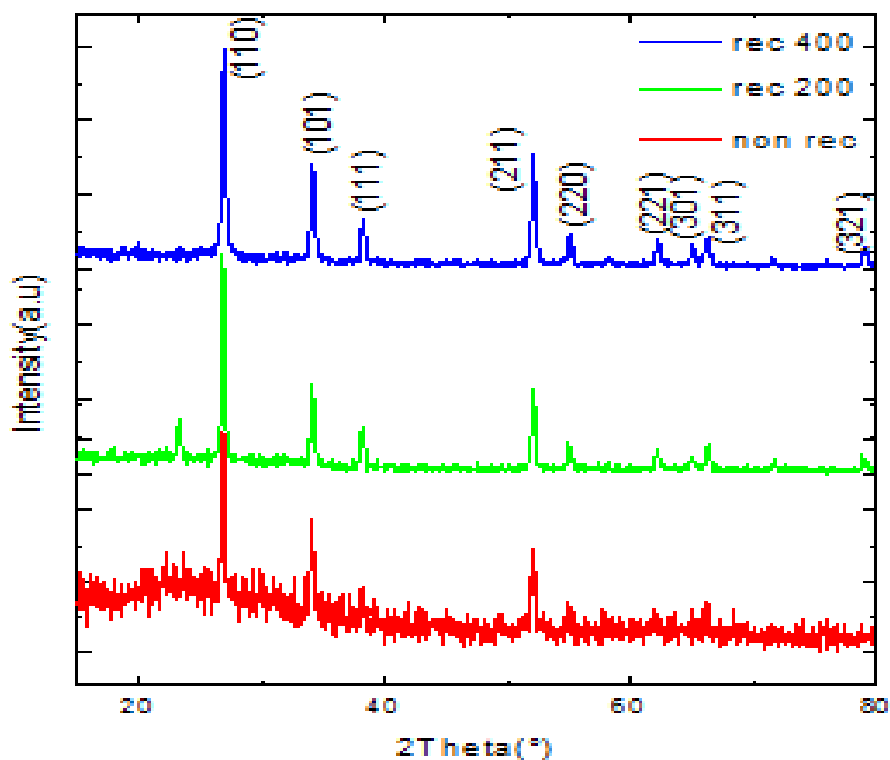


Figure 1: XRD patterns of SnO₂ thin films. Unheated sample (red) heated 200°C (green), 400°C (bleu). Figure 2 shows the FTIR spectra of the samples treated under the same annealing temperatures. The absorption peaks positions demonstrated that the SnO₂ samples had the same chemical bonding characteristics.

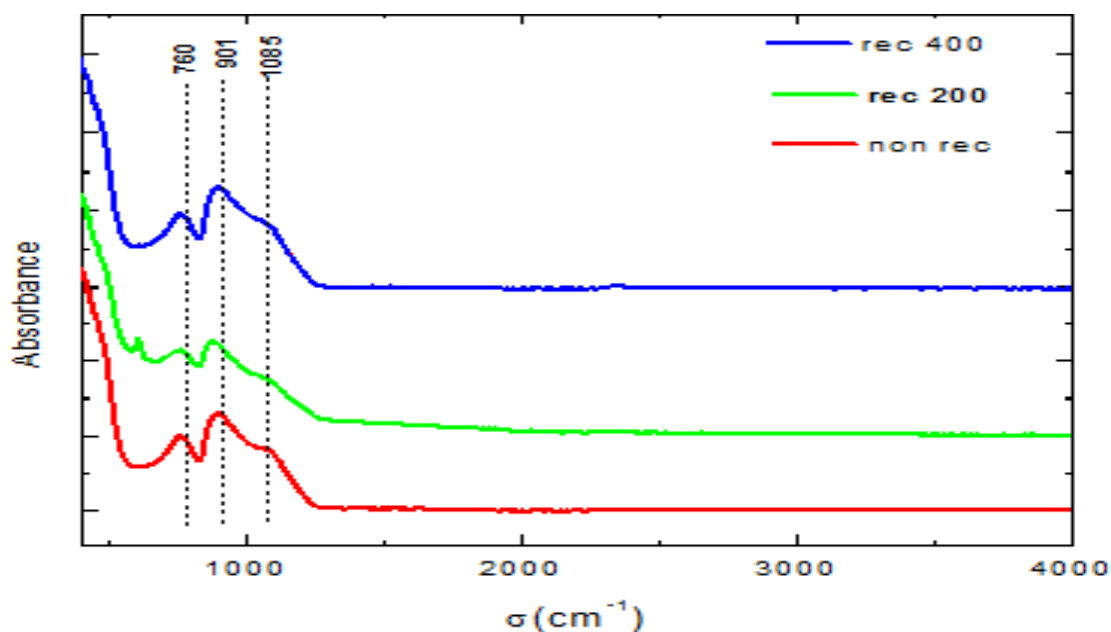


Figure 2: FTIR spectra of SnO₂ thin films. Unheated sample (red) heated 200°C (green) and 400°C (bleu)

in the range of 700-970 cm^{-1} are due to the vibration of the oxygen bonds of the surface cations Sn=O and Sn-O. peak observed at about 1085 cm^{-1} was due to Sn-OH There is not any peaks assigned to the carboxyl groups.

Conclusion

The results show that the obtained layers correspond to the rutile SnO₂ structure of poly crystalline nature of preferential orientation according to the plane (110) which was confirmed by the literature. Both, line width and peak intensity depends on the annealing temperature. FTIR results confirm the XRD ones.

References

1. Rasheed, Rashed T., and Sariya D. Al-Algawi. "Annealing effect of SnO₂ nanoparticles prepared by the sol-gel method." *Journal of Advanced Physics* 5.3 (2016): 236-240.
2. Khan.A, Mazhar.M, Aslam.M, Ashraf.M *Applied Surface Science* 256 (2010) 2252–2258
3. Chatelon, J. P., C. Terrier, and J. A. Roger. "Influence of elaboration parameters on the properties of tin oxide films obtained by the sol-gel process." *Journal of Sol-Gel Science and Technology*.

Po68

Characterization of Interfacial and Mechanical Properties Between Fiber and Polymer Matrix in Composite Materials

Hanane Ibrahim*, Dalila Hammiche, Amar Boukerrou

Department of process engineering, University of Abderrahmane Mira- Bejaia, Algeria

*Corresponding author

Introduction

The trend toward biobased materials is not only interesting in terms of environmental impact but also constitutes an alternative solution to fossil-based materials. Therefore, many scientists investigate the possibilities to reinforce some polymers with plant fibers ^[1,2]. However, the poor adhesion between fiber and matrix is the major problem when applying natural fibers ^[3,4]. Surface modification of fibers is necessary for improving their performance ^[5-7]. Therefore, the use of surfactants should have a significant impact on enhancing the mechanical properties of biocomposites. Good quality of dispersion-wettability and a homogeneous distribution of fiber within the matrix, as well as the level of interfacial interaction between the filler and the polymer, are the key points for the production of polymeric biocomposites with significantly improved properties ^[8].

Experimental/Theoretical Study

The polymer used in this work is Poly (lactic acid) (2003D grade) in the form of pellets. It was procured from Nature Works LLC, USA. Alfa used was collected from the M'sila region of Algeria. The surfactant has been kindly given by BYK-CHEMIE whose properties are reported previously ^[9]. Biocomposites based on PLA and 30 wt% of treated or untreated alfa fibers, were performed using a twin-screw extruder (type 5&15 micro compounder DSM Xplore method) at a uniform temperature (180 °C) and a constant screw rotation speed (50 tr/min). The samples with 1 mm thickness were prepared by compression molding (CARVER press) at T = 180 °C and P = 1.3 MPa for 5 min.

Results and Discussion

The mechanical properties of PLA and composites indicate that surface treatment leads to an increase in flexural modulus. Indeed, we obtained a value of 4800 MPa for virgin PLA and 4900 and 29000 MPa for the composites before and after treatment, respectively. This increase in the modulus indicates that the rigidity of the composites is increased. Since stiffness is not very sensitive to the modification of interfacial adhesion and interaction ^[10]. Really, it can be explained only from the change of the deformation mechanism. The rigidity and the good dispersion of fiber after treatment lead to changes in interaction and chain mobility. So, the use of the dispersing agent enhances the dispersion state of rigid fiber which prevents the movement of PLA chains and increases the modulus. This result is confirmed by SEM analysis (Figure 1). As can be seen, SEM micrographs of the treated composites (figure 1.b) indicated clearly that better fiber dispersion is achieved and the clogging issue is alleviated, arising from alfa agglomerates during processing.



Conclusion

The results indicated that the addition of surfactant had beneficial effects on the PLA/alfa composites, resulting in inhomogenous load distribution and strong adhesion between the fiber and the PLA matrix. The comparative study showed that the treatment effect of fiber is more pronounced using surfactant.

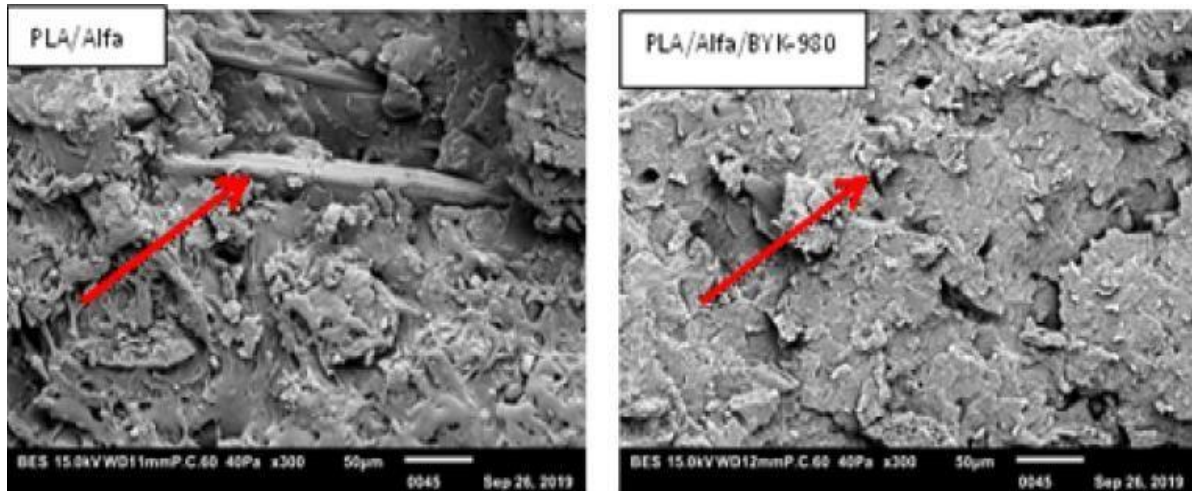


Figure 1. SEM micrographs of the fracture surface of a (PLA)/alfa composite (_50 magnification).

(a) PLA alfa, (b) PLA/alfa/ BYK W-980.

References

1. J. Cruz, R. Figueiro, *Procedia Eng.* 2016, 155, 285.
2. K. S. Chun, S. Husseinsyah, 2012, doi:10.1007/s10965-012-9859-8.
3. F. P. La Mantia, M. Morreale, *Compos. Part A* 2011, 42, 579.
4. B. . Mitra, *Def. Sci. J.* 2014, 64, 244.
5. R. Mehta, V. Kumar, H. Bhunia, S. N. Upadhyay, *J. Macromol. Sci. - Polym. Rev.* 2005, 45, 325.
6. F. E. El-abbassi, M. Assarar, R. Ayad, N. Lamdouar, *Compos. Struct.* 2015, 133, 451.
7. Y. Zhao et al., *Appl. Polym. Sci.* 2004, 91, 2143.
8. V. Mazzanti et al., *Compos. Sci. Technol.* 2019, 180, 51.
9. H. Ibrahim, D. Hammiche, A. Boukerrou, C. Delaite, *Mater. Today Proc.* 2020, doi:10.1016/j.matpr.2020.05.120.
10. H. Ibrahim, A. Boukerrou, D. Hammiche, *Macromol. Symp.* 2021, 2000266, 3.

Abstracts of
1st International Conference on
Computational & Applied Physics

Editor: **BOUAMRA Faiza**

ICCAP'2021

Organized by:

**Surfaces, Interfaces and Thin Films Laboratory (LASICOM),
Department of Physics, Faculty of Science,
University Saad Dahleb Blida 1, Algeria**

26–28 September 2021



LASICOM

To learn more about AIJR Publisher
Please visit us at: www.aijr.org

AiJR



ISBN 978-81-954993-3-5



9 788195 499335